Topics in Theoretical Astrophysics

Thesis by

Chao Li

In Partial Fulfillment of the Requirements
for the Degree of
Doctor of Philosophy

California Institute of Technology
Pasadena, California

2009
(Defended Sep 29, 2008)

Acknowledgements

First and foremost, I would like to thank Yanbei Chen, Asantha Cooray, and Kip Thorne, for being great advisors, for constant support and encouragement on my research, for stimulating discussions, and for painstakingly teaching me how to write scientific papers and give clear and well-organized presentations. Without their advice, guidance, and encouragement, this work would not have been possible. I am deeply thankful to Re'em Sari for inspiring collaborations that have contributed a great portion of what I have learned during my time as a graduate student at Caltech. They taught me a lot about cosmic microwave background, dark energy, 21cm cosmology, gamma ray bursts, and relativistic hydrodynamics.

Rana Adhikari and Marc Kamionkowski have my thanks for serving on my oral or defense committee.

I would like to thank Jeandrew Brink, Duncan Brown, Karsten Danzmann, Hua Fang, Jonathan R. Gair, Daniel E. Holz, Geoffrey Lovelace, Ilya Mandel, Helge Müller-Ebhardt, Yi Pan, Henning Rehbein, Roman Schnabel, Tristan L. Smith, and Kentaro Somiya, for collaborating with me and for many useful discussions.

In addition to the above, I would like to thank Benjamin F. Collins, Ehud Nakar, Rob Owen, Jonathan Pritchard, Etienne Racine, Pavlin Savov, Sherry H. Suyu, Huan Yang for useful discussions, and all others who attend Kip and Lee's group meeting, where I learned a lot of astrophysics and numerical relativity through interesting discussions.

I thank Chris Mach for solving my computer problems, and I thank JoAnn Boyd, Donna Driscoll, and Shirley Hampton for helping me with administrative matters.

Finally I would like to thank my parents Youcai and Zhixiu, and my wife Yuxue. Without their love, support, and encouragement, my accomplishments thus far would have been impossible.

The research presented in this thesis was supported in part by NASA grants NAG5-12834, NAG5-10707, NNG04GK98G, NNG05GG52G, NNG05GG51G; by NSF grants PNY-0099568, PHY-0601459, PHY-0244906, DMS-0553302, PHY-0312072, PHY-0354631; by the Gordon and Betty Moore Foundation. I wish to thank Dr. and Mrs. Gordon and Betty Moore for their generous donation to Caltech, from which I obtained enough support to finish my Ph. D degree in physics.

Abstract

This thesis presents a study of various interesting problems in theoretical astrophysics, including gravitational wave astronomy, gamma ray bursts and cosmology.

Chapters 2, 3, and 4 explore prospects for detecting gravitational waves from stellar-mass compact objects spiraling into intermediate-mass black holes (BHs) ($M \approx 50M_\odot$ to $350M_\odot$) with ground-based observatories. It is shown in chapter 2 that if the central body is not a BH but its metric is stationary, axisymmetric, reflection symmetric and asymptotically flat, then the waves will likely be triperiodic, as for a BH. Chapters 3 and 4 show that the evolutions of the waves' three fundamental frequencies and of the complex amplitudes of their spectral components encode (in principle) details of the central body's metric, the energy and angular momentum exchange between the central body and the orbit, and the time-evolving orbital elements.

Chapter 5 studies a local readout method to enhance the low frequency sensitivity of detuned signal-recycling interferometers. It is well known that high power detuned signal-recycling interferometers, currently planned for second-generation interferometric gravitational-wave detectors (for example Advanced LIGO), are characterized by two resonances in the detection band, an optical resonance and an optomechanical resonance, which is upshifted from the suspension pendulum frequency due to the so-called optical-spring effect. The detector's sensitivity is enhanced around these two resonances. However, at frequencies below the optomechanical resonance frequency, the sensitivity of such interferometers is significantly lower than non-optical-spring configurations with comparable circulating power. Chapter 5 proposes to add a local readout scheme, which measures the motion of the arm-cavity front mirror, which at low frequencies moves together with the arm-cavity end mirror (*optical bar effect*), under the influence of gravitational waves. This scheme improves the low-frequency quantum-noise-limited sensitivity of optical-spring interferometers significantly and can be considered as an incorporation of the optical-bar scheme into currently planned second-generation interferometers. It can also be regarded as an extension of the usual optical bar scheme. Chapter 5 provides both the results of improvement in quantum noise and the implementation details in Advanced LIGO.

Chapter 6 applies and generalizes causal Wiener filter to data analysis in macroscopic quantum mechanical experiments. Since the continuous improvement of sensitivities of laser interferometers,

doing macroscopic quantum mechanical experiments become feasible. With the causal Wiener filter method, we demonstrate that, in theory, we can put the test masses in the interferometer to its quantum mechanical ground states. A related study also implies that it is possible to swap the quantum states of two coherently measured laser interferometers by stochastic optimal control method.

Chapter 7 presents some analytical solutions for expanding fireballs, the common theoretical model for gamma ray bursts (GRBs) and soft gamma ray repeaters (SGRs). The fireball is an optically thick concentration of radiation energy with a high ratio of energy density to rest mass. It is assumed in chapter 7 that an ultrarelativistic fireball consists of electron-positron pairs and photons. First we show that in the ultrarelativistic limit, after photons decouple from the pairs, the photon distribution function remains a blackbody spectrum in some appropriate Lorentz frame, allowing us to define an effective Lorentz factor and temperature for the photon gas. Second we study the freezing out of electron-positron pairs and their asymptotic Lorentz factor γ_∞. The dependence of these quantities on initial conditions is described by simple scaling laws. Finally we apply our results to SGR 1806-20 and rediscover the mismatch between the model and the afterglow observations. A viable solution for the energy budget is that the fireball is loaded by baryons or electromagnetic flux.

Chapter 8 discusses the reconstruction of the scalar-field potential of the dark energy. While the accelerated expansion of the Universe is by now well established, the underlying physics remains a complete mystery. Chapter 8 assumes that the acceleration is driven by a single scalar field and attempts to reconstruct this potential using recent supernova (SN) data. Current approaches to such reconstructions are based upon simple parametric descriptions of either the luminosity distance or the dark energy equation of state (EOS). It is shown in chapter 8 that these various approximations lead to a range of derived evolutionary histories of the dark energy equation of state (although there is considerable overlap between the different potential shapes allowed by the data). Instead of these indirect reconstruction schemes, we discuss a technique to determine the potential directly from the data by expressing it in terms of a binned scalar field. We apply this nonparametric technique to a recent SN dataset, and compare the results with parametric approaches. In a similar fashion to direct estimates of the dark energy equation of state, we advocate direct reconstruction of the scalar field potential as a way to minimize prior assumptions on the shape, and thus minimize the introduction of bias in the derived potential.

Chapter 9 discusses gravitational lensing modifications to cosmic microwave background (CMB) anisotropies and polarization, produced by a stochastic background of primordial gravitational waves between us and the last scattering surface. While density fluctuations perturb CMB photons via gradient-type deflections only, foreground gravitational waves distort CMB anisotropies via both gradient- and curl-type displacements. The latter is a rotation of background images, while the former is related to the lensing convergence. For a primordial background of inflationary gravitational waves, with an amplitude corresponding to a tensor-to-scalar ratio below the current upper limit of ≈ 0.3, the resulting modifications to the angular power spectra of CMB temperature anisotropy and polarization are below the cosmic variance limit on large scales. At tens of arcminute angular scales and below, however, these corrections are above the level at which systematics must be controlled in all-sky anisotropy and polarization maps with no instrumental noise and other secondary and foreground signals.

Chapter 10 calculates the non-Gaussian covariance of CMB B-modes of polarization. The B-mode polarization lensing signal is a useful probe of the neutrino mass and to a lesser extent the dark energy equation of state as the signal depends on the integrated mass power spectrum between us and the last scattering surface. This lensing B-mode signal, however, is non-Gaussian and the resulting non-Gaussian covariance to the power spectrum cannot be ignored as correlations between B-mode bins are at a level of 0.1. In chapter 10 we find that the non-Gasussian covariance is not significant for temperature and E-mode polarization power spectra. However, the non-Gaussian covariance cannot be neglected for B-mode polarization power spectra. The resulting degradations in the measurement accuracies for neutrino mass and dark energy equation of state are about a factor of 2 to 3 when compared to the case where statistics are simply considered to be Gaussian. We also discuss parameter uncertainties achievable in upcoming experiments and show that at a given angular resolution for polarization observations, increasing the sensitivity beyond a certain noise value does not lead to an improved measurement of the neutrino mass or dark energy equation of state using the B-mode power spectrum. For Planck, the resulting constraints on the sum of the neutrino masses is $\sigma_{\Sigma m_\nu} \sim 0.2$ eV and on the dark energy equation of state parameter we find, $\sigma_w \sim 0.5$.

Contents

List of Figures

List of Tables

Chapter 1

Introduction

1.1 Detection of Gravitational Waves from Intermediate-Mass-Ratio Inspiral

First generation interferometric gravitational-wave (GW) detectors, such as the Laser Interferometer Gravitational-Wave Observatory (LIGO) [1] and Virgo [2], have searched for GWs at or near their design sensitivities. In the next decade, Advanced LIGO (AdvLIGO) [3] and its international partners will increase the volume of the Universe searched a thousandfold or more. The most promising GW sources for this network are the inspiral and coalescence of black hole (BH) and/or neutron star (NS) binaries. Current inspiral searches target sources with total mass $M \leq 40\,M_\odot$: NS binaries with masses $1\,M_\odot \simeq 3\,M_\odot$, BH binaries with masses $3\,M_\odot \simeq 40\,M_\odot$, and NS-BH binaries with components in these mass ranges [4, 5].

Ultraluminous x-ray observations and simulations of globular cluster dynamics suggest the existence of intermediate-mass black holes (IMBHs) with masses $10^2\,M_\odot \simeq 10^4\,M_\odot$ [9]. The GWs from the inspiral of a NS or stellar-mass BH into an IMBH with mass $50\,M_\odot \simeq 350\,M_\odot$ will lie in the frequency band of AdvLIGO. These *intermediate-mass-ratio inspirals* (IMRIs) are analogous to the extreme-mass-ratio inspirals (EMRIs) of $\sim 10M_\odot$ objects spiraling into $\sim 10^6 M_\odot$ BHs, targeted by the planned LISA observatory [10]. If we consider the possibility that the central body of an IMRI (or EMRI) is not a BH, but some other general relativistic object (e.g., a boson star or a naked singularity [11]), then AdvLIGO and LISA can quantify the accuracy with which it has the properties predicted for a BH, i.e., the accuracy with which: (i) it obeys the BH no-hair theorem (its spacetime geometry is the Kerr metric, fully determined by its mass and spin), and (ii) its *tidal coupling* (tide-induced transfer of energy and angular momentum between orbit and body) agrees with BH predictions. Searching for non-BH objects may yield an unexpected discovery.

In chapter 2, chapter 3, and chapter 4, I report progress in scoping out the prospects for AdvLIGO to detect GWs from IMRIs and probe the properties of IMRIs' central bodies.

1.1.1 Chapter 2: IMRI and EMRI Orbits and Waves: Triperiodic or Ergodic

Chapter 2 is a paper by Jonathan Gair, Ilya Mandel and me, published in *Physical Review D* [6]. Thorne proposed the project, i.e., he suggested us to explore the gravitational-wave signatures of non-Kerr stationary, axisymmetric, reflection symmetric, asymptotically flat (SARSAF) spacetimes. Gair and Mandel did numerical experiments with geodesics in the Manko-Novikov spacetime [7], while Geoffrey Lovelace and I did similar things for geodesics in a perturbed Kerr spacetime. After comparing our results, we found that some geodesics look triperiodic but some look ergodic. We then tried to understand this phenomenon from different viewpoints: (i) I did some calculation of orbits in Newtonian gravity for nonspherical but SARSAF potential and, with the help of Wang Yan from the Chinese Academy of Science, showed that the orbits can be decomposed into several harmonic components up to high accuracy. This gave some indirect evidence of the triperodic orbits in non-Kerr spacetime, (ii) Gair found a relevant paper by Guéron and Letelier [8] which discussed the chaotic orbits in another non-Kerr spacetime. Gair and Mandel replicated and extended the studies of that paper. Our paper (chapter 2) was mainly written by Gair, with some revisions from Mandel and me.

The SARSAF spacetimes that we explore in Chapter 2 have a metric with the form

$$ds^2 = -\alpha^2 dt^2 + \varpi^2 (d\phi - \omega dt)^2 + g_{\theta\theta} d\theta^2 + g_{rr} dr^2,$$

where all the metric coefficients are independent of the Killing time t and axial angle ϕ. Why do we focus on SARSAF spacetime? If the spacetime initially is not axisymmetric, rotation will make it nonstationary; then presumably GW emission drives it to stationarity and axisymmetry on astrophysically small timescales. Almost all stationary, axially symmetric, self-gravitating objects studied observationally or theoretically are reflection symmetric.

A SARSAF solution to the vacuum Einstein equations is determined uniquely by two families of scalar multipole moments: *mass moments* $M_0 \equiv M$ (the mass), M_2 (mass quadrupole moment), $M_4, \ldots$; and *current moments* S_1 (spin angular momentum), $S_3, S_5, \ldots$[12]. For the Kerr metric (describing astrophysical BHs), the moments are fully determined by the mass M and dimensionless angular momentum $\chi \equiv S_1/M^2$ via the complex formula

$$M_l + iS_l = M^{l+1}(i\chi)^l;$$

this is the no-hair theorem. LISA plans to measure as many moments as possible, via EMRI waves, and determine the accuracy with which each moment satisfies this Kerr formula; AdvLIGO can do the same for IMRIs.

For EMRIs and IMRIs, the orbiting object moves along an orbit that is nearly a geodesic of the background metric; radiation reaction drives it slowly from one geodesic to another. If the central body is a Kerr BH, then (i) each geodesic has three isolating integrals of the motion: energy E, axial angular momentum L_z, and Carter constant Q (and a fourth, "trivial" integral, the length of the orbit's tangent vector), and (ii) the emitted gravitational waves are triperiodic with

$$h^{\mu\nu} = \mathrm{Re} \sum_{Pkmn} h^{\mu\nu}_{Pkmn} e^{i(k\Omega_\theta + m\Omega_\phi + n\Omega_r)t},$$

where k, m, n are integers [13]. Here $P = +, \times$ is the polarization, and the three fundamental frequencies $\Omega_\theta, \Omega_\phi, \Omega_r$, in a precise but subtle sense, are associated with the orbital motion in the polar (θ), azimuthal (ϕ), and radial (r) directions. The fundamental frequencies and complex amplitudes evolve with time as the orbit evolves through a sequence of geodesics.

If the Carter constant is lost in SARSAF spacetimes, the orbital motion may be ergodic rather than triperiodic, which would make detection of the gravitational waves difficult. Guéron and Letelier [8] have used Poincaré maps to search for ergodic geodesics in the static ($S_l = 0$) Erez-Rosen metric. In chapter 2 Gair, Mandel and I have carried out similar studies for a variant of the stationary ($S_l \neq 0$) Manko-Novikov metric [7]. Both of these metrics have an arbitrary mass quadrupole moment M_2, and higher-order moments fixed by M_2, S_1 and M. The Poincaré maps in these spacetimes reveal that there are geodesics at very small radii $r \approx$ few M, which appear ergodic, but all orbits at at large radii appear triperiodic. In chapter 2 we found ergodic geodesics only for oblate ($M_2 < 0$) perturbations of the Kerr spacetime, but in the case of Manko-Novikov spacetime or Erez-Rosen spacetime, ergodicity appears only for prolate ($M_2 > 0$) perturbations. Radiation reaction drives the evolution of energy and angular momentum in a way that makes it unlikely that the apparently ergodic geodesics could be encountered in the course of an inspiral. For the apparently nonergodic (integrable) geodesics, the spatial coordinates are multiperiodic functions of Killing time t to a numerical accuracy of 10^{-7}, and a general argument based on the structure of the gravitational propagator shows that their gravitational waves will have the same kind of triperiodic form as for Kerr BHs.

There are three possible explanations for the presence of large-radius orbits that appear integrable and small-radius orbits that appear ergodic in the same spacetime: (i) The orbits are actually integrable and actually ergodic, respectively. (ii) All the orbits are ergodic, but at large radii they appear integrable to numerical accuracy because of the Kolmogorov-Arnold-Moser theorem [14]. (iii) All the orbits are integrable, but at small radii they are made to appear chaotic by some ill-understood numerical instability. It is important to learn which is the case (and Jeandrew Brink is searching for the answer [15, 16]), but for EMRI and IMRI wave observations, apparent integrability (or ergodicity) has the same observational implications as actual integrability (or ergodicity).

1.1.2 Chapters 3 and 4: Information Carried by IMRI (EMRI) Waves; Generalizing Ryan's Theorem

Chapter 3, is a paper written by Geoffrey Lovelace and me, and published in*Physical Review D* [17]. Thorne proposed the project. I discovered that Ryan's theorem [18] discussed below could be generalized to include tidal coupling if the energy loss to infinity was insensitive to the nature of the central body. I carried out my calculation following the framework of Chandrasekhar [19]. After that, Thorne suggested that Lovelace and I redo the calculation using physical tidal fields which were more relevant to the physical picture of the problem. Then Lovelace and I did the calculation independently and obtained the same result in the form reported in the paper. The text of this chapter was written largely by Lovelace, but with significant contributions from Thorne and me.

Chapter 4 is a paper written by myself, and is in preparation for submission to*Physical Review D.* Thorne proposed the project to me. In this chapter I developed an algorithm that generalized Ryan's theorem to nearly equatorial but eccentric orbits. Based on discussions with my colleges, I also presented two different ways to generalize Ryan's theorem to generic orbits. This paper was written by me, but with significant editing by Thorne.

When a small object orbits a SARSAF central body (i.e., for an EMRI or IMRI), what information about the central body is encoded in the gravitational waveforms? In chapter 3 and 4 we answer this question, assuming from the outset that the waveforms are triperiodic. In principle, a large amount of information can be encoded in the time evolution of the waves' three fundamental frequencies $\Omega_\theta(t), \Omega_\phi(t), \Omega_r(t)$, and their complex amplitudes $h_{Pkmn}(t)$. It has been speculated that these encode, fully and separably, the values of all the central body's multipole moments M_l, S_l (and hence also its full metric) [18], the rates at which the orbiting object's tidal pull deposits energy and angular momentum into the central body, $\dot{E}_{\rm body}$ and $\dot{L}_{\rm body}$ (*tidal coupling*) [20], and the orbit's semilatus rectum $p(t)$, eccentricity $e(t)$, and inclination angle $\iota(t)$ (which carry the same information as the isolating integrals). This has been suggested by a special case studied by Ryan [18]. Specifically, for nearly circular, nearly equatorial orbits in a SARSAF spacetime, Ryan showed that the waves encode all the central body's multiple moments M_l, S_l; This is *Ryan's theorem.* A trivial extension of Ryan's theorem, proved in chapter 3, leads to the following algorithm for extracting information from the waves. Observe the time-evolving modulation frequencies as functions of the time-evolving fundamental frequency $f = \Omega_\phi/\pi$. From these, deduce the functions $\Omega_A(\Omega_\phi)$ and then $\Omega_A(v)$ for $A = \theta, r$; expand in powers of $v \equiv (M\Omega_\phi)^{1/3} \simeq$ (orbital velocity); and read out the moments (redundantly) from the two expansions. Then, knowing the moments and thence the metric, use the geodesic equation to deduce $p(t)$ from $\Omega_\phi(t)$ and use wave-generation theory to deduce $e(t)$ and $\iota(t)$ from particular modulation amplitudes, $h_{Pkmn}(t)$.

We have generalized Ryan's theorem to strongly elliptical but nearly equatorial orbits in chapter

4. For strongly elliptical but nearly equatorial orbits the three fundamental frequencies are independent of ι at first order. We expand these frequencies $\Omega_A(M_l, S_l, e, p)$ (with $A = \theta, \phi, r$) in powers of $1/p$, with coefficients that depend on e and the moments. Suppose we observe a series of $2N+1$ values of $\Omega_\theta, \Omega_\phi, \Omega_r$ (for any integer N) during the course of an inspiral. This gives us $6N+3$ numbers, from which we can read off (via an algorithm based on our expansions of the fundamental frequencies in chapter 4): (i) the time evolution of $e(t)$ and $p(t)$ ($2N+1$ values of each), (ii) the lowest $N+1$ mass moments, and (iii) the lowest N current moments. By observing the evolving amplitudes of the orbital-precession-induced modulations encoded in h_{Pkmn}, we can recover the time evolution of ι. Hence, in principle, we have a full description of the spacetime. In practice the methods of extracting the information may be quite different from these algorithms.

In chapter 4 we also explore routes for generalizing Ryan's theorem to generic orbits. We show that, whatever route one might choose, one must use details of gravitational-wave emission in SARSAF spacetimes. And we exhibit two specific routes that are likely to produce successful generalizations. One route makes use of snapshots of the complex amplitudes of the waves' harmonics along with their three frequencies; the other makes use of the time evolutions of the waves' three fundamental frequencies.

In the absence of tidal coupling Ryan demonstrated that, for a nearly circular, nearly equatorial orbit, the central body's moments are encoded not only in the waves' modulations, but also in the time evolution of the waves' dominant harmonic $f = \Omega_\phi/\pi$, or equivalently, that harmonic's phase. In chapter 3 we have extended this analysis to deduce the power being deposited in the central body by tidal coupling, $\dot{E}_{\rm body}$. We assume the moments and metric have been deduced from the precessional modulations and then use deviations from the Ryan's theorem phase evolution to deduce $\dot{E}_{\rm body}$. Following Ryan, we quantify the waves' phase evolution by

$$\Delta N(t) \equiv f^2/\dot{f} = d(\text{number of wave cycles})/d\ln f.$$

From this definition of ΔN, we infer the rate of change of orbital energy:

$$\dot{E}_{\rm orb} = (dE_{\rm orb}/d\Omega_\phi)(\Omega_\phi^2/\pi\Delta N).$$

All (time-evolving) quantities on the right side can be deduced from observation plus the geodesic equation (for $dE_{\rm orb}/d\Omega_\phi$). From the deduced metric and the frequency $f(t)$ we can compute the power radiated to infinity $\dot{E}_\infty$; and then by energy conservation we can deduce the power being deposited in the central body $\dot{E}_{\rm body} = -\dot{E}_{\rm orb} - \dot{E}_\infty$. We can also infer the angular momentum transferred tidally to the central body, $\dot{L}_{\rm body}$, via $\dot{L}_{\rm body} = \dot{E}_{\rm body}/\Omega_\phi$ (valid for nearly circular, nearly equatorial orbits).

The above argument assumes that we can compute $\dot{E}_\infty$ without knowing the boundary conditions of the inspiral-induced metric perturbation at the central body, since we do not know the nature of the central body a priori. For highly compact central bodies (those deep inside the perturbing field's "effective potential") this is true to high but not complete accuracy. The effect of boundary conditions at the central body on the inspiral phase evolution is communicated outward to infinity mainly at low frequencies (the orbital frequency and its low-order harmonics), and these perturbations have great difficulty penetrating through the effective potential. If the spacetime metric is Kerr, we have shown that the influence of the inner boundary condition on the energy radiated to infinity is $\delta\dot{E}_\infty \sim v^{10}\dot{E}_\infty$, which is five orders smaller in the linear velocity v than the tidal coupling $\dot{E}_{\rm body} \sim v^5\dot{E}_\infty$[21]. Thus, to high accuracy we can deduce $\dot{E}_\infty$ and then $\dot{E}_{\rm body}$ from observations, without knowing the body's precise nature.

1.2 Chapter 5: Local Readout Enhancement for Detuned Signal-Recycling Interferometers

Chapter 5, is a paper published in *Physical Review D* [22] by Henning Rehbein, Helge Mueller-Ebhardt, Kentaro Somiya, Chao Li, Roman Schnabel, Karsten Danzmann, and Yanbei Chen. This paper was based on Chen's idea of incorporating the Braginsky-Khlili optical-bar scheme into Advanced LIGO to enhance its low-frequency sensitivity. Following Chen's suggestions, Rehbein and Mueller-Ebhardt solved the joint Heisenberg equations of motion for the test masses, beam splitter, and optical fields. They also evaluated the optimal combined GW sensitivity of the two readout channels and observed the improvement in low frequency sensitivities. They and I independently proved that the use of control schemes does not affect this sensitivity. Somiya also considered practical issues for a possible implementation in Advanced LIGO. This paper was mainly written by Rehbein, Mueller-Ebhardt, Somiya and Chen, with some revisions from me.

First-generation laser interferometric gravitational-wave (GW) detectors (LIGO [23], VIRGO [24], GEO [25] and TAMA [26]) have reached or neared their design sensitivities. These interferometers are usually Michelson interferometers with Fabry-Perot cavities in the arms, and with power recycling (PR) at the laser input port (with the exception of GEO, which uses *dual-recycling* [27]), and operating close to the dark-port condition.

In order to have a flexible sensitivity to specific astrophysical sources, and for other technical reasons such as lowering the optical power at the beam splitter (BS), second-generation interferometers, such as Advanced LIGO [28], plan to use the so-called signal-recycling (SR) configuration, in which an additional mirror is placed at the dark port of a Fabry-Perot Michelson interferometer, modifying the optical resonant structure of the interferometer. By adjusting the location and reflectivity of the signal-recycling mirror, one can vary the optical resonance frequency and bandwidth, respectively. Near the optical resonance, the sensitivity to GWs is improved. When the signal-recycling cavity (the cavity formed by the input test-mass mirrors (ITM) and the signal-recycling mirror) is neither resonant nor antiresonant with respect to the carrier frequency, the optical configuration is called *detuned* signal-recycling. In detuned configurations, the peak sensitivity is achieved by placing the optical resonance of the interferometer away from the carrier frequency.

As demonstrated theoretically by Buonanno and Chen [29, 30, 31] and experimentally by Somiya et al. [32] and Miyakawa et al. [33], detuned signal-recycling also makes the power inside the interferometer depend on the motion of the mirrors, creating an *optical spring*, and can shift the eigenfrequency of the test masses from the pendulum frequency ($\sim 1\,\mathrm{Hz}$) up to the detection band. The optical spring helps to improve the interferometer's response to GWs around the optomechanical resonant frequency, even allowing the interferometer to surpass the free-mass Standard Quantum Limit (SQL). However, the quantum-noise-limited sensitivity of optical-spring interferometers at frequencies below the optomechanical resonant frequency is dramatically lower than that of non-optical-spring interferometers. This debilitation of sensitivity is caused by the optical spring, which rigidly connects the front and the end mirror of the arm cavities at frequencies below the optomechanical resonance. The general principle underlying this effect has been explained in the works of Braginsky, Gorodetsky and Khalili, namely in their proposal of the *optical bar* detection scheme [34]. At frequencies substantially below the optomechanical resonance, the optical spring behaves like a rigid optical bar, connecting rigidly the ITM and the end test-mass mirror (ETM) of each arm. It is then easy to understand that the carrier light, which senses the change in arm-cavity length, or the difference in ITM and ETM motion, cannot be used to measure GWs efficiently at these frequencies.

On the other hand, since the ITM and the ETM are rigidly connected, they both move, in the local inertial frame of the BS, by $1/2$ the amount the ETM would have moved if there were no optical spring present (assuming the ITM and ETM to have equal masses). For this reason, if one also measures the local motion of the ITM using an additional *local readout* scheme, one can recover the low-frequency sensitivity dramatically. This idea, by Chen, is analyzed in chapter 5. Braginsky, Gorodetsky and Khalili proposed an optical-bar detection scheme, in which only the local motion of the ITM is measured [34]. In this sense, Chen's proposal can be considered as directly incorporating the optical-bar scheme into currently planned second-generation interferometers.

From an astrophysical point of view, the addition of the local readout scheme, which broadens the detection band, will allow the interferometer to search for multiple sources simultaneously, as well as examine each source over a wider frequency range.

1.3 Chapter 6: Optimal Quantum Filtering in Advanced LIGO Inteferometers

Chapter 6, is a project proposed by Yanbei Chen. Thorne and Chen proposed a research program of doing quantum mechanical experiments using macroscopic laser interferometers. As a well-known fact, the quantum mechanical noise creates a fundamental constraint to the instrument sensitivities in gravitational-wave interferometers. On the other hand, as we improve the sensitivities by suppressing the classical noises such as the thermal noise, probably we can investigate the quantum mechanical behaviors of the interferometers, which has arm lengths of a few kilometers and test masses weights of a few kilograms. Chen suggested me to investigate the theory of optimal filter and control so that we could apply the techniques there to macroscopic quantum mechanical experiments, where these optimal filters must be used to remove the classical randomness in the test-mass motion, which normally dominates, leaving behind largely quantum uncertainty.

In chapter 6 we first build the connection between causal Wiener filters and ordinary linear regression. This connection allow us to do straightforward optimal filtering in the time domain. With this technique we calculate the conditional variance of the test masses under linear measurements and show that it is possible to reach quantum mechanical ground states by decreasing the temperature or increasing the quality factor. As an independent study, we found another connection between the optimal Wiener filter and quantum non-demolition measurements by the path-integral approach. This approach is largely based on my discussions with Yasushi Mino. This connection helps us to understand optimal filter from another perspective.

This chapter was largely written by me, with some revision from Chen.

1.4 Chapter 7: Analytical Solutions for Expanding Fireballs

Chapter 7 is a paper by me and Re'em Sari, and published in *The Astrophysical Journal* [35]. Sari proposed this project for me. Specifically, Sari proposed to solve the hydrodynamical equations of expanding fireballs in dimensionless form. I worked out the full details and discovered the analytical formulae that were reported in the paper. I also obtained the accurate scaling laws of the terminal energy with respect to initial conditions and discussed the corresponding energy budget problem in SGR 1806-20. This paper was largely written by me, but had significant revisions from Sari.

Many models of Gamma Ray Bursts (GRBs) [37, 38, 39, 40, 41] as well as of Soft Gamma Ray repeaters (SGRs) [42, 43, 44] involve a fireball: an optically thick concentration of radiation energy with a high ratio of energy density to rest mass. The evolution of an electron-positron-photon fireball consists of several phases [36, 39]. Initially, the electrons, positrons and photons are in thermal equilibrium due to high temperature and large optical depth. As the fireball expands, its temperature decreases, and the equilibrium number density of electrons and positrons decreases. The optical depth for pair annihilation drops below unity, and their density deviates from thermal equilibrium below a temperature of about 20 keV. Around the same time, the optical depth for photon scattering drops below unity so that photons decouple from pairs and begin freestreaming. Further expansion causes the density of electron-positron pairs to decrease, but their total number is now conserved. The Lorentz factor of the electrons increases until the optical depth for scattering off photons becomes small. Then the pairs decouple from the photons and therefore no longer accelerate. If we consider the fireball as a steady-state wind, there will be a constant number of pairs per unit time $\dot{N}_\infty$ arriving at infinity with Lorentz factor γ_∞.

In this chapter we study the asymptotic behavior of an ultrarelativistic fireball consisting of electron-positron pairs and photons. We show that in the ultrarelativistic limit, after photons decouple from the pairs, the photon distribution function remains a blackbody spectrum in some appropriate Lorentz frame, allowing us to define an effective Lorentz factor and temperature for the photon gas. We also study the freezing out of electron-positron pairs and their asymptotic Lorentz factor γ_∞. The dependence of these quantities on initial conditions (radius r_i and temperature T_i) can be described by simple scaling laws [equations (7.18), (7.26)]:

$$\begin{aligned}\gamma_\infty &\approx 1.46\left(\frac{8\pi^5 r_i T_i^4 k_B^4 \sigma_{\rm tot}}{45 m_e h^3 c^5}\right)^{1/4},\\ \dot{N}_\infty &\approx \frac{3}{1+(\ln 8 - 3\gamma_{Eu})T_\pm - 3T_\pm \ln T_\pm}\,\frac{4\pi r_i c^2}{\langle\sigma_{\rm ann} v\rangle}\left(\frac{T_i}{T_\pm}\right)^3,\end{aligned}$$

where the equilibrium-breaking temperature is [Eq. (7.14)]

$$T_\pm \approx \frac{m_e c^2/k_B}{\ln x - (3/2)\ln\ln x}, \quad x \equiv (2\pi)^{1/2}\alpha^2 (r_i/\lambda_e).$$

We apply our results to SGR 1806-20, and find that the energy carried by electron-positron pairs is higher than calculated by former estimates [36, 45], but is still an order of magnitude short of the minimum energy required to produce the observed afterglow [45]. A viable solution of this energy budget problem is that the fireball is loaded by baryons or electromagnetic flux [46, 47].

1.5 Chapter 8: Direct Reconstruction of the Dark Energy Scalar-Field Potential

Chapter 8 is a paper by Asantha Cooray, Daniel Holz and me, and published in *Physical Review D* [48]. Cooray proposed this project for me. He suggested that I fit the various existing models of dark energy to recent supernova data. After I fitted the models, Cooray, Holz and I found quite large differences among the four popular models. Cooray then proposed to use the non-parametric method to fit the data, because this introduced less bias than the parametric models. I worked out the full details of his proposal. The paper is mainly written by Cooray, with revisions from Holz and me.

Distance estimates for Type Ia supernovae (SNe) are currently a preferred probe of the expansion history of the Universe [49, 50, 51], and have led to the discovery that the expansion is accelerating [52, 53]. Observations show that a mysterious dark energy, with an energy density $\sim$70% of the total energy density of the universe, is responsible for the accelerated expansion [54]. While the presence of acceleration is now well established by various cosmological probes, the underlying physics remains a complete mystery. As the precise nature of the dark energy has profound implications, understanding its properties is one of the biggest challenges today.

With the advent of large surveys for Type Ia supernovae, such as the Supernova Legacy Survey (SNLS) [1] and Essence [2] among others, it is hoped that we will study details of the expansion, and thereby elucidate the physics responsible for the acceleration. Under the assumption that the dark energy is due to a single scalar field ϕ rolling down a potential $V(\phi)$, several studies have considered how future data might be used to reconstruct the potential, either based on various analytical descriptions of the luminosity distance as a function of redshift [55], or through specific assumptions about the potential, such as a polynomial function in the scalar field [56]. It is already well established that certain parametric descriptions of the distance-redshift relation lead to biased estimates for the dark energy equation-of-state (EOS) and the potential [57]. While improved parametric forms of fitting functions have been suggested [58, 59], it is unclear how to select an optimal approach for reconstructing the dark energy scalar field potential from SN distances (for a review of various possibilities, see reference [60]).

In chapter 8 we discuss issues related to potential and dark energy EOS reconstruction by making use of a recent set of SN data from the SNLS survey [61]. The sample includes 73 high redshift supernovae (SNe) complemented with a sample of 44 nearby SNe [61]. We compare and contrast a variety of methods to reconstruct the potential and the dark energy EOS. Based on our model reconstruction of the potential, we find that while there is significant overlap of the allowed $V(\phi)$ region favored by each of the four reconstruction methods, the models give rise to different histories for the EOS, especially within the two parameter plane, w–w' (the EOS parameter, w, and its time derivative, $w' \equiv dw/d\ln a$, as functions of redshift [63]). We argue that existing parametric fitting functions for either the distance-redshift relation or the EOS lead to biased reconstructions of the potential. In the literature, however, there exist model-independent approaches to the reconstruction of the dark energy density [64] and the EOS [65], which bin the parameters directly as a function

---

[1] http://www.cfht.hawaii.edu/SNLS/

[2] http://www.ctio.noao.edu/ wsne/

of redshift, with the number and width of the bins determined by the statistical quality of data. These estimates can also be arranged to be uncorrelated [65], allowing unique insights into the evolution without being subject to prior assumed redshift dependencies. Here we suggest a similar model-independent approach to the reconstruction of the scalar potential from SN data. Instead of utilizing a polynomial expansion for the potential [56], which assumes a limited range of models (once the expansion is truncated at a certain order), we propose a binning scheme for the potential that can be applied to data with a minimal, and easily controlled and understood, number of assumptions for the potential shape.

1.6 Chapter 9: Weak Lensing of the Cosmic Microwave Background by Foreground Gravitational Waves

Chapter 9 is a paper by Asantha Cooray and me, and published in*Physical Review D* [66]. Cooray proposed the project for me. I calculated the effect of lensing distortion of the cosmic microwave background anisotropies and obtained the analytical expressions for angular power spectra. Cooray implemented these expressions numerically and generated figures that are reported in the paper. Cooray wrote the main part of the paper, with some revisions from me.

The weak lensing of cosmic microwave background (CMB) anisotropies and polarization by intervening mass fluctuations, or scalar perturbations, is now well studied in the literature [67, 68], with a significant effort spent on improving the accuracy of analytical and numerical calculations (see recent review in [69]). The non-Gaussian pattern of CMB anisotropies and polarization, created by non-linear mapping associated with lensing angular deflections, aids the extraction of certain statistical properties of the foreground mass distribution [70]. Weak lensing deflections by intervening mass also *leak* CMB polarization power from the E-mode to the B-mode [71]. This lensing B-mode signal presents a significant confusion when searching for primordial gravitational wave signatures in the CMB polarization [72]. The lensing reconstruction techniques discussed in the literature, however, allow the possibility to “clean” CMB polarization maps so as to search for a background of inflationary gravitational waves with an energy scale as low as 10^{15} GeV [73].

Similar to gravitational lensing by density perturbations, if there is a background of gravitational waves in the foreground, then one would expect metric perturbations associated with these waves to distort and gravitationally lens background images [74]. While the lensing deflections by the density field can be written as the gradient of the projected gravitational potential, lensing displacements due to gravitational waves can be decomposed into both a gradient and a curl-like component [75, 76, 77]. In these two components, gradient-type displacements are related to the lensing convergence, while curl-type displacements are related to the image rotation, though both types of displacements lead to image shear. While linear density perturbations do not produce rotations, second-order corrections to weak lensing by scalar perturbations, such as due to the coupling of two lenses along the line of sight, can produce rotational modes [78].

While the study of CMB lensing by foreground density fluctuations is now well developed [69], there has been little analysis of CMB lensing by foreground gravitational waves. In the context of large-scale structure weak lensing surveys with galaxy shapes [79], the rotational power spectrum of background galaxy images when lensed by primordial gravitational waves in the foreground has been discussed in Ref. [76]. In the context of lensing reconstruction with CMB temperature and polarization maps, the curl component of the displacement field can be used to monitor systematics [77], though lensing by gravitational waves will leaving a non-zero contribution to the curl component.

In chapter 9, we extend the calculation in Ref. [76] by studying both the curl and the gradient modes of the deflection field produced by primordial gravitational waves through which pass CMB photons propagating from the last scattering surface. Our calculations are both useful and important given the increasing interest in, and plans for, high-sensitivity CMB anisotropy and polarization measurements, including a potential space-based mission after Planck, called CMBpol. Such an experiment is expected to study polarization B-modes in exquisite detail, and it is important to understand potentially interesting secondary signals beyond those that are routinely mentioned in the literature. Based on the calculations presented here, we find that gravitational lensing of CMB by a background of primordial gravitational waves from inflation, with an amplitude below the current tensor-to-scalar ratio upper limit of 0.3, will produce an undetectable modification to anisotropy and polarization power spectra. Moreover, since the corrections are below the cosmic variance level, it is unlikely that one needs to account for these secondary corrections when making precise cosmological measurements. If observations are all-sky measurements with no instrumental noise, then these effects may be present in the form of systematic corrections to the primary anisotropy and polarization measurements.

1.7 Chapter 10: Non-Gaussian Covariance of CMB B-modes of Polarization and Parameter Degradation

Chapter 10 is a paper by Asantha Cooray, Tristan Smith and me, and published in*Physical Review D* [84]. Cooray proposed this project for me. I did the calculation and obtained the expressions for non-Gaussian covariance matrices for CMB power spectra. After that Smith generated the derivatives of power spectra with respect to cosmological parameters. Then I combined the derivative information with the covariance matrices to obtain the Fisher Information Matrices, from which Smith generated the error ellipses that were reported in the paper. Cooray wrote the draft of the paper. Smith and I did some revisions afterward.

The applications of cosmic microwave background (CMB) anisotropy measurements are well known [80]. The anisotropy's ability to constrain most, or certain combinations of, parameters that define the currently favored cold dark matter cosmologies with a cosmological constant is well demonstrated with data from the Wilkinson Microwave Anisotropy Probe [81]. Furthermore the advent of high sensitivity CMB polarization experiments with increasing sensitivity [82] suggests that we will soon detect the small amplitude B-mode polarization signal. While at degree scales one expects a unique B-mode polarization signal due to primordial gravitational waves [72], at arcminute angular scales the dominant signal will be related to cosmic shear conversion of E-modes to B-modes by the large-scale structure during the photon propagation from the last scattering surface to the observer today [71].

This weak lensing of the CMB polarization by intervening mass fluctuations is now well studied in the literature [67, 68], with a significant effort spent on improving the accuracy of analytical and numerical calculations (see recent review in Ref. [69]). As discussed in recent literature [83], the lensing B-mode signal carries important cosmological information on the neutrino mass and possibly the dark energy, such as its equation of state [83], since the lensing signal depends on the integrated mass power spectrum between us and the last scattering surface, weighted by the lensing kernel. The dark energy dependence involves the angular diameter distance projections while the effects related to a non-zero neutrino mass come from suppression of small scale power below the free-streaming scale.

Since the CMB lensing effect is inherently a non-linear process, the lensing corrections to CMB temperature and polarization are expected to be highly non-Gaussian. This non-Gaussianity at the four-point and higher levels is exploited when reconstructing the integrated mass field via a lensing analysis of CMB temperature and polarization [70]. The four-point correlations are of special interest since they also quantify the sample variance and covariance of two-point correlation or power spectrum measurements [85]. A discussion of lensing covariance of the temperature anisotropy power spectrum is available in Ref. [86]. In the case of CMB polarization, the existence of a large sample variance for B-mode polarization is already known [87], though the effect on cosmological parameter measurements is yet to be quantified. Various estimates of parameter measurement accuracies in the literature ignore the effect of non-Gaussianities and could have overestimated the use of CMB B-modes to tightly constrain parameters such as a neutrino mass or the dark energy equation of state. To properly understand the extent to which future polarization measurements can constrain these parameters, a proper understanding of non-Gaussian covariance is needed. In chapter 10, we calculated the non-Gaussian covariance matrices in CMB power spectra and discussed the implications for future observations and data analysis. The resulting degradation on neutrino mass and dark energy equation of state is about a factor of 2 to 3 compared to the case where statistics are simply considered to be Gaussian. For Planck, the resulting constraints on the sum of the neutrino masses is $\sigma_{\Sigma m_\nu} \sim 0.2$ eV, and on the dark energy equation of state parameter, $\sigma_w \sim 0.5$.

1.8 Bibliography

[1] B. C. Barish and R. Weiss, *Phys. Today* **10**, no. 10, 44 (1999).

[2] F. Acernese et al., *Class. Quant. Grav.* **23**, S635 (2006).

[3] P. Fritschel, arXiv:gr-qc/0308090 (2003).

[4] B. Abbott et al., *Phys. Rev. D* **72**, 082001 (2005).

[5] B. Abbott et al.,*Phys. Rev. D* **73**, 062001 (2006).

[6] J. R. Gair, C. Li and I. Mandel, *Phys. Rev. D* **77**, 024035 (2008).

[7] V. S. Manko and I. D. Novikov, *Class. Quant. Grav.* **9**, 2477 (1992).

[8] E. Guéron and P. S. Letelier, *Phys. Rev. E* **66**, 046611 (2002).

[9] M. C. Miller and E. J. M. Colbert, *Int. J. Mod. Phys. D* **13**, 1 (2004).

[10] J. R. Gair et al., *Class. Quant. Grav.* **21**, S1595 (2004).

[11] F. D. Ryan, *Phys. Rev. D* **55**, 6081 (1997).

[12] R. Hansen, *J. Math. Phys.* (N.Y.) **15**, 46 (1974).

[13] S. Drasco and S. A. Hughes, *Phys. Rev. D* **69**, 044015 (2004).

[14] M. Tabor, *Chaos and Integrability in Nonlinear Dynamics* (New York: John Wiley and Sons Inc., 1989).

[15] J. Brink, preprint, arXiv:0807.1178 (2008).

[16] J. Brink, preprint, arXiv:0807.1179 (2008).

[17] C. Li and G. Lovelace, *Phys. Rev. D* **77**, 064022 (2008).

[18] F. D. Ryan, *Phys. Rev. D* **52**, 5707 (1995).

[19] S. Chandrasekhar, *The Mathematical Theory of Black Holes* (Oxford University Press, USA; 1998).

[20] H. Fang and G. Lovelace, *Phys. Rev. D* **72**, 124016 (2005).

[21] H Tagoshi et al., *Prog. Theor. Phys.* **98**, 829 (1997).

[22] H. Rehbein, H. Mueller-Ebhardt, K. Somiya, C. Li, R. Schnabel, K. Danzmann and Y. Chen, *Phys. Rev. D* **76**, 062002 (2007).

[23] D. Shoemaker, and The LIGO Scientific Collaboration,*Nucl. Inst. and Meth. A* **517**, 154 (2004).

[24] L. D. Fiore, and VIRGO collaboration, *Class. Quant. Grav.* **19**, 1421 (2002).

[25] B. Willke, et al., *Class. Quantum Grav.* **19**, 1377 (2002).

[26] M. Ando, and TAMA collaboration, *Phys. Rev. Lett.* **86**, 3950 (2001).

[27] G. Heinzel, A. Freise, H. Grote, K. Strain, and K. Danzmann, *Class. Quant. Grav.* **19**, 1547 (2002).

[28] www.ligo.caltech.edu/advLIGO.

[29] A. Buonanno and Y. Chen, *Phys. Rev. D* **64**, 042006 (2001).

[30] A. Buonanno and Y. Chen, *Phys. Rev. D* **65**, 042001 (2002).

[31] A. Buonanno and Y. Chen, *Phys. Rev. D* **67**, 062002 (2003).

[32] K. Somiya, P. Beyersdorf, K. Arai, S. Sato, S. Kawamura, O. Miyakawa, F. Kawazoe, S. Sakata, A. Sekido, and N. Mio, *Appl. Opt.* **44**, 3179 (2005).

[33] O. Miyakawa, et al., *Phys. Rev. D* **74**, 022001 (2006).

[34] V. B. Braginsky, M. L. Gorodetsky, and F. Y. Khalili, *Phys. Lett. A* **232**, 340 (1997).

[35] C. Li and R. Sari, *The Astrophysical Journal* . **677** 425 (2008).

[36] O. M. Grimsrud, and I. Wasserman, *Monthly Notices of the RAS* , **300**, 1158 (1998).

[37] J. Goodman, *The Astrophysical Journal* , **308**, L47 (1986).

[38] B. Paczynski, *The Astrophysical Journal* , **308**, L43 (1986).

[39] A. Shemi, and T. Piran, *The Astrophysical Journal* , **365**, L55 (1990).

[40] T. Piran, A. Shemi and R. Narayan, *Monthly Notices of the RAS* , **263**, 861 (1993).

[41] P. Mészáros, P. Laguna, and M. J. Rees, *The Astrophysical Journal* , 415, 181 (1993).

[42] C. Kouveliotou, et al. *Nature* **393** 235 (1998).

[43] C. Thompson and R. Duncan, *Monthly Notices of the RAS* **275** 255 (1995).

[44] C. Thompson and R. Duncan, *The Astrophysical Journal* **473** 322 (1996).

[45] E. Nakar, T. Piran and R. Sari, *The Astrophysical Journal* , **635**, 516 (2005).

[46] G. B. Taylor and J. Granot, *Mod. Phys. Lett. A* **21**, 2171 (2006).

[47] X. Wang, et al., *The Astrophysical Journal* , **623**, L29 (2005).

[48] C. Li, D. E. Holz and A. Cooray, *Phys. Rev. D* **75**, 103503 (2007).

[49] A. G. Riess et al., B. J. Barris et al., arXiv:astro-ph/0310843.

[50] R. A. Knop et al., arXiv:astro-ph/0309368(2003).

[51] J. L. Tonry et al., *The Astrophysical Journal* **594**, 1 (2003).

[52] S. Perlmutter et al., *The Astrophysical Journal* **517**, 565 (1999).

[53] A. Riess et al., *Astron. J.* **116**, 1009 (1998).

[54] D. N. Spergel et al. [WMAP Collaboration], *Astrophys. J. Suppl.* **148**, 175 (2003).

[55] D. Huterer and M. S. Turner, *Phys. Rev. D* **60** 081301 (1999).

[56] M. Sahlen, A. R. Liddle and D. Parkinson, *Phys. Rev. D* **72**, 083511 (2005) [arXiv:astro-ph/0506696].

[57] J. Weller and A. Albrecht, *Phys. Rev. D* **65**, 103512 (2002) [arXiv:astro-ph/0106079].

[58] B. F. Gerke and G. Efstathiou, *Monthly Notices of the RAS* **335**, 33 (2002) [arXiv:astro-ph/0201336].

[59] Z. K. Guo, N. Ohta and Y. Z. Zhang, *Phys. Rev. D* **72**, 023504 (2005) [arXiv:astro-ph/0505253].

[60] V. Sahni and A. Starobinsky, arXiv:astro-ph/0610026.

[61] P. Astier et al.,*Astron. Astrophys.* **447** 31 (2006), astro-ph/0510447.

[62] E. V. Linder, *Phys. Rev. Lett.* **90** 091301 (2003)

[63] R. R. Caldwell and E. V. Linder, *Phys. Rev. Lett.* **95**, 141301 (2005) [arXiv:astro-ph/0505494].

[64] Y. Wang and M. Tegmark, *Phys. Rev. D* **71**, 103513 (2005) [arXiv:astro-ph/0501351].

[65] D. Huterer and A. Cooray, *Phys. Rev. D* **71**, 023506 (2005) [arXiv:astro-ph/0404062].

[66] C. Li and A. Cooray, *Phys. Rev. D* **74**, 023521 (2006).

[67] See, e.g., U. Seljak and M. Zaldarriaga, Phys. Rev. Lett. **82**, 2636 (1999) [arXiv:astro-ph/9810092]; Phys. Rev. D **60**, 043504 (1999) [arXiv:astro-ph/9811123]; M. Zaldarriaga and U. Seljak, Phys. Rev. D **59**, 123507 (1999) [arXiv:astro-ph/9810257]; W. Hu, Phys. Rev. D **64**, 083005 (2001) [arXiv:astro-ph/0105117].

[68] W. Hu, *Phys. Rev. D* **62**, 043007 (2000) [arXiv:astro-ph/0001303].

[69] A. Lewis and A. Challinor, arXiv:astro-ph/0601594.

[70] W. Hu and T. Okamoto, *The Astrophysical Journal* **574**, 566 (2002) [arXiv:astro-ph/0111606]; M. Kesden, A. Cooray, and M. Kamionkowski, *Phys. Rev. D* **67**, 123507 (2003) [arXiv:astro-ph/0302536]; C. M. Hirata and U. Seljak, *Phys. Rev. D* **68**, 083002 (2003) [arXiv:astro-ph/0306354].

[71] M. Zaldarriaga and U. Seljak, *Phys. Rev. D* **58**, 023003 (1998) [arXiv:astro-ph/9803150].

[72] M. Kamionkowski, A. Kosowsky, and A. Stebbins, *Phys. Rev. Lett.* **78**, 2058 (1997) [arXiv:astro-ph/9609132]; U. Seljak and M. Zaldarriaga, *Phys. Rev. Lett.* **78**, 2054 (1997) [arXiv:astro-ph/9609169].

[73] M. Kesden, A. Cooray, and M. Kamionkowski, *Phys. Rev. Lett.* **89**, 011304 (2002) [arXiv:astro-ph/0202434]; L. Knox and Y.-S. Song, *Phys. Rev. Lett.* **89**, 011303 (2002) [arXiv:astro-ph/0202286]; U. Seljak and C. Hirata, *Phys. Rev. D* **69**, 043005 (2004) [arXiv:astro-ph/0310163].

[74] N. Kaiser and A. H. Jaffe, *The Astrophysical Journal* **484**, 545 (1997) [arXiv:astro-ph/9609043].

[75] A. Stebbins, preprint, arXiv:astro-ph/9609149.

[76] S. Dodelson, E. Rozo and A. Stebbins, *Phys. Rev. Lett.* **91**, 021301 (2003) [arXiv:astro-ph/0301177].

[77] A. Cooray, M. Kamionkowski and R. R. Caldwell, *Phys. Rev. D* **71**, 123527 (2005) [arXiv:astro-ph/0503002].

[78] A. Cooray and W. Hu, *The Astrophysical Journal* **574**, 19 (2002) [arXiv:astro-ph/0202411]; C. Shapiro and A. Cooray, arXiv:astro-ph/0601226. C. M. Hirata and U. Seljak, *Phys. Rev. D* **68**, 083002 (2003) [arXiv:astro-ph/0306354].

[79] J. Miralda-Escude, *The Astrophysical Journal* **380**, 1 (1991); R. D. Blandford, A. B. Saust, T. G. Brainerd and J. Villumsen, *Monthly Notices of the RAS* **251**, 600 (1991); N. Kaiser, *The Astrophysical Journal* **388**, 272 (1992); For recent reviews, see, M. Bartelmann and P. Schneider, *Phys. Rept.* **340**, 291 (2001); P. Schneider Gravitational Lensing: Strong, Weak & Micro, Lecture Notes of the 33rd Saas-Fee Advanced Course, (Berlin: Springer-Verlag)

[80] L. Knox, *Phys. Rev. D* , **52** 4307 (1995); G. Jungman, M. Kamionkowski, A. Kosowsky and D.N. Spergel,*Phys. Rev. D* , **54** 1332 (1995); J.R. Bond, G. Efstathiou and M. Tegmark, *Monthly Notices of the RAS* , **291** L33 (1997); M. Zaldarriaga, D.N. Spergel and U. Seljak, *The Astrophysical Journal* , **488** 1 (1997); D.J. Eisenstein, W. Hu and M. Tegmark, *The Astrophysical Journal* , **518** 2 (1999)

[81] D. N. Spergel et al., arXiv:astro-ph/0603449.

[82] B. G. Keating, A. G. Polnarev, N. J. Miller and D. Baskaran, arXiv:astro-ph/0607208 (2006).

[83] M. Kaplinghat, L. Knox and Y. S. Song, *Phys. Rev. Lett.* **91**, 241301 (2003) [arXiv:astro-ph/0303344]; K. Ichikawa, M. Fukugita and M. Kawasaki, *Phys. Rev. D* **71**, 043001 (2005) [arXiv:astro-ph/0409768]; J. Lesgourgues, L. Perotto, S. Pastor and M. Piat, *Phys. Rev. D* **73**, 045021 (2006) [arXiv:astro-ph/0511735].

[84] C. Li, T. L. Smith and A. Cooray, *Phys. Rev. D* **75**, 083501 (2007).

[85] R. Scoccimarro, M. Zaldarriaga and L. Hui, *The Astrophysical Journal* , **527**, 1 (1999); D. J. Eisenstein and M. Zaldarriaga, *The Astrophysical Journal* , **546**, 2 (2001). A. Cooray and W. Hu, *The Astrophysical Journal* , **554**, 56 (2001).

[86] A. Cooray, *Phys. Rev. D* **65**, 063512 (2002) [arXiv:astro-ph/0110415].

[87] K. M. Smith, W. Hu and M. Kaplinghat, *Phys. Rev. D* **70**, 043002 (2004) [arXiv:astro-ph/0402442].

Chapter 2

Observable Properties of Orbits in Exact Bumpy Spacetimes

We explore the properties of test-particle orbits in "bumpy" spacetimes—stationary, reflection-symmetric, asymptotically flat solutions of Einstein equations that have a non-Kerr (anomalous) higher-order multipole-moment structure but can be tuned arbitrarily close to the Kerr metric. Future detectors should observe gravitational waves generated during inspirals of compact objects into supermassive central bodies. If the central body deviates from the Kerr metric, this will manifest itself in the emitted waves. Here, we explore some of the features of orbits in non-Kerr spacetimes that might lead to observable signatures. As a basis for this analysis, we use a family of exact solutions proposed by Manko and Novikov which deviate from the Kerr metric in the quadrupole and higher moments, but we also compare our results to other work in the literature. We examine isolating integrals of the orbits and find that the majority of geodesic orbits have an approximate fourth constant of the motion (in addition to the energy, angular momentum and rest mass) and the resulting orbits are triperiodic to high precision. We also find that this fourth integral can be lost for certain orbits in some oblately deformed Manko-Novikov spacetimes, leading to ergodic motion. However, compact objects will probably not end up on these chaotic orbits in nature. We compute the location of the innermost stable circular orbit (ISCO) and find that the behavior of an orbit in the approach to the ISCO can be qualitatively different depending on whether the location of the ISCO is determined by the onset of an instability in the radial or vertical direction. Finally, we compute periapsis and orbital-plane precessions for nearly circular and nearly equatorial orbits in both the strong and weak field, and discuss weak-field precessions for eccentric equatorial orbits.

Originally published as J. Gair, C. Li and I. Mandel, *Phys. Rev. D* **77**, 024035 (2008).

2.1 Introduction

The space-based gravitational-wave (GW) detector LISA is expected to detect gravitational waves generated during the inspirals of stellar-mass compact objects (white dwarfs, neutron stars or black holes) into supermassive bodies in the centers of galaxies—extreme-mass-ratio inspirals (EMRIs). LISA could detect gravitational waves from these systems for several years prior to the plunge of the compact object into the central body and hence observe several hundred thousand waveform cycles. Such observations will provide an exquisite probe of the strong gravity region close to supermassive central bodies (see [1] for a review). In principle, the emitted gravitational waveform encodes the multipole structure of the spacetime outside the central object [2]. One of the hopes for LISA EMRI observations is to extract this spacetime structure from the data and use it to test whether the central objects are indeed Kerr black holes, as we suppose, or something else [2, 3]. (Intermediate-mass-ratio inspirals detectable by Advanced LIGO may reveal the spacetime structure outside intermediate-mass central bodies with more modest precision [4].)

For a Kerr black hole, the spacetime is uniquely determined by the mass and angular momentum of the hole and all higher multipole moments depend on these in a simple way

$$M_l + \mathrm{i}S_l = M(\mathrm{i}\chi M)^l. \tag{2.1}$$

Here M_l and S_l are the lth mass and current multipole moments of the gravitational field, M is the mass of the black hole and χ is its dimensionless spin parameter, $\chi \equiv S_1/M^2 \equiv a/M$. As a consequence of relation (2.1), if the quadrupole or higher multipole moments of a supermassive body are measured from an EMRI observation and these are inconsistent with the values predicted by its mass and spin, the body cannot be a Kerr black hole with a vacuum exterior. The “no-hair” theorem states that, in pure gravity, any pseudostationary, vacuum and asymptotically flat spacetime containing an event horizon and with no closed timelike curves exterior to the horizon must be described by the Kerr metric [5, 6]. If the Cosmic Censorship Conjecture is correct, all astrophysical singularities will be enclosed by a horizon. It is therefore most likely that the supermassive central bodies which are observed to inhabit the nuclei of most galaxies are indeed Kerr black holes. However, LISA should be able to test this assumption. Alternatives to Kerr black holes include “dirty” Kerr black holes with external masses (e.g., an accretion disk), exotic supermassive stars such as boson stars [7], and naked singularities. “Hairy” black hole solutions are also allowed when gravity is coupled to other fields, e.g., a Yang-Mills field (these solutions have been shown to be unstable to perturbations [8]) or a Skyrme field [9] (stability to generic perturbations is an open question). Sufficiently accurate measurements may allow us to distinguish between these possibilities.

In order to prepare us to interpret LISA observations of EMRIs, to identify any deviations from Kerr that are manifest in the waveforms and even to facilitate detection of inspirals into highly non-Kerr spacetimes, we need to understand how these deviations influence the emitted gravitational waveforms. In an extreme-mass-ratio inspiral, the time-scale for the orbital inspiral due to radiation of energy and angular momentum is generally much longer than the orbital time-scale. We can therefore approximate the inspiral as quasistationary, by assuming the inspiraling object is always nearly on a geodesic orbit of the spacetime, and evolving the parameters determining this geodesic slowly over the inspiral (this is usually referred to as the "adiabatic approximation" in the literature [10] since the fluxes of energy and angular momentum used to evolve the sequence of geodesics are computed by assuming the object is on an exact geodesic of the spacetime). In this slow-inspiral limit, the emitted waveforms depend sensitively on the properties of the geodesic orbits in the spacetime—the dominant frequency components in the gravitational waveform at any moment are harmonics of the orbital frequencies of the underlying geodesic. We can thus understand some of the main consequences of deviations from the Kerr metric by examining the effect of such deviations on test particle orbits in the spacetime. By considering a spacetime with an arbitrary set of multipole moments, Ryan demonstrated that, for nearly circular and nearly equatorial orbits, the periapsis and orbital-plane precessions encoded all of the multipole moments at different orders in a weak field expansion [2].

A multipole moment decomposition is not very practical, however, since an infinite number of multipoles are required to characterize the Kerr spacetime. For this reason, Collins & Hughes [11] and Glampedakis & Babak [12] took a different approach and explored test particle dynamics in "bumpy" spacetimes, which were constructed as first-order perturbations of the Schwarzschild and Kerr spacetimes respectively and therefore could be made arbitrarily close to Schwarzschild/Kerr by dialing a parameter to zero. Collins & Hughes coined the phrase "bumpy" black hole to describe these spacetimes. In their case, the presence of stresses exterior to the black hole meant that the horizon could be preserved in the presence of the black hole deformation without violating the no-hair theorem. In the present case, this name is not strictly applicable since the spacetimes we consider are not black holes at all, but rather naked singularities not enclosed by an event horizon. However, the term "bumpy" black hole is still a good one to describe how the spacetime appears to an observer away from the central object.

One drawback of the perturbative approach is that the perturbation is not necessarily small close to the central body, and so the first-order perturbation theory used to construct the spacetime breaks down. As a result, the perturbative solutions may only be used relatively far from the central object. In this work, we therefore take an alternative approach and consider the properties of orbits and inspirals in a family of spacetimes that are exact solutions of the vacuum field equations of relativity and which include the Kerr and Schwarzschild spacetimes in a certain limit. We use a family of spacetimes that were derived by Manko & Novikov [13]. As exact solutions, the spacetimes are valid everywhere and can thus be used to probe the orbital dynamics in the strong field as well as the weak field. The family has an infinite number of free parameters, which can be chosen to make the multipole moments of the spacetime match those of the Kerr spacetime up to a certain order, and then deviate at higher order. In this paper, we choose to make the multipole moments deviate at the mass quadrupole order and higher, by varying a single parameter, although the formalism generalizes to other types of deviation. We use this family of spacetimes as a test bed for an exploration of various observable consequences of deviations from the Kerr metric, but we compare to previous work in the literature as we proceed.

The main new results of the current work are as follows. By studying the properties of orbits in the strong field of the spacetime, we find that most geodesics in the spacetime appear to have a fourth isolating integral of the motion, in addition to the energy, angular momentum and rest mass that are guaranteed by the stationarity and axisymmetry of the metric. The corresponding orbits are triperiodic to high accuracy. This was not guaranteed, since the separability of the geodesic equations in Kerr and corresponding existence of a fourth integral (the Carter constant) was unusual. Additionally, we find that for some oblate perturbations of the Kerr spacetime, there are regions of the spacetime in which there appears to be no fourth integral, leading to ergodic motion. If observed, ergodicity would be a clear "smoking-gun" for a deviation from Kerr. Ergodic motion has been found in other exact relativistic spacetimes by other authors, although these investigations were not carried out in the context of their observable consequences for EMRI detections. Sota, Suzuki and Maeda [14] described chaotic motion in the Zipoy-Voorhees-Weyl and Curzon spacetimes; Letelier & Viera [15] found chaotic motion around a Schwarzschild black hole perturbed by gravitational waves; Guéron & Letelier observed chaotic motion in a black hole spacetime with a dipolar halo [16] and in prolate Erez-Rosen bumpy spacetimes [17]; and Dubeibe, Pachon, and Sanabria-Gomez found that some oblate spacetimes which are deformed generalizations of the Tomimatsu-Sato spacetime could also exhibit chaotic motion [18]. The new features of our current results are the presence of potentially ergodic regions for a wider range of magnitudes of the perturbation, and an examination of whether the ergodic regions are astrophysically relevant. We find that, in the context of an EMRI, the ergodic regions exist only very close to the central body, and these regions are probably not astrophysically accessible, at least in the Manko-Novikov spacetime family.

We also look at the properties of the last stable orbit for circular equatorial inspirals. The frequency of this orbit will be a gravitational-wave observable, and depends significantly on the magnitude of any deviations from Kerr. For certain choices of the quadrupole perturbation, we find that the last stable orbit is defined by the onset of a vertical instability, rather than the radial instability which characterizes the last stable orbit in Kerr. This is a qualitative observable that could be another "smoking-gun" for a deviation from Kerr.

Finally, we look at the periapsis and orbital-plane precession frequencies. We do this primarily for nearly circular and nearly equatorial orbits, since these can be characterized in a gauge-invariant way in terms of the orbital frequency measured by an observer at infinity. Although such precessions were computed by Ryan [2], his results only apply in the weak field. We find results that are consistent with Ryan's in the weak field, but also explore the properties of precessions in the strong field and find they depend significantly on the nature and location of the last stable orbit. Collins & Hughes [11] and Glampedakis & Babak [12] did explore strong field precessions, but they did so as a function of spacetime coordinates, rather than as a function of observable quantities which we do here. The perturbative spacetimes are also not totally applicable in the vicinity of the last stable orbit, so our results are more generally applicable. We also briefly discuss precessions for eccentric equatorial orbits in the weak field and how this is relevant for LISA observations.

The paper is organized as follows. In section 2.2, we introduce our chosen family of spacetimes, describe some properties of these solutions and discuss our approach to computing geodesics in the spacetimes. In section 2.3 we analyze geodesics in these bumpy spacetimes and use Poincaré maps to identify the presence of an effective fourth integral of the motion. We show that most orbits are regular and triperiodic, but also demonstrate the onset of ergodic motion in certain oblately deformed spacetimes. In section 2.4 we find the last stable orbit for circular equatorial orbits and discuss its properties. In section 2.5 we report our results on the periapsis precession and orbital-plane precession in these spacetimes. Finally, in section 2.6 we summarize our results and discuss further extensions to this work. This paper also includes two appendices, in which we present results demonstrating ergodic motion in Newtonian gravity (appendix 2.7) and an expansion of the precessions in the weak field (appendix 2.8). Throughout this paper we will use units such that $c = G = 1$.

2.2 Bumpy Black Hole Spacetimes

In this section, we briefly summarize the Manko-Novikov metric [13]. This is the test metric for which we will explore the dynamics of orbits in Sections 2.3–2.5. The Manko-Novikov metric is an exact stationary, axisymmetric solution of the vacuum Einstein equations that allows for deviations away from the Kerr spacetime by a suitable choice of parameters characterizing the higher-order multipole moments. The presence of these deviations destroys the horizon, so this is no longer a black-hole spacetime. However, its geometry is very similar to that of a Kerr black hole with additional anomalous multipole moments until close to the expected horizon location. We choose a subclass of the Manko-Novikov metric, parametrized by a parameter β. For $\beta = 0$, the metric corresponds to the usual Kerr metric. (In the notation of [13], our parametrization corresponds to setting $\alpha_2 = \beta$ and $\alpha_n = 0$ for all $n \neq 2$).

This subclass of the Manko-Novikov metric can be described by a Weyl-Papapetrou line element in prolate spheroidal coordinates as (cf. Eq. (1) of [13]):

$$ds^2 = -f(dt - \omega d\phi)^2 + k^2 f^{-1} e^{2\gamma}(x^2 - y^2)\left(\frac{dx^2}{x^2-1} + \frac{dy^2}{1-y^2}\right) + k^2 f^{-1}(x^2-1)(1-y^2)d\phi^2,$$

where (cf. Eqs. (9, 10, 12, 13 of [13]):

$$\begin{aligned}
f &= e^{2\psi} A/B, && \text{(2.2a)}\\
\omega &= 2ke^{-2\psi} C A^{-1} - 4k\alpha(1-\alpha^2)^{-1}, && \text{(2.2b)}\\
e^{2\gamma} &= \exp\left(2\gamma^{'}\right) A(x^2-1)^{-1}(1-\alpha^2)^{-2}, && \text{(2.2c)}\\
A &= (x^2-1)(1+ab)^2 - (1-y^2)(b-a)^2, && \text{(2.2d)}\\
B &= [x+1+(x-1)ab]^2 + [(1+y)a + (1-y)b]^2, && \text{(2.2e)}\\
C &= (x^2-1)(1+ab)[b-a-y(a+b)] + (1-y^2)(b-a)[1+ab+x(1-ab)], && \text{(2.2f)}\\
\psi &= \beta R^{-3} P_2, && \text{(2.2g)}\\
\gamma^{'} &= \frac{1}{2}\ln\frac{x^2-1}{x^2-y^2} + \frac{9\beta^2}{6R^6}(P_3P_3 - P_2P_2) && \text{(2.2h)}\\
&+ \beta\sum_{\ell=0}^{2}\left(\frac{x-y+(-1)^{2-\ell}(x+y)}{R^{\ell+1}}P_\ell - 2\right), &&\\
a(x,y) &= -\alpha\exp\left(-2\beta\left(-1+\sum_{\ell=0}^{2}\frac{(x-y)P_\ell}{R^{\ell+1}}\right)\right), && \text{(2.2i)}\\
b(x,y) &= \alpha\exp\left(2\beta\left(1+\sum_{\ell=0}^{2}\frac{(-1)^{3-\ell}(x+y)P_\ell}{R^{\ell+1}}\right)\right), && \text{(2.2j)}\\
R &\equiv (x^2+y^2-1)^{1/2}, && \text{(2.2k)}\\
P_n &\equiv P_n(xy/R) \qquad \text{where } P_n(x) = \frac{1}{2^n n!}\left(\frac{d}{dx}\right)^n (x^2-1)^n. && \text{(2.2l)}
\end{aligned}$$

Here k, α, and β are free parameters which determine the multipole moments of this spacetime. The first few multipole moments have the following values (we correct a typo in Eq. (14) of [13] following [19]):

$$\begin{aligned}
M_0 &= k(1+\alpha^2)/(1-\alpha^2) & S_0 &= 0\\
M_1 &= 0 & S_1 &= -2\alpha k^2(1+\alpha^2)/(1-\alpha^2)^2\\
M_2 &= -k^3[\beta + 4\alpha^2(1+\alpha^2)(1-\alpha^2)^{-3}] & S_2 &= 0\\
M_3 &= 0 & S_3 &= 4\alpha k^4[\beta + 2\alpha^2(1+\alpha^2)(1-\alpha^2)^{-3}]/(1-\alpha^2).
\end{aligned} \tag{2.3}$$

Therefore, for a given choice of mass $M \equiv M_0$, spin $\chi \equiv S_1/M^2$ and anomalous (additional to Kerr) dimensionless quadrupole moment $q \equiv -(M_2 - M_2^{\text{Kerr}})/M^3$, the three metric parameters are:

$$\alpha = \frac{-1+\sqrt{1-\chi^2}}{\chi}, \qquad k = M\frac{1-\alpha^2}{1+\alpha^2}, \qquad \beta = q\frac{M^3}{k^3}.$$

A given choice of M, χ and q uniquely defines the metric. With this definition of q, a choice $q > 0$ represents an oblate perturbation of the Kerr metric, while $q < 0$ represents a prolate perturbation. A spacetime is oblate if it has $M_2 < 0$, e.g., for Kerr $M_2 = -\chi^2 M^3$. When we say a prolate/oblate perturbation we mean a perturbation that makes the spacetime more prolate/oblate relative to Kerr. In particular, for $-\chi^2 < q < 0$ the spacetime is still oblate, although it has a prolate perturbation relative to the Kerr metric. We note that taking $q \neq 0$ changes all higher moments from their Kerr values, so these solutions deviate not only in the mass quadrupole moment but also in the current octupole moment, the mass hexadecapole moment etc.

To present our results, we find it useful to display them in terms of cylindrical coordinates ρ, z and ϕ. These are related to the prolate spheroidal coordinates $x,\ y$ by [19]

$$\rho = k(x^2-1)^{1/2}(1-y^2)^{1/2}, \qquad z = kxy, \tag{2.4}$$

and the line element in cylindrical coordinates is

$$ds^2 = -f(dt - \omega d\phi)^2 + f^{-1}\left[e^{2\gamma}(dz^2 + d\rho^2) + \rho^2 d\phi^2\right]. \tag{2.5}$$

2.2.1 Spacetime Properties

The Manko-Novikov spacetimes are vacuum and have the multipolar structure given in Eq. (2.3). As a consequence of the no-hair theorem, the spacetimes must therefore either lack an event horizon or contain closed timelike curves exterior to a horizon. In fact, both of these statements are true. The central singularity is enclosed by a partial horizon at coordinates $\rho = 0$, $|z| \leq k$. However, this horizon is broken in the equatorial plane by a circular line singularity at $x = 1,\ y = 0$ ($\rho = z = 0$) [20]. For $\chi = 0$ the spacetime is otherwise regular, but for $\chi \neq 0$, the spacetimes contain both an ergosphere and a region where closed timelike curves exist. The structure of the spacetimes is quite similar to that of the $\delta = 2$ Tomimatsu-Sato spacetime, as described in [21]. The boundary of the ergosphere is determined by the condition $g_{tt} = 0$. Inside this region, timelike observers cannot be at rest. Such a region is entirely physical, and also exists in the Kerr spacetime, where it is of interest since it allows energy extraction via the Penrose process. We show the location of the ergosphere for $\chi = 0.9$ and various choices of q in the top panel of Figure 2.1. The shape of the ergosphere is more complicated when $q \neq 0$, having a multiple lobed structure. This structure is also qualitatively different depending on the sign of q—for $q > 0$ there are three separate ergoregions, one of which intersects the equatorial plane, one which is entirely above the equatorial plane and one which is entirely below; for $q < 0$ there are only two regions, one of which is entirely above the equatorial plane and one of which is entirely below.

For a metric of this type, the region where closed timelike curves (CTCs) exist is determined by the condition $g_{\phi\phi} < 0$. In the bottom panel of Figure 2.1 we show the portion of the spacetime where CTCs exist for the same choices of q and $\chi = 0.9$. Particles orbiting inside the CTC region are moving backward in time. This is not inconsistent with relativity, but CTC zones are sometimes regarded as unphysical. A spacetime with no CTC zone can be constructed by adding an inner boundary in the spacetime, and just using the portion of the Manko-Novikov solution exterior to that boundary. The CTC zone again has a multiple lobed structure and is different depending on the sign of q. We note in particular that for $q < 0$ the ergosphere does not intersect the equatorial plane, although the CTC region does. For $q > 0$ both regions intersect the equatorial plane, and the outermost edge of the CTC region is inside the ergoregion.

2.2.2 Geodesic Motion

Geodesic motion in an arbitrary spacetime is described by the second-order equations

$$\frac{d^2x^\alpha}{d\tau^2} = -\Gamma^\alpha_{\beta\gamma}\frac{dx^\beta}{d\tau}\frac{dx^\gamma}{d\tau}, \tag{2.6}$$

where the connection coefficients $\Gamma^\alpha_{\beta\gamma}$ are given by

$$\Gamma^\alpha_{\beta\gamma} = \frac{1}{2}g^{\alpha\mu}\left(g_{\mu\beta,\gamma} + g_{\mu\gamma,\beta} - g_{\beta\gamma,\mu}\right). \tag{2.7}$$

The spacetimes we are interested in are axisymmetric and time-independent and the metric correspondingly has two ignorable coordinates—t and ϕ. There are therefore two constants of geodesic motion: the energy E and the z-component of angular momentum L_z, which are given by

$$E = -g_{tt}\dot{t} - g_{t\phi}\dot{\phi}, \qquad L_z = g_{t\phi}\dot{t} + g_{\phi\phi}\dot{\phi},$$

where a dot $\dot{}$ denotes the derivative with respect to proper time τ. Another first integral of the motion can be obtained from conservation of the rest mass of the orbiting particle:

$$-1 = g_{\alpha\beta}\dot{x}^\alpha\dot{x}^\beta.$$

In practice, we numerically integrate the second-order geodesic equations (2.6) rather than use these first integrals, and we use the constancy of E, L_z and $g_{\alpha\beta}\dot{x}^\alpha\dot{x}^\beta$ as cross-checks to verify the quality of our numerical results. The results reported below typically show the conservation of

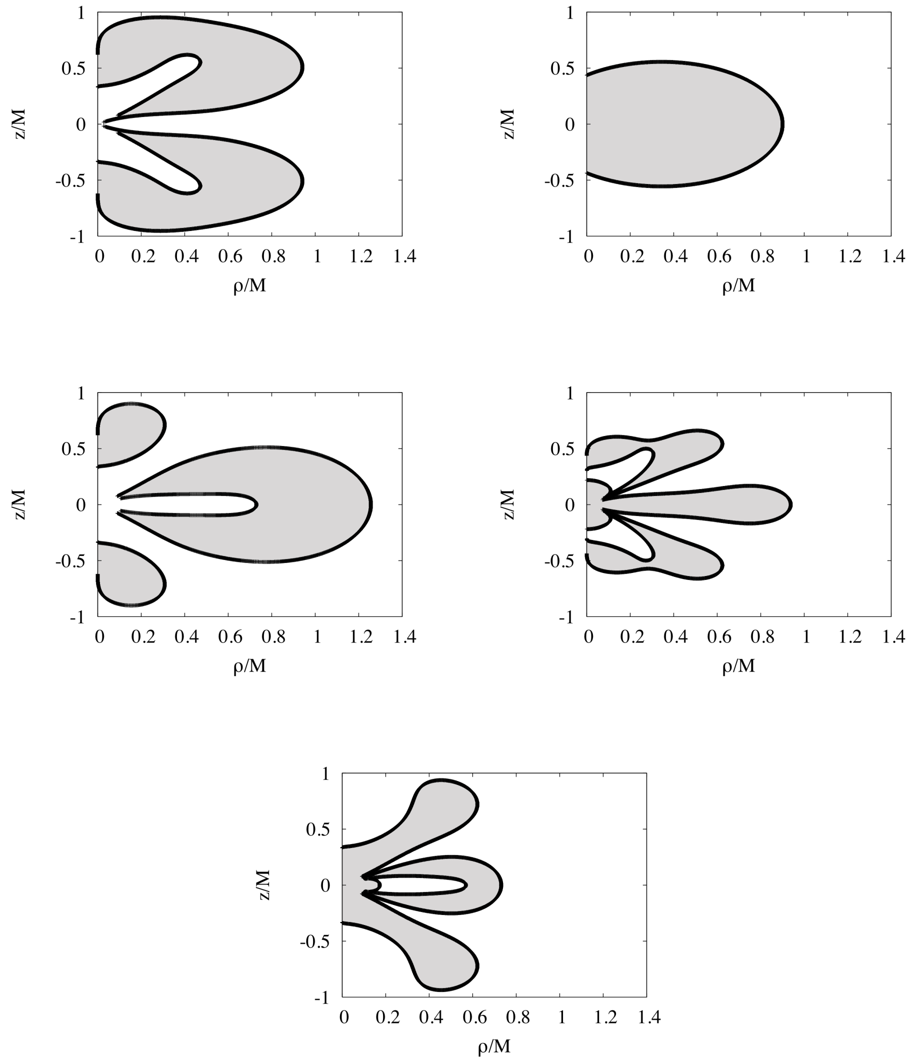

Figure 2.1: Spacetime structure for $\chi = 0.9$. The upper row shows zeros of g_{tt} for $q = -1$ (left column), $q = 0$ (middle column) and $q = 1$ (right column). This defines the boundary of the ergoregion of the spacetime. The region with $g_{tt} > 0$ is shaded. The bottom row shows points where $g_{\phi\phi}$ changes sign for the same values of q, and the region where $g_{\phi\phi} < 0$ is shaded. This defines the region where closed timelike curves exist. The middle bottom panel is empty since there is no such region in the Kerr spacetime. The shape of the two boundaries is qualitatively the same for other values of q with the same sign, although both regions grow as $|q|$ is increased.

these quantities to a few parts in 10^{10} over the time of integration; see Fig. 2.2. We compute the connection coefficients analytically from expressions for the metric functions f, ω and γ defined in Eqs. (2.2). The only difficulty arises at points where a metric component $g_{\mu\nu}$ vanishes and its inverse $g^{\mu\nu}$ diverges. When this occurs, we analytically factor out the terms that tend to zero to avoid issues in numerical integration. To perform the numerical integration we write the coupled system of four second-order ordinary differential equations (2.6) in first-order form and integrate numerically in C++ via the Bulirsch-Stoer method.

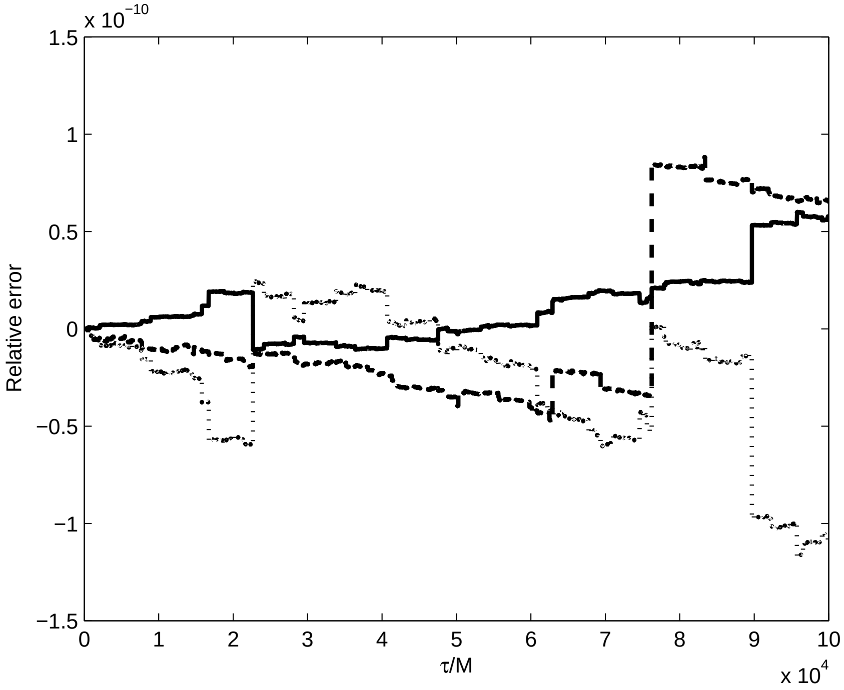

Figure 2.2: The fractional errors in energy E (solid line), angular momentum L_z (dashed line), and the quantity $g_{\alpha\beta}\dot{x}^\alpha\dot{x}^\beta$ (dotted line) accumulated over 1700 orbits of a geodesic with $E = 0.92$ and $L_z = 2.5M$ in a spacetime with spin $\chi = 0.9$ and anomalous quadrupole moment $q = 0.95$.

Some general properties of geodesic motion can be understood by using the first integrals (2.8)–(2.8). The energy and angular momentum conservation equations (2.8) can be used to write $\dot{t}$ and $\dot{\phi}$ in terms of E, L_z, ρ and z:

$$\dot{t} = \frac{E g_{\phi\phi} + L_z g_{t\phi}}{g_{t\phi}^2 - g_{tt} g_{\phi\phi}}; \qquad \dot{\phi} = \frac{-E g_{t\phi} - L_z g_{tt}}{g_{t\phi}^2 - g_{tt} g_{\phi\phi}}.$$

These expressions can be substituted into Eq. (2.8) to give

$$\frac{\mathrm{e}^{2\,\gamma(\rho,z)}}{f(\rho,z)}\left(\dot{\rho}^2 + \dot{z}^2\right) = \frac{E^2}{f(\rho,z)} - \frac{f(\rho,z)}{\rho^2}\left[L_z - \omega(\rho,z)\,E\right]^2 - 1 \equiv V_{\mathrm{eff}}(E, L_z, \rho, z). \tag{2.8}$$

The motion in ρ and z may thus be thought of as motion in the effective potential V_{eff}. In particular, since the left hand side of Eq. (2.8) is strictly positive or zero, motion can only exist in regions where $V_{\text{eff}} \geq 0$. Finding the zeros of the effective potential therefore allows us to find allowed regions of the motion. As an illustration, we show the zeros of the effective potential in Figure 2.3 for the simple case of the Kerr metric with spin parameter $\chi = 0.9$, energy $E = 0.95$ and angular momentum $L_z = 3M$. There are two regions of allowed motion—one region at larger radius that corresponds to bound orbits, and another region at very small radii that corresponds to rising and plunging orbits.

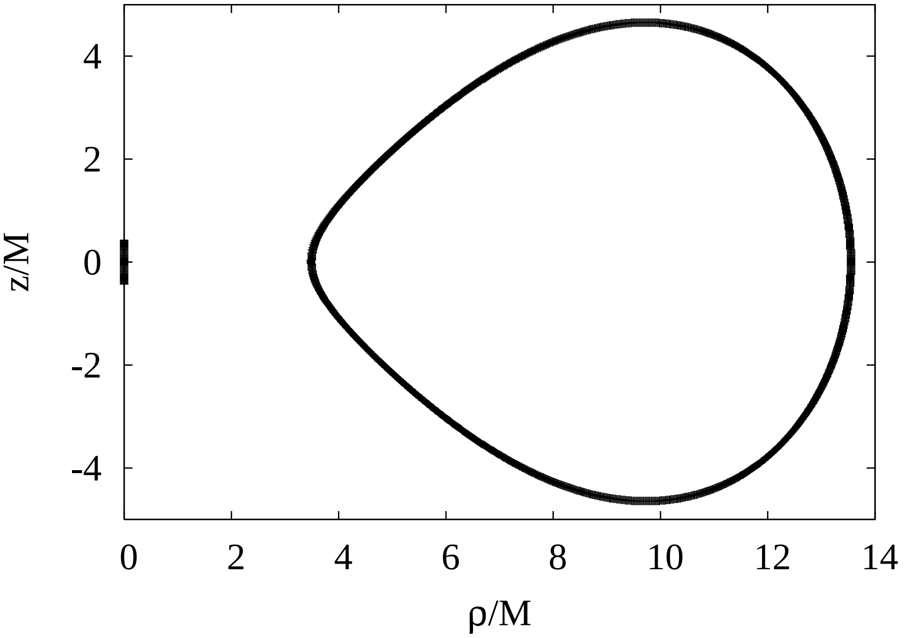

Figure 2.3: Effective potential for geodesic motion around a Kerr black hole, with $E = 0.95$, $L_z = 3M$ and $\chi = 0.9$. The curves indicate zeros of the effective potential. Allowed orbits are found in the small region around $\rho = 0$, $z = 0$ (rising and plunging orbits) or in the region containing $\rho = 10$, $z = 0$ (bound orbits).

We now turn our attention to the Manko-Novikov spacetime with $q \neq 0$. For spacetimes with $\chi = 0$, and for spacetimes with $\chi \neq 0$ and $q < 0$ (prolate perturbation of the Kerr metric at large radii), the addition of the perturbation does not fundamentally change the nature of the effective potential – there are still two bounded regions, one attached to the origin corresponding to rising and plunging orbits and one at larger radii corresponding to bound orbits. The shapes of these regions change as $|q|$ is increased and if $|q|$ is increased sufficiently at fixed E and L_z the two regions merge, so that all allowed orbits can reach the origin. Even after this has occurred, there appear to be two types of orbit in the single allowed region – those that rise and plunge and those that undergo many periods of radial oscillation. We do not know if the latter remain non-plunging forever in principle. In practice, perturbations due to external material or radiation reaction may cause bound orbits to diffuse onto plunging orbits over time. For fixed $q < 0$, the two allowed regions also change shape as the energy and angular momentum are varied. In particular, the plunging region connected to the partial horizon at $\rho = 0$, $|z| \leq k$ develops a multi lobed structure. For sufficiently large $|q|$ and sufficiently low E and L_z, two of these lobes can touch in the equatorial plane. This leads to the existence of circular, equatorial orbits that are unstable to vertical perturbations, which we will encounter again in Section 2.4.

For $\chi \neq 0$ and $q > 0$ (oblate perturbation of the Kerr metric at large radii), the behavior is qualitatively different. For any arbitrarily small $|q|$, an additional allowed region appears in the effective potential, which is bounded away from $\rho = 0$ and therefore corresponds to bound orbits. For small $|q|$ this new region is very close to $\rho = 0$. The other two allowed regions still exist, and merely change shape as the value of $|q|$ is increased. The additional bound region is always outside the region where closed timelike curves (CTCs) exist, and is therefore in the portion of the spacetime that can be regarded as physical. However, in the plane $z = 0$ the outermost edge of the CTC region touches the innermost edge of the region of bound motion. This additional region also extends inside the spacetime ergosphere.

We consider as an example the case with $\chi = 0.9$ and $q = 0.95$. The zeros of the effective potential V_{eff} are plotted in Figure 2.4 for geodesics with energy $E = 0.95$ and angular momentum $L_z = 3M$. In this figure there are three distinct allowed regions as described above: (i) a foliated "plunging" region connected to $\rho = 0$, where all orbits rapidly plunge through the horizon (this region also intersects the CTC region); (ii) an inner bound region, which is located between $\rho/M \approx 0.72$ and $\rho/M \approx 2.12$ for the chosen values of E and L_z; and (iii) an outer bound region between $\rho/M \approx 2.39$ and $\rho/M \approx 13.6$. We show the trajectory of a typical orbit in the outer region. This has a regular pattern or intersections throughout the (ρ, z) plane, which is characteristic of an orbit with an approximate fourth integral.

If $|q|$ is increased from the value shown in Figure 2.4, the two regions of bound motion eventually merge. When this first occurs, the "neck" joining the regions is extremely narrow. Geodesics exist which can pass through the neck, but this requires extreme fine tuning. As $|q|$ is further increased, the neck gradually widens and eventually disappears. At that stage, the single allowed region for bound orbits has a similar shape to the outer region of Figure 2.4.

These general properties of the effective potential seem to be common to all spacetimes with $q > 0$ and $\chi \neq 0$. More relevant for the EMRI problem is to fix q and χ and to vary E and L_z. For $E = 1$ and sufficiently large L_z, there are two regions of allowed motion bounded away from the origin, in addition to the plunging zone connected to $\rho = 0$, $|z| \leq k$. The outermost of the allowed regions stretches to infinity and contains parabolic orbits. The inner region of bounded motion is the analogue of the inner bound region described above and lies very close to the central object. If the angular momentum is decreased, while keeping $E = 1$, the two non-plunging regions get closer together and eventually merge to leave one allowed region that stretches to infinity. For fixed $E < 1$ the behavior is qualitatively the same, except that for $L_z \gg M$ there is no outer region (there is a

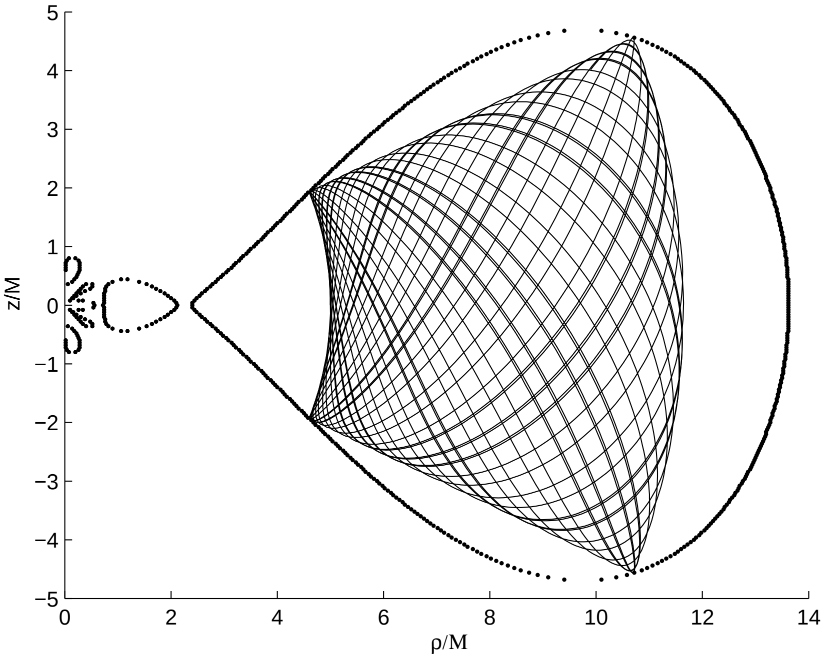

Figure 2.4: Effective potential for geodesic motion around a bumpy black hole with $\chi = 0.9$, $q = 0.95$, $E = 0.95$, and $L_z = 3M$. The thick dotted curves indicate zeros of the effective potential. The trajectory of a typical geodesic in the outer region is shown by a thin curve. The regular pattern of self-intersections of the geodesic projection onto the $\rho - z$ plane indicates (nearly) regular dynamics.

maximum allowed angular momentum for bound orbits of a given energy, as in the Kerr spacetime). As L_z is decreased, the outer region for bound motion appears and then eventually merges with the inner region. Decreasing L_z further eventually causes the bound region to merge with the plunging region. At fixed L_z, if there are two distinct non-plunging allowed regions for $E = 1$, these regions do not merge as E is decreased, but the outer region eventually disappears (there is a minimum allowed energy for orbits of a given angular momentum, as in the Kerr spacetime). If there is only one non-plunging region for $E = 1$, then as E is decreased, this region eventually splits into two allowed regions, and the outer region eventually disappears as E is decreased further. The properties are similar for all $\chi \neq 0$, but decreasing χ with the other parameters fixed tends to bring the two allowed regions of motion closer to merger with one another.

2.3 Isolating Integrals

The isolating integrals given by the conservation equations (2.8)–(2.8) do not completely describe the motion, since the motions in ρ and z are coupled. Thus, solution of the geodesic equations requires use of the second-order form of those equations (2.6). However, it was demonstrated by

Carter [22] that in the Kerr spacetime there is a fourth isolating integral for geodesic motion, the Carter constant, which arises as a constant of separability of the Hamilton-Jacobi equation and was later shown to be associated with a Killing tensor in the spacetime. Carter found the form of all metrics that were both Schrödinger and Hamilton-Jacobi separable. Imposing the further requirement that the metric be a solution of the vacuum Einstein-Maxwell equations leads to the Kerr metric as the only spacetime of this form that does not include a gravomagnetic monopole. Thus, the separability of the equations in Kerr is somewhat fortuitous and we would not expect that the fourth integral would be preserved when we add an anomalous quadrupole moment as we do here. As a consequence, the properties of geodesics might be expected to be somewhat different, and might even be ergodic. As mentioned in the introduction, ergodic geodesic motion has been found in other relativistic spacetimes by several other authors [14, 15, 16, 17, 18].

A fourth integral of the motion essentially gives another relationship between $\dot{\rho}^2$ and $\dot{z}^2$. Combining this with the effective potential equation (2.8) allows us to eliminate $\dot{z}^2$ for instance and hence obtain an expression for $\dot{\rho}^2$ as a function of ρ and z only. Similarly we can obtain an expression for $\dot{z}^2$ as a function of ρ and z.

A standard way to examine equations of motion and look for ergodicity is to plot a Poincaré map. This involves integrating the equations of motion and recording the value of ρ and $\dot{\rho}$ every time the orbit crosses a plane $z =$ constant. From the preceding arguments, if a fourth integral exists, the value of $\dot{\rho}$ will be a function only of ρ and z (the function could be multi valued, depending on the order at which the velocities appear in the constants of motion). Therefore such a map must show a closed curve. Similarly, if the Poincaré map of an orbit shows a closed curve for every value of z, then this defines a relationship between $\dot{\rho}$, ρ and z which is then an effective fourth integral of the motion. The Poincaré analysis thus provides a means to identify whether an effective fourth integral exists or the motion is apparently "chaotic". In the latter case, the absence of the integral would be manifested on the Poincaré maps as space-filling trajectories rather than closed curves.

The absence of a full set of isolating integrals does not necessarily mean that all orbits will exhibit full-blown chaos. For some initial conditions, orbits may show obvious signs of ergodicity, while for other initial conditions in the same spacetime, orbits may appear to behave in an integrable fashion, suggesting that an approximate additional invariant exists. Although this behavior may appear surprising at first glance, it is consistent with the predictions of the KAM theorem and with many known examples of chaotic behavior. (The KAM theorem, due to Kolmogorov, Arnold and Moser, states that if the Hamiltonian of a system with a full set of integrals of motion is analytically weakly perturbed, then phase-space motion in the perturbed system will be confined to the neighborhoods of invariant tori in phase space, except when angle-variable frequencies of the unperturbed system are nearly commensurate, in which case motion will be chaotic [23].)

As an illustration, we show in Figure 2.5 the Poincaré map for geodesic motion along orbits with three different initial conditions in the Kerr spacetime with the same E, L_z and χ as Figure 2.3. The Poincaré maps are all closed curves, consistent with the existence of the fourth isolating integral, the Carter constant. In appendix 2.7 we present results for motion under gravity in a Newtonian quadrupole-octupole potential and demonstrate the existence of both regular and ergodic orbits. This example serves to put the relativistic results described here in a Newtonian context.

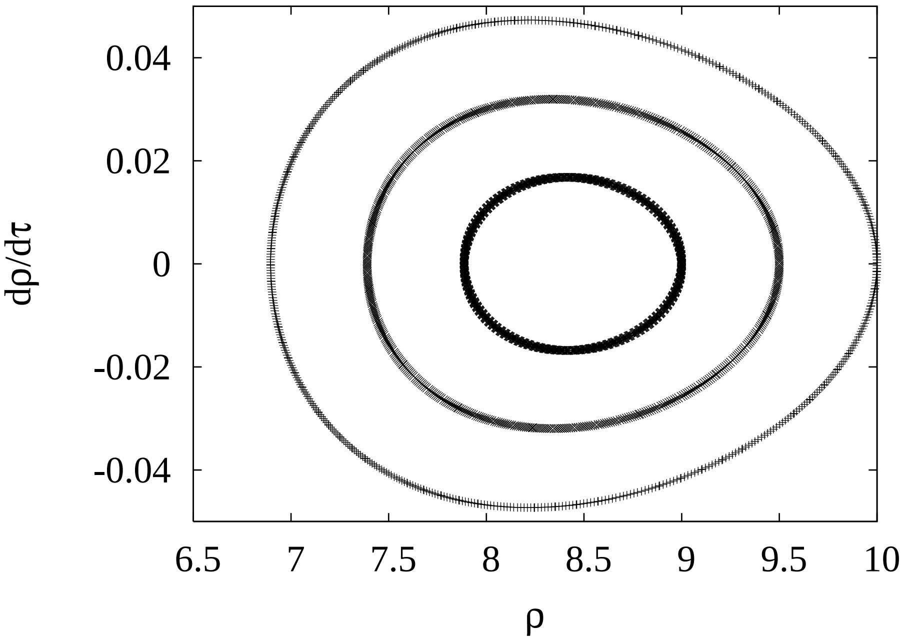

Figure 2.5: Poincaré map showing $d\rho/d\tau$ vs ρ for crossings of the $z = 0$ plane for a sequence of orbits in the outer allowed region of the Kerr spacetime with $E = 0.95$, $L_z = 3M$ and $\chi = 0.9$. The closed curves indicates the presence of a fourth isolating integral, which we know to be the Carter constant.

2.3.1 Poincaré Maps for the Manko-Novikov Spacetimes

The regularity properties of geodesics appear to be highly correlated with the nature of the effective potential as described in the previous section. For spacetimes with $\chi = 0$ and those with $\chi \neq 0$ but $q < 0$, all orbits appear to be regular, i.e., they show closed Poincaré maps similar to those in Figure 2.5. These are the spacetimes in the Manko-Novikov family that have effective potentials which are qualitatively the same as the Kerr case.

For $q > 0$, the effective potential can have two allowed regions for bound motion. What is striking is that whereas orbits in the outer allowed bound region (which corresponds to the allowed region in the $q = 0$ limit) appear to be regular, with closed Poincaré maps, those in the inner allowed region appear chaotic. In Figures 2.6 and 2.7 we show Poincaré maps for one orbit in each of the outer and inner regions of the effective potential illustrated in Figure 2.4 ($q = 0.95$, $E = 0.95$, $L_z = 3M$,

$\chi = 0.9$). Orbits in the outer region show closed Poincaré maps, suggesting that the motion is regular or very nearly so and has an approximate fourth invariant of the motion. This is reinforced by the projection of the orbit onto the ρ-z plane, which was shown in Fig. 2.4. The geodesic shows a regular grid pattern, with four possible velocities at each point, corresponding to $\pm|\dot{\rho}|$ and $\pm|\dot{z}|$. If these orbits do not have a true invariant, the regularity of the Poincaré map suggests that it may still be possible to find an algebraic expression for an approximate constant of the motion.

Orbits in the inner region, by contrast, seem to fill up all possible points in a subdomain of the allowed parameter space (with $V_{\rm eff} > 0$) and are therefore apparently ergodic in this subdomain. It seems likely, in view of the KAM theorem, that all orbits in the spacetime are strictly speaking chaotic, and no true isolating integral exists, but in the outer region there is a quantity that is nearly invariant along the orbits [4]. Either the thickness of the region mapped out by the chaotic motion is small, or the time over which ergodicity manifests itself is very long. From an observational standpoint, whether the motion is actually regular or whether only an approximate invariant exists is irrelevant, since the time-scale over which ergodicity would manifest itself in the waveform would be much longer than the time during which the orbiting object moves on an approximate geodesic.

It is unusual, given that chaotic and nearly regular regions are generally interspersed in most KAM theorem applications [23], that we find the family of geodesics is divided into two distinct regions such that geodesics in one region are ergodic while those in the other exhibit nearly regular orbital dynamics. We have been unable to find any strongly ergodic geodesics in the outer region, or any non-ergodic geodesics in the inner region. As described in the previous section, adjusting the orbital parameters can cause the two allowed regions to merge. When this first occurs, the two regions are connected by a very narrow neck. The narrowness of the neck means that extreme fine tuning is required to get a geodesic to pass through the neck. By choosing initial conditions in the neck, and integrating forward and backward in time, we obtained orbits that traversed the neck once and found that the motion was apparently ergodic while in the inner region, but apparently regular in the outer region. This behavior is consistent with the predictions of the KAM theorem, but observationally the fact that the orbits in the outer region are technically ergodic does not matter as long as they appear regular on long time-scales. We were unable to find an orbit that traversed the neck more than once. Further adjustment of the orbital parameters causes the neck to widen and eventually disappear. At that stage, most of the orbits appear to be regular, but orbits that pass very close to the inner edge of the merged region (i.e., close to the CTC zone) have not been fully investigated.

An alternative explanation of these results [24] is that the geodesic equations are numerically unstable in the inner region, and therefore small numerical round-off errors in the integration routines are driving the orbits away from their true values. Once again, this distinction is not relevant observationally. An astrophysical system harboring an EMRI will not be isolated. The gravitational perturbations from distant stars etc. will serve the same role in perturbing the orbits as numerical errors might on a computer. The end result—that the orbit is apparently ergodic— is the same.

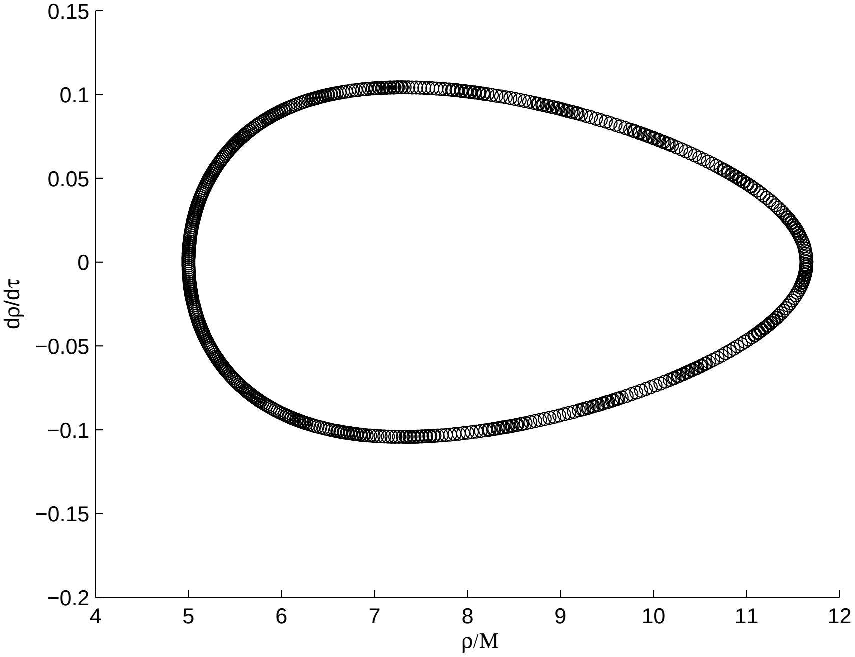

Figure 2.6: Poincaré map for a geodesic in the outer region of Fig. 2.4.

2.3.2 Frequency Component Analysis

The above conclusions are supported by a frequency-domain analysis of the ρ and z motion in the two regions. The absolute values of Fourier transforms of $\rho(t)$ and $z(t)$ are plotted in Figures 2.8 and 2.9. Fig. 2.9 shows an absence of clearly identifiable frequency peaks for geodesics in the inner region, a result consistent with full-blown chaos. By contrast, Fig. 2.8 shows discrete frequency peaks in the outer region. Generally such frequency peaks, corresponding to harmonics of a few fundamental frequencies, occur in problems with a full set of isolating integrals. We find that the frequency components measured for the ρ and z motion in the outer region can be represented as low order harmonics of two fundamental frequencies at a high level of precision (1 part in 10^7 for the first ~ 10 harmonics). This multi periodicity of the geodesics implies that the gravitational waveforms will also be multi periodic. Indeed, we find that an approximate gravitational waveform, constructed using a semirelativistic approximation for the gravitational-wave emission (as used to construct Kerr EMRI waveforms in [25]), is also tri-periodic (the third frequency arises from the ϕ motion since the observer is at a fixed sky location). The absolute value of the Fourier transform of the $h_+(t)$ component of this gravitational waveform is also plotted in Fig. 2.8 and is clearly multi

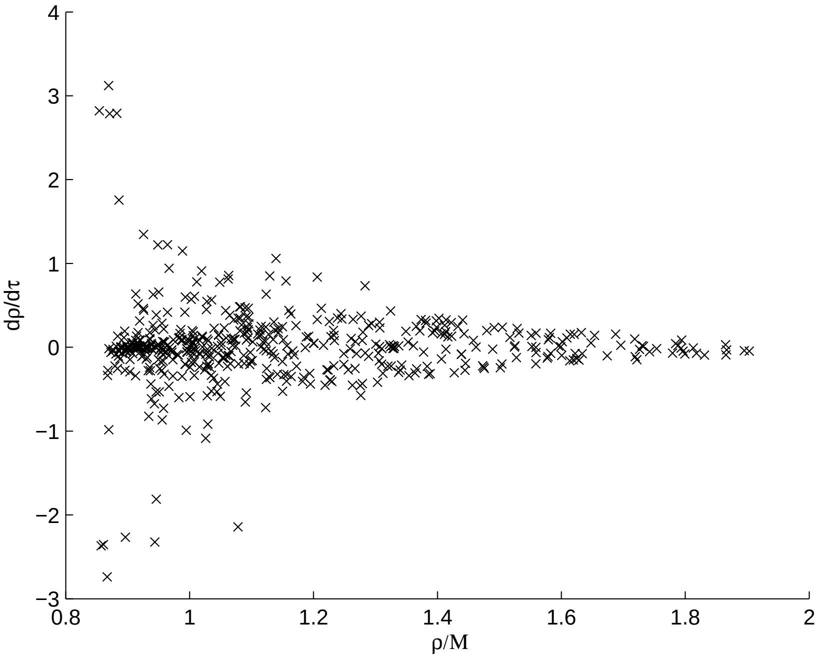

Figure 2.7: Poincaré map for a geodesic in the inner region of Fig. 2.4.

periodic. This periodicity has important consequences for data analysis and parameter extraction.

2.3.3 Comparison to Other Results

Our results are consistent with previous work by other authors who have found chaotic geodesic motion in various spacetimes. Generally, chaotic motion only occurs in the strong field region close to the central object, and for a limited range of geodesic parameters. As an example, Guéron and Letelier [17] found chaos in a prolate Erez-Rosen spacetime, which represented a deformation of a Schwarzschild black hole. They demonstrated that, for a particular value of the energy and angular momentum, when the deformation parameter had a value $k_2 = -5$, there was a single allowed region of bounded motion, but for $k_2 = -5.02$ the region split into two separate regions. After the split, orbits in the inner region appeared chaotic while those in the outer region appeared regular. For the merged region, orbits that passed into the inner part also appeared ergodic while those that were purely in the outer part looked regular. This is qualitatively very similar to what we have found in the Manko-Novikov spacetime, although we find chaotic motion only when $\chi \neq 0$, while Guéron and Letelier presented examples for both a perturbed non-spinning black hole and a spinning black hole. As a test of our codes, we repeated Guéron and Letelier's calculation and found consistent results. As well as providing another example of chaos for relativistic geodesics, the results here show some new features. In particular, the inner allowed region appears for any $q > 0$ and as far

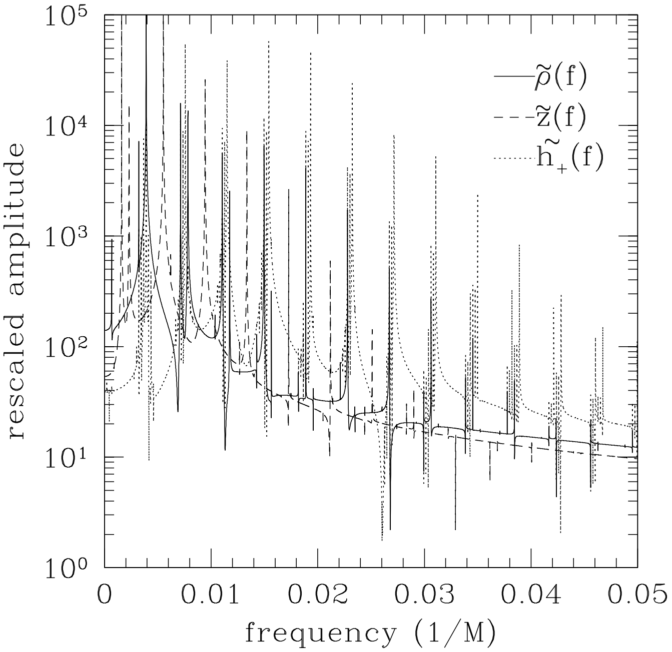

Figure 2.8: Absolute values of the Fourier transforms of $\rho(t)$ (solid line), $z(t)$ (dashed line), and the gravitational wave component $h_+(t)$ (dotted line) in the frequency domain for an orbit in the outer region of Fig. 2.4. The frequency is displayed in units of $1/M$; the amplitude scaling is arbitrary.

as we have been able to ascertain the motion is always ergodic in that region. This contrasts to the spacetime considered by Guéron and Letelier, in which chaotic motion exists only for a small range of k_2 (by the time k_2 has increased to $k_2 = -5.1$, the motion is no longer apparently ergodic). Previous authors have also not considered the issue of accessibility of the ergodic region to stars, and we discuss that in the next subsection.

Sota et al. [14] discussed what might cause chaos in relativistic geodesic motion, and suggested that it might arise either due to a change in the signs of the eigenvalues of the Weyl tensor, which would lead to "local instability" or due to the presence of homoclinic orbits. The Manko-Novikov spacetimes do contain homoclinic orbits, but Sota et al. [14] found that this only led to chaos in non-reflection symmetric spacetimes, so this explanation probably does not apply here. We have not explored the properties of the eigenspace of the Weyl tensor for these spacetimes, but "local instability", could be a plausible explanation for our results. The CTC region of the Manko-Novikov spacetime might also be causing the ergodicity. The region where ergodic motion occurs touches the CTC region at a single point, so the singular behavior of the metric as the CTC region is approached might explain the observed behavior, either by causing a region of "local instability" or through some other mechanism.

We note that in the regime where chaos occurs, the perturbation to the Kerr metric cannot be regarded as purely quadrupolar, but the deviations in the higher multipole moments are also

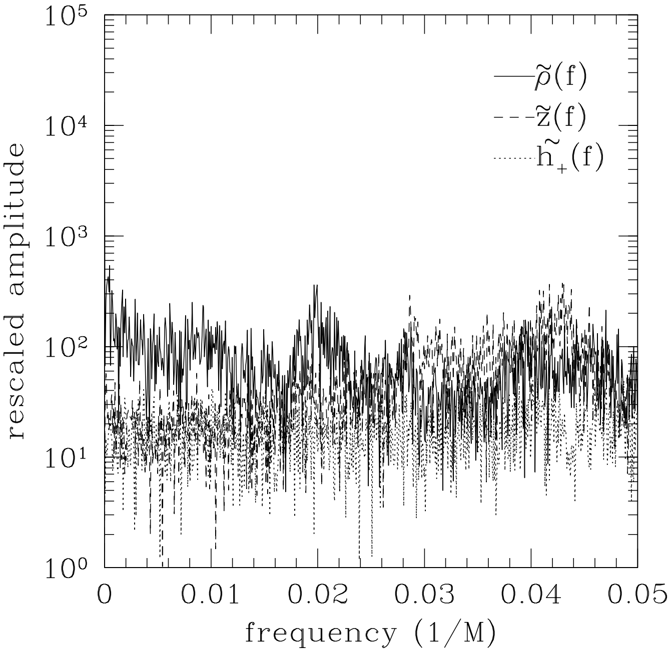

Figure 2.9: Absolute values of the Fourier transforms of $\rho(t)$ (solid line), $z(t)$ (dashed line), and the gravitational wave component $h_+(t)$ (dotted line) in the frequency domain for an orbit in the inner region of Fig. 2.4. The frequency is displayed in units of $1/M$; the amplitude scaling is arbitrary.

significant. This is similar to the Newtonian result described in Appendix 2.7 since we find chaos in the Newtonian quadrupole-octupole potential but not a pure quadrupole potential. The relativistic results are somewhat different, however, since we find chaos only for $\chi \neq 0$, so for these spacetimes we also need a non-zero current dipole moment to observe chaotic behavior.

2.3.4 Accessibility of the Ergodic Domain

While the existence of ergodic motion is mathematically interesting, an important question for EMRIs that has not been addressed so far is whether ergodicity could ever be observed in nature. In other words, is it possible, during the course of an inspiral, for a captured object to find itself on an ergodic geodesic?

In typical astrophysical scenarios, the inspiraling compact object will start out far away from the central body with energy close to 1 [1]. Unless the angular momentum is very small (which in the Kerr spacetime would represent an object on a plunging orbit), this will correspond to an orbit in the outer region of allowed motion if two regions exist, so the orbit will initially be regular. As the star inspirals, the energy and angular momentum will gradually change and this causes the separation between the outermost point of the inner region of bound motion and the innermost point of the outer region, $\Delta\rho$, to change. For example, when $E = 0.99$ and $L_z = 4.33M$ in a Manko-Novikov spacetime with $\chi = 0.9$, and $q = 0.95$, we find that $\Delta\rho/M \approx 6.4$. When $E = 0.95$

and $L_z = 3M$ in the same spacetime, the separation between regions is only $\Delta\rho \approx 0.27M$. For sufficiently small choices of energy and angular momentum (e.g., $E = 0.92$ and $L_z = 2.5M$) only a single region remains. This suggests that the two regions will come closer together as energy and angular momentum are radiated away during an inspiral, until they eventually merge. We conjecture that $\mathrm{d}(\Delta\rho)/\mathrm{d}t$ is always negative; that is, the two regions are always merging rather than separating. To test this conjecture, we must explore the behavior of $\Delta\rho$ along an extreme-mass-ratio inspiral characterized by slowly evolving E and L_z.

To do this, we use an approximate scheme to evolve the energy and angular momentum during an inspiral. Our scheme is based on combining exact relativistic expressions for the evolution of orbital elements with approximate post-Newtonian formulae for energy and angular-momentum fluxes. This scheme was previously devised to describe EMRIs into Kerr black holes [26] and has been shown to give reliable results in that context. For the current calculation, we must augment the fluxes with an additional post-Newtonian term to represent the effect of the anomalous quadrupole moment q on the evolution of energy and angular momentum. A Kerr black hole has quadrupole moment $M_2/M^3 = -\chi^2$. It is the quadrupole moment that leads to the lowest order terms in χ^2 in the expressions for the energy and angular momentum radiated during an inspiral. Therefore, to include the excess quadrupole moment, we just change the χ^2 terms in the flux expressions to $\chi^2 + q$, while leaving the lower order terms unchanged (this approach was also used in [27]). We then numerically find the roots of the effective potential $V_{\rm eff} = 0$ in the equatorial plane at various times and compute the evolution of $\Delta\rho$ along the inspiral.

The result of one such computation of $\Delta\rho$ is plotted in Fig. 2.10. That figure corresponds to an inspiral in a spacetime with $\chi = 0.9$, and $q = 0.95$. The inspiral starts out at $\rho = 100M$ with an orbital inclination of 60 degrees and initial eccentricity $e = 0.8$ (these orbital parameters correspond to $E \approx 0.9982$ and $L_z \approx 5.0852M$) and proceeds until plunge. The separation between the inner and outer bounded regions gradually shrinks, until the two regions merge (on the plot, this is shown as $\Delta\rho = 0$). Afterward, the bounded regions remain joined until eventually merging with the plunging region.

We have found the same qualitative behavior described above for a wide range of parameter choices. Therefore, in all these cases, our conjecture is true—the inspiraling object can never find itself in the isolated inner region where all orbits appear to be ergodic. We should point out, however, that we have carried out this numerical investigation only for a range of specific choices of χ, q, and initial orbital parameters, and have used an approximation to the energy and angular momentum radiated during an inspiral. This is therefore not a definitive proof that chaotic motion can never be observed in the course of an inspiral in the Manko-Novikov spacetime.

Assuming this evolution really is typical, there are two important consequences. Firstly, an inspiraling object can never end up in the inner of two allowed regions of bound motion, where

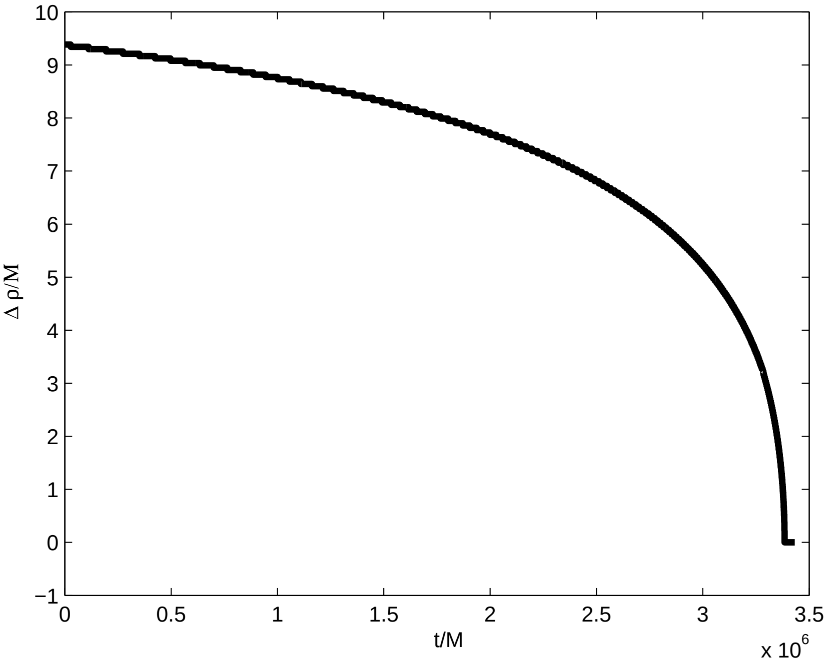

Figure 2.10: The evolution of the separation $\Delta\rho$ between the inner and outer bounded regions in the equatorial plane along an inspiral in a Manko-Novikov spacetime with $\chi = 0.9$ and $q = 0.95$. $\Delta\rho = 0$ means that the two regions have merged and there is a single bounded region.

ergodic motion is prevalent. Secondly, inspirals always start out in a phase where the motion is regular. This is very important, since it will allow the systems to be detected in this early inspiral stage by gravitational-wave detectors using matched filtering or a time-frequency analysis. The inspiraling object will eventually end up in the merged region formed after the two regions of bounded motion converge. Both ergodic and regular geodesics exist in that region, so in principle the particle could find itself on an ergodic orbit. However, most orbits in the merged region appear to be regular so it would require fine tuning to put the object onto such a geodesic (e.g., the "neck traversing" geodesics discussed earlier). It thus seems unlikely that this would occur in practice.

Although these results apply only to the Manko-Novikov family of spacetimes, the conclusions are consistent with other examples of chaotic geodesics in relativity. For instance, in the prolate Erez-Rosen spacetime considered in [17], if an object had arrived in the region where ergodic motion is observed during the course of an inspiral, its orbital energy and angular momentum would have been larger earlier in the inspiral. However, if either the energy or angular momentum is increased from the values that give ergodic motion, the effective potential changes so that it has only one allowed region, which includes "escape zones" connected to the central singularity. All geodesics in such a zone plunge into the central object in a short time so an astrophysical inspiral could not persist through that zone. We deduce that for that spacetime as well the ergodic region is inaccessible to objects captured at large distances.

If there was some other mechanism that could put an inspiraling object onto an ergodic geodesic, there is the question of how the ergodicity could be identified in practice. Detection of EMRIs will rely on matched filtering or possibly time-frequency techniques [1]. In either case, it will probably not be possible to identify the gravitational radiation as being emitted from an ergodic orbit, but only that radiation from a regular orbit has ceased. It is clear from Figure 2.9 that during an ergodic phase, the emitted power is spread among many harmonics, which will consequently not be individually resolvable. This radiation will increase the broadband power in our detector, whereas if the orbit had plunged the radiated power would rapidly die away. However, the energy released during a typical EMRI is comparatively low, so it is unlikely that we could identify the presence of such broadband power over the instrumental noise. Therefore, the chances are that we will not be able to distinguish observationally between an inspiral that "ends" at a transition into an ergodic phase and one which ends by plunging into a black hole.

One potentially observable signature of ergodicity would be an inspiral that turned "off" and "on" as it progressed through ergodic phases interspersed with regular phases. This would occur if the object could move into and out of the inner ergodic region during an inspiral, but the preceding analysis indicates that this should not happen. An object on a "neck-traversing" geodesic would also show this behavior. However, the periods where the orbit is ergodic serve to randomize the phase of the orbit in the regular periods. A signal of this type would only be observable if each apparently regular phase could be individually resolved with enough signal to noise ratio. This would require a very narrow "neck" in order to trap the orbit for many cycles in the regular zone. However, fine tuning of the energy and angular momentum is necessary to make the neck very narrow, so if an object was on such an orbit, the neck would be widening rapidly as energy and angular momentum were radiated away. In practice, it is doubtful that sufficient signal-to-noise would accumulate to allow a detection to be made before the neck widened too much.

We conclude that for astrophysically relevant inspirals in the Manko-Novikov spacetime family, an object would probably not end up on an ergodic geodesic. If some other mechanism conspired to put an object on such an orbit, it is unlikely that we would be able to identify this in gravitational-wave observations. If these findings carry over to a more generic class of spacetimes, then chaotic motion is merely a mathematical curiosity which is unlikely to manifest itself practically or be important for gravitational-wave data analysis considerations.

2.4 Last Stable Orbit

During an inspiral into a Kerr black hole, an EMRI will evolve quasistationarily through a sequence of near-geodesic orbits as orbital energy and angular momentum are radiated away. There is a minimum energy (which is dependent on angular momentum) for which bound orbits exist. When the inspiral reaches that separatrix, the object will rapidly plunge into the central body. The gravitational radiation emission undergoes a transition at this point, and so the frequency of this last stable orbit is in principle another quantity that is observable from the detected gravitational waves. For a Kerr inspiral, the "transition" is a rapid die-off in the gravitational-wave emission as the particle plunges into the black hole. If the central object is not a black hole, the radiation may persist for longer after the last stable orbit is passed [7], but there will still be a significant qualitative change in the emitted radiation as the orbit changes suddenly at that point. We focus on the innermost stable circular equatorial orbit in this analysis, since this is well defined in these spacetimes.

2.4.1 Circular Equatorial Orbits

The geodesic equations for an arbitrary spacetime (2.6) may be written in the alternative form

$$\frac{\mathrm{d}}{\mathrm{d}\tau}\left(g_{\mu\alpha}\frac{\mathrm{d}x^\alpha}{\mathrm{d}\tau}\right) = \frac{1}{2}\partial_\mu g_{\nu\sigma}\frac{\mathrm{d}x^\nu}{\mathrm{d}\tau}\frac{\mathrm{d}x^\sigma}{\mathrm{d}\tau}. \tag{2.9}$$

For a circular, equatorial orbit in an axi- and reflection-symmetric spacetime of the form (2.5), $\mathrm{d}\rho/\mathrm{d}\tau = \mathrm{d}z/\mathrm{d}\tau = \mathrm{d}^2\rho/\mathrm{d}\tau^2 = 0$; hence the ρ-component of the geodesic equation (2.9) gives

$$\partial_\rho g_{\phi\phi}\dot{\phi}^2 + 2\partial_\rho g_{t\phi}\dot{t}\dot{\phi} + \partial_\rho g_{tt}\dot{t}^2 = 0, \tag{2.10}$$

in which a dot denotes $\mathrm{d}/\mathrm{d}\tau$ as before. We can thus express the azimuthal frequency as observed at infinity $\Omega_\phi \equiv \dot{\phi}/\dot{t}$ in the form

$$\Omega_\phi = \frac{-\partial_\rho g_{t\phi} \pm \sqrt{(\partial_\rho g_{t\phi})^2 - \partial_\rho g_{tt}\partial_\rho g_{\phi\phi}}}{\partial_\rho g_{\phi\phi}},$$

where the $+/-$ signs are for prograde and retrograde orbits respectively. In the equatorial plane, the right-hand side is a function of the spacetime parameters and ρ only, so given a particular choice of azimuthal frequency Ω_ϕ, Eq. (2.11) can be inverted to determine the value of ρ such that a circular orbit at that ρ has frequency Ω_ϕ.

Equation (2.8) provides another relation between $\dot{t}$ and $\dot{\phi}$, from which we can deduce

$$\dot{t} = \left(-g_{tt} - 2\Omega_\phi g_{t\phi} - \Omega_\phi^2\, g_{\phi\phi}\right)^{-\frac{1}{2}}, \tag{2.11}$$

and then the energy and angular momentum equations (2.8) give us E and L_z as a function of ρ for circular equatorial orbits.

2.4.2 Innermost Stable Circular Orbit

The location of the innermost stable circular orbit (ISCO) in the equatorial plane can be found using the effective potential (2.8). Circular equatorial orbits are located at simultaneous zeros and turning points of $V_{\rm eff}$, where $V_{\rm eff} = \partial V_{\rm eff}/\partial\rho = \partial V_{\rm eff}/\partial z = 0$. As we will see in Section 2.5 the second derivatives of $V_{\rm eff}$ determine the frequencies of small oscillations about the circular orbit. For the circular orbit to be stable, we need the orbit to sit at a local maximum of $V_{\rm eff}$, i.e., we require $\partial^2 V_{\rm eff}/\partial\rho^2$ and $\partial^2 V_{\rm eff}/\partial z^2$ to be negative. In the following we will use $\tilde{V}_{\rho\rho}(\rho)$ ($\tilde{V}_{zz}(\rho)$) to denote the value of $\partial^2 V_{\rm eff}/\partial\rho^2$ ($\partial^2 V_{\rm eff}/\partial z^2$) evaluated for the circular equatorial orbit at radius ρ. For the Kerr spacetime, $\tilde{V}_{zz}(\rho) < 0$ at all radii, but $\tilde{V}_{\rho\rho}(\rho)$ has a single root at a critical radius $\rho_{\rm ISCO}$. This tells us that the orbit becomes radially unstable at that point, which defines the ISCO. For $\chi = 0$, $\rho_{\rm ISCO} \approx 4.90M$, while for $\chi = 0.9$, $\rho_{\rm ISCO} \approx 1.25M$ for prograde orbits and $\rho_{\rm ISCO} \approx 7.705M$ for retrograde orbits. Note that ρ is a cylindrical Weyl coordinate, which is why these results differ from the familiar black-hole ISCO radii, which are normally quoted in Boyer-Lindquist coordinates.

For the Manko-Novikov solutions with $\chi = 0$, the shape of the functions $\tilde{V}_{\rho\rho}(\rho)$ and $\tilde{V}_{zz}(\rho)$ does not change significantly as q is increased with $q > 0$: $\tilde{V}_{zz}(\rho) < 0$ everywhere and $\tilde{V}_{\rho\rho}(\rho) = 0$ has a single solution that defines the ISCO. However, as $|q|$ is increased with $q < 0$, there is a transition in behavior at $q \approx -0.163$. For $q \lesssim -0.163$, the function $\tilde{V}_{\rho\rho}(\rho)$ has two zero-crossings. Thus, in addition to the radially stable circular orbits at large radii, we find additional such orbits exist very close to the central singularity. If $|q|$ is increased still further, the two roots converge at $q \approx -0.654$ and for $q \lesssim -0.654$ radially stable orbits exist at all values of ρ. However, at the point where the second branch of the radial roots appears, there is also a transition in the shape of $\tilde{V}_{zz}(\rho)$, so that there are now orbits which are vertically unstable. For $q \lesssim -0.163$, the ISCO is defined by this vertical instability, rather than the radial instability characteristic of the Kerr spacetime, and Manko-Novikov spacetimes with $q > 0$. In the range $-0.654 \lesssim q \lesssim -0.163$, there are two regimes where stable circular orbits exist—an outer zone with $\rho > \rho_{\rm ISCO}$, and an inner zone with $\tilde{\rho}_{\rm ISCO} < \rho < \rho_{\rm OSCO}$ (we use "OSCO" to indicate "outermost stable circular orbit" and $\tilde{\rho}_{\rm ISCO}$ to denote the ISCO for the inner set of circular orbits). The energy and angular momentum of an orbit at the "OSCO" are greater than the energy and angular momentum at the ISCO of the outer zone, $\rho_{\rm ISCO}$. Thus, an object inspiraling from large distances on a circular equatorial orbit will reach $\rho_{\rm ISCO}$ and plunge into the central body, rather than finding itself in the inner range of circular orbits. Compact objects could only find themselves in the inner range if they came in on an eccentric/inclined orbit and then radiated away energy and angular momentum in exactly the right proportions. It is therefore unlikely that this inner zone would be populated in practice. However, any object on a circular equatorial orbit in this inner zone would reach $\tilde{\rho}_{\rm ISCO}$ and then plunge into the central body.

In Figure 2.11 we show the location of the ISCO as a function of q for spacetimes with $\chi = 0$.

We also show the orbital frequency at the ISCO as a function of q, computed using Eq. (2.11). For spacetimes with spin, the behavior is qualitatively similar, but there are now two ISCO radii, corresponding to prograde and retrograde orbits respectively. We show results for a spin of $\chi = 0.9$ in Figure 2.12. We note that the ISCO radius is always outside the boundary of the causality-violating region of the spacetime. For $\chi \neq 0$ and $q > 0$, the ISCO radius is determined by the energy at which the outer allowed region for bound motion (which is a single point for a circular equatorial orbit) merges with the inner allowed region. In that case when the object reached the ISCO it would undergo a transition onto an eccentric/inclined geodesic.

The value of the ISCO frequency depends not only on q but also M and χ. However, as we shall discuss in the next section, it is possible to measure these other parameters using precessions measured when the orbit is in the weak field. Thus, the ISCO frequency is a powerful probe of the nature of the spacetime since it can be very different even for comparatively small deviations from Kerr.

2.5 Periapsis and Orbital-Plane Precessions

In Section 2.3 we saw that astrophysically relevant orbits in the Manko-Novikov spacetime are multi periodic to high precision. In such cases, there is no smoking-gun signature that indicates the presence of "bumpiness" in the spacetime. Instead, the imprint of the spacetime bumpiness will be observationally apparent in the location of the last stable orbit, as discussed in the previous section, and in the following ways: (i) in the three fundamental frequencies of the gravitational waves generated while the inspiraling object is on an instantaneous geodesic orbit; (ii) in the harmonic structure of the gravitational-wave emission, i.e., the relative amplitudes and phases of the various harmonics of the fundamental frequencies; and (iii) in the evolution of these frequencies and amplitudes with time as the object inspirals. A full analysis of the accuracies that could be achieved in observations would involve computing gravitational waveforms in the bumpy spacetimes, performing a Fisher-Matrix analysis to account for parameter correlations, and comparing to a similar analysis for Kerr. That is beyond the scope of this paper. However, we can examine the first of these observational consequences by comparing the fundamental frequencies between the bumpy and Kerr spacetimes.

The complication in such an analysis is to identify orbits between different spacetimes. Identifying orbits by the ρ and z coordinates is not gauge invariant since the meaning of these coordinates depends on the spacetime structure. Identifying orbits via the energy and angular momentum is gauge invariant, but these quantities are not directly measurable observationally. However, circular orbits in the equatorial plane of the spacetime are characterized by a single observable — the azimuthal frequency of the orbit. We can use this frequency to identify circular equatorial orbits in different spacetimes.

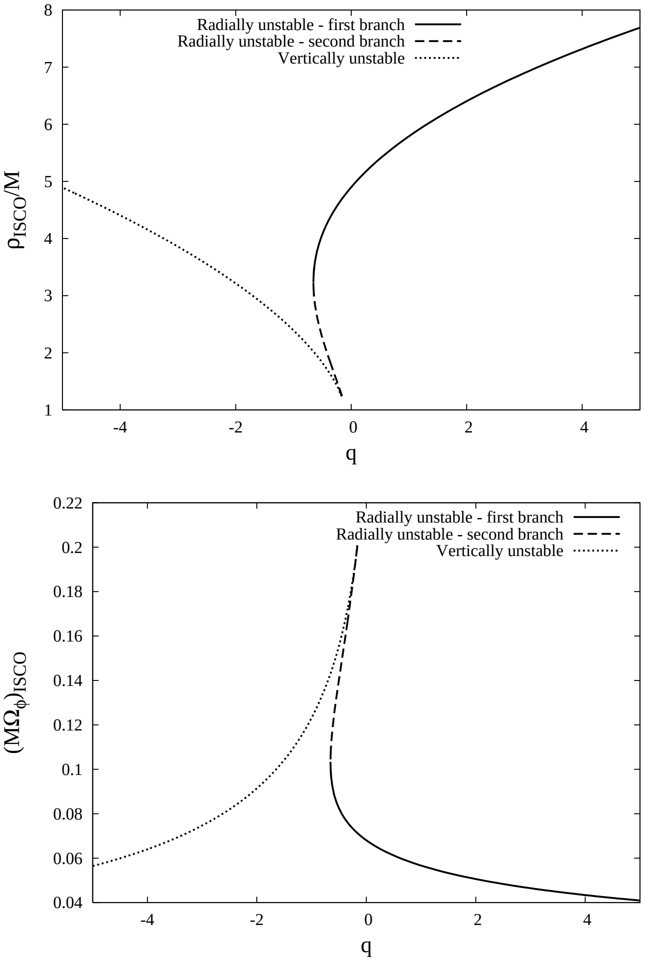

Figure 2.11: Properties of the equatorial ISCO in spacetimes with $\chi = 0$, as a function of q. We show the ρ coordinate of the ISCO (left panel) and the dimensionless frequency of the orbit at the ISCO (right panel). As described in the text, the ISCO radius has three branches, depending on whether it is determined by one of the two branches of radial instability or the branch of vertical instability. These branches are indicated separately in the diagram. For values of q where all three branches are present, the dashed line denotes the "OSCO" and the dotted line denotes $\tilde{\rho}_{\rm ISCO}$ as discussed in the text. Allowed orbits lie above the curve in the left panel, and below the curve in the right panel.

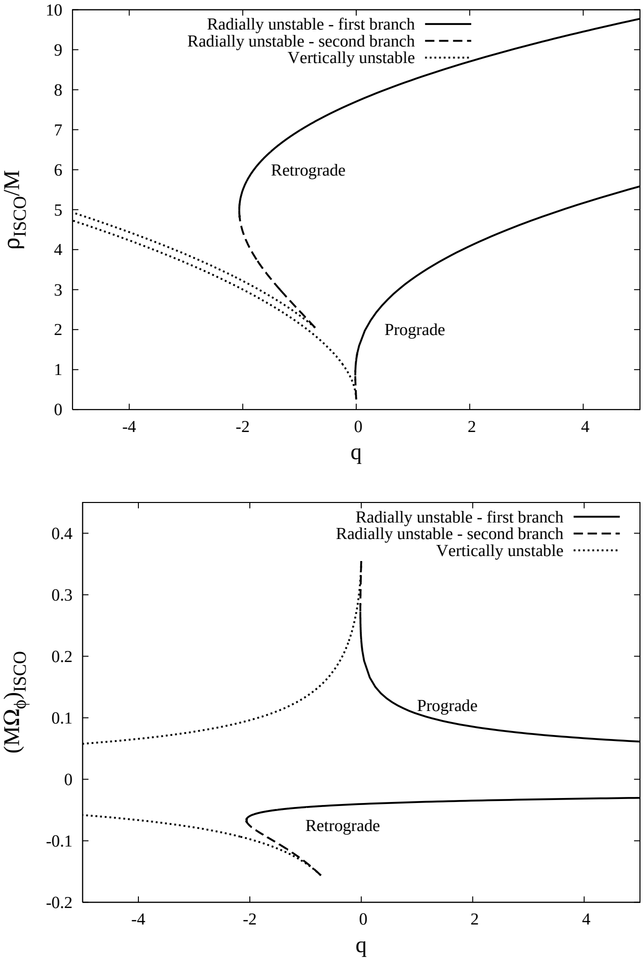

Figure 2.12: As Figure 2.11, but now for a spin of $\chi = 0.9$. There are now two ISCO curves, one for prograde orbits and one for retrograde orbits. The allowed range of orbital frequencies is given by the region in between the two curves in the right hand panel.

Precession frequencies are absent in exactly circular equatorial orbits. However, if the circular orbit is perturbed radially, it will undergo small oscillations at the radial epicyclic frequency, which is characteristic of the periapsis precession frequency at that radius. Likewise, if the orbit is perturbed vertically it will undergo small oscillations at the vertical epicyclic frequency, which is characteristic of the orbital-plane precession frequency at that radius. We thus compare these epicyclic frequencies, as a function of the circular orbital frequency, between Kerr and bumpy spacetimes. This comparison was employed by Ryan, who used it to derive his theorem stating that all spacetime multipole moments are encoded in the gravitational waves generated by nearly circular, nearly equatorial EMRIs [2].

An eccentric equatorial orbit can be characterized by two observables — the orbital frequency and the periapsis precession frequency. These two frequencies can therefore be used to identify orbits in different spacetimes (provided there is an orbit with corresponding frequencies in the Kerr metric). Likewise, the orbital-plane precession frequency can be used to identify inclined orbits between spacetimes [1]. With such an identification, differences in the multipole structure of the spacetime will show up only in the relative amplitudes of the harmonics and in the evolution of the fundamental frequencies over the inspiral. We will discuss this some more at the end of this section, but a full analysis requires treatment of inspiral in an arbitrary spacetime and is beyond the scope of the current paper.

2.5.1 Epicyclic Frequencies

The frequency of epicyclic motion can be derived by perturbing a circular, equatorial orbit in either the radial or vertical direction. The second-order geodesic equations (2.9) for z and ρ take the form

$$\begin{aligned} \frac{\mathrm{d}}{\mathrm{d}\tau}\left(2\,g_{XX}\,\frac{\mathrm{d}X}{\mathrm{d}\tau}\right) &= \partial_X g_{tt}\left(\frac{\mathrm{d}t}{\mathrm{d}\tau}\right)^2 + 2\partial_X g_{t\phi}\left(\frac{\mathrm{d}t}{\mathrm{d}\tau}\right)\left(\frac{\mathrm{d}\phi}{\mathrm{d}\tau}\right) + \partial_X g_{\phi\phi}\left(\frac{\mathrm{d}\phi}{\mathrm{d}\tau}\right)^2 \\ &\quad + \partial_X g_{\rho\rho}\left(\frac{\mathrm{d}\rho}{\mathrm{d}\tau}\right)^2 + \partial_X g_{zz}\left(\frac{\mathrm{d}z}{\mathrm{d}\tau}\right)^2 . \end{aligned}$$

Here X denotes either ρ or z. The dependence on $\mathrm{d}t/\mathrm{d}\tau$ and $\mathrm{d}\phi/\mathrm{d}\tau$ can be eliminated by using the energy and angular momentum conservation equations to express these in terms of E, L_z, ρ and z, as in Eq. (2.8). Using this form of the equations we can take a circular, equatorial orbit, $\rho = \rho_c$, $z = 0$, and perturb it either in the radial direction, $\rho = \rho_c + \delta\rho$, $z = 0$, or in the vertical direction, $\rho = \rho_c$, $z = \delta z$. Considering the equations of motion at leading order in the small orbital

---

[1] The "orbital-plane" is not well defined in the strong field. However, we know the gravitational waves should be triperiodic and, in the weak field, the three periods correspond to the orbital period and the two precessions. When we refer to "orbital-plane precession frequency" we really mean the frequency component of the orbit that corresponds to orbital-plane precession in the weak field. This will be the frequency of the vertical motion, averaged over many orbits.

perturbation, it is easy to see that the frequencies of these small epicyclic oscillations are given by

$$\begin{aligned}\left(\frac{g_{\phi\phi}E-g_{t\phi}L_z}{g_{tt}g_{\phi\phi}-g_{t\phi}^2}\right)^2\Omega_X^2 &= \\ \frac{1}{2g_{XX}}\frac{\partial}{\partial X}&\left(\frac{\partial_X g_{tt}\left(g_{\phi\phi}E-g_{t\phi}L_z\right)^2+2\partial_X g_{t\phi}\left(g_{\phi\phi}E-g_{t\phi}L_z\right)\left(g_{tt}L_z-g_{t\phi}E\right)}{(g_{tt}g_{\phi\phi}-g_{t\phi}^2)^2}\right) \\ &+\frac{1}{2g_{XX}}\frac{\partial}{\partial X}\left(\frac{\partial_X g_{\phi\phi}\left(g_{tt}L_z-g_{t\phi}E\right)^2}{(g_{tt}g_{\phi\phi}-g_{t\phi}^2)^2}\right)\end{aligned}$$

As before, X denotes either ρ (for the radial epicyclic frequency Ω_ρ) or z (for the vertical epicyclic frequency Ω_z). The same result can be derived starting from the effective potential equation (2.8): the frequency Ω_X is determined by $\partial^2 V_{\text{eff}}/\partial X^2$ evaluated at the circular orbit.

2.5.2 Precessions

We are interested in precessions rather than the epicyclic frequency. We define the periapsis precession as the number of cycles by which the periapsis advances per radial period (i.e., over one complete epicyclic oscillation). Likewise, the *orbital-plane precession* is defined as the number of cycles by which the azimuthal angle to the highest point of the orbit advances during one vertical oscillation. These precessions, which we denote by p_X, are related to the epicyclic frequencies, Ω_X, by

$$p_X=\frac{\Omega_\phi}{\Omega_X}-1. \tag{2.12}$$

The behavior of the precessions can be understood in terms of what happens in the weak field, far from the black hole, and in the strong field, close to the ISCO. In the weak field it is possible to derive expressions for the precessions as functions of the orbital frequency. This was originally done for nearly circular, nearly equatorial orbits by Ryan [2], who demonstrated that the various spacetime multipole moments enter the precession rate expansion at different orders of $(M\Omega_\phi)^\alpha$. This was the basis for a theorem that, in principle, the weak field precessions can be used to extract the lowest order spacetime multipole moments. The weak field expansion of the precessions is summarized in Appendix 2.8.

In the strong field, we find that one or the other precession diverges at a certain frequency. This frequency corresponds to the frequency of the ISCO. To understand what is happening, we use the effective potential (2.8) and consider radial oscillations. For the energy and angular momentum corresponding to the circular equatorial orbit at radius $\rho=\rho_c$, the effective potential in the equatorial plane takes the form $V_{\text{eff}}(\rho,z=0)=-\tilde{V}(\rho)(\rho-\rho_-)(\rho-\rho_c)^2$. Here $\tilde{V}(\rho)$ is a function that is strictly positive for $\rho>\rho_-$. The radius ρ_- is the other solution to $V_{\text{eff}}(\rho,z=0)=0$, and $\rho_-<\rho_c$. As the ISCO is approached, the effective potential develops a point of inflection at the location of the turning point rather than a maximum since $\rho_- \to \rho_c$. The epicyclic frequency for radial oscillations is $\Omega_\rho^2 \propto \tilde{V}(\rho_c)(\rho_c - \rho_-)$, which thus tends to zero as the ISCO is approached. The corresponding periapsis precession diverges. The radius ρ_- corresponds to an unstable circular orbit, and associated with any unstable circular orbit is a bound, eccentric orbit that has an infinite period — the object comes in from larger radii, and asymptotically approaches the radius of the circular orbit. This is referred to as a "homoclinic" orbit, or as a "zoom-whirl" orbit in the EMRI literature. As the ISCO is approached, a small perturbation from the location of the circular orbit will put the object onto an orbit that is close to the homoclinic orbit associated with the unstable circular orbit. Hence, it takes a very long time for the object to complete a radial oscillation, but it is moving rapidly in the azimuthal direction the whole time, building up a large periapsis precession.

This understanding leads us to expect the precession to diverge at the location of the ISCO, and this divergence should be like $(\rho_c - \rho_{\rm ISCO})^{-1/2}$, or $(\Omega_{\phi,{\rm ISCO}} - \Omega_\phi)^{-1/2}$. The above argument applies to an ISCO defined by a radial instability (as in the Kerr metric). As we saw in Section 2.4, the ISCO in the Manko-Novikov spacetimes can be determined by the onset of a vertical instability. In that case, the above argument still applies, but it is now the orbital-plane precession that will diverge as the ISCO is approached. This provides another potential 'smoking-gun' for a deviation from the Kerr metric. The divergence in the precession at the ISCO arises as a result of one of the two epicyclic frequencies going to zero. It is these frequencies that will, in principle, be observable in the gravitational waves. If an inspiral is observed starting in the weak field and up until the last stable orbit (LSO), the different frequency components could be tracked, and one frequency will tend to zero as the LSO is approached. This is in principle an observable, and if it is the orbital-plane precession that goes to zero the central body cannot be a Kerr black hole. A more careful treatment of the gravitational-wave emission will be required to understand how practical it will be to make such observations.

In Figures 2.13–2.16 we show the precessions as a function of $M\Omega_\phi$ for a variety of values of q. In Figures 2.17–2.19 we present the same results, but now we show the differences between precessions in a bumpy spacetime with a given q and precessions in the Kerr spacetime with the same spin parameter χ: $\Delta p_X = p_X - p_X^{\rm Kerr}$. The variable Δp_X represents the number of cycles of difference, so for instance a value of $\Delta p_\rho = 0.1$ means that the orbits in the two spacetimes, although having the same azimuthal frequency, would drift an entire cycle out of phase in the epicyclic radial oscillation within ten radial orbits. We do not show results for the difference in the orbital-plane precession for $\chi = 0$, since there is no orbital-plane precession in the Schwarzschild spacetime, and hence that plot would be identical to Figure 2.15.

Figures 2.13 and 2.17 show the periapsis precession $r_\rho(\Omega_\phi)$ for $\chi = 0$ while Figures 2.14 and 2.18 show the periapsis precession for $\chi = 0.9$. We see that as the value of q decreases from zero,

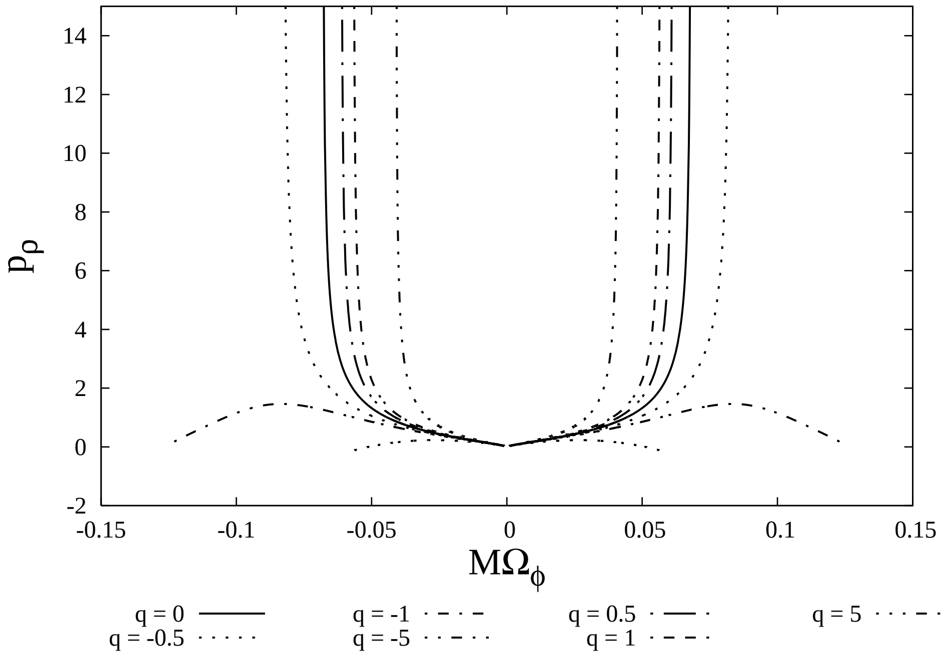

Figure 2.13: Periapsis precession p_ρ vs azimuthal frequency Ω_ϕ for $\chi = 0$ and various values of q.

the periapsis precession decreases relative to the corresponding value in the Kerr/Schwarzschild spacetime. By contrast, if q is increased from zero, the periapsis precession increases. In spacetimes with non-zero spin, the difference is more extreme for prograde orbits than for retrograde orbits. This is presumably because retrograde orbits do not get as close to the central object, and so do not "feel" the strong field deviations in the bumpy metric.

For $q \geq -0.5$, the radial epicyclic frequency $\Omega_\rho(\Omega_\phi)$ approaches zero as the ISCO is approached and the periapsis precession r_ρ goes to infinity for the reasons described above. This is not true of the $q < -0.5$ spacetimes shown, since for those the ISCO is defined by a vertical instability. Figure 2.15 shows the orbital-plane precession $r_z(\Omega_\phi)$ for $\chi = 0$ and Figures 2.16 and 2.19 show the orbital-plane precession for $\chi = 0.9$. As for the case of the periapsis precession, the orbital-plane precession behaves qualitatively differently depending on the sign of q. The orbital-plane precession is greater for $q < 0$ and smaller for $q > 0$ compared to the non-bumpy value. As expected, the orbital-plane precession tends to a constant at the ISCO for $q > -0.5$, while it diverges for $q < -0.5$, since the ISCO for the latter spacetimes is defined by a vertical instability as discussed earlier.

Previous authors have looked at precessions in "bumpy" spacetimes. As mentioned above, Ryan [2] derived a weak field expansion for the precessions. Collins & Hughes [11] looked at precessions for eccentric equatorial orbits in a perturbed Schwarzschild spacetime, and Glampedakis & Babak [12] did the same for a perturbed Kerr black hole. However, both pairs of authors did this by comparing orbits with the same coordinates, which is rather unphysical. Our results are consistent with this previous work in the weak field, but our calculation is the first that can be applied in the

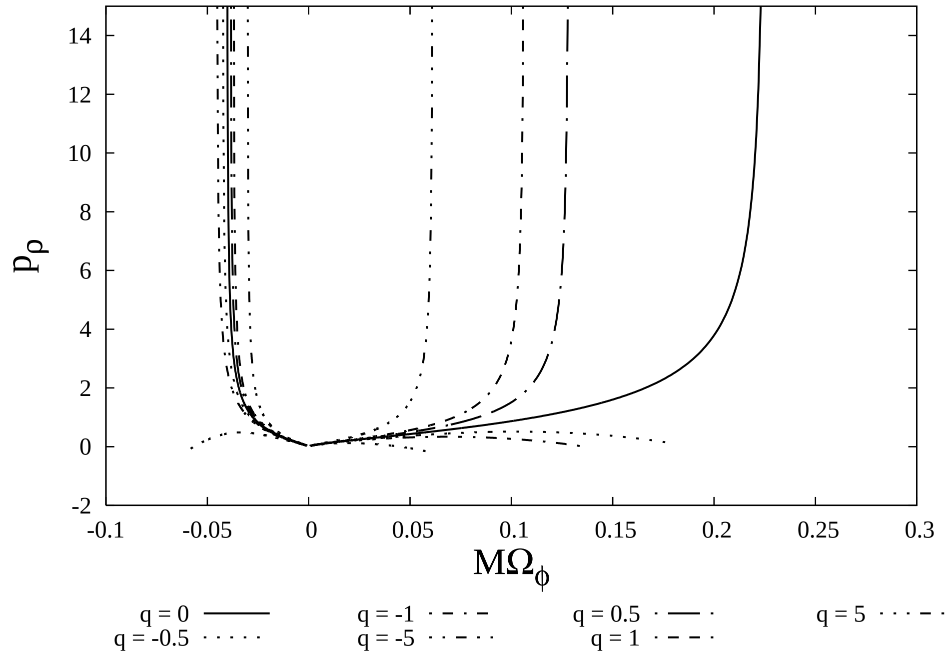

Figure 2.14: Periapsis precession p_ρ vs azimuthal frequency Ω_ϕ for $\chi = 0.9$ and various values of q.

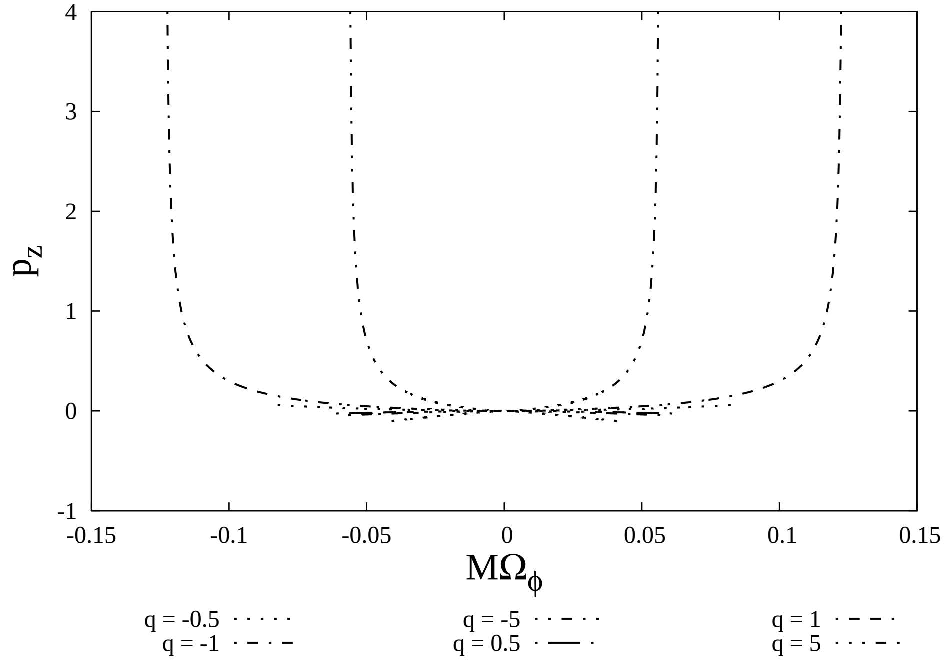

Figure 2.15: Orbital-plane precession p_z versus azimuthal frequency Ω_ϕ for $\chi = 0$ and various values of q. We do not show the case $q = 0$ here, since there is no orbital-plane precession in Schwarzschild.

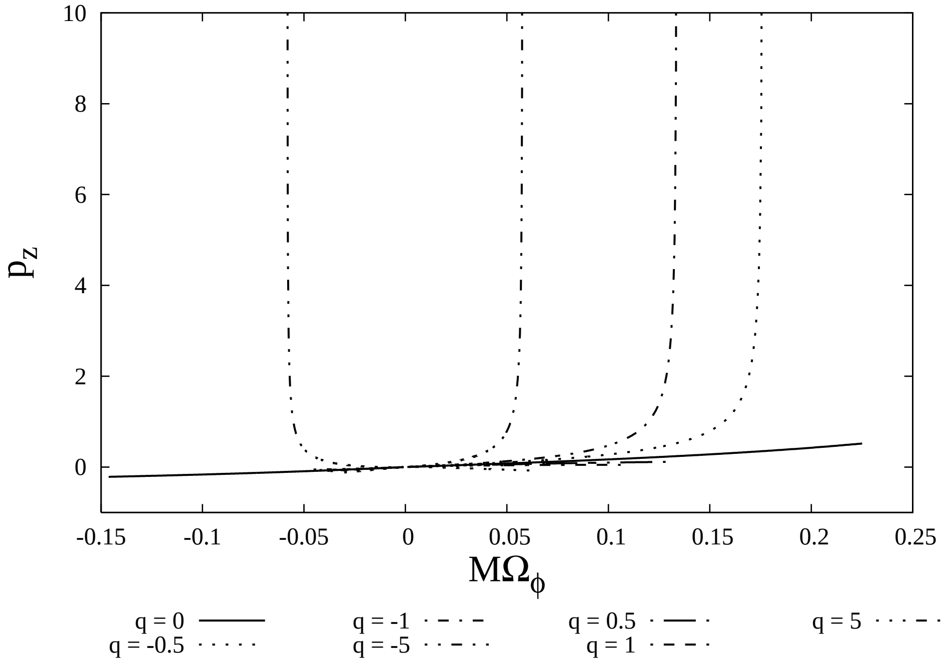

Figure 2.16: Orbital-plane precession p_z vs azimuthal frequency Ω_ϕ for $\chi = 0.9$ and various values of q.

strong field, since Ryan's work used a weak field expansion, and the other work used perturbative spacetimes that break down close to the central body. The behavior in the approach to the ISCO is thus a new result.

It is possible to fit the precessions as a sum of a weak field expansion (as given in Appendix 2.8) plus a term $A/\sqrt{\Omega_{\phi,\mathrm{ISCO}} - \Omega_\phi}$. However, only a comparatively few weak field terms are required to give a good fit, implying that the divergence at the ISCO limits the number of multipole moments that can be recovered from such an expansion. To quantify this statement properly, we must do a full analysis, that includes the effect of inspiral, uses an instrumental noise curve to restrict the observable bandwidth and accounts for parameter correlations via the Fisher Matrix. We can do this by constructing semirelativistic inspiral waveforms for bumpy spacetimes in the same way that has been used for Kerr inspirals [26, 25]. This is beyond the scope of the present paper. However, there are several things that we can take away from the current results — the location of the ISCO has a strong influence on precessions that could be observable, in particular the nature of the instability that defines the ISCO could be a clear indicator of a non-Kerr system; precessions can be very different in the strong field in the presence of a deviation; circular orbits with frequencies very different from the Kerr value exist in some bumpy spacetimes, so another observable signature would be that an inspiral persists at frequencies inside the Kerr ISCO.

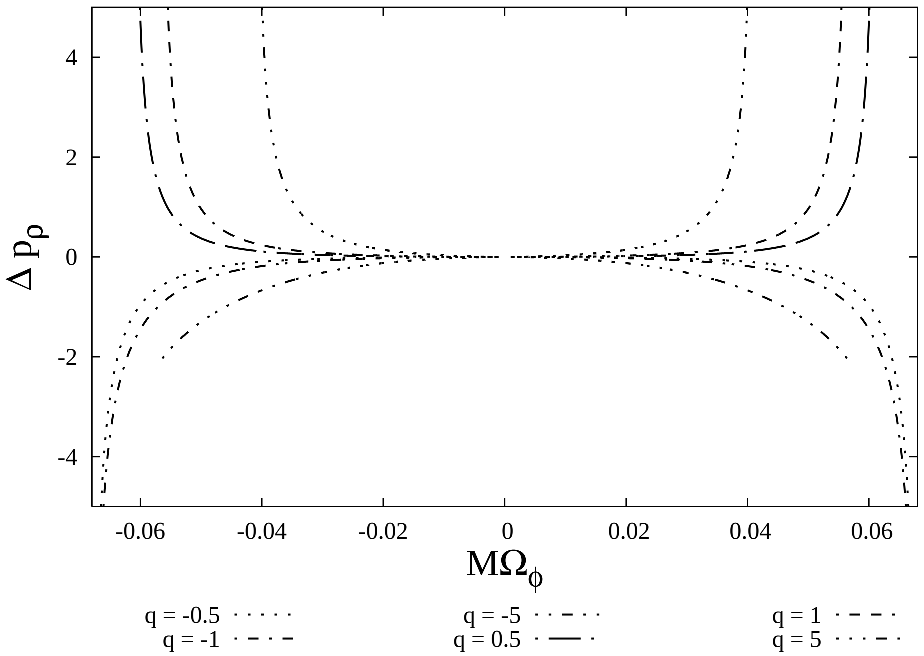

Figure 2.17: Difference between periapsis precessions in a bumpy spacetime with $\chi = 0$ and the Schwarzschild spacetime, $\Delta p_\rho(\Omega_\phi, q) = p_\rho(\Omega_\phi, q) - p_\rho(\Omega_\phi, q = 0)$.

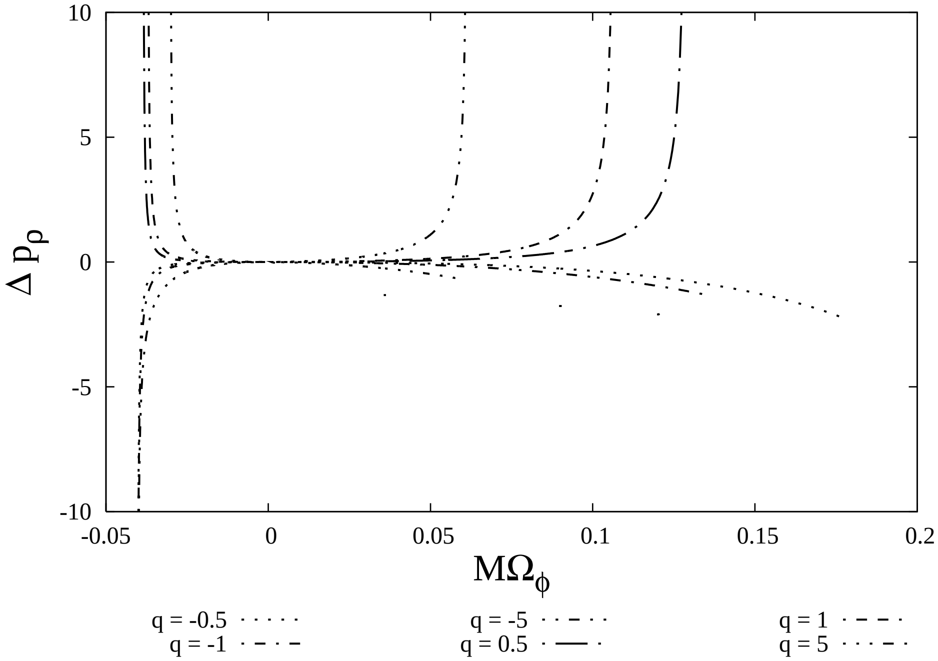

Figure 2.18: Difference between periapsis precessions in a bumpy spacetime with $\chi = 0.9$ and the Kerr spacetime with $\chi = 0.9$, $\Delta p_\rho(\Omega_\phi, q) = p_\rho(\Omega_\phi, q) - p_\rho(\Omega_\phi, q = 0)$.

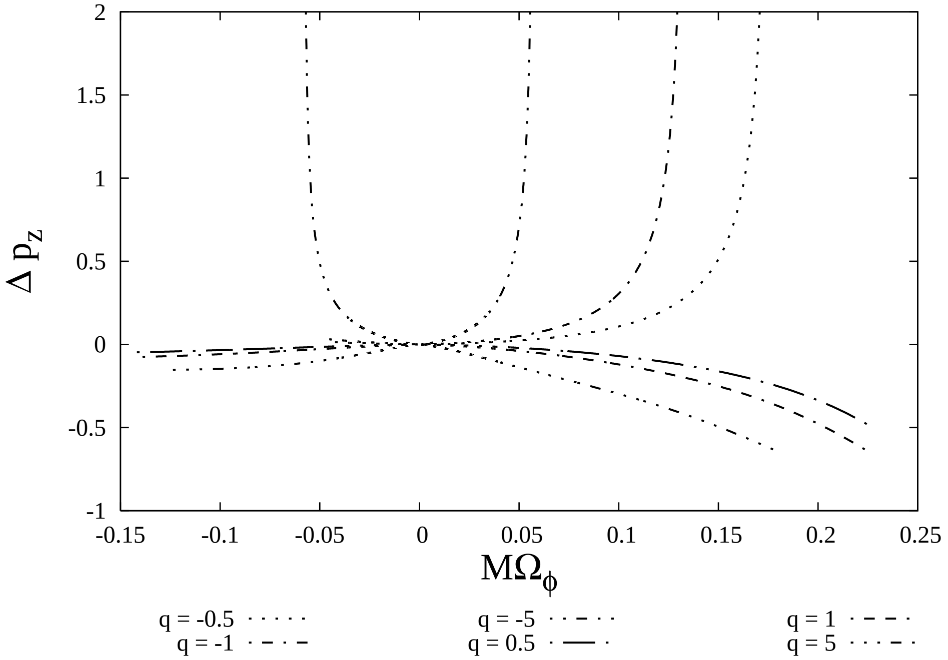

Figure 2.19: Difference between orbital-plane precessions in a bumpy spacetime with $\chi = 0.9$ and the Kerr spacetime with $\chi = 0.9$, $\Delta p_z(\Omega_\phi, q) = p_z(\Omega_\phi, q) - p_z(\Omega_\phi, q = 0)$.

2.5.3 Effect of Eccentricity

As discussed above, the measurement of the precessions as a function of orbital frequency for nearly circular, nearly equatorial orbits would in principle allow measurement of the spacetime multipole moments [2]. In practice, however, the precessions will only be manifest in the observed gravitational waves if the orbit is not circular and equatorial, so we need to understand how the dependence of the precessions on azimuthal frequency differs when we relax the assumption of near circularity. In the following, we shall focus on the periapsis precession of eccentric but equatorial orbits.

The eccentricity of an orbit modifies two things — i) the frequency associated with the periapsis precession as a function of the orbital frequency; ii) the relative amplitudes of different harmonics of these two frequencies in the observed GWs. To accurately compute the dependence of the harmonic structure on eccentricity for a generic orbit, we need to know details of GW generation in a spacetime with arbitrary multipole moments. This is a difficult problem, so we focus on the effect of eccentricity on the periapsis precession frequency itself. We consider an eccentric equatorial orbit in the Kerr spacetime, and use Ω_ϕ to denote the average azimuthal frequency (i.e., the total advance in ϕ over one radial period, divided by the period of the radial motion). We define an orbital eccentricity, e, such that the ratio of the Boyer-Lindquist radii of the periapsis, r_p, and apapsis, r_a, of the radial motion is $r_p/r_a = (1-e)/(1+e)$. With these definitions, the periapsis precession as defined above can be found to be

$$\begin{aligned} p_\rho &= 3\left(\frac{M\Omega_\phi}{(1-e^2)^{\frac{3}{2}}}\right)^{\frac{2}{3}} - 4\chi\left(\frac{M\Omega_\phi}{(1-e^2)^{\frac{3}{2}}}\right) + \frac{3(18-7e^2+2\chi^2)}{4}\left(\frac{M\Omega_\phi}{(1-e^2)^{\frac{3}{2}}}\right)^{\frac{4}{3}} \\ &\quad -(34-18e^2)\,\chi\left(\frac{M\Omega_\phi}{(1-e^2)^{\frac{3}{2}}}\right)^{\frac{5}{3}} + \cdots \end{aligned} \tag{2.13}$$

where we are expanding in the weak field limit, $M\Omega_\phi \ll 1$. The corresponding result for a spacetime with an excess quadrupole moment can be found at lowest order by replacing the term in χ^2 with $\chi^2 + q$, since the quadrupole moment of a Kerr black hole is χ^2 as discussed earlier.

In the circular limit, $e = 0$, the expansion (2.13) allows us to extract M from the coefficient of $\Omega_\phi^{2/3}$, χ from the coefficient of Ω_ϕ, q from the coefficient of $\Omega_\phi^{4/3}$ etc. However, if we expand to lowest order in the eccentricity, e, it is clear that the effect of a small excess oblate quadrupole moment $q > 0$ could be mimicked, at leading order, by an eccentricity evolving as $e^2 = 2(M\Omega_\phi)^{-2/3}q$. The two possibilities are then distinguished by knowing how the eccentricity should evolve with $M\Omega_\phi$.

The expansion (2.13) contains redundancy, since the coefficient of $M\Omega_\phi^{5/3}$ also depends only on the lowest current moment, χ. If the eccentricity of the orbit did not evolve with time the first four terms in the expansion would determine M, χ, q and the eccentricity e, and higher terms would determine the remaining multipole moments as in the circular case. However, the eccentricity does evolve with time. In practice, we will only observe EMRIs as they evolve through a finite range of frequencies (determined by the detector sensitivity). During that period, the evolution will be driven entirely by gravitational-wave emission. This means that we can quantify the eccentricity of the orbit by a single number — the periapsis at which the eccentricity was equal to 1 if we integrated the inspiral backwards in time, assuming a purely GW driven inspiral. Specifying this parameter *and the multipole structure of the spacetime* determines the eccentricity as a function of $M\Omega_\phi$. Determining this relationship, however, requires knowing the details of GW emission in an arbitrary spacetime.

A complication arises because the ratio $M\Omega_\phi/(1-e^2)^{3/2}$ tends to a constant at the point where $e = 1$. Assuming that this occurred in the weak field, $M\Omega_\phi/(1-e^2)^{3/2} \ll 1$, this can be seen by considering the leading order term in $\mathrm{d}e/\mathrm{d}\Omega_\phi$ in the weak field (see for instance [26])

$$\frac{\mathrm{d}e}{\mathrm{d}(M\Omega_\phi)} = \frac{-(304+121e^2)(1-e^2)e}{3(M\Omega_\phi)(96+292e^2+37e^4)}. \tag{2.14}$$

Denoting $X = 1 - e^2$ and expanding in the limit $M\Omega_\phi \to 0$, $X \to 1$, we find

$$\frac{\mathrm{d}X}{\mathrm{d}(M\Omega_\phi)} \approx \frac{2}{3}\frac{X}{M\Omega_\phi} \Rightarrow X = X_0(M\Omega_\phi)^{\frac{2}{3}} + O(\Omega_\phi^{\frac{4}{3}}) \tag{2.15}$$

in which X_0 is a constant that is related to the periapse at “capture” when $X = 0$. If the capture occurs in the strong field, the ratio $M\Omega_\phi/(1-e^2)^{3/2}$ would still tend to a constant if we integrated backward until $e \to 1$. Although the inspiral would not be observed as $e \to 1$, that section of the inspiral does affect the portion that we can observe.

We now substitute the asymptotic behavior (2.15) into Eq. (2.13), to obtain an expansion of the periapsis precession as a function of the angular frequency in the form $p_\rho = a_0 + a_2(M\Omega_\phi)^{2/3} + a_3(M\Omega_\phi) + \cdots$, where a_0, a_2, a_3 etc. are constants. In contrast to the circular case, each of these coefficients depends on all the spacetime multipole moments, so multipole extraction from the periapsis precession expansion is no longer straightforward. The reason for this qualitative difference between circular and eccentric orbits is that it is only possible to observe an eccentric inspiral over a finite range of periapsis, since the orbit is captured with a certain finite periapsis, while a circular orbit could inspiral from infinity. The various multipole moments have different radial dependencies, thus if one can observe the precession frequency at any radius it makes sense that all the moments can be separately extracted, while this is more difficult if only a finite section of the spacetime is explored.

In practice, this difficulty also arises when observing a circular inspiral, since the radiation can only be detected in a certain frequency range. One can parameterize an observation by the frequency at the start of the observation, $\Omega_0 = \Omega_\phi(t=0)$. A Taylor series expansion of the precession (see Eq. (2.32) in the appendix) then gives

$$\begin{aligned} p_\rho &= \left(3\left(M\Omega_0\right)^{\frac{2}{3}} - 4\chi\left(M\Omega_0\right) + \frac{3}{2}\left(9+\chi^2+q\right)\left(M\Omega_0\right)^{\frac{4}{3}} + \cdots\right) \\ &\quad + \left(2\left(M\Omega_0\right)^{\frac{2}{3}} - 4\chi\left(M\Omega_0\right) + 2\left(9+\chi^2+q\right)\left(M\Omega_0\right)^{\frac{4}{3}} + \cdots\right)\frac{\Omega_\phi-\Omega_0}{\Omega_0} \\ &\quad + \left(-\frac{1}{3}\left(M\Omega_0\right)^{\frac{2}{3}} + \frac{1}{3}\left(9+\chi^2+q\right)\left(M\Omega_0\right)^{\frac{4}{3}} + \cdots\right)\left(\frac{\Omega_\phi-\Omega_0}{\Omega_0}\right)^2 + \cdots \\ &= b_0 + b_1\frac{\Omega_\phi-\Omega_0}{\Omega_0} + b_2\left(\frac{\Omega_\phi-\Omega_0}{\Omega_0}\right)^2 + \cdots \end{aligned} \tag{2.16}$$

In this kind of expansion the multipole moments again contribute at all orders. However, provided the initial frequency $M\Omega_0 \ll 1$, the dominant piece of the constant term, b_0, is $(M\Omega_0)^{\frac{2}{3}}$, so this term can be used to estimate M. Similarly, the dominant piece of $2b_0 - 3b_1$ is $4\chi\left(M\Omega_0\right)$, so this can be used to estimate χ, and that estimate of χ can be used to improve the estimate of M from b_0. The dominant piece of $b_0 - b_1 + 3b_2$ is $\left(9+\chi^2+q\right)/2\left(M\Omega_0\right)^{\frac{4}{3}}$, so this can be used to estimate the excess quadrupole moment q and so on. In the same way, if an eccentric inspiral is observed in a regime where the initial frequency is small (and hence the frequency at capture was also small), we can use the same type of expansion and use combinations of the coefficients to successively extract each multipole moment and the initial eccentricity. To do this requires an expansion of $e^2 - e_0^2$ as a function of $\Omega_\phi/\Omega_0 - 1$. The necessary derivatives $\mathrm{d}e^2/\mathrm{d}(M\Omega_\phi)$ are known in the weak field, and to lowest order in the multipoles (see, for example, reference [26]). However, this calculation is somewhat involved and beyond the scope of this paper.

The above discussion indicates that the periapsis precession rate can be used on its own to measure the multipole moments from an eccentric equatorial inspiral, although this is more difficult than for the circular equatorial case. However, the value of the precession is not the only observable. As mentioned earlier, the relative amplitude of the various harmonics of the orbital frequencies is a powerful probe of the orbital eccentricity. To exploit this harmonic structure we also need to know how the amplitudes of the harmonics depend on the spacetime multipole moments. However, if the deviations from the Kerr metric multipole structure are small, we could imagine using the Kerr harmonic amplitude relation to estimate the eccentricity (and inclination) of the orbit, and then use the precessions to extract the multipole structure. Proper insight can be gained using the approximate semirelativistic waveforms described earlier or post-Newtonian expansions of the gravitational waveforms. Such an investigation will be an important extension of the current work.

2.6 Summary

In this paper we have discussed various observational signatures that could leave an imprint on an EMRI gravitational waveform if the spacetime in which the EMRI was occurring deviated from the Kerr metric. We have seen that some orbits in "bumpy" spacetimes lack a fourth integral of the motion and appear ergodic. Geodesics in the Kerr spacetime have a complete set of integrals, so if an apparently ergodic orbit was observed it would be a clear signature of a non-Kerr central object. However, regions of ergodic motion only appear very close to the central object, in a regime which is probably inaccessible to a star inspiraling from large distances. Most astrophysically relevant orbits are regular and appear to possess an approximate fourth integral of the motion, and the orbits are tri-periodic to high accuracy. The deviations of the central body from Kerr then manifest themselves only in the changes in the three fundamental frequencies of the motion and the relative amplitude of the different harmonics of these frequencies present in the gravitational waves. For nearly circular, nearly equatorial orbits, the dependence of the precession frequencies on the orbital frequency is well fit by a combination of a weak field expansion that encodes the multipole moments at different orders, plus a term that diverges as the innermost stable circular orbit is approached. The frequency of the ISCO and its nature (whether it is defined by a radial or vertical instability) is another observable signature of a non-Kerr central object.

To derive these results, we have focussed on a particular family of spacetimes due to Manko and Novikov [13]. However, we expect the generic features of the results in the weak field and as the ISCO is approached to be true for a wide range of spacetimes. Chaos has been found for geodesic motion in several different metrics by various authors [14, 15, 16, 17, 18]. In all cases, however, the onset of chaos was qualitatively similar to what we found here — it occurred only very close to the central object, and for a very limited range of orbital parameters. The conclusion that gravitational waves from ergodic EMRIs are unlikely to be observed is thus probably quite robust.

Precessions for spacetimes that deviate from the Kerr metric have also been considered by several authors [2, 11, 12]. Our results agree with this previous work in the weak field as they should. However, the results in the present paper are the first that are valid in the strong field since previous work was either based on a weak field expansion [2] or a perturbative spacetime [11, 12]. The main feature of the precessions in the strong field — the divergence of one of the precessions as the ISCO is approached — is expected from spacetime-independent considerations and therefore should be a general feature of inspirals in any spacetime. The present work, and earlier research [11, 12], has also considered only solutions that first differ from the Kerr metric in the mass quadrupole moment. The Manko-Novikov solutions [13] include spacetimes that first differ at higher orders. While we have not considered such solutions, we expect the generic features to be similar. The precessions will be closer to the Kerr values for a greater fraction of the inspiral, and the ISCO will be at a different frequency, but the qualitative behavior in the approach to ISCO should be the same.

The next step in understanding how gravitational-wave detectors might identify non-Kerr central objects from EMRI observations is to consider the gravitational waveforms produced during an inspiral. Any analysis should account for both parameter correlations and the finite bandwidth and observation time of gravitational-wave detectors by using a Fisher Matrix analysis. Glampedakis and Babak [12] constructed approximate gravitational waveforms generated by orbits in a perturbed Kerr spacetime, but they considered only waveforms from geodesics (i.e., not inspirals) and compared waveforms with the same orbital parameters. These are not observable quantities (unlike the frequency of the orbit which we used as a basis for comparison here) and such a calculation does not account for parameter correlations. Barack and Cutler [27] did a full Fisher Matrix analysis of this problem, and estimated that a LISA observation of an EMRI could measure the quadrupole moment of a body to an accuracy of 10^{-3} while simultaneously measuring the mass and spin to 10^{-4}. That calculation was based on an approximate waveform model devised to describe Kerr inspirals. The expressions governing the inspiral were modified by adding the leading order effect of a quadrupole moment to the energy and angular momentum fluxes. The waveform generation part of the algorithm was left unchanged. Although this result is a good guide, the calculation contained a number of inconsistencies. For Kerr inspirals, semirelativistic "kludge" waveforms based on combining exact geodesic motion with approximate gravitational-wave emission formulae have proven to give accurate results [26, 25]. The same method could be used to produce waveforms for inspiral in the Manko-Novikov spacetimes, by changing the geodesic equations and augmenting the inspiral fluxes appropriately. Such an approach will not generate totally accurate gravitational waveforms, but it will reproduce the main features of the orbit — the precession frequencies, the orbital shape and the frequency of the ISCO. A study of gravitational waveforms generated in "bumpy" spacetimes will provide useful guidance for future detectors such as to what precision an observation could determine that an inspiral is an inspiral into a Kerr black hole and how well observations can distinguish different types of deviation from Kerr, e.g., an exotic central object from a naked singularity from a Kerr black hole with external matter.

2.7 Appendix: Chaotic Motion in Newtonian Gravity

The classic example from astrophysics of a system that exhibits chaos in classical (Newtonian) gravity is the two dimensional Hénon-Heiles potential $V(r,\theta) = r^2/2 + r^3\sin(3\theta)/3$ (see [28] for example). Guéron and Letelier [16] also found chaos in the Paczyńki-Witta potential ($\Phi = M/(r - r_S)$, where $r_S = 2M$ is the Schwarzschild radius) with a dipolar perturbation. Neither of these spacetimes is reflection symmetric, so for a better analogy to the relativistic spacetimes considered in this paper, we examine the Newtonian quadrupole-octupole potential

$$\Phi(\rho, z) = -\frac{M}{r} - \frac{M_2}{2\,r^3}\left(1 - 3\frac{z^2}{r^2}\right) + \frac{M_4}{8\,r^5}\left(35\frac{z^4}{r^4} - 30\frac{z^2}{r^2} + 3\right). \tag{2.17}$$

Here, M, M_2 and M_4 denote the monopole (mass), quadrupole and octupole multipole moments of the potential. Stationarity and axisymmetry ensure that energy E and angular momentum $L_z = r^2\mathrm{d}\phi/\mathrm{d}t$ are conserved as usual, which leads us to the Newtonian analogue of the effective potential equation (2.8)

$$\frac{1}{2}\left(\left(\frac{\mathrm{d}r}{\mathrm{d}t}\right)^2 + \left(\frac{\mathrm{d}z}{\mathrm{d}t}\right)^2\right) = V_{\text{eff}}(E, L_z, \rho, z) = \frac{1}{2}\left(E^2 - 1\right) - \frac{L_z^2}{2\rho^2} - \Phi(\rho, z) \tag{2.18}$$

where we have replaced the standard Newtonian energy by the relativistic expression $(E^2 - 1)/2$ for consistency with (2.8). The equation of motion in this potential takes the usual form $\mathrm{d}^2\mathbf{r}/\mathrm{d}t^2 = -\nabla\Phi$. If we take the multipole moments to have the values $M_2 = 2M^3$ and $M_4 = 10M^5$, and choose the angular momentum to be $L_z = 1.7M$, we find that for a range of values of the energy E, bound orbits occur quite close to the origin. For sufficiently large values of E, there is a single allowed region for motion (defined by $V_{\text{eff}} \geq 0$). Orbits in that regime appear to be regular, and show closed Poincaré maps. If the energy is reduced, the allowed region eventually splits into two separate regions, one bounded away from $r = 0$, and one connected to $r = 0$. Orbits in the outermost region after this transition exhibit ergodic behavior. In Figure 2.20 we show four plots. Two of these plots are for an orbit with $E = 0.82$, which exhibit regular behavior. The other two are for $E = 0.81$ and exhibit ergodic behavior. We choose the initial conditions of both orbits to be $\dot{\rho} = 0 = z$ and $\rho = 3M$, with $\dot{z}$ determined from the assigned energy (2.18). The upper panels in the figure show

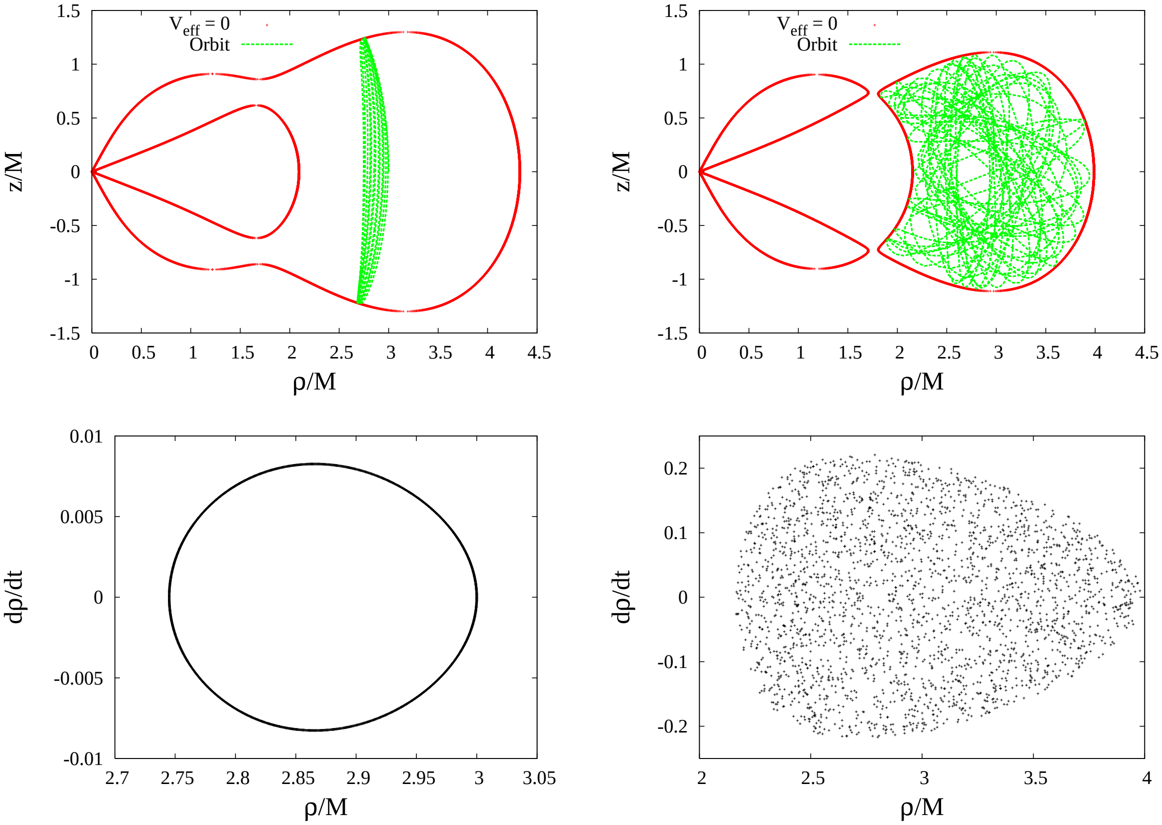

Figure 2.20: Example of onset of chaos in the Newtonian quadrupole-octupole potential (2.17). All plots are for orbits which start with $\dot{\rho} = 0 = z$, $\rho/M = 3$ and have specific angular momentum $L_z = 1.7M$. The left hand panels are for energy $E = 0.82$, while the right hand panels have energy $E = 0.81$. The top two plots show zeros of the effective potential, $V_{\text{eff}} = 0$, as defined by equation (2.18), and the paths followed by the orbits in the (ρ, z) plane. The bottom two plots are Poincaré maps for crossings of the $z = 0$ plane in each case.

the orbit in the (ρ, z) plane, and the boundary of the allowed region of motion (defined by $V_{\text{eff}} = 0$). The lower panels show Poincaré maps for the two orbits. The ergodicity of the orbit with $E = 0.81$ is quite evident from the Poincaré map. We also find that this orbit fills up the entire allowed range of ρ and z. By contrast, the regular orbit with $E = 0.82$ explores only a narrow torus in space.

A thorough examination of when ergodicity appears in this potential, as a function of energy, angular momentum and the multipole moments M_2 and M_4 is peripheral to the focus of this paper. However, the results presented here provide a Newtonian example to which we can compare the relativistic results of Section 2.3.

2.8 Appendix: Weak Field Precessions

2.8.1 Relativistic Precession

In Boyer-Lindquist coordinates, the energy, angular momentum and rest-mass conservation equations (2.8)–(2.8) for geodesic motion in the Kerr metric can be used to derive the equation of motion in the form (see for instance [29])

$$\begin{aligned}\frac{1}{2}\left(\left(\frac{\mathrm{d}r}{\mathrm{d}t}\right)^2+\Delta\left(\frac{\mathrm{d}\theta}{\mathrm{d}t}\right)^2\right) &= \\ \frac{\left(E(r^2+a^2)-aL_z\right)^2-\Delta\left(r^2+(L_z-aE)^2+L_z^2\cos^2\theta+a^2\cos^2\theta(1-E^2)\right)}{2\left(E((r^2+a^2)^2/\Delta-a^2\sin^2\theta)-2MaL_zr/\Delta\right)^2} & \qquad (2.19)\end{aligned}$$

where $\Delta = r^2 - 2Mr + a^2$, and $a = M\chi$. The prograde equatorial circular orbit at radius r has energy and angular momentum

$$E = \frac{1-2v^2+av^3/M}{\sqrt{1-3v^2+2av^3/M}} \qquad (2.20)$$

$$L_z = rv\frac{1-2av^3/M+a^2v^4/M^2}{\sqrt{1-3v^2+2av^3/M}} \qquad (2.21)$$

where $v^2 = M/r$. The frequency of a prograde circular orbit is given by

$$\Omega_\phi = \frac{\mathrm{d}\phi}{\mathrm{d}t} = \frac{\sqrt{M}}{r^{3/2}+a\sqrt{M}}. \qquad (2.22)$$

The epicyclic frequencies for radial and vertical perturbations of the orbit are given by the second derivatives of the right hand side of equation (2.19) with respect to r and θ (the right hand side of Eq. (2.19) is the effective potential for the Kerr spacetime). To obtain the form of these frequencies in the weak field, we wish to expand in $1/r$. With some manipulation and keeping terms up to r^{-5} only, we obtain the expansion

$$\Omega_\rho^2 = \frac{M}{r^3} - 6\frac{M^2}{r^4} + 6\chi\frac{M^{5/2}}{r^{9/2}} - 3\chi^2\frac{M^3}{r^5} + \cdots \qquad (2.23)$$

$$\Omega_z^2 = \frac{M}{r^3} - 6\chi\frac{M^{5/2}}{r^{9/2}} + 3\chi^2\frac{M^3}{r^5} + \cdots \qquad (2.24)$$

where we use Ω_ρ, Ω_z to denote the radial and vertical epicyclic frequencies to be consistent with the results earlier in the paper. With further manipulation, expressions for the precessions, p_X, as a function of the orbital frequency, Ω_ϕ, may be derived

$$\begin{aligned} p_\rho &= 3\left(M\Omega_\phi\right)^{\frac{2}{3}} - 4\chi\left(M\Omega_\phi\right) + \frac{3}{2}\left(9+\chi^2\right)\left(M\Omega_\phi\right)^{\frac{4}{3}} - 34\chi\left(M\Omega_\phi\right)^{\frac{5}{3}} \\ &\quad + \frac{1}{2}\left(135+67\chi^2\right)\left(M\Omega_\phi\right)^2 + \cdots \qquad (2.25) \\ p_z &= 2\chi\left(M\Omega_\phi\right) - \frac{3}{2}\chi^2\left(M\Omega_\phi\right)^{\frac{4}{3}} + 8\chi^2\left(M\Omega_\phi\right)^2 + \cdots \qquad (2.26) \end{aligned}$$

Results for retrograde orbits may be obtained by the substitutions $\chi \to -\chi$, $\Omega_\phi \to -\Omega_\phi$ and $L_z \to -L_z$ in the above expressions (NB $\Omega_\phi < 0$ for retrograde orbits, so $-\Omega_\phi$ is equivalent to $|\Omega_\phi|$).

2.8.2 Precession due to a Quadrupole Moment

The precession induced by a quadrupole moment can be derived using the Newtonian quadrupole potential

$$\Phi = -\frac{M}{r} - \frac{1}{2}\frac{Q}{r^3}\left(1 - 3\frac{z^2}{r^2}\right).$$

Here $r = \sqrt{x^2+y^2+z^2}$ is the distance from the origin, z is the vertical coordinate and we will use $\rho = \sqrt{x^2+y^2}$ to denote the cylindrical polar radial coordinate. The radial equation of motion in this potential takes the form

$$\frac{1}{2}\left(\frac{\mathrm{d}\rho}{\mathrm{d}t}\right)^2 = E - \frac{L_z^2}{2\rho^2} + \frac{M}{r} + \frac{1}{2}\frac{Q}{r^3}\left(1 - 3\frac{z^2}{r^2}\right) \qquad (2.27)$$

and the energy, angular momentum and orbital frequency of a circular, equatorial orbit with radius ρ are

$$\begin{aligned} E &= \frac{Q}{4\rho^3} - \frac{M}{2\rho} \\ L_z &= \sqrt{M\rho + \frac{3}{2}\frac{Q}{\rho}} \\ \Omega_\phi &= \sqrt{\frac{M}{\rho^3} + \frac{3}{2}\frac{Q}{\rho^5}} \qquad (2.28) \end{aligned}$$

Differentiating Eq. (2.27) twice with respect to ρ and z, we find the epicyclic frequencies take the form

$$\begin{aligned} \Omega_\rho^2 &= \frac{M}{\rho^3} - \frac{3}{2}Q\frac{M}{r^5} + \cdots \qquad (2.29) \\ \Omega_z^2 &= \frac{M}{\rho^3} + \frac{3}{2}Q\frac{M}{r^5} + \cdots . \qquad (2.30) \end{aligned}$$

Hence we derive the precession frequencies

$$\begin{aligned} p_\rho &= -\frac{3}{2}\frac{Q}{M^3}\left(M\Omega_\phi\right)^{\frac{4}{3}} + \cdots \\ p_z &= \frac{3}{2}\frac{Q}{M^3}\left(M\Omega_\phi\right)^{\frac{4}{3}} + \cdots . \end{aligned} \tag{2.31}$$

The lowest order form of these expressions was also given in Collins and Hughes [11], although they expressed the precession in terms of a radial coordinate, rather than the observable Ω_ϕ. We also use a slightly different definition for the quadrupole moment Q so that it is consistent with $Q = -\chi^2 M^3$ for the Kerr metric. As we would expect, the leading-order terms in these expressions agree with the leading order terms in χ^2 in the Kerr expressions.

Combining this result with Eq. (2.26), we obtain the weak field precessions for the Manko-Novikov solution with spin parameter χ and excess quadrupole moment q

$$\begin{aligned} p_\rho &= 3\left(M\Omega_\phi\right)^{\frac{2}{3}} - 4\chi\left(M\Omega_\phi\right) + \frac{3}{2}\left(9+\chi^2+q\right)\left(M\Omega_\phi\right)^{\frac{4}{3}} - 34\chi\left(M\Omega_\phi\right)^{\frac{5}{3}} \\ &\quad + \frac{1}{2}\left(135+67\chi^2+39q\right)\left(M\Omega_\phi\right)^2 + \cdots \\ p_z &= 2\chi\left(M\Omega_\phi\right) - \frac{3}{2}\left(\chi^2+q\right)\left(M\Omega_\phi\right)^{\frac{4}{3}} + \left(8\chi^2-3q\right)\left(M\Omega_\phi\right)^2 + \cdots . \end{aligned} \tag{2.32}$$

In the above, the lowest order term that is omitted is the order at which the excess current quadrupole moment would first contribute. This result is also given in Ryan [2], although he quotes an expression for $\tilde{\Omega}_\rho/\Omega_\phi$, where $\tilde{\Omega}_\rho$ is equal to $\Omega_\phi - \Omega_\rho$. Our result is consistent with his once this is taken into account. We note that some of the terms in expression (2.32) come from relativistic corrections to the effect of the quadrupole moment. These cannot be derived using only the results quoted in this appendix, but are given in Ryan's paper [2].

2.9 Bibliography

[1] Amaro-Seoane, P., Gair, J. R., Freitag, M., Miller, M. C., Mandel, I., Cutler, C. J., Babak, S., *Class. Quant. Grav.* **24**, R113 (2007).

[2] Ryan F. D. *Phys. Rev. D* **52**, 5707 (1995).

[3] Hughes, S. A., *AIP Conf. Proc.* **873**, 233 (2006).

[4] Brown, D. A., Brink, J., Fang, H., Gair, J. R., Li, C., Lovelace, G., Mandel, I., and Thorne, K. S., *Phys. Rev. Lett.* **99**, 201102 (2007).

[5] Carter, B. *Phys. Rev. Lett.* **26**, 331 (1971).

[6] Robinson, D. C. *Phys. Rev. Lett.* **34**, 905 (1975).

[7] Kesden, M., Gair, J. R., and Kamionkowski, M., *Phys. Rev. D* **71**, 044015 (2005).

[8] Straumann, N., and Zhou, Z., *Phys. Lett. B* **243**, 33 (1990).

[9] Droz, S., Heusler, M., and Straumann, N., *Phys. Lett. B* **268**, 371 (1991).

[10] Hughes, S. A., Drasco, S., Flanagan, E. E., and Franklin, J., *Phys. Rev. Lett.* **94**, 221101 (2005).

[11] Collins, N. A. & Hughes, S. A., *Phys. Rev. D* **69**, 124022 (2004).

[12] Glampedakis, K. & Babak, S., *Class. Quant. Grav.* **23**, 4167 (2006).

[13] Manko, V. S. &Novikov, I. D., *Class. Quant. Grav.* **9**, 2477 (1992).

[14] Sota, Y., Suzuki, S. & Maeda, K., *Class. Quant. Grav.* **13**, 1241 (1996).

[15] Letelier, P. S. & Viera, W. M. 1997, *Class. Quant. Grav.* **14**, 1249 (1997).

[16] Guéron, E. & Letelier, P. S., *Astron. Astrophys.* **368**, 716 (2001).

[17] Guéron, E. & Letelier, P. S., *Phys. Rev. E* **66**, 046611 (2002).

[18] Dubeibe, F. L., Pachon, L. A., Sanabria-Gomez, J. D., *Phys. Rev. D* **75**, 023008 (2007).

[19] Fang, H., Ph.D. thesis, California Institute of Technology, 2007.

[20] Brink, J. (private communication)

[21] Kodama, H. & Hikida, W., *Class. Quant. Grav.* **20** 5121 (2003).

[22] Carter B. *Comm. Math. Phys.* **10**, 280 (1968).

[23] Tabor M., *Chaos and Integrability in Nonlinear Dynamics: An Introduction* (John Whiley & Sons, New York, 1989), Chap. 3.4.

[24] Brink, J. (to be published)

[25] Babak, S., Fang, H., Gair, J. R., Glampedakis, K., Hughes, S. A., *Phys. Rev. D* **75**, 024005 (2007).

[26] Gair, J. R. & Glampedakis, K., *Phys. Rev. D* **73**, 064037 (2006).

[27] Barack, L. & Cutler, C., *Phys. Rev. D* **75**, 042003 (2007).

[28] Contopoulos, G.,*Order and Chaos in Dynamical Astronomy* (Springer, New York, 2002).

[29] Chandrasekhar, S., *The Mathematical Theory of Black Holes* (Clarendon, Oxford, 1983).

Chapter 3

A Generalization of Ryan's Theorem: Probing Tidal Coupling with Gravitational Waves from Nearly Circular, Nearly Equatorial, Extreme-Mass-Ratio Inspirals

Extreme-mass-ratio inspirals (EMRIs) and intermediate-mass-ratio inspirals (IMRIs)—binaries in which a stellar-mass object spirals into a massive black hole or other massive, compact body—are important sources of gravitational waves for LISA and LIGO, respectively. Thorne has speculated that the waves from EMRIs and IMRIs encode, in principle, all the details of (i) the central body's spacetime geometry (metric), (ii) the tidal coupling (energy and angular momentum exchange) between the central body and orbiting object, and (iii) the evolving orbital elements. Fintan Ryan has given a first partial proof that this speculation is correct: Restricting himself to nearly circular, nearly equatorial orbits and ignoring tidal coupling, Ryan proved that the central body's metric is encoded in the waves. In this paper we generalize Ryan's theorem. Retaining Ryan's restriction to nearly circular and nearly equatorial orbits, and dropping the assumption of no tidal coupling, we prove that Thorne's conjecture is nearly fully correct: the waves encode not only the central body's metric but also the evolving orbital elements and (in a sense slightly different from Thorne's conjecture) the evolving tidal coupling.

Originally published as C. Li and G. Lovelace, *Phys. Rev. D* **77**, 064022 (2008).

3.1 Introduction and Summary

The LIGO-GEO-VIRGO-TAMA network of broadband ground-based laser interferometers, aimed at detecting gravitational waves in the high-frequency band 10–10^4 Hz, is already operating at or near its initial design sensitivities. In the next decade, LISA (the Laser Interferometer Space Antenna) will open up the low-frequency gravitational-wave window (10^{-4}–0.1 Hz).

Among the most important sources of gravitational waves for LISA are extreme-mass-ratio inspirals (EMRIs), which are systems in which a small object (with mass $\mu \sim M_\odot$) orbits a supermassive black hole or other central body (boson star [1, 2] or soliton star [3] or naked singularity) with mass $M \sim 10^6 M_\odot$. Recently, Brown and collaborators [4] have estimated that advanced detectors in LIGO (the Laser Interferometric Gravitational-Wave Observatory) may detect up to $\sim 10-30$ yr^{-1} *intermediate mass ratio inspirals* (IMRIs), which are analogous to EMRIs but have less massive central bodies (masses M in the range of $\sim 10^2 \text{to} 10^4 M_\odot$).

Thorne has conjectured[1] that the waves from an EMRI or IMRI contain, encoded in themselves (at least in principle): (i) the spacetime geometry (metric) of the massive central body, (ii) the tidal coupling (evolving rate of energy and angular momentum exchange) between the orbiting object and the central body, and (iii) the evolving orbital elements. This conjecture (which has been partially proved; see below) has motivated placing EMRIs high on LISA's list of target sources [8], and has motivated research to: (a) prove Thorne's conjecture with the widest generality possible, or, if it is false, determine what information actually *is* encoded in the EMRI and IMRI waves [4, 9]; (b) develop data analysis techniques for searching for EMRI and IMRI waves in LISA [10, 11] and LIGO [12] data; (c) scope out the accuracy with which LISA and LIGO can extract the encoded information from EMRI and IMRI waves (and if the central body appears to be a black hole, the accuracy with which its properties agree with those of a hole) [13, 14]; and (d) develop data analysis techniques for extracting the waves' information [15].

Fintan Ryan [6] has proved a theorem that is an important step toward verifying Thorne's conjecture. Specifically, he has proved that it is possible in principle to recover the full spacetime geometry from EMRI waves under the following assumptions: (i) the central body is general-relativistic, stationary, axisymmetric, reflection-symmetric, and asymptotically flat (SARSAF), (ii) the small object travels on a nearly circular and nearly equatorial orbit, and (iii) there is no tidal coupling. Moreover, Ryan has shown that the multipole moments that determine the spacetime geometry are *redundantly* encoded in the gravitational waves and can be extracted using *either* of the two

---

[1] Thorne's conjecture has grown over time. Originally, in the early 1990s, he conjectured (or, more precisely, asserted!) that the waves encode "a portion" of the spacetime geometry (e.g., p. 326 of [5]). By 1994, when Fintan Ryan proved his theorem, Thorne was arguing that the entire spacetime geometry would be encoded (see, e.g., the introduction to Ryan's paper [6]). In 2002, when thinking about how LISA might test the laws of black hole physics, Thorne realized that the tidal coupling might also be encoded along with the central body's spacetime geometry; see Ref. [7]. Only recently, when advising the authors about their research, did Thorne realize that the evolving orbital elements might also be extractable (private communication).

precession frequencies (about a circular orbit and about the equatorial plane) *or* the waves' phase evolution.

The purpose of this paper is to generalize Ryan's theorem. We retain assumptions (i) and (ii) (SARSAF spacetime and nearly circular, nearly equatorial orbit) but relax assumption (iii) by allowing for a small amount of tidal coupling. We show that in this case, Thorne's conjecture is nearly correct: the waves encode not only the central body's metric but also the evolving orbital elements and (in a sense slightly different from Thorne's conjecture) the evolving tidal coupling. (Assumption (ii), that the orbit is nearly circular and nearly equatorial, is relaxed in a companion paper by Li [9]).

Motivated by the result of Fang and Lovelace [16] that the only unambiguous part of the tidal coupling is the time-dependent, dissipative portion (at least when the central body is a non-spinning black hole and the orbit is large and circular), we characterize the tidal coupling by the rates of energy and angular momentum exchange between the central body and the orbiting object, $\dot{E}_{\rm body}$ and $\dot{L}_{\rm body}$. (Throughout this paper, a dot means derivative with respect to the coordinate time t, which is the time measured by an inertial observer in the asymptotically flat region of the spacetime.) Actually, we only need to consider $\dot{E}_{\rm body}$, because once it is known, $\dot{L}_{\rm body}$ can be deduced from the standard energy-angular momentum relation for circular orbits and their influence on waves and tides, $\dot{E} = \Omega_{\rm orbit}\dot{L}$. (Here $\Omega_{\rm orbit}$ is the orbital angular velocity, which is the same as the waves' observed primary angular frequency aside from a factor 2.)

This paper is organized as follows: In Sec. 3.2, we begin by noting that, when there is a small amount of tidal coupling (as we assume), then the redundancy in Ryan's analysis is broken. One can still use Ryan's algorithm for the precession frequencies to recover the central body's spacetime geometry. Then, by making use of the observed (time-independent) spacetime geometry and the measured, evolving amplitudes associated with the precession frequencies, one can also recover from the EMRI waves the evolving orbital parameters. Having relied on non-dissipative aspects of the waves to deduce the spacetime geometry and orbit, one can then—as we show in Sec. 3.3—use the waves' dissipation-induced phase evolution to deduce the tidal coupling.

In our somewhat delicate discussion of deducing the tidal coupling (Sec. 3.3), we begin by noting that the sum of the power radiated to infinity and the power fed into the central body via tidal coupling, $\dot{E}_{\rm total} = \dot{E}_\infty + \dot{E}_{\rm body}$ is equal to the power lost from the orbit, which can be deduced from the waves' observed phase evolution. The central body influences this observed $\dot{E}_{\rm total}$ in two ways: (i) by generating a nonzero $\dot{E}_{\rm body}$, the quantity that interests us, and (ii) by very slightly altering $\dot{E}_\infty$. To help quantify these two body influences, in Sec. 3.3.2 we show how one can deduce, from the observations, the rate $\dot{E}_{\infty{\rm NBI}}$ that energy would be radiated to infinity if there were *no body influences*. The difference between the measured $\dot{E}_{\rm total}$ and the deduced $\dot{E}_{\infty{\rm NBI}}$ is the influence of the body's structure on the total energy loss from the orbit, $\dot{E}_{\rm total,BI} \equiv \dot{E}_{\rm total} - \dot{E}_{\infty{\rm NBI}}$. This measured/deduced body influence on the total energy loss consists of two tiny pieces: the power that actually goes into the body via tidal coupling, $\dot{E}_{\rm body}$, and the body's tiny influence on the power radiated to infinity, $\dot{E}_{\infty{\rm BI}} \equiv \dot{E}_{\infty} - \dot{E}_{\infty{\rm NBI}}$:

$$\dot{E}_{\rm total,BI} \equiv \dot{E}_{\infty{\rm BI}} + \dot{E}_{\rm body}\ . \tag{3.1}$$

In principle (as described above), from the observational data plus general-relativity theory we know the body's influence on the total energy loss $\dot{E}_{\rm total,BI}$ with complete precision. This is not quite what Thorne conjectured, but it is close, and it is the only complete-precision statement we have been able to make about measuring the influence of tidal coupling.

Thorne conjectured we could deduce $\dot{E}_{\rm body}$ from the observed waves. This, in fact appears not to be possible (in principle) with complete precision. However, we argue in Sec. 3.3.3 and the appendix that, if the central body is highly compact, then the unknown $\dot{E}_{\infty{\rm BI}}$ will be smaller than $\dot{E}_{\rm body}$ by $\sim v^n \ll 1$, where v is the orbital velocity and n is some high power; and we show that, when the body's external metric is that of Schwarzschild or Kerr, then $n = 5$. As a result, aside from a very small $\mathrm{O}(v^n)$ uncertainty due to the influence of the body on the energy radiated to infinity, the tidal coupling power $\dot{E}_{\rm body}$ is equal to the known influence of the body on the total energy loss $\dot{E}_{\rm total,BI}$.

A brief conclusion is made in Sec. 3.4.

3.2 Extracting the Spacetime Geometry and Orbital Elements

Aside from allowing tidal coupling, we treat the same class of EMRIs as did Ryan:

First, we assume the central body's exterior spacetime is a vacuum, stationary, axisymmetric, reflection symmetric, and and asymptotic flat (SARSAF) solution of Einstein's equations. The exterior spacetime metric can be written as (e.g., Eq. (7.1.22) of Ref. [17])

$$ds^2 = -F(dt - \omega d\phi)^2 + \frac{1}{F}[e^{2\gamma}(d\rho^2 + dz^2) + \rho^2 d\phi^2], \tag{3.2}$$

where F, ω and γ are functions of ρ and $|z|$. In SARSAF spacetimes, there is a one to one correspondence between the spacetime metric and a series of scalar multipole moments (M_{2i}, S_{2i+1}), $\quad i = 0, 1, \dots$ [18, 19]. Here $M_0 \equiv M$ is the mass of the central body, S_1 is its spin, M_2 is its mass quadrupole moment, etc. To extract the geometry of the spacetime surrounding the central body, it is sufficient to extract the multipole moments $\{M_\ell, S_\ell\}$ [6].

Second, we let a small object with mass $\mu \ll M$ move about the central body in a nearly circular, nearly equatorial orbit.

For precisely circular, equatorial, geodesic motion, the waves obviously have a single fundamental frequency Ω_ϕ that is associated with the circular motion $\phi = \Omega_\phi t$. When the geodesic orbit is slightly nonradial, it is easy to show that its radius ρ undergoes periodic motion with some angular frequency Ω_ρ; and when slightly nonequatorial, its vertical coordinate z undergoes periodic motion with another angular frequency Ω_z. These geodesic motions give rise to gravitational waves that are triperiodic: a discrete spectrum with frequencies equal to Ω_ϕ, Ω_ρ, Ω_z, and their sums and differences (see Ref. [9] for a proof, patterned after the proof by Drasco and Hughes [20] for the Kerr metric). The frequency difference $\Omega_\rho - \Omega_\phi$ shows up as an orbital periapsis precession, and $\Omega_z - \Omega_\phi$ as an orbital plane precession; these precessions produce corresponding modulations of the gravitational waveforms.

In our case, the orbits are not geodesics; they evolve due to gravitational radiation reaction. Because of the extreme mass ratio, the radiation reaction can be described by the adiabatic approximation. In this approximation, on the timescale of an orbital period, the small object moves very nearly along a geodesic of the central body's gravitational field. On a timescale much larger than the orbital period, the object moves from one geodesic to another as it loses energy and angular momentum to gravitational radiation. It follows that the three frequencies $\{\Omega_\phi(t), \Omega_\rho(t), \Omega_z(t)\}$ each evolve with time on the radiation reaction timescale which is much longer than the orbital periods.

In principle, a large amount of information can be encoded in the time evolution of the waves' three fundamental frequencies $\{\Omega_\phi(t), \Omega_\rho(t), \Omega_z(t)\}$ and the complex amplitudes (amplitudes and phases) of the various spectral components. The largest amplitudes are likely to be those for the second harmonic of Ω_ϕ and for the two precessions, $h_{2\Omega_\phi}(t)$, $h_{\Omega_\rho-\Omega_\phi}(t)$, and $h_{\Omega_\rho-\Omega_z}(t)$. We shall call these the primary-frequency component, and the precessional components of the waves. To simplify our prose, we shall refer to Ω_ρ and Ω_z as the "precession frequencies" even though the actual frequencies of precession are $\Omega_\rho - \Omega_\phi$ and $\Omega_z - \Omega_\phi$.

Thorne's conjecture can be expressed mathematically as the claim that these time evolving frequencies and amplitudes encode fully and separably,

1. the values of all the central body's multipole moments $\{M_\ell, S_\ell\}$,
2. the rates $\dot{E}_{\rm body}$ and $\dot{L}_{\rm body}$ at which the orbiting object's tidal pull deposits energy and angular momentum into the central body, and
3. the time-evolving orbital elements, i.e., the orbit's semi-latus rectum $p(t)$, eccentricity $e(t)$ and inclination angle $\iota(t)$.

Ryan's theorem [6] states that if there is no tidal coupling, then all the SARSAF moments $\{M_{2i}, S_{2i+1}\}$ are encoded in the time evolving frequencies fully, separably, and redundantly. Ryan did not explicitly address the encoding of the three orbital elements $p(t)$, $e(t)$ and $\iota(t)$. However, their encoding is an almost trivial extension of his analysis:

Specifically, Ryan noticed that the three fundamental frequencies are independent of e and ι to first order in these small quantities, i.e., they are functions solely of the moments and the semi-latus rectum p. One can eliminate p by regarding the precession frequencies Ω_z and Ω_ρ as functions of the moments and Ω_ϕ, or equivalently as functions of the moments and the Post-Newtonian (PN) expansion parameter $v \equiv (M\Omega_\phi)^{1/3} \simeq$ (orbital velocity). Expanding $\Omega_z(v; S_\ell, M_\ell)$ and $\Omega_\rho(v; S_\ell, M_\ell)$ in powers of v, Ryan found the following pattern of coefficients (with each moment first appearing at a different power of v), from which all the moments can be extracted separably (Eqs. (18,19) of Ref. [6]):

$$\begin{aligned} \frac{\Omega_\rho}{\Omega_\phi} &= 3v^2 - 4\frac{S_1}{M^2}v^3 + \left(\frac{9}{2} - \frac{3M_2}{2M^3}\right)v^4 + \cdots , \\ \frac{\Omega_z}{\Omega_\phi} &= 2\frac{S_1}{M^2}v^3 + \frac{3M_2}{2M^3}v^4 + \cdots . \end{aligned} \tag{3.3}$$

This result leads to Ryan's algorithm for extracting information. *First,* from the waves' observed time-evolving precession frequencies and time-evolving primary frequency, one can deduce the functions $\Omega_{z,\rho}(\Omega_\phi)$ and thence $\Omega_{z,\rho}(v)$; *second,* expanding in powers of v, one can then read out the multipole moments $\{M_\ell, S_\ell\}$ from either $\Omega_z(v)$ or $\Omega_\rho(v)$.

We almost trivially augment onto Ryan's algorithm the following steps for extracting the time-evolving orbital elements: *Third,* knowing the moments and thence the metric, one can use the geodesic equation to deduce $p(t)$ from $\Omega_\phi(t)$. *Fourth*, one can use wave-generation theory and knowledge of the metric to deduce $e(t)$ and $\iota(t)$ from the amplitudes $h_{\Omega_\rho - \Omega_\phi}$ and $h_{\Omega_z - \Omega_\phi}$ of the wave modulations due to periapse precession and orbital plane precession.

3.3 Probing Tidal Coupling

We now drop Ryan's restriction of no tidal coupling. This does not alter Eqs. (3.3) for Ω_ρ and Ω_z as functions of v, i.e. of the orbital frequency Ω_ϕ, since all three frequencies only depend on the geodesic motion and hence only depend on the multipole moments $\{M_\ell, S_\ell\}$. On the other hand, the evolution of the frequencies, *as functions of time, will* depend on the tidal coupling.

More generally, we can divide the physical quantities of our analysis into two categories: (i) "static": those quantities related to the geodesic motion of the orbiting object, and (ii) "dynamic": those quantities related to the inspiral of the object (i.e., to the evolving rate at which the object moves from geodesic to geodesic). All static quantities are independent of tidal coupling and all dynamic quantities depend on it.

This suggests that Ryan's analysis can be extended to include tidal coupling. First, the static quantities can be used to deduce the the central body's multipole moments, just as in Ryan's original argument as sketched above. Then, the dynamic quantities, combined with knowledge of the spacetime metric, can be used to extract tidal-coupling information. This extension is discussed in the following subsections.

3.3.1 The Phase Evolution When Tidal Coupling is Neglected

Following Ryan, we characterize the phase evolution of EMRI waves by the number of primary-frequency cycles of waves per logarithmic frequency interval, as a function of the primary waves' slowly increasing frequency $f = \Omega_\phi/\pi$. This quantity can be written as (Eq. (4) of Ref. [6])

$$\Delta N(f) \equiv \frac{f\,dt}{d\ln f} = \frac{f^2}{df/dt}. \tag{3.4}$$

This phase evolution $\Delta N(f)$ can be measured by gravitational-wave detectors with high precision.

If there is no tidal coupling *and* no other influence of the structure of the central body on the waves, as Ryan assumed, then it is possible to read off the multipole moments (and also the small object's mass[2]) from a PN expansion of $\Delta N(f)$ (Eq. (57) of Ref. [6]):

$$\begin{aligned}\Delta N_{\rm NBI} \;=\; & \frac{5}{96\pi}\left(\frac{M}{\mu}\right) v^{-5}\Bigg[1+\frac{743}{336}v^2-4\pi|v|^3+\frac{113}{12}\frac{S_1}{M^2}v^3+\left(\frac{3058673}{1016064}-\frac{1}{16}\frac{S_1^2}{M^4}+5\frac{M_2}{M^3}\right)v^4 \\ & +\sum_{\ell=4,6,\ldots}\frac{(-1)^{\ell/2}(4\ell+2)(\ell+1)!!\,[M_\ell+\mathrm{TNILM}]\,v^{2\ell}}{3\ell!!M^{\ell+1}} \\ & +\sum_{\ell=3,5,\ldots}\frac{(-1)^{(\ell-1)/2}(8\ell+20)\ell!!\,[S_\ell+\mathrm{TNILM}]\,v^{2\ell+1}}{3(\ell-1)!!M^{\ell+1}}\Bigg].\end{aligned} \tag{3.5}$$

Here "NBI" stands for *no body influence* and "TNILM" stands for *terms nonlinear in lower moments.* (Recall that $v = (M\Omega_\phi)^{1/3} = (\pi M f)^{1/3}$.) So long as tidal coupling is negligible, then, the spacetime multipole moments can be determined redundantly from *either* $\Delta N(f)$ (Eq. (3.5)) *or* the periapse precession frequency $\Omega_\rho(\Omega_\phi)$ *or* the orbital-plane precession frequency $\Omega_z(\Omega_\phi)$ (Eqs. (3.3)).

3.3.2 Tidal Coupling and the Phase Evolution

When tidal coupling effects are included, the redundancy is broken. The multipole moments $\{M_\ell, S_\ell\}$ can still (Eq. (3.3)) be determined from $\Omega_{\rho,z}(\Omega_\phi)$, while (as the following discussion shows), the tidal coupling can be determined from $\{M_\ell, S_\ell\}$ and $\Delta N(f)$.

As a preliminary to discussing this, we explain why it is sufficient, in analyzing tidal coupling, to focus on energy exchange between the orbit, the body and the waves, and ignore angular momentum exchange. Since the body is in a (nearly) circular, geodesic orbit, changes in its orbital energy and

---

[2] The mass of the small object can be determined from $\Delta N(f)$ *even when there is tidal coupling.* The leading-PN-order part of the energy flux (equivalently, the leading-PN-order part of $\Delta N(f)$) is independent of tidal coupling. One can thus equate the leading-PN-order parts of $\Delta N(f)$ and $\Delta N_{\rm NBI}$ (Eq. (3.5)). After inserting the mass M (obtained from one of the precession frequencies), one can solve for μ. The precession frequencies, in contrast, are independent of μ (Eqs. (3.3)).

angular momentum are related by

$$\dot{E}_{\rm orbit} = \Omega_\phi \, \dot{L}_{\rm orbit}, \tag{3.6a}$$

aside from second-order corrections due to the slight orbital ellipticity and inclination angle. Our entire analysis is restricted to first-order corrections, so those second-order corrections are negligible. Similarly, since the energy and angular momentum radiated to infinity are carried by the primary waves, with angular frequency $\omega = 2\pi f = 2\Omega_\phi$ (aside from negligible contributions from the precessions, which are second order in the ellipticity and inclination), each graviton carries an energy $\hbar\omega = 2\hbar\Omega_\phi$ and an angular momentum $2\hbar$ (with this last 2 being the graviton spin). Therefore, the energy and angular momentum radiated to infinity are related by

$$\dot{E}_\infty = \Omega_\phi \, \dot{L}_\infty. \tag{3.6b}$$

Conservation of energy and of angular momentum, together with Eqs. (3.6a) and (3.6b), then imply that

$$\dot{E}_{\rm body} = \Omega_\phi \, \dot{L}_{\rm body}, \tag{3.6c}$$

for the energy and angular momentum deposited in the body by tidal coupling. Equations (3.6) imply that, once we understand, observationally, the energy exchange, an understanding of the angular momentum exchange will follow immediately.

Now turn to the influence of the body's internal structure on the observed energy exchange.

The total rate that energy is lost from the orbit (which then goes to infinity and the body) is related to the phase evolution $\Delta N(f)$ by

$$\dot{E}_{\rm total} = -\dot{E}_{\rm orbit} = -\frac{dE_{\rm orbit}}{df}\frac{df}{dt} = -f^2 \frac{dE_{\rm orbit}}{df}\frac{1}{\Delta N}. \tag{3.7}$$

The phase evolution ΔN and the primary frequency f are known from observation, and, after using the precession frequencies to compute the spacetime metric (Sec. 3.2), it is possible to compute $dE_{\rm orbit}/df$ via the geodesic equation[3]To do this, first insert the multipole moments $\{M_\ell, S_\ell\}$ into the geodesic equation. Then, solve the geodesic equation for the family of circular, equatorial orbits about the central body. Each orbit i will have a particular value of energy $E_{{\rm orbit},i}$ and frequency f_i; this one-to-one mapping between $E_{\rm orbit}$ and f can then be used to compute $dE_{\rm orbit}/df$. Thus everything on the right-hand side of Eq. (3.7) can be determined from observed quantities, which means that $\dot{E}_{\rm total}$ is measurable.

---

[3] .

Another measurable quantity, we claim, is the rate that energy would be lost from the orbit if the body's structure had no influence. This quantity is [by analogy with Eq. (3.7)]

$$\dot{E}_{\rm total,NBI} = -f^2 \frac{dE_{\rm orbit}}{df} \frac{1}{\Delta N_{\rm NBI}}. \tag{3.8}$$

Knowing the moments as a function of frequency from measurements of the precessions, $\Delta N_{\rm NBI}$ can be computed from the moments via Ryan's phasing relation,[4] (3.5) and, as we have seen, $dE_{\rm orbit}/df$ can also be computed from the observations; so $\dot{E}_{\rm total,NBI}$ is, indeed, observable, as claimed. Therefore the influence of the body's structure on the orbit's total energy loss

$$\dot{E}_{\rm total,BI} = \dot{E}_{\rm total} - \dot{E}_{\rm total,NBI} \tag{3.9}$$

is also observable.

This body influence on the total energy loss consists of two parts: the energy that goes into the body via tidal coupling, $\dot{E}_{\rm body}$, and a tiny body-influenced modification of the rate that the waves carry energy to infinity

$$\dot{E}_{\rm total,BI} = \dot{E}_{\rm body} + \dot{E}_{\infty\rm BI} \ , \tag{3.10}$$

where

$$\dot{E}_{\infty\rm BI} = \dot{E}_{\infty} - \dot{E}_{\rm total,NBI} \ . \tag{3.11}$$

Thorne conjectured that the energy exchange due to tidal coupling, $\dot{E}_{\rm body}$, would be observable. We doubt very much that it is, since in general we see no way to determine the relative contributions of $\dot{E}_{\rm body}$ and $\dot{E}_{\infty\rm BI}$ to the observed total body influence $\dot{E}_{\rm total,BI}$. The best one can do, in general, in validating Thorne's conjecture, is to extract the central body's total influence on the orbital energy loss, $\dot{E}_{\rm total,BI}$. However, in the special case of a body that is exceedingly compact, we can do better, as we shall explain in the next subsection.

3.3.3 The Dependence of $\dot{E}_{\infty}$ on the Central Body's Internal Structure

Consider a central body sufficiently compact that gravity near its surface blueshifts the orbiting object's tidal field, making it appear like ingoing gravitational waves as seen by stationary observers. This is the case, for example, when the central body is a black hole. Then, we claim, the ratio

---

[4] Ryan calculates the phasing relation to 2PN order (i.e., to $O(v^4)$ past leading order). By extending Ryan's calculation to higher post-Newtonian orders, the terms omitted from Eq. (3.5) can be written explicitly.

$\dot{E}_{\infty\mathrm{BI}}/\dot{E}_{\mathrm{body}}$ is very small:

$$\frac{\dot{E}_{\infty\mathrm{BI}}}{\dot{E}_{\mathrm{body}}} \sim v^n \ll 1 \; , \tag{3.12}$$

where n is a large number, very likely 5. For LISA, almost all of the wave cycles used in extracting information from the waves will be from radii where $v \lesssim 0.5$ so $v^5 \lesssim 0.03$. For example, for a Kerr black hole, if the spin parameter is $a/M \lesssim 0.5$, then at the innermost stable circular orbit, $v \lesssim 0.5$. Consequently, almost all of the measured $\dot{E}_{\mathrm{total,BI}}$ will go into the body itself via tidal coupling, so $\dot{E}_{\mathrm{body}}$ will be measured to good accuracy.

To understand our claim that $\dot{E}_{\infty\mathrm{BI}}/\dot{E}_{\mathrm{body}} \sim v^n$ for some large n, consider a central body whose external metric is that of a Kerr black hole. In this case, one can use the Teukolsky formalism [21] (first-order perturbation theory in the mass ratio μ/M) to compute the energies radiated to infinity and tidally coupled into the central body. We have carried out that Teukolsky analysis for general a/M and present the details for the special case $a = 0$ in the appendix. Here we explain the underlying physics. We begin with some preliminaries:

We need only consider the primary-frequency waves, $f = \Omega_\phi/\pi$, since they account for all the energy loss and transfer, up to corrections second order in the eccentricity e and inclination angle ι. This means, correspondingly, that we can restrict ourselves to a precisely circular and equatorial orbit. The waves and tidal coupling then have predominantly spheroidal harmonic order $\ell = m = 2$ and frequency f (angular frequency $\omega = 2\pi f = 2\Omega_\phi$). Since we only want to know, to within factors of order unity, the ratio $\dot{E}_{\infty\mathrm{BI}}/\dot{E}_{\mathrm{body}}$, it will be sufficient to restrict ourselves to these dominant $\ell = m = 2$, $\omega = 2\Omega_\phi$ perturbations.

In the Teukolsky formalism, these perturbations are embodied in a radial "wave function" that can be normalized in a variety of different ways. The usual normalization, based on the Newman-Penrose field ψ_4, is bad for physical insight because it treats outgoing waves and ingoing waves quite differently; see the appendix. One normalization that treats them on the same footing sets the radial wave function equal to that of the tidal gravitational field ("electric-type" components of the Weyl or Riemann curvature tensor) measured by "zero-angular-momentum" observers, ZAMOs (a family of observers, each of whom resides at fixed radius r and polar angle θ). We shall denote that tidal field (with $e^{-i\omega t}$ × (spheroidal harmonic) factored out so the field is complex, not real) by $\mathcal{E}$. Another, closely related normalization for the radial wave function sets its modulus squared equal to the rate of flow of energy. We shall denote this choice by Ψ. At large radii, $\mathcal{E} \sim (\ddot{h}_+ + i\ddot{h}_\times) = \omega^2(h_+ + ih_\times)$, where h_+ and $h_\times$ are the dimensionless gravitational wave fields; so the radiated energy is $\dot{E}_\infty \sim r^2|\dot{h}_+ + i\dot{h}_\times|^2 \sim (r/\omega)^2\mathcal{E}_\infty^2$, which tells us that $\Psi_\infty \sim (r/\omega)\mathcal{E}_\infty$. Near the body's surface (i.e., near where the horizon would be if the body were a Kerr black hole), the energy flux is $\dot{E} \sim (r/\omega)^2|\alpha^2\mathcal{E}|^2$, where α is the Kerr-metric lapse function, which goes to zero at the horizon

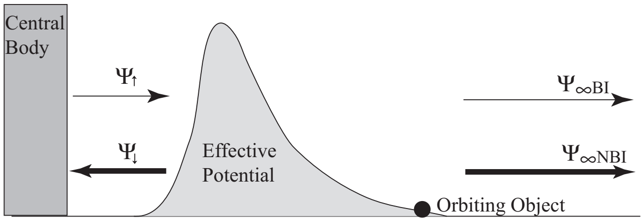

Figure 3.1: The renormalized tidal gravitational fields Ψ produced near a central body's surface and at large radii by the orbiting object, when the central body has the same exterior metric as a Kerr black hole.

radius. (The ZAMOs' divergently large outward speed, relative to infalling observers, causes them to see a divergently large tidal field; the factor α^2 corrects for that divergence; see, e.g., the discussion in Sec. VI.C.2 of [22].) Thus, in order to ensure that the power flow is the square of the renormalized radial wave function,

$$\dot{E} \sim |\Psi|^2 \, , \tag{3.13}$$

we must renormalize the ZAMO-measured tidal field $\mathcal{E}$ by

$$\begin{aligned} \Psi &\sim (r/\omega)\mathcal{E} \text{ at } r \to \infty \, , \\ \Psi &\sim (\alpha^2 r/\omega)\mathcal{E} \text{ near body} \, . \end{aligned} \tag{3.14}$$

With these preliminaries finished, we can give our physical argument for Eq. (3.12) in terms of the radial wave function Ψ. Our argument relies on Fig. 3.1.

If the central body is a Kerr black hole, then the boundary condition on Ψ at its surface (the horizon) is purely downgoing waves, and at infinity, purely outgoing waves. The ratio of downgoing power at the horizon to outgoing power at infinity has the standard Kerr values [23][24]: $\dot{E}_{\mathrm{body}}/\dot{E}_{\infty\mathrm{NBI}} \sim v^8$ if the hole's spin angular velocity Ω_H is much less than the orbital angular velocity Ω_ϕ; and $\dot{E}_{\mathrm{body}}/\dot{E}_{\infty\mathrm{NBI}} \sim v^5$ if $\Omega_H \gg \Omega_\phi$. (Here we have used the *no-body-influence* notation $\dot{E}_{\infty\mathrm{NBI}}$ for the outgoing power because a central black hole's internal structure is unable to influence the waves radiated to infinity.) Correspondingly, by virtue of Eq. (3.13), the ratio of the downgoing field at the horizon $\Psi_\downarrow$ to the outgoing field at infinity $\Psi_{\infty\mathrm{NBI}}$ is

$$\frac{\Psi_\downarrow}{\Psi_{\infty\mathrm{NBI}}} \sim \left\{ \begin{array}{c} v^4 \\ v^{5/2} \end{array} \right\} \text{ for } \left\{ \begin{array}{c} \Omega_H \ll \Omega_\phi \\ \Omega_H \gg \Omega_\phi \end{array} \right\} . \tag{3.15}$$

This suppression of the downgoing field relative to the outgoing is due, mathematically, to a reflective effective potential in the wave equation that Ψ satisfies (Fig. 3.1). Physically, it is due to coupling of the field Ψ to the central body's spacetime curvature.

Now suppose the central body is not a black hole, but some other object so compact that its surface is well beneath the peak of the effective potential. This mathematical assumption is equivalent to our physical assumption that the ZAMOs see the downgoing field $\Psi_\downarrow$ so strongly blue shifted by the central body's gravity that it looks like radiation. The only way, then, that the central body can influence the energy radiated to infinity is to reflect a portion of this downgoing radiation back upward. Mathematically, this corresponds to replacing the black hole's downgoing boundary condition by

$$\Psi_\uparrow = \mathcal{R}\psi_\downarrow, \tag{3.16}$$

at some chosen radius just above the body's surface. Here $\Psi_\downarrow$ and $\Psi_\uparrow$ are the downgoing and upgoing components of Ψ; see Fig. 3.1. For simplicity, we shall assume that the amplitude reflection coefficient $\mathcal{R}$ is small, $|\mathcal{R}| \ll 1$. Otherwise we would have to deal with a possible resonant buildup of energy between the reflective central body and the reflective effective potential — though that would not change our final answer (see, e.g., the more detailed analysis in the appendix).

The upgoing waves $\Psi_\uparrow$ have great difficulty getting through the effective potential. The fraction of the upgoing power that gets transmitted through, successfully, is $\sim (M\omega)^6$ if the hole rotates slowly, and $\sim (M\omega)^5$ if rapidly [Eq. (8.83) of [22] with $\ell = 2$ and $\sigma_\infty = \omega$]. Since the fields Ψ are the square roots of the powers (aside from complex phase) and since $M\omega = 2M\Omega_\phi = 2v^3$, this power transmissivity corresponds to

$$\frac{\Psi_{\infty\mathrm{BI}}}{\Psi_\uparrow} \sim \left\{ \begin{array}{c} v^9 \\ v^{15/2} \end{array} \right\} \text{ for } \left\{ \begin{array}{c} \Omega_H \ll \Omega_\phi \\ \Omega_H \gg \Omega_\phi \end{array} \right\} . \tag{3.17}$$

Combining Eqs. (3.17), (3.16), and (3.15), we see that

$$\frac{\Psi_{\infty\mathrm{BI}}}{\Psi_{\infty\mathrm{NBI}}} \sim \left\{ \begin{array}{c} v^{13} \\ v^{10} \end{array} \right\} \text{ for } \left\{ \begin{array}{c} \Omega_H \ll \Omega_\phi \\ \Omega_H \gg \Omega_\phi \end{array} \right\} . \tag{3.18}$$

If these two complex outgoing fields are not precisely out of phase with each other (phase difference $\pm\pi/2$), then the outgoing power is $|\Psi_{\infty\mathrm{NBI}} + \Psi_{\infty\mathrm{BI}}|^2 \simeq |\Psi_{\infty\mathrm{NBI}}|^2 + 2\Re\left(\Psi_{\infty\mathrm{NBI}}\Psi^*_{\infty\mathrm{BI}}\right)$, which means that the ratio of the radiated body-influenced power to radiated no-body-influence power is

$$\frac{\dot{E}_{\infty\mathrm{BI}}}{\dot{E}_{\infty\mathrm{NBI}}} \sim \left\{ \begin{array}{c} v^{13} \\ v^{10} \end{array} \right\} \text{ for } \left\{ \begin{array}{c} \Omega_H \ll \Omega_\phi \\ \Omega_H \gg \Omega_\phi \end{array} \right\} . \tag{3.19}$$

In the unlikely case (which we shall ignore) that the two fields are precisely out of phase, the ratio will be the square of this.

By combining Eq. (3.19) with the square of Eq. (3.15), we obtain the ratio of the body-influence power radiated to infinity over the tidal coupling power into the central body:

$$\dot{E}_{\infty \mathrm{BI}}/\dot{E}_{\mathrm{body}} \sim v^5 \tag{3.20}$$

independent of whether the body rotates slowly or rapidly. This is the claimed result.

If the central body's external metric is not Kerr, then the first-order perturbation equations for the orbiting body's spacetime curvature will probably not be separable in $\{r, \theta\}$, so the analysis will be much more complex. Nevertheless the physical situation presumably is unchanged in this sense: The body's spacetime curvature will couple to the perturbation field in such a way as to resist energy flow through the region between the body's surface and the object's orbit. Correspondingly, the perturbation fields and power flows are very likely to behave in the same manner as for the Kerr metric, with the same final result, $\dot{E}_{\mathrm{body}}/\dot{E}_{\infty \mathrm{BI}} \sim v^n$ with n very likely still 5 but possibly some other number significantly larger than one.

If this is, indeed, the case, then for any sufficiently compact central body the power tidally deposited into the body $\dot{E}_{\mathrm{body}}$ will be very nearly equal to $\dot{E}_{\mathrm{total},BI}$, which is measurable; and therefore the tidal power will be measurable.

3.4 Conclusion

In this paper, we have extended Ryan's analysis to show that in principle it is possible to recover not only the spacetime geometry of the central body, but also the evolving orbital parameters of the inspiraling object and the evolving tidal coupling between the small object and the central body. Therefore, in principle we can obtain a full description of the SARSAF spacetime, the tidal coupling, and the inspiral orbit from EMRI or IMRI waveforms. In practice, the method of extracting the information is likely to be quite different from the algorithm we have presented here.

Further generalizations of Ryan's theorem and development of practical methods to implement it are topics of our ongoing research.

3.5 Appendix: an Explicit Derivation of Results in Section 3.3.3

3.5.1 Teukolsky Perturbation Formalism

In this subsection, we use the Teukolsky perturbation theory to justify our results in Sec. 3.3.3. We first briefly review the standard Teukolsky perturbation formalism. Details can be found in, e.g., Ref. [25]. To shorten our expressions, in this appendix we restrict ourselves to a nonrotating central body with external metric the same as a Schwarzschild black hole but with a finite reflectivity. The generalization to the Kerr metric is straightforward but with more cumbersome algebra. We have carried it out, obtaining the same result as is found by the physical argument in the text.

In the Teukolsky formalism, people usually calculate the perturbation to a Newman-Penrose quantity ψ_4 that is related to the ZAMO-measured tidal field $\mathscr{E}$ by a linear transformation of the basis vectors. This ψ_4 can be decomposed into Fourier-Harmonic components according to

$$\psi_4 = \frac{1}{r^4}\int_{-\infty}^{\infty} d\omega \sum_{lm} R_{\omega lm}(r)\,{}_{-2}Y_{lm}(\theta,\phi)e^{-i\omega t}, \tag{3.21}$$

where ${}_{-2}Y_{lm}(\theta,\phi)$ are the spin-weighted spherical harmonics. The radial function $R_{\omega lm(r)}$ satisfies the inhomogeneous Teukolsky equation

$$\left[r^2\alpha^2\frac{d^2}{dr^2} - 2(r-M)\frac{d}{dr} + U(r)\right] R_{\omega lm}(r) = T_{\omega lm}, \tag{3.22}$$

where $\alpha^2 = 1 - 2M/r$ is the lapse function for the Schwarzschild metric. The expressions for the potential $U(r)$ and the source $T_{\omega lm}$ can be found in, e.g., Ref. [23], Eqs. (2.3), (A1).

In order to solve this equation, we construct two linearly independent solutions to the homogeneous Teukolsky equation, which satisfy the following boundary conditions,

$$\begin{aligned}
R^{\rm IN}_{\omega lm} &\to \begin{cases} (\omega r)^4\alpha^4 e^{-i\omega r^*}, & r \to 2M, \\ (\omega r)^{-1}Q^{\rm in}_{\omega lm}e^{-i\omega r^*} + (\omega r)^3 Q^{\rm out}_{\omega lm}e^{i\omega r^*}, & r \to +\infty, \end{cases} \\
R^{\rm UP}_{\omega lm} &\to \begin{cases} (\omega r)^4\alpha^4 P^{\rm out}_{\omega lm}e^{-i\omega r^*} + P^{\rm in}_{\omega lm}e^{i\omega r^*}, & r \to 2M, \\ (\omega r)^3 e^{i\omega r^*}, & r \to +\infty, \end{cases}
\end{aligned} \tag{3.23}$$

where $d/dr^* = \alpha^2 d/dr$. From these two homogeneous solutions, we can construct the inhomogeneous solution according to

$$\begin{aligned}
R_{\omega lm}(r) &= \frac{1}{{\rm Wronskian}[R^{\rm UP}_{\omega lm}, R^{\rm IN}_{\omega lm}]} \qquad (3.24)\\
&\times \left(R^{\rm UP}_{\omega lm}(r)\int_{2M}^{r} dr' R^{\rm IN}_{\omega lm}(r')\mathcal{T}_{\omega lm}(r') + R^{\rm IN}_{\omega lm}(r)\int_{r}^{\infty} dr' R^{\rm UP}_{\omega lm}(r')\mathcal{T}_{\omega lm}(r')\right),
\end{aligned}$$

where $\mathcal{T}_{\omega lm}(r) \equiv T_{\omega lm}(r)(r^2 - 2Mr)^{-2}$. This solution has only outgoing waves at infinity and satisfies the *purely ingoing boundary condition:* (Ref. [23], Eqs. (2.8) and (2.9))

$$\begin{aligned}
R_{\omega lm}(r\to\infty) &\sim \mu\omega^2 Z^{\rm IN}_{\omega lm} r^3 e^{i\omega r^*}, \\
R_{\omega lm}(r\to 2M) &\sim \mu\omega^3 Z^{\rm UP}_{\omega lm} r^4\alpha^4 e^{-i\omega r^*},
\end{aligned} \tag{3.25}$$

where

$$Z^{\mathrm{IN,UP}}_{\omega lm} = \frac{1}{2i\mu\omega^2 Q^{\mathrm{in}}_{\omega lm}} \times \int_{2M}^{\infty} dr \left[(r^2 - 2Mr)^{-2} R^{\mathrm{IN,UP}}_{\omega lm}(r) T_{\omega lm}(r)\right]. \tag{3.26}$$

At infinity, where the spacetime is almost flat, ψ_4 is directly related to the outgoing gravitational wave strains according to

$$\psi_4 = \frac{1}{2}\left(\ddot{h}_+ - i\ddot{h}_\times\right), \tag{3.27}$$

and we can obtain the luminosity formula (Ref. [23], Eq. (2.21))

$$\dot{E}_\infty = \frac{1}{4\pi}\left(\frac{\mu}{M}\right)^2 \sum_{lm} (M\omega)^2 |Z^{\mathrm{IN}}_{\omega lm}|^2. \tag{3.28}$$

3.5.2 Inner Boundary Condition

The above purely ingoing boundary condition makes sense when the central body is a black hole because we know everything is absorbed at the horizon of the black hole. If the central body is some other kind of object, the only way it can influence the perturbation field $R_{\omega lm}$ just above its surface is by producing an outgoing-wave component via some effective reflectivity $\mathcal{R}$. The result will be a modified field

$$R_{\omega lm}(r \to 2M) \sim e^{-i\omega r^*} + (\mathrm{something}) e^{i\omega r^*}. \tag{3.29}$$

The "something" will be proportional to $\mathcal{R}$, and it will also have a peculiar radial dependence because ψ_4 relies for its definition on an ingoing null tetrad and thereby treats ingoing and outgoing waves in very different manners.

3.5.3 Chandrasekhar Transform

To learn what the "something" should be, we can transform to a new radial wave function that treats ingoing and outgoing waves on the same footing. Two such functions were introduced and used in Sec. 3.3.3: the ZAMO-measured tidal field $\mathcal{E}$ and a field Ψ whose modulus squared is the power flow, for both outgoing and ingoing waves. Those choices are good for the physical, order-of-magnitude arguments, but at general radii r they not related in any simple way to ψ_4. A choice that *is* simply related to ψ_4 is the Regge-Wheeler function X, and we shall use it here.

The radial wave function R for the Newman-Penrose ψ_4 is related to the Regge-Wheeler function X by the Chandrasekhar transform, Eq. (A6) of Ref. [23]. This Chandrasekhar transform takes the form

$$R^{\mathrm{IN,UP}}_{\omega lm} = \chi^{\mathrm{IN,UP}}_{\omega lm} C_\omega X^{\mathrm{IN,UP}}_{\omega lm}, \tag{3.30}$$

where

$$\begin{aligned} \chi^{\mathrm{IN}}_{\omega lm} &= \frac{16(1-2iM\omega)(1-4iM\omega)(1+4iM\omega)}{(l-1)l(l+1)(l+2)-12iM\omega}(M\omega)^3, \\ \chi^{\mathrm{UP}}_{\omega lm} &= -\frac{1}{4}. \end{aligned} \tag{3.31}$$

C_ω is a second order differential operator, and $X^{\mathrm{IN,UP}}_{\omega lm}$ are two linearly independent solutions of the homogeneous Regge-Wheeler equation

$$\left[\frac{d^2}{dr^{*2}} + \omega^2 - V(r)\right] X_{\omega lm}(r) = 0, \tag{3.32}$$

where

$$V(r) = \alpha^2 \left[\frac{l(l-1)}{r^2} - \frac{6M}{r^3}\right]. \tag{3.33}$$

The asymptotic expressions for $X^{\mathrm{IN,UP}}_{\omega lm}$ are (Ref. [23], Eq. (2.7))

$$\begin{aligned} X^{\mathrm{IN}}_{\omega lm} &\to \begin{cases} e^{-i\omega r^*}, & r \to 2M, \\ A^{\mathrm{in}}_{\omega lm} e^{-i\omega r^*} + A^{\mathrm{out}}_{\omega lm} e^{i\omega r^*}, & r \to +\infty, \end{cases} \\ X^{\mathrm{UP}}_{\omega lm} &\to \begin{cases} -B^{\mathrm{out}}_{\omega lm} e^{-i\omega r^*} + B^{\mathrm{in}}_{\omega lm} e^{i\omega r^*}, & r \to 2M, \\ e^{i\omega r^*}, & r \to +\infty, \end{cases} \end{aligned} \tag{3.34}$$

Here we note that by the conservation of the Wronskian, it is straightforward to show that $B^{\mathrm{in,out}} = A^{\mathrm{in,out}}$.

3.5.4 $\dot{E}_\infty$ with a Reflective Inner Boundary Condition

Because the Regge-Wheeler function treats outgoing and ingoing waves on the same footing, the desired, reflective inner boundary condition for it takes the simple form

$$\tilde{X}^{\mathrm{IN}}_{\omega lm}(r \to 2M) \quad \sim \quad e^{-i\omega r^*} + \mathcal{R} e^{i\omega r^*}. \tag{3.35}$$

Here $\tilde{X}^{\mathrm{IN}}_{\omega lm}$ is a new homogeneous solution of the Regge-Wheeler equation.

This new homogeneous solution is a superposition of both ingoing and outgoing waves at the horizon. It is shown in Ref. [26] that because the Regge-Wheeler function treats outgoing and ingoing waves in the same manner, $|\mathcal{R}|^2$ has the physical meaning of the energy flux reflectivity, i.e., the ratio between outgoing and ingoing energy flux at the horizon.

The homogeneous solution (3.35), which satisfies the new inner boundary condition can be constructed from the old homogeneous solutions:

$$\tilde{X}^{\mathrm{IN}}_{\omega lm} = \beta_1 X^{\mathrm{IN}}_{\omega lm} + \beta_2 X^{\mathrm{UP}}_{\omega lm}, \tag{3.36}$$

where

$$\beta_1 = 1 + \frac{\mathcal{R} A^{\mathrm{out}}_{\omega lm}}{A^{\mathrm{in}}_{\omega lm}}, \qquad \beta_2 = \frac{\mathcal{R}}{A^{\mathrm{in}}_{\omega lm}}. \tag{3.37}$$

After doing an inverse Chandrasekhar transform, we obtain the corresponding homogeneous solution of the homogeneous Teukolsky equation

$$\tilde{R}^{\mathrm{IN}}_{\omega lm} = R^{\mathrm{IN}}_{\omega lm} + \frac{\beta_2}{\beta_1}\frac{\chi^{\mathrm{IN}}_{\omega lm}}{\chi^{\mathrm{UP}}_{\omega lm}} R^{\mathrm{UP}}_{\omega lm}. \tag{3.38}$$

Now we can replace R^{IN} by $\tilde{R}^{\mathrm{IN}}$ in Eq. (3.25) to obtain the solution $\tilde{R}_{\omega lm}(r)$, which satisfies the inhomogeneous Teukolsky equation with upgoing and downgoing waves at the horizon and purely outgoing waves at infinity. From this $\tilde{R}_{\omega lm}(r)$ we identify the new amplitudes $\tilde{Z}^{\mathrm{IN}}_{\omega lm}$ as in Eq. (3.25):

$$\tilde{Z}^{\mathrm{IN}}_{\omega lm} = Z^{\mathrm{IN}}_{\omega lm} + \frac{\beta_2}{\beta_1}\frac{\chi^{\mathrm{IN}}_{\omega lm}}{\chi^{\mathrm{UP}}_{\omega lm}} Z^{\mathrm{UP}}_{\omega lm}. \tag{3.39}$$

From these new $\tilde{Z}^{\mathrm{IN}}_{\omega lm}$ the calculation of the luminosity at infinity is straightforward.

In Ref. [23] Poisson and Sasaki have already worked out all the relevant formulae, so we only give the results. For the original expressions in Ref. [23], please refer to Eq. (3.25) for $A^{\mathrm{in}}, A^{\mathrm{out}}$, Eq. (A7) for $\chi^{\mathrm{IN}}, \chi^{\mathrm{UP}}$, Eqs. (5.4), (5.6), (5.11), (5.12) for $Z^{\mathrm{IN}}_{\omega lm}, Z^{\mathrm{UP}}_{\omega lm}$.

The leading luminosity correction comes from the $l = 2, m = \pm 2$ mode, and we have

$$\dot{E}_\infty = \dot{E}_\infty\Big|_{\mathrm{Schwarzschild}} \left|1 - \frac{128 i \mathcal{R} v^{13}}{15\beta_1}\right|^2, \tag{3.40}$$

where v is the same PN expansion parameter as that in Sec. 3.3.3. Unless the reflection coefficient $\mathcal{R}$ is precisely real, this gives

$$\dot{E}_\infty = \dot{E}_\infty\Big|_{\mathrm{Schwarzschild}} \left[1 + \frac{256}{15}\Im\left(\frac{\mathcal{R}}{\beta_1}\right), v^{13}\right] \tag{3.41}$$

in agreement with Eq. (3.19). The change in $\dot{E}_{\rm body}$ should be

$$\dot{E}_{\rm body} = \dot{E}_{\rm body}\Big|_{\rm Schwarzschild} \left(\frac{1-|\mathcal{R}|^2}{|\beta_1|^2}\right), \tag{3.42}$$

where β_1 is defined in Eq. (3.37).

3.6 Bibliography

[1] M. Colpi, S. L. Shapiro, and I. Wasserman, *Phys. Rev. Lett.* **57**, 2485 (1986).

[2] F. D. Ryan, *Phys. Rev. D* **55**, 6081 (1997).

[3] T. D. Lee, *Phys. Rev. D* **35**, 3637 (1987).

[4] D. Brown et al., submitted to Phys. Rev. Lett., URL `http://www.arxiv.org/gr-qc/0612060`.

[5] A. Abramovici et al., Science **256**, 325 (1992).

[6] F. D. Ryan, *Phys. Rev. D* **52**, 5707 (1995).

[7] K. S. Thorne, in *The Future of Theoretical Physics and Cosmology: Celebrating Stephen Hawking's 60th Birthday*, edited by G. W. Gibbons, S. J. Rankin, and E. P. S. Shellard (Cambridge University Press, 2003), pp. 74–104.

[8] T. Prince and K. Danzmann, Tech. Rep., LISA International Science Team, URL `http://www.rssd.esa.int/SYS/docs/ll_transfers/LISA_Science_Requirements.pdf`. (2007)

[9] C. Li, in preparation, (2008).

[10] J. R. Gair et al., *Class. Quant. Grav.* **21**, S1595 (2004).

[11] J. Gair and L. Wen, *Class. Quant. Grav.* **22**, S1359 (2005).

[12] D. Brown, in preparation, (2008).

[13] N. A. Collins and S. A. Hughes, *Phys. Rev. D* **69**, 124022 (2004).

[14] K. Glampedakis and S. Babak, *Class. Quant. Grav.* **23**, 4167 (2006).

[15] A. Stroeer, J. Gair, and A. Vecchio, in *Laser Interferometer Space Antenna: 6th International LISA Symposium*, edited by S. Merkowitz and J. C. Livas (2006), vol. 873 of *AIP Conference Proceedings*, p. 444.

[16] H. Fang and G. Lovelace, *Phys. Rev. D* **72**, 124016 (2005).

[17] R. M. Wald, *General Relativity* (University of Chicago Press, Chicago, 1984).

[18] R. Geroch, J. Math. Phys. **11**, 2580 (1970).

[19] R. Hansen, J. Math. Phys. **15**, 46 (1974).

[20] S. Drasco and S. A. Hughes, *Phys. Rev. D* **73**, 024027 (2006).

[21] S. A. Teukolsky, Astrophys. J. **185**, 635 (1973).

[22] K. S. Thorne, R. Price, and D. MacDonald, *Black Holes: The Membrane Paradigm* (Yale University Press, New Haven, 1986).

[23] E. Poisson and M. Sasaki, *Phys. Rev. D* **51**, 5753 (1995).

[24] H. Tagoshi, S. Mano, and E. Takasugi, Prog. Theor. Phys. **98**, 829 (1997).

[25] M. Sasaki and H. Tagoshi, *Living Rev. Relativity* **6** (2003), "Analytical Black Hole Perturbation Approach to Gravitational Radiation", URL `http://www.livingreviews.org/lrr-2003-6`.

[26] S. Chandrasekhar, *The Mathematical Theory of Black Holes* (Oxford University Press, Oxford, 1985), chap. 4, 9.

Chapter 4

Mapping Spacetime with Gravitational Waves from EMRIs: Generalization of Ryan's Theorem to Eccentric, Nearly Circular Orbits and to Generic Orbits

I consider the gravitational waves emitted by an EMRI, which consists of a small object orbiting around a massive body whose gravitational field is a SARSAF solution of the vacuum Einstein equations. The emitted gravitational waves depend on the central body's spacetime metric, which can be fully characterized by two families of multipole moments M_l and S_l, and on the moon's slowly evolving geodesic orbital parameters. Using action-angle variable theory, the KAM theorem in classical mechanics, and the results of numerical experiments, I give strong evidence that the coordinates of these geodesics as functions of the moon's proper time τ can be expanded into discrete Fourier series with four fundamental frequencies $(\Lambda_\rho, \Lambda_z, \Lambda_\phi, \Lambda_t)$. I also use a Green's function to show that, as functions of time t far from the EMRI, the emitted gravitational waveforms can also be expanded into Fourier series with three fundamental frequencies $(\Omega_\rho \equiv \Lambda_\rho/\Lambda_t, \Omega_z \equiv \Lambda_z/\Lambda_t, \Omega_\phi \equiv \Lambda_\phi/\Lambda_t)$. The evolution of these three frequencies and the evolution of the waveforms' harmonic amplitudes contain rich information about the metric of the central body and the orbital parameters of the moon. In particular, (one variant of) *Ryan's Theorem* [1] states that, for nearly circular, nearly equatorial orbits, a sequence of snapshots of the frequencies contains the full spacetime metric of the central body. In this paper I show that this is also true when the orbit is arbitrarily eccentric but still nearly equatorial, and I give an algorithm for extracting the map in this case — one that might, in fact, be practical. I also sketch two different routes by which a generalization to generic orbits might be achieved.

C. Li, paper in preparation.

4.1 Introduction and Overview

We are in an era when a network of broadband ground-based laser interferometers [the Laser Interferometer Gravitational Wave Observatory (LIGO), VIRGO, GEO600, TAMA][2], aimed at detecting high-frequency, astrophysical gravitational waves, has already operated for two years and is now being upgraded; and plans for the space-based, low-frequency Laser Interferometer Space Antenna (LISA) [3] are maturing. One of LISA's high-profile goals is *bothrodesy* — the black-hole analog of geodesy: use observed waveforms from extreme mass ratio inspirals (EMRIs) to measure the spacetime metric of a massive black hole orbited by a small object ("moon"), and compare the measured metric with that of Kerr. Thorne [2, 4] has argued since the early 1990s that it should be possible to extract details of the massive hole's metric from its EMRI waves, and the author and colleagues have recently shown that LIGO can likely also do so (though with far lower accuracy) using waves from intermediate mass ratio inspirals, IMRIs [5]. LISA and LIGO can not only measure the spacetime metrics of black holes, but can also search, via mapping, for other types of massive central bodies (e.g., hypothesized boson or soliton stars and naked singularities). Even if no such bodies exist, a search for them, will provide a way to place quantitative, high-precision observational limits on the black-hole "no-hair" theorem, which says that a black holes' spacetime metric is fully determined by its mass and spin angular momentum.

Extracting high-precision maps of the spacetime metric from LISA's EMRI waves is feasible because of bothrodesy's very high potential precision: in the last year of its inspiral, a stellar-mass object orbiting a (say) $10^6 M_\odot$ black hole emits roughly 200,000 cycles of waves, with a very rich, time-evolving harmonic and modulational structure. Because of the extreme mass ratio $\mu/M \sim 10^{-6}$, the inspiral is very slow and so the last year's waves are all emitted from the intense-gravity regime $r \lesssim 8M$ near the black-hole horizon [6]. With so many cycles, such rich structure, and such intense gravity, LISA is expected to have great power in exploring the spacetime metric.

Our confidence that this mapping is feasible is based largely on a theorem due to Fintan Ryan [1] (and its generalization by the author and Geoffrey Lovelace [7]). This theorem says that (under certain assumptions discussed below) the EMRI waves contain, encoded in themselves, the central body's full spacetime metric and full details of the evolving orbital parameters (and also details of the dissipative tidal coupling between the orbiting moon and central body [7] — though that will be irrelevant for the present paper). This theorem is also accomapnied by algorithms for extracting this information from the observed waveforms [1, 7]. A generalization to a massive body with electric charge and currents has been given by Sotiriou and Apostolatos [8].

Ryan's theorem [1, 7] relies on the following *idealizing assumptions:*

(i) The compact, massive central body has a vacuum, external gravitational field, which is Stationary and Axisymmetric (otherwise it presumably would emit gravitational waves until its asymmetries disappear), and also Reflection Symmetric across the equatorial plane and Asymptotically Flat (SARSAF). (In the unlikely case that it is nonrotating, a massive body's intense self-gravity presumably will have driven it into a spherical and thus axisymmetric shape.) Xanthopolous and others [9, 10] showed, in the 1970s, that there is a one-to-one correspondence between a SARSAF vacuum solution of the Einstein field equations and two families of scalar multipole moments [11, 12, 13]: the spacetime's "mass moments" $\{M_0, M_2, M_4, M_6, ...\}$ and its "current moments" $\{S_1, S_3, S_5, S_7, ...\}$. Therefore, to map the spacetime metric, we only need to determine these multipole moments from the observed gravitational waveforms.

(ii) The inspiraling moon is sufficiently compact and its mass is sufficiently small that the radiation reaction timescale is much longer than its orbital period. (This is reasonable for LISA since a mass ratio of $\mu/M \sim 10^{-6}$ is expected, but less so for LIGO where $\mu/M \approx 1/10$ to $1/100$.) This assumption allows us to make the usual adiabatic approximation so that the moon moves on geodesics of the central body and spirals from geodesic to geodesic on a timescale much longer than one orbital period.

(iii) The moon's orbit is nearly circular and nearly equatorial; i.e., it lies in the equatorial plane and is circular, plus has small radial and vertical perturbations.

These three assumptions enabled Ryan to show [Ref. [1] Eqs.(18)–(19)] that the spacetime's multipole moments, and hence its metric, can be extracted from the observed frequencies of the radial and vertical perturbations, expressed as functions of the slowly evolving fundamental orbital frequency. Ryan accompanied this theorem with algorithms for extracting the moments and hence the map of the body's metric from the observed waveforms.

Remarkably, Ryan's algorithms and his proof of his theorem did not require any substantial details of gravitational-wave-generation theory. Lovelace and I have shown [7] that if one is willing to invoke wave-generation theory, then from the time evolution of the waves' phase (or, equally well of their fundamental frequency), one can deduce full details of the dissipative tidal coupling between the moon and the central body. We also showed how to extract the time evolution of the orbital elements from the observed waveforms.

In this paper (Sec. 4.5), without using wave-generation theory I generalize Ryan's theorem and map-extracting algorithm to arbitrarily eccentric orbits. Unfortunately, my proof requires that the orbit remain nearly equatorial, with small vertical perturbations. In Sec. 4.4, I give strong evidence that, in order to relax my nearly equatorial assumption (in order to generalize Ryan to generic orbits), it will be necessary to rely on substantial details of wave-generation theory.

In my algorithm and theorem, (like Ryan) I avoid wave-generation theory by using only observables related to *gravitational-wave snapshots*, which do not depend on the rate, as a function of time, of the orbital inspiral and thus also do not depend on the dissipative tidal coupling between the central body and the moon. In the adiabatic approximation, these snapshots are emitted by the moon when it is moving on a fixed geodesic. I work out the multiperiodic functional forms of these snapshot waveforms explicitly in Sec.4.3. In Sec. 4.4 I discuss the extra dynamical evolution information contained in the rate at which the orbit evolves from one snapshot to another (the rate of orbital inspiral), and I discuss the crucial role that this extra information is likely to play in any generalization of Ryan's theorem to generic orbits.

In some realistic astrophysical situations, the orbits might have non-negligible eccentricity and inclination angle (e.g., Ref. [14]). For such situations, a generalization to generic orbits is much needed. However, when the massive central body has had a sufficiently dense accretion disk in the equatorial plane for a sufficiently long time in the past, Miller [15] suggests that the inclination angle might have been driven to near zero. Then we can apply the theorem of this paper and use its algorithm (Sec. 4.5.5) to map the spacetime geometry.

Phinney [16] has given evidence that a large fraction of LISA's EMRIs will have nearly circular orbits (in the sense of Keplerian orbits). Hence a generalization of Ryan's theorem to inclined, nearly circular orbits (in the sense of general relativity) might be more interesting than my generalization to eccentric, nearly equatorial orbits. *If the central body is a black hole,* then "near circularity" is well defined independent of the orbit's inclination to the equatorial plane; and for black holes, Phinney's evidence for near circularity is tied to a theorem that, under radiation reaction, eccentric inclined orbits circularize, and circular orbits (orbits of constant Boyer-Lindquist radius r) evolve into circular orbits. However, *in a general SARSAF spacetime*, for inclined orbits no such theorem is known and there is no obvious well-defined meaning for circularity; so it is not at all obvious how one would generalize Ryan's theorem to inclined, nearly circular orbits.

This paper is arranged as follows. In Sec. 4.2, I discuss geodesics in a SARSAF spacetime. I show that, if the Hamilton-Jacobi equation is completely separable (as is the case in some but not all such spacetimes), then the geodesics are multi-periodic functions of the geodesic's proper time τ. When the Hamilton-Jacobi equation is not separable (or we do not know if it is separable), then numerical integration of the geodesic equation [17] shows that the orbits are still multi-periodic, at least in all SARSAF spacetimes that have been studied and for orbits that are not too extremely small. This may be due to the KAM Theorem. These considerations provide strong evidence that geodesic orbits are multi-periodic in SARSAF spacetimes, and the remainder of the paper presumes this to be true. In Sec.4.3, I show that one can deduce the orbit's fundamental frequencies from gravitational-wave snapshots [Eq. (4.28)]. In Sec.4.4, I discuss some general issues related to the full generalization of Ryan's theorem (generalization to generic orbits). Most importantly, I show that any such generalization must involve details of wave-generation theory in SARSAF spacetimes that are not now in hand, and I suggest two routes by which the generic generalization might be carried out: one involving snapshots of the complex amplitudes of the waves' harmonics along with their three frequencies; the other involving the time evolutions of the waves' fundamental frequencies.

With all these preliminaries finished, in Sec. 4.5, I formulate and prove my generalization of Ryan's theorem for a moon that is in an eccentric but nearly equatorial orbit; and as the foundation for this generalization, I derive an algorithm for extracting the map carried by the waves. The basic idea underlying my proof and algorithm is as follows. For any generic multiperiodic geodesic orbit in a fixed SARSAF spacetime, the waves' three fundamental frequencies, Ω_ρ, Ω_z and Ω_ϕ [Eq. (4.28)] depend on the three orbital parameters p, e, and ι and on the spacetime's metric or multipole moments. However, when the orbit is nearly equatorial, the fundamental frequencies are *not* influenced by the orbital inclination angle ι (at first order in ι). As a result, the evolution of the *three* frequencies turns out to contain enough information to solve for the evolution of the *two* orbital elements p, e on which they depend, plus the spacetime's two families of multipole moments and thence its metric.

In Sec. 4.6, I summarize the paper's most important results.

This paper is a generalization of Ryan [1]; hence I use the same notations and geometric units ($G = c = 1$) as he.

4.2 Geodesics in SARSAF Spacetimes

As a foundation for extracting spacetime information from gravitational waves, we must understand some properties of an EMRI's gravitational waves. Because of the extreme mass ratio $\mu/M \sim 10^{-6}$, the EMRI's radiation reaction timescale is much longer than its orbital period, and correspondingly, the gravitational waves can be well described by the adiabatic approximation. Specifically, we can approximate the moon as moving along a geodesic of the central body. The moon's gravitational waves carry away orbital energy, causing the moon to spiral from one geodesic to another, with the timescale for substantial changes being much longer than one orbital period. Consequently, the emitted gravitational waves can be considered as a series of snapshots [18], with each corresponding to one geodesic.

Obviously the snapshot waveforms depend on the details of the geodesics, so we need to know some properties of the geodesics in SARSAF spacetimes before discussing wave generation. In this section, I discuss the multi-periodic properties of geodesics [Eqs. (4.8), (4.10) and (4.17)–(4.19)].

4.2.1 SARSAF Spacetime

As our starting point, I spell out the coordinates and spacetime metric that will be used throughout this paper.

I use so-called Weyl coordinates (ρ, z, ϕ, t), in which the stationary, axisymmetric spacetime metric takes the form

$$ds^2 = -F(dt - \omega d\phi)^2 + \frac{1}{F}[e^{2\gamma}(d\rho^2 + dz^2) + \rho^2 d\phi^2], \tag{4.1}$$

where F, ω, γ are functions of ρ and $|z|$. These functions are fully determined by the complex Ernst potential $\tilde{\mathcal{E}}$ (e.g., Refs. [13, 19, 20]). The explicit relations are (e.g., Refs. [1], Eqs.(20)–(22), (28))

$$\begin{aligned} F + i\psi &= \frac{\sqrt{\rho^2 + z^2} - \tilde{\mathcal{E}}}{\sqrt{\rho^2 + z^2} + \tilde{\mathcal{E}}}, \\ \gamma &= \frac{1}{4}\int_\rho^\infty \left[\frac{\rho'}{g_{tt}^2}\left(\frac{dg_{tt}}{d\rho'}\right)^2 - \frac{g_{tt}^2}{\rho'}\left(\frac{d(g_{t\phi}/g_{tt})}{d\rho'}\right)^2\right], \\ g_{tt} &= -F, g_{t\phi} = F\omega = -F\int_\rho^\infty \frac{\rho'}{F^2}\frac{\partial\psi}{\partial z}d\rho'\bigg|_{\text{constant z}}. \end{aligned} \tag{4.2}$$

The Ernst potential, which contains all the information about the spacetime geometry in a single complex function, can be expanded as (Ref. [13]. Eq. (15))

$$\tilde{\mathcal{E}} = \sum_{j,k=0}^{\infty} a_{jk}\frac{\rho^j z^k}{(\rho^2 + z^2)^{j+k}}. \tag{4.3}$$

The a_{jk} are nonzero only for non-negative, even j and non-negative k. Because of the reflection symmetry across the equatorial plane, a_{jk} is real for even k and imaginary for odd k. The Einstein field equation enforces the following recursion relation between these coefficients:

$$\begin{aligned} a_{r,s+2} &= \frac{1}{(s+2)(s+1)}\{-(r+2)^2 a_{r+2,s} \\ &+ \sum_{k,l,p,q} a_{kl}a^*_{r-k-p,s-l-q}[a_{pq}(p^2+q^2 \\ &-4p - 5q - 2pk - 2ql - 2) \\ &+a_{p+2,q-2}(p+2)(p+2-2k) \\ &+a_{p-2,q+2}(q+2)(q+1-2l)]\}. \end{aligned} \tag{4.4}$$

The sum is over all integer values of k, l, p and q that give nonzero contributions. If we know all the a_{j0} and a_{j1} for $j = 0, 2, \ldots, m$, then this recursion relation determines all a_{jk} for $j + k \leq m$.

Since the complex Ernst potential fully determines the spacetime metric, and the metric is also fully determined by the body's multipole moments, there must be relations between the coefficients a_{jk} and the moments. These relations, which have been worked out in Refs. [13, 1], have the general form (Ref. [1], Eq. (43))

$$\begin{aligned} a_{2n,0} &= (-1)^n \frac{(2n-1)!!}{(2n)!!} M_{2n} + \mathrm{LOM}, \\ a_{2n,1} &= i(-1)^n \frac{(2n+1)!!}{(2n)!!} S_{2n+1} + \mathrm{LOM}; \end{aligned} \tag{4.5}$$

here LOM means lower order multipole moments. Equivalently, there is a known algorithm in [13] (also in Ref. [1] Eqs.(36)–(41)) for computing the multipole moments from the coefficients a_{jk}.

To summarize, in order to extract the spacetime metric from an EMRI's gravitational waves, we only need to determine the coefficients a_{j0}, a_{j1} in the source's complex Ernst potential $\tilde{\mathcal{E}}$ from observations of gravitational-wave snapshots. From those coefficients we can compute both the spacetime metric and the spacetime multipole moments.

4.2.2 Geodesics in Completely Separable Spacetimes

In this subsection I use the phrase "completely separable spacetime" to denote any spacetime in which the Hamilton-Jacobi equation is completely separable in some coordinate system. In a completely separable spacetime, action-angle-variable theory can be used to show that the geodesics are multi-periodic with respect to the proper time τ. Below I sketch a derivation of this conclusion. Details can be found in Sec.10.7 of Ref. [21] and other standard textbooks such as [22, 23].

As a well-known fact, the geodesic equation for a moon's orbit can be derived from the Lagrangian $L = g_{\alpha\beta} u^\alpha u^\beta$, with the moon's proper time τ as the time parameter. Usually there are eight canonical variables, $(\rho, z, \phi, t, p_\rho, p_z, p_\phi, p_t)$. In a SARSAF spacetime, (ϕ, t) are cyclic coordinates so their corresponding canonical momenta (p_ϕ, p_t) are conserved. Therefore we can choose the usual energy and angular momentum as constants of motion and eliminate the following two velocities,

$$u^\phi = \frac{d\phi}{d\tau}, \qquad u^t = \frac{dt}{d\tau}. \tag{4.6}$$

In other words, we can reduce the solution of the geodesic equation to a two-dimensional problem with canonical variables (ρ, z, p_ρ, p_z) and two constants $(L \equiv p_\phi, E \equiv -p_t)$; cf., e.g., [24].

Since I assume the Hamilton-Jacobi equation is completely separable in some coordinates (X, Y) (not necessarily (ρ, z)), and the geodesic is bounded, there exist action-angle variables $(\omega_1, J_1), (\omega_2, J_2)$ with J_1, J_2 constants of motion and [Ref. [21], Eq. (10-106)]

$$\omega_1 = v_1 \tau + \beta_1, \quad \omega_2 = v_2 \tau + \beta_2. \tag{4.7}$$

Here τ is the moon's proper time, β_i are integral constants and v_i are frequencies related to the geodesic's periodic motion. Furthermore, as shown in Eq. (10-110) of Ref. [21], the canonical coordinates (X, Y) are biperiodic functions of (ω_1, ω_2), and their canonical momenta (P_X, P_Y) are also biperiodic functions of (ω_1, ω_2). Hence (ρ, z), which are related to (X, Y, P_X, P_Y) by some canonical transformation, are also biperiodic functions of (ω_1, ω_2) (Eq. (10-115) in [21]). Therefore, the motion of (ρ, z) can be Fourier decomposed as follows:

$$\begin{aligned} \rho(\tau) &= \sum_{mn} \rho_{mn} e^{i(m\Lambda_\rho + n\Lambda_z)\tau}, \\ z(\tau) &= \sum_{mn} z_{mn} e^{i(m\Lambda_\rho + n\Lambda_z)\tau}. \end{aligned} \tag{4.8}$$

Here we introduce the new symbols $(\Lambda_\rho \equiv v_1, \Lambda_z \equiv v_2)$ to emphasize that these two frequencies are related to the coordinates ρ and z.

As for the two cyclic coordinates (ϕ, t), it is easy to see that they are related to the energy and angular momentum by

$$\begin{aligned} \frac{dt}{d\tau} &= u^t = \frac{E g_{\phi\phi} + L g_{t\phi}}{g_{t\phi}^2 - g_{\phi\phi} g_{tt}}, \\ \frac{d\phi}{d\tau} &= u^\phi = -\frac{E g_{t\phi} + L g_{tt}}{g_{t\phi}^2 - g_{\phi\phi} g_{tt}}. \end{aligned} \tag{4.9}$$

The RHSs are biperiodic functions of (ω_1, ω_2), which means the RHSs can be decomposed into Fourier series similar to Eqs. (4.8). We can integrate out these Fourier series and express the results as

$$\begin{aligned} \phi(\tau) &= \Lambda_\phi \tau + \sum_{mn} \phi_{mn} e^{i(m\Lambda_\rho + n\Lambda_z)\tau}, \\ t(\tau) &= \Lambda_t \tau + \sum_{mn} t_{mn} e^{i(m\Lambda_\rho + n\Lambda_z)\tau}. \end{aligned} \tag{4.10}$$

Similar to Eq. (10-113) in Ref. [21], there are two parts in Eq. (4.10); one grows linearly with proper time, and the other is biperiodic.

In Eqs. (4.8) and (4.10) we see that the geodesics of a SARSAF spacetime are determined by four fundamental frequencies. In Sec.4.3, I will show that three combinations of them,

$$\Omega_\rho = \frac{\Lambda_\rho}{\Lambda_t}, \quad \Omega_z = \frac{\Lambda_z}{\Lambda_t}, \quad \Omega_\phi = \frac{\Lambda_\phi}{\Lambda_t}, \tag{4.11}$$

can be observed from the phase evolution of a gravitational wave snapshot.

4.2.3 Geodesics in Nonseparable Spacetimes and the KAM Theorem

The set of SARSAF spacetimes that are *known* to be fully separable (i.e., have Hamilton-Jacobi equations that are separable) is very small compared to all SARSAF spacetimes [25]. So in this section

I discuss geodesics in non-separable SARSAF spacetimes, i.e., spacetimes in which the Hamilton-Jacobi equation is not separable in any coordinate system.

In such spacetimes, the above action-angle variable theory is not applicable, and our knowledge of the properties of geodesics comes primarily from high-precision numerical integrations of the geodesic equations. These numerical integrations (restricted, of course, to a few specific SARSAF spacetimes) have revealed [26, 17] that there are both multi-periodic geodesics and chaotic geodesics; but in all cases studied thus far, the chaotic geodesics (if they exist at all) are confined to a tiny spatial region at very small radii, and there is evidence that they might never be accessible via radiation-reaction-induced inspiral from large radii [17].

The apparent multiperiodicity might be a result of the well-known Kolmogorov-Arnold-Moser (KAM) theorem (for example, Ref. [21] Sec.11.2), which deals with orbits in non-integrable Hamilton systems. The main idea of the KAM theorem is as follows. If we add a small perturbation H_ϵ to an integrable Hamiltonian H_0 so that the new Hamiltonian

$$H = H_0 + H_\epsilon, \tag{4.12}$$

is non-integrable, and if we further assume the perturbation is small and the fundamental frequencies ω_i of H_0 are incommensurate, then most of the orbits in H_0 continue to be multi-periodic; only a small fraction of the orbits become chaotic. As we increase the perturbation Hamiltonian H_ϵ, the fraction of chaotic orbits becomes larger.

If the spacetime is SARSAF but not fully separable, then at sufficiently large radii, it may be close enough to a fully separable spacetime (e.g., one of Carter's [25]) for the KAM theorem to apply. This could explain the multiperiodicity seen in all high-precision integrations carried out thus far [26, 17]. Alternatively, it might be that most or all SARSAF spacetimes have fully integrable geodesics (i.e., geodesics with four isolating integrals of the motion), except sometimes at extremely small radii; and, consequently, their geodesics are fully multi-periodic. Brink [24, 27] is exploring this possibility and thinks it likely to be true.

Throughout the rest of this paper I shall *assume* that the orbit of the EMRI I study spirals inward through geodesics that *are* multiperiodic, at least to the accuracy that LISA or LIGO can explore them via gravitational waves. It is very important to carry out further studies of this assumption.

In Sec. 4.3, I will discuss the gravitational waves emitted by the moon when it moves through these multi-periodic orbits.

4.2.4 Geodesic Described in Coordinate Time

In the above discussion, I investigated the geodesic equation in proper time τ. In this subsection, I describe the geodesics in coordinate time t, which is the time we measure at infinity (i.e. at Earth).

In Sec. 4.3, I will show that the geodesics' fundamental frequencies with respect to coordinate time are among LISA's and LIGO's physical observables.

The following argument parallels that of Drasco and Hughes [28], who discussed the same problem assuming the central body to be a Kerr black hole.

The Fourier transform of $\rho(t)$ is

$$\begin{aligned}\rho(\omega) &= \int \rho(t)e^{i\omega t}dt = \int \rho(\tau)e^{i\omega t(\tau)}\frac{dt}{d\tau}d\tau \\ &= \int e^{i\omega\Lambda_t\tau}\left(\rho(\tau)e^{i\omega(t(\tau)-\Lambda_t\tau)}\frac{dt}{d\tau}\right)d\tau. \end{aligned} \tag{4.13}$$

To simplify this expression, we note that the expression in the big bracket is a biperiodic function with two fundamental frequencies Λ_ρ, Λ_z, so it can be decomposed as

$$\left(\rho(\tau)e^{i\omega(t(\tau)-\Lambda_t\tau)}\frac{dt}{d\tau}\right) = \sum_{mn} f_{mn}e^{i(m\Lambda_\rho+n\Lambda_z)\tau}. \tag{4.14}$$

Hence

$$\begin{aligned}\rho(\omega) &= \int e^{i\omega\Lambda_t\tau}\sum_{mn} f_{mn}e^{i(m\Lambda_\rho+n\Lambda_z)\tau}d\tau \\ &= \sum_{mn} f'_{mn}\delta(\omega - m\Omega_\rho - n\Omega_z), \end{aligned} \tag{4.15}$$

where

$$\Omega_\rho = \Lambda_\rho/\Lambda_t, \Omega_z = \Lambda_z/\Lambda_t. \tag{4.16}$$

This shows that the Fourier transform of $\rho(t)$ has a discrete spectrum; it therefore can be expanded in a Fourier series as

$$\rho(t) = \sum_{mn} \rho_{mn}e^{i(m\Omega_\rho+n\Omega_z)t}. \tag{4.17}$$

Following the same argument, the z-motion can be written in coordinate time as

$$z(t) = \sum_{mn} z_{mn}e^{i(m\Omega_\rho+n\Omega_z)t}. \tag{4.18}$$

As for the ϕ-motion, using the fact that $\phi(t) - \Omega_\phi t$ is biperiodic, it is easy to derive the following Fourier-expansion expression:

$$\phi(t) = \Omega_\phi t + \sum_{mn} \phi_{mn}e^{i(m\Omega_\rho+n\Omega_z)t}, \tag{4.19}$$

where

$$\Omega_\phi = \Lambda_\phi / \Lambda_t. \tag{4.20}$$

Therefore we see that the geodesic is multi-periodic with respect to coordinate time t, with frequencies $\Omega_\rho, \Omega_z, \Omega_\phi$.

4.3 Gravitational-Wave Snapshots in SARSAF Spacetimes

In this section I show that the fundamental frequencies $(\Omega_\rho, \Omega_z, \Omega_\phi)$ can be extracted from the phase evolution of the gravitational waves. Therefore, these frequencies are observables, when one monitors the EMRI gravitational wave snapshots with high precision. When the central body is a Kerr black hole, this conclusion is well known; e.g., [28]. The following argument has been suggested by Mino [29].

Because of the extreme mass ratio, we can approximate the moon as the source of the gravitational waves, and we can use a Green's function to calculate the waves. Let us denote by $(\rho_0, z_0, \phi_0, t_0)$ the coordinates of the gravitational wave detector, and by (ρ', z', ϕ', t') the coordinates of the source (the moon), and by $G(\rho_0, \rho', z_0, z', \phi_0, \phi', t_0, t')$ the waves' radiative Green's function in the central body's SARSAF spacetime. By virtue of the spacetime's rotational symmetry and time translational symmetry, the radiative Green's function can be decomposed as follows,

$$\begin{aligned} G^{\alpha\beta\mu\nu} &= \int d\omega \sum_m \\ &\quad \times G_m^{\alpha\beta\mu\nu}(\rho_0, \rho', z_0, z') e^{im(\phi_0 - \phi')} e^{i\omega(t_0 - t')}. \end{aligned} \tag{4.21}$$

The source term is

$$T^{\mu\nu} = \int d\tau \frac{\mu}{\sqrt{-g}} \frac{dx'^\mu}{d\tau} \frac{dx'^\nu}{d\tau} \delta(x' - x(\tau)), \tag{4.22}$$

where $x'^\mu = (\rho', z', \phi', t')$, $g = \det(g_{\alpha\beta})$ and

$$\begin{aligned} &\delta(x' - x(\tau)) \\ =\ &\delta(\rho' - \rho(\tau))\delta(\phi' - \phi(\tau))\delta(z' - z(\tau))\delta(t' - t(\tau)). \end{aligned} \tag{4.23}$$

Here $\rho(\tau), \phi(\tau), z(\tau), t(\tau)$ are the multiperiodic functions given in Eqs. (4.8) and (4.10). From the

Green's function and the source term, the observed gravitational wave snapshots must be

$$\begin{aligned}
& h^{\alpha\beta}(\rho_0, z_0, \phi_0, t_0) \\
= & \int dV' \int d\omega \sqrt{-g} \sum_m G_m^{\alpha\beta\mu\nu}(\rho_0, \rho', z_0, z') \\
\times & \ e^{im(\phi_0-\phi')+i\omega(t_0-t')} \int d\tau \frac{\mu}{\sqrt{-g}} \frac{dx'^\mu}{d\tau} \frac{dx'^\nu}{d\tau} \\
\times & \ \delta(\rho' - \rho(\tau))\delta(\phi' - \phi(\tau))\delta(z' - z(\tau))\delta(t' - t(\tau)) \\
= & \int d\omega d\tau \sum_m e^{im(\phi_0-\Lambda_\phi \tau)+i\omega(t_0-\Lambda_t \tau)} H_m^{\alpha\beta}(\tau),
\end{aligned} \tag{4.24}$$

where

$$\begin{aligned}
H_m^{\alpha\beta}(\tau) = \mu \frac{dx^\mu}{d\tau} \frac{dx^\nu}{d\tau} & G_m^{\alpha\beta\mu\nu}(\rho_0, \rho(\tau), z_0, z(\tau)) \\
& \times e^{im(\Lambda_\phi \tau - \phi(\tau))+i\omega(\Lambda_t \tau - t(\tau))}.
\end{aligned} \tag{4.25}$$

From Eqs. (4.8), (4.10) and (4.25) we see that $H_m^{\alpha\beta}(\tau)$ are biperiodic functions with two fundamental frequencies Λ_ρ, Λ_z. Therefore, we can expand $H_m^{\alpha\beta}$ in a Fourier series as

$$H_m^{\alpha\beta}(\tau) = \sum_{n,l} \mathcal{H}_{mnl}^{\alpha\beta} e^{-in\Lambda_\rho \tau - il\Lambda_z \tau}. \tag{4.26}$$

From Eqs. (4.24) and (4.26) we have

$$\begin{aligned}
& h^{\alpha\beta}(\rho_0, z_0, \phi_0, t_0) \\
= & \int d\omega d\tau \sum_{mnl} \mathcal{H}_{mnl}^{\alpha\beta} e^{im(\phi_0-\Lambda_\phi \tau)+i\omega(t_0-\Lambda_t \tau)-in\Lambda_\rho \tau - il\Lambda_z \tau} \\
= & \int d\omega \sum_{mnl} h_{mnl}^{\alpha\beta} \delta(\omega + m\Omega_\phi + n\Omega_\rho + l\Omega_z) e^{im\phi_0 + i\omega t_0} \\
= & \sum_{mnl} h_{mnl}^{\alpha\beta} e^{im\phi_0 - i(m\Omega_\phi + n\Omega_\rho + l\Omega_z)t_0},
\end{aligned} \tag{4.27}$$

where $\Omega_\rho, \Omega_z, \Omega_\phi$ are defined in Eqs. (4.16) and (4.20), and $h_{mnl}^{\alpha\beta} = 2\pi \mathcal{H}_{mnl}^{\alpha\beta}/\Lambda_t$.

If we absorb the constant phase factors $e^{im\phi_0}$ into the amplitudes $h_{mnl}^{\alpha\beta}$, the gravitational wave snapshots can be written as

$$h^{\alpha\beta}(t_0) = \sum h_{mnl}^{\alpha\beta} e^{-i(m\Omega_\phi + n\Omega_\rho + l\Omega_z)t_0}. \tag{4.28}$$

Thus, we can read out $\Omega_\rho, \Omega_\phi, \Omega_z$ from the phase evolution of gravitational wave snapshots. This nice phase property allows the possibility to extract the central body's metric from EMRI gravitational waves observed by LISA and LIGO.

4.4 Strategies for Generalizing Ryan's Theorem to Generic Orbits

In this section, I discuss possible ways of generalizing Ryan's theorem on the possibility to extract the orbital parameters and the central body's spacetime metric from an EMRI's gravitational waves.

For a generic orbit, the multi-periodic form of a gravitational-wave snapshot is given by Eq. (4.28). It is determined by three fundamental frequencies $\Omega_\rho, \Omega_z, \Omega_\phi$ and by complex amplitudes $h^{\alpha\beta}_{mnl}$ for the various harmonics of these frequencies. These are snapshot-dependent constants, i.e., they are constants when the moon is in a specific geodesic, and they change values as the moon moves from one geodesic to another. These snapshot-dependent constants and their slow time evolutions are our gravitational-wave observables.

First, let us consider what we can learn if we only observe the waves' phase evolution. From this, we can obtain the three fundamental frequencies $(\Omega_\rho, \Omega_z, \Omega_\phi)$ for each snapshot. I will argue below that if the geodesic is both inclined and eccentric, then we *cannot* deduce the spacetime metric from a sequence of snapshots of these fundamental frequencies. The reason is as follows. The fundamental frequencies depend on both the spacetime metric and the orbital parameters. Assume we have obtained N snapshots and therefore $3N$ items of data. For each snapshot, there are 3 unknown orbital parameters (the semi-latus rectum p, the eccentricity e and the inclination angle ι). Therefore we have $3N$ unknown orbital parameters plus an infinite number of unknown parameters for the spacetime metric. Hence, the number of unknown parameters is far larger than the number of observed variables and we can not do anything without further information.

This does not contradict Ryan's theorem [1], because Ryan restricted himself to orbits that are nearly circular and nearly equatorial, and he showed that in this case, to leading order in the orbit's small perturbations (vertical and/or radial), the three frequencies only depend on the radius of the underlying circular equatorial orbit. In this case, N snapshots give $3N$ items of information, from which (at least in principle) one can solve for the N unknown values of the orbital radius, plus the spacetime's $2N$ lowest-order moments. For details and a parameter-extraction algorithm, see Ryan's paper [1].

In Sec. 4.5 we shall generalize Ryan's argument to nearly equatorial but significantly eccentric orbits. In this case, the three fundamental frequencies depend on two parameters: the orbit's semi-latus rectum p and eccentricity e. Therefore, from the $3N$ measured values of fundamental frequencies, obtained in N snapshot wave measurements, we can extract the N unknown values of p, the N unknown values of e, and the first N multipole moments. This is the basis for an information-extraction algorithm worked out in Sec. 4.5

If we do not place any restrictions on the orbits, then to extract the central body's spacetime metric, we must make use of additional information beyond measured snapshot values of the three fundamental frequencies. There are two possibilities:

First, we can use measured snapshot values of the complex amplitudes $h^{\alpha\beta}_{mnl}$. (An example of this has been given in Fig. 9 of Finn and Thorne [6]. There the central body was assumed to be a Kerr black hole, the orbit was assumed precisely equatorial and circular, and it was shown that the orbital radius and the black-hole spin can be obtained from snapshot values of the ratios h_1/h_2 and h_3/h_2. See also Drasco's [30] exploration of the harmonics' amplitudes for generic orbits around Kerr black holes.) The complex amplitudes are governed by the details of snapshot gravitational-wave generation (whereas the fundamental frequencies rely only on the details of geodesics). Wave-generation theory has been worked out in full detail for the Kerr metric, but not yet for general SARSAF spacetimes. Therefore, generalizing Ryan in this complex-amplitude direction must await the development of SARSAF wave-generation theory.

The second way we might generalize Ryan to generic orbits is to augment the measured snapshot values of the fundamental frequencies $\Omega_\rho, \Omega_z, \Omega_\phi$ with the details of how they evolve as functions of time. That time evolution is governed, of course, by gravitational-radiation reaction, which in turn depends on the details of wave generation. The radiation reaction is sensitive to the rate at which energy and angular momentum are exchanged with the central body via tidal coupling. (This is the basis for an algorithm that Lovelace and I have given for measuring the tidal coupling when the orbit is nearly circular and equatorial [7].) Therefore, to implement this time-evolution generalization to generic orbits, it will be necessary to work out the details of wave generation and radiation reaction in SARSAF spacetimes, and either solve for the details of dissipative tidal coupling along with the metric, or else make assumptions about the physical nature of the central body and thence about the tidal coupling. (The complex-amplitude method of generalizing to generic orbits, discussed above, will also be sensitive to tidal coupling, or more precisely to boundary conditions at the central body; but I expect it to be much less sensitive than the time-evolution generalization.)

In summary, I have argued that in order to generalize Ryan's theorem, we must make one of two choices

1. Retain one restriction on the orbits—e.g., require them to be nearly equatorial; or
2. Remove all orbital restrictions, and make use of additional observational data that can be interpreted only after we understand the details of gravitational-wave generation in general SARSAF spacetimes.

In Sec. 4.5, I will present an algorithm following the first choice.

4.5 Generalizing Ryan's Theorem to Eccentric, Nearly Equatorial Orbits

The map-extraction algorithm underlying Ryan's theorem relies on the assumption that the orbit is nearly equatorial and nearly circular. In this section I shall show how we can lift the restriction of near circularity; i.e., I shall sketch an algorithm for extracting the nearly equatorial orbit's semi-latus rectum p and eccentricity e, and the central body's spacetime metric (or equivalently multipole moments) from snapshot-waveform values of the three fundamental frequencies $(\Omega_\rho, \Omega_\phi, \Omega_z)$.

As foundations for my algorithm, in Sec. 4.5.1, I will describe, mathematically, an eccentric, precisely equatorial orbit; in Sec. 4.5.2, I will analyze vertical perturbations of such an orbit; in Sec. 4.5.3, I will develop a procedure for computing the three fundamental frequencies of a vertically perturbed orbit in terms of its semi-latus rectum p and eccentricity e and the spacetime's multipole moments; and in Sec. 4.5.4, I will develop an *approximate* formula for the three fundamental frequencies in terms of p, e, the lowest $N+1$ mass moments, and the lowest N current moments. Then in Sec. 4.5.5, I will use this approximate formula to formulate an iterative procedure, that may well turn out to be practical, for extracting p, e, and the moments from a sequence of snapshot values of the three fundamental frequencies.

4.5.1 Eccentric, Precisely Equatorial Orbit

In this subsection, as a first foundation for my algorithm, I discuss unperturbed, precisely equatorial, geodesic orbits; in the next subsection I will add perturbations in the vertical, z direction.

Assuming the orbit to be in the equatorial plane, we have three nonvanishing velocities

$$u^\rho = \frac{d\rho}{d\tau}, \quad u^\phi = \frac{d\phi}{d\tau}, \quad u^t = \frac{dt}{d\tau}. \tag{4.29}$$

Here τ is the proper time of the moon along the geodesic. Because of the SARSAF symmetries, there are three isolating integrals of the motion: energy, angular momentum and the norm of the 4-velocity,

$$\begin{aligned} E &= -g_{tt}u^t - g_{t\phi}u^\phi, \quad L = g_{t\phi}u^t + g_{\phi\phi}u^\phi, \\ -1 &= g_{tt}(u^t)^2 + 2g_{t\phi}u^t u^\phi + g_{\phi\phi}(u^\phi)^2 + g_{\rho\rho}(u^\rho)^2. \end{aligned} \tag{4.30}$$

From these equations we obtain

$$\begin{aligned} u^t &= \frac{Eg_{\phi\phi}+Lg_{t\phi}}{g_{t\phi}^2-g_{\phi\phi}g_{tt}}, \quad u^\phi = -\frac{Eg_{t\phi}+Lg_{tt}}{g_{t\phi}^2-g_{\phi\phi}g_{tt}}, \\ (u^\rho)^2 &= \frac{E^2g_{\phi\phi}+2ELg_{t\phi}-g_{t\phi}^2+L^2g_{tt}+g_{\phi\phi}g_{tt}}{g_{\rho\rho}(g_{t\phi}^2-g_{tt}g_{\phi\phi})}. \end{aligned} \tag{4.31}$$

Similar to what we have done in Sec.4.2.2, the solution to this equatorial geodesic equation can be written as

$$\begin{aligned} \rho(\tau) &= \sum_n \rho_n e^{in\Lambda_\rho\tau}, \quad \phi(\tau) = \Lambda_\phi\tau + \sum_n \phi_n e^{in\Lambda_\rho\tau}, \\ t(\tau) &= \Lambda_t\tau + \sum_n t_n e^{in\Lambda_\rho\tau}, \end{aligned} \tag{4.32}$$

where

$$\begin{aligned} T_\rho &\equiv \oint d\tau, \qquad \Lambda_\rho \equiv \frac{2\pi}{T_\rho}, \\ \Lambda_\phi &= \frac{1}{T_\rho}\oint u^\phi d\tau, \quad \Lambda_t = \frac{1}{T_\rho}\oint u^t d\tau; \end{aligned} \tag{4.33}$$

here $\oint$ means integration over a complete radial cycle, i.e, from the perihelion to the aphelion and back to the perihelion.

4.5.2 Nearly Equatorial Orbit

In this subsection, I analyze a nearly equatorial orbit with a perturbation in the z direction.

Since the orbit is nearly but not precisely equatorial, the three fundamental frequencies $\Omega_z, \Omega_\rho, \Omega_\phi$ will all show up in the phase evolution of a gravitational-wave snapshot. Below I argue that these fundamental frequencies will not depend on the inclination angle ι to first order in the vertical perturbation.

These frequencies will evolve as the orbit evolves. This evolution might carry one or another of them through zero (e.g. for a circular equatorial orbit, frame dragging can drive the orbit from retrograde to prograde as it shrinks, causing Ω_ϕ to pass from negative through zero to positive). However, almost all of the time, all three frequencies should be well away from zero, and we shall restrict our analysis to such times. Then the snapshot values of the frequencies will have finite values plus corrections quadratic in ι, which we shall ignore.

Therefore, when we include first-order perturbations in the vertical direction, the three frequencies only depend on the semi-latus rectum p and eccentricity e. Below I will give a routine derivation of this result again, during which I will work out all the mathematical details.

In analyzing a vertically perturbed, geodesic orbit, I start from the standard geodesic equation for z motion (in Weyl coordinates (4.1), $g_{\rho\rho} = g_{zz}$):

$$\frac{d^2z}{d\tau^2} + \Gamma^z_{ab} u^a u^b = 0, \tag{4.34}$$

where

$$\begin{aligned}
\Gamma^z_{\rho\rho} &= -\frac{1}{2} g^{\rho\rho} g_{\rho\rho,z}, \Gamma^z_{zz} = \frac{1}{2} g^{\rho\rho} g_{\rho\rho,z}, \\
\Gamma^z_{\rho z} &= \frac{1}{2} g^{\rho\rho} g_{\rho\rho,\rho}, \Gamma^z_{tt} = -\frac{1}{2} g^{\rho\rho} g_{tt,z}, \\
\Gamma^z_{t\phi} &= -\frac{1}{2} g^{\rho\rho} g_{t\phi,z}, \Gamma^z_{\phi\phi} = -\frac{1}{2} g^{\rho\rho} g_{\phi\phi,z}.
\end{aligned} \tag{4.35}$$

Multiplied by $g_{\rho\rho}$, this geodesic equation can be written as

$$\begin{aligned}
0 \quad &= g_{\rho\rho} \frac{d^2z}{d\tau^2} + \frac{1}{2} g_{\rho\rho,z} (u^z)^2 + g_{\rho\rho,\rho} u^\rho u^z \\
- \quad &\frac{1}{2} \left[g_{\rho\rho,z} (u^\rho)^2 + g_{tt,z} (u^t)^2 + g_{\phi\phi,z} (u^\phi)^2 + 2 g_{t\phi,z} u^t u^\phi \right].
\end{aligned} \tag{4.36}$$

Assuming that the orbit is nearly equatorial and its z motion is small, I expand the metric $g_{\alpha\beta}$ around $z = 0$ and keep terms up to z^2. (Reflection symmetry across the equatorial plane kills the terms that are linear in z.) After making this approximation, we have

$$g_{\alpha\beta,z} = \left[\frac{d^2 g_{\alpha\beta}}{dz^2} (\rho, z = 0) \right] z, \tag{4.37}$$

for all the metric z-derivatives. Therefore we can neglect the $g_{\rho\rho,z}(u^z)^2/2$ term and substitute the unperturbed, equatorial versions of u^ρ, u^t, u^ϕ into Eq. (4.36). This leads to the following first-order version of Eq. (4.36):

$$\mathcal{F}_1(\rho) \frac{d^2z}{d\tau^2} + \mathcal{F}_{1,\rho}(\rho) u^\rho u^z + \mathcal{F}_2(\rho) z = 0, \tag{4.38}$$

where

$$\begin{aligned}
\mathcal{F}_1(\rho) &= g_{\rho\rho}(\rho, z = 0), \\
\mathcal{F}_2(\rho) &= -\frac{1}{2} [g_{\rho\rho,zz} (u^\rho)^2 + g_{tt,zz} (u^t)^2 \\
&\qquad + g_{\phi\phi,zz} (u^\phi)^2 + 2 g_{t\phi,zz} u^t u^\phi]|_{z=0}.
\end{aligned} \tag{4.39}$$

Multiplying Eq. (4.38) by $g^{\rho\rho}(\rho, z = 0)$ we obtain the simpler equation

$$\frac{d^2z}{d\tau^2} + \mathcal{K}_1(\rho(\tau)) \frac{dz}{d\tau} + \mathcal{K}_2(\rho(\tau)) z = 0, \tag{4.40}$$

where

$$\mathcal{K}_1(\rho(\tau)) = \frac{\mathcal{F}_{1,\rho}(\rho)u^\rho}{\mathcal{F}_1(\rho)}, \quad \mathcal{K}_2(\rho(\tau)) = \frac{\mathcal{F}_2(\rho)}{\mathcal{F}_1(\rho)}. \tag{4.41}$$

Since ρ is periodic in τ, so are $\mathcal{K}_1$ and $\mathcal{K}_2$:

$$\mathcal{K}_1(\rho) = \sum_n K_{1n} e^{in\Lambda_\rho \tau}, \quad \mathcal{K}_2(\rho) = \sum_n K_{2n} e^{in\Lambda_\rho \tau}. \tag{4.42}$$

Since the geodesic is assumed to be multi-periodic, its z motion can be expressed as as

$$z(\tau) = \sum_{mn} z_{mn} e^{i(m\Lambda_\rho + n\Lambda_z)\tau}. \tag{4.43}$$

By plugging this expression into the equation of motion (4.40), we obtain

$$\sum_{mn} G_{mn}(z_{mn}, \Lambda_z) e^{i(m\Lambda_\rho + n\Lambda_z)\tau} = 0, \tag{4.44}$$

where

$$\begin{aligned} G_{mn} &= z_{mn}(m\Lambda_\rho + n\Lambda_z)^2 \\ &+ \sum_{p+q=m} K_{1p} i(q\Lambda_\rho + n\Lambda_z) z_{qn} + \sum_{p+q=m} K_{2p} z_{qn}. \end{aligned} \tag{4.45}$$

This equation can be satisfied for all times τ if and only if

$$G_{mn}(z_{qn}, \Lambda_z) = 0 \tag{4.46}$$

for all m, n. These equations determine the coefficients z_{qn} and the frequency Λ_z. They are linear and homogeneous with respect to z_{qn}; therefore, in order to have a solution, the determinant of the matrix of coefficients of the z_{qn} must vanish. This zero-determinant condition determines Λ_z.

We cannot evaluate the determinant of an infinite square matrix, so we need to put some cutoff on the indices q, n. I implement the cutoff by assuming that

$$z_{qn} \neq 0, \text{ only for } |q| + |n| < N, \tag{4.47}$$

where N is a positive integer number. This cutoff will give us a finite number of linear, homogeneous equations for the nonvanishing z_{qn}. Let us denote the determinant of the finite-dimensional square matrix of coefficients by Det_N; then from

$$\mathrm{Det}_N = 0, \tag{4.48}$$

we can obtain an approximate expression for Λ_z, which I denote by $\Lambda_{z,N}$. As we increase N, we will obtain better and better approximate expressions for Λ_z.

In conclusion, by assuming the multi-periodic, geodesic orbit is nearly equatorial, we obtain the following expressions for the three frequencies, which show up in the phase evolution of each gravitational-wave snapshot:

$$\Omega_\rho = \frac{\Lambda_\rho}{\Lambda_t}, \quad \Omega_z = \frac{\Lambda_z}{\Lambda_t}, \quad \Omega_\phi = \frac{\Lambda_\phi}{\Lambda_t}, \tag{4.49}$$

where

$$\begin{aligned} T_\rho &\equiv \oint d\tau, \qquad \Lambda_\rho \equiv \frac{2\pi}{T_\rho}, \quad \Lambda_\phi = \frac{1}{T_\rho}\oint u^\phi d\tau, \\ \Lambda_t &= \frac{1}{T_\rho}\oint u^t d\tau, \quad \Lambda_z = \Lambda_{z,N}, \end{aligned} \tag{4.50}$$

and the integration is over one full radial cycle. Here the expression for Λ_z depends on the cutoff number N.

If the orbits are nearly equatorial and nearly circular, Eq. (4.50) will degenerate to Ryan's formulae, Eqs. (9) and (14) of Ref. [1].

4.5.3 Fundamental Frequencies as Functions of p, e, and Multipole Moments

In this subsection I use the results of previous subsections to construct an algorithm by which a nearly equatorial orbit's fundamental frequencies Ω_ϕ, Ω_ρ, Ω_z can be computed as explicit functions of the orbit's semi-latus rectum p and eccentricity e, and the central body's multipole moments.

As a preparation, I recall the definitions of p and e (e.g., [31]): If the radial coordinate ρ is parametrized in the Newtonian-like way

$$\rho = \frac{p}{1 + e\cos\chi}, \tag{4.51}$$

then the orbit's aphelion and perihelion occur at $\chi = 0, \pi$ and are related to p and e by

$$\rho_\pm = \frac{p}{1 \pm e}. \tag{4.52}$$

Now suppose that the central body's multipole moments M_{2n}, S_{2n+1}, $n = 0, 1, 2, ...$ have all been specified. Then we can compute the orbit's fundamental frequencies as functions of these moments and the orbit's p and e via the following algorithm:

1. Using Eqs. (43) of Ryan [1] (Eqs. (4.5) above), compute the coefficients $a_{2n,0}$ and $a_{2n,1}$ from

the moments, and then use the recursion relation (4.4) to compute all the other a_{jk}. Use these coefficents to compute the central body's complex Ernst potential via Eq. (4.3), and thence the metric coefficients and metric via Eqs. (4.2) and (4.1).

2. The radial velocity u^ρ of the unperturbed (no z motion) equatorial orbit vanishes at its perihelion and aphelion:

$$\begin{aligned} & u^\rho(\rho = \rho_\pm) = 0 \\ = \;& \frac{E^2 g_{\phi\phi} + 2ELg_{t\phi} - g_{t\phi}^2 + L^2 g_{tt} + g_{\phi\phi} g_{tt}}{g_{\rho\rho}(g_{t\phi}^2 - g_{tt} g_{\phi\phi})}. \end{aligned} \tag{4.53}$$

   Use the two solutions of this equation, $\rho = \rho_+$ and $\rho = \rho_-$, to solve for the orbit's conserved energy and angular momentum in terms of $\rho_\pm$ and thence (via Eq. (4.52)) in terms of p, e and the multipole moments which appear in the metric components:

$$E = E(p, e.\text{moments}), \quad L = L(p, e, \text{moments}). \tag{4.54}$$

3. From Eqs. (4.31), (4.33) and (4.54), do the following integration to get T_ρ and hence $\Lambda_\rho = 2\pi/T_\rho$ in terms of (p, e) and the multipole moments

$$\begin{aligned} T_\rho &= \oint d\tau = \int_0^{2\pi} d\chi \frac{d\tau}{d\rho}\frac{d\rho}{d\chi} \\ &= \int_0^{2\pi} d\chi \frac{1}{u^\rho(p, e, \chi)} \frac{pe\sin\chi}{(1 + e\cos\chi)^2}; \end{aligned} \tag{4.55}$$

   and similarly for Λ_ϕ and Λ_t. Use Eq. (4.48) to compute $\Lambda_{z,N}$, and take the limit as $N \to \infty$ to obtain Λ_z as a function of p, e and the moments. (Note: it is not really necessary to take this limit, in practice, as our mapping algorithm (Sec. 4.5.5 below) will revert to an order-by-order procedure, but for pedagogical reasons, we imagine taking the limit.)

4. Compute $\Omega_\rho = \Lambda_\rho/\Lambda_t$, $\Omega_\phi = \Lambda_\phi/\Lambda_t$, $\Omega_z = \Lambda_z/\Lambda_t$. These fundamental frequencies, like the Λs, will be functions of p, e, and the central body's multipole moments:

$$\Omega_\alpha = \Omega_\alpha(p, e, \text{moments}) \text{ for } \alpha = \phi, \rho, z. \tag{4.56}$$

In principle, if we have a sequence of snapshot waveforms, from which we deduce a sequence of values of Ω_ϕ, Ω_ρ, Ω_z, we can invert Eqs. (4.56) to obtain the corresponding sequence of p and e plus the dominant multipole moments. In practice, inverting these equations might be difficult. To facilitate the inversion, in the next section we develop a truncated version of Eqs. (4.56), in which only a controlled, finite set of moments appears.

4.5.4 Truncated Fundamental-Frequency Equations

In practice, it seems likely that moments of low order will have a much stronger influence on the central body's metric and thence on the fundamental frequencies than moments of high order; and, more specifically, the influence of a moment will tend to decrease as its order becomes larger and larger. This motivates us to develop, in this section, an approximate version of the fundamental-frequency equations (4.56) in which only the first $N+1$ mass moments $M_0, M_2, ..., M_{2N}$ and and first N current moments $S_1, S_3, ..., S_{2N-1}$ appear. These "truncated" fundamental-frequency equations will become the foundation for a moment-extraction algorithm (Sec. 4.5.5) that is likely to be computationally practical.

Suppose that the first $N+1$ mass moments and first N current moments are known. Then to get truncated fundamental-frequency equations that depend only on these $2N+1$ moments, we proceed as follows:

1. From these moments, using Eqs. (43) of Ryan [1] (Eq. (4.5) above), compute the coefficients $a_{2j,0}$ for $j = 0, 1, ..., N$ and $a_{2j,1}$ for $j = 0, 1, ..., N-1$; and then use the recursion relation (4.4) to compute all the other a_{jk} with $j + k \leq 2N$. Use these coefficents to compute a truncated complex Ernst potential (Eq. (4.3)),

$$\tilde{\mathcal{E}}_N = \sum_{j+k \leq 2N} a_{jk} \frac{\rho^j z^k}{(\rho^2 + z^2)^{j+k}}. \tag{4.57}$$

   From this truncated potential, compute truncated metric components $g^N_{\mu\nu}$ via Eqs. (4.2) and (4.1).

2. Using this truncated metric in Eqs. (4.53), compute a truncated expression for the orbital energy and angular momentum, $E_N(p, e, \text{lowest } 2N+1 \text{ moments})$ and $L_N(p, e, \text{lowest } 2N+1 \text{ moments})$.

3. Using these truncated equations in Eq. (4.55), compute a truncated $\Lambda_{\rho,N} = 2\pi/T_{\rho,N}$, and similarly for $\Lambda_{\phi,N}$ and $\Lambda_{t,N}$. Using Eq. (4.48), compute the truncated $\Lambda_{z,N}$, which, like the other $\Lambda_{\alpha,N}$, depends only on the lowest $2N+1$ moments.

4. Finally, compute $\Omega_{\alpha,N} = \Lambda_{\alpha,N}/\Lambda_{t,N}$, for $\alpha = \phi, \rho, z$. These fundamental frequencies, like the truncated Λ's, will be functions of p, e, and the lowest $2N+1$ multipole moments:

$$\begin{aligned} \Omega_{\alpha,N} &= \Omega_{\alpha,N}(p, e; M_0, \ldots, M_{2N}; S_1, \ldots, S_{2N-1}) \\ &\quad \text{for } \alpha = \phi, \rho, z. \end{aligned} \tag{4.58}$$

   Equations (4.58) are the foundations for our moment-extraction algorithm.

That algorithm will require that at least two of the $\Omega_{\alpha,N}$ actually *do* depend on the highest-order moments M_{2N} and S_{2N-1}. Ryan has shown (by expanding Ω_ρ and Ω_z in powers of Ω_ϕ) that this is truly the case for circular orbits, $e = 0$. As we turn on the orbital eccentricity e and crank it up to finite values, it is reasonable to expect that this will continue to be so.

4.5.5 Generalizing Ryan's Theorem to Eccentric, Nearly Equatorial Orbits

Suppose, now, that we have a large sequence of snapshot waveforms. We can use the truncated fundamental-frequency equations (4.58) to solve, in a step-by-step manner, for each snapshot's p and e, and for the central body's moments — beginning with M_0 in the first step, then M_0, M_2, S_1 in the second step, and so forth.

Suppose that step $N-1$ has been taken, yielding the first $2N-1$ moments. The next step, number N, makes use of $2N+1$ snapshot waveforms, which yield $3(2N+1)$ fundamental-frequency values — of which $3(2N-1)$ were used in step $N-1$, and 3 are new. Approximating these $3(2N+1)$ fundamental-frequency values by the truncated frequency equations (4.58), we get $3(2N+1)$ equations for the same number of unknowns: $2N+1$ values of p (one for each snapshot), $2N+1$ values of e, $N+1$ mass moments, and N current moments. These $3(2N+1)$ equations can be inverted with the aid of the previous step's (less accurate) values of $2N-1$ p's, $2N-1$ e's and the first N mass moments and first $N-1$ current moments. The inversion will give improved values of the already-known parameters, plus first approximations to the two new p's, two new e's and the new M_{2N} and S_{2N-1}.

This step-by-step algorithm generalizes Ryan's theorem to significantly eccentric, but still nearly equatorial orbits. It exhibits how to extract the evolving orbital elements and the central body's moments (and thence spacetime metric) from a sequence of snapshot waveforms. Of course, we cannot be sure of how robust and rapidly convergent this algorithm will be until it is tested (a daunting but manageable task).

4.6 Conclusion

In this paper, I have given a detailed analysis of Ryan's theorem and some possible generalizations. I argued that most or all observed geodesics in a general SARSAF spacetime are likely to be multi-periodic with four fundamental frequencies (Eqs. (4.8), (4.10)); and I showed that, if this is so, then the adiabatic snapshot waveforms are also multi-periodic, with three fundamental frequencies (Eq. (4.28)). A snapshot's observables are these three frequencies $\Omega_\rho, \Omega_\rho, \Omega_z$, plus the complex gravitational-wave amplitudes $h^{\mu\nu}_{mnl}$ of the various harmonics. For generic orbits, in Sec.4.4 I discussed how these observables might be used to extract the orbital evolution and the central body's multipole moments (or, equivalently, its spacetime metric); and I argued that, in the generic case, any algorithm for this extraction will require a detailed knowledge of gravitational-wave generation in SARSAF spacetimes. After this generic discussion, I specialized to a nearly equatorial but significantly eccentric orbit, and for it I derived, in Sec. 4.5.5, a detailed algorithm for extracting the central body's moments and the orbital evolution from a sequence of gravitational-wave shapshots—without any detailed knowledge of wave-generation theory for SARSAF spacetimes.

It should be possible for LISA to measure the three slowly evolving fundamental frequencies with high accuracy. Using these data, the algorithm I have presented here might be realistic and practical.

4.7 Bibliography

[1] F. D. Ryan, *Phys. Rev. D* **52**, 5707 (1995).

[2] See, e.g., A. Abramovici et al., *Science* 256, 325 (1992); B. Caron et al., *Class. Quant. Grav.* **14**, 1461 (1997); H. Lück et al., *Class. Quant. Grav.* . **14**, 1471 (1997); M. Ando et al., *Phys. Rev. Lett.* **86**, 3950 (2001).

[3] K. Danzmann, et al., LISA: Proposal for a Laser Interferometric Gravitational Wave Detector in Space (Max Planck Institut für Quantenoptik, Garching bei München, Germany, 1993).

[4] K. S. Thorne, "Gravitational waves," in *Proceedings of the Snowmass'94 Summer Study on Particle and Nuclear Astrophysics and Cosmology*, eds. E. W. Kolb and R. Peccei (World Scientific, Singapore, 1995), pp. 160-84.

[5] D. A. Brown, J. Brink, H. Fang, J. R. Gair, C. Li, G. Lovelace, I. Mandel, and K. S. Thorne, *Phys. Rev. Lett.* , 99, 201102 (2007).

[6] L. S. Finn and K. S. Thorne, *Phys. Rev. D* , 62, 124021 (2000).

[7] C. Li and G. Lovelace, *Phys. Rev. D* **77** 064022 (2008).

[8] T. P. Sotiriou and T. A. Apostolatos, *Phys. Rev. D* **71** 044005 (2005).

[9] B. C. Xanthopulos, *J. Math. Phys.*, 22 1254 (1981).

[10] B. C. Xanthopulos, *J. Phys. A*, 7 1025 (1979).

[11] R. Geroch, *J. Math. Phys.* . **11**, 2580 (1970).

[12] R. O. Hansen, *J. Math. Phys.* . **15**, 46 (1974).

[13] G. Fodor, C. Hoenselaers and Z. Perjés, *J. Math. Phys.* . **30**, 2252 (1989).

[14] D. Hils and P. L. Bender, *The Astrophysical Journal* . **445**, L7 (1995).

[15] C. Miller, private communication (2007).

[16] E. S. Phinney, private communication (2007).

[17] J. Gair, C. Li and I. Mandel, *Phys. Rev. D* **77**, 024035 (2008).

[18] S. A. Hughes, S. Drasco, E. E. Flanagan and J. Franklin, *Phys. Rev. Lett.* **94**, 221101 (2005).

[19] F. J. Ernst, *Phys. Rev.* **167**, 1175 (1968).

[20] W. Dietz, in *Solutions of Einstein's Equations, Techniques and Results,* edited by C. Hoenselaers and W. Deitz (Springer, Heiderberg, 1984).

[21] H. Goldstein, *Classical Mechanics*, 3rd Edition (Addison-Wesley, San Francisco, CA, 2002) chapter 10.

[22] J. Binney and S. Tremaine, *Galactic Dynamics*, (Princeton University Press, Princeton, NJ, 1987) chapter 3.

[23] V. I. Arnold, *Mathematical Methods of Classical Mechanics*, (Springer-Verlag, New York, 1989).

[24] J. Brink, *Phys. Rev. D* , submitted; arxiv/0807.1179

[25] B. Carter, *Commum. Math. Phys.*, **10** 280-310

[26] Guéron and P. S. Letelier *Phys. Rev. E*, **63** 035201 (2001).

[27] J. Brink, papers in preparation (2008).

[28] S. Drasco and S. A. Hughes, *Phys. Rev. D* **69**, 044015 (2004).

[29] Y. Mino, private communication (2007).

[30] S. Drasco, *Phys. Rev. D* , submitted. arXiv:07114644v1

[31] N. A. Collins and S. A. Hughes, *Phys. Rev. D* , **69**, 124022 (2004).

Chapter 5

Local Readout Enhancement for Detuned Signal-Recycling Interferometers

High power detuned signal recycling interferometers currently planned for second-generation interferometric gravitational-wave detectors (for example Advanced LIGO) are characterized by two resonances in the detection band, an optical resonance and an optomechanical resonance, which is upshifted from the suspension pendulum frequency due to the so-called optical-spring effect. The detector's sensitivity is enhanced around these two resonances. However, at frequencies below the optomechanical resonance frequency, the sensitivity of such interferometers is significantly lower than non-optical-spring configurations with comparable circulating power; such a drawback can also compromise high-frequency sensitivity when an optimization is performed on the overall sensitivity of the interferometer to a class of sources. In this paper, we clarify the reason of such a low sensitivity, and propose a way to fix this problem. Motivated by the *optical-bar* scheme of Braginsky, Gorodetsky, and Khalili, we propose to add a local readout scheme which measures the motion of the arm-cavity front mirror, which at low frequencies moves together with the arm-cavity end mirror under the influence of gravitational waves. This scheme improves the low-frequency quantum-noise-limited sensitivity of optical-spring interferometers significantly and can be considered as a incorporation of the optical-bar scheme into currently planned second-generation interferometers. On the other hand it can be regarded as an extension of the optical bar scheme. Taking compact-binary inspiral signals as an example, we illustrate how this scheme can be used to improve the sensitivity of the planned Advanced LIGO interferometer, in various scenarios, using a realistic classical-noise budget. We also discuss how this scheme can be implemented in Advanced LIGO with relative ease.

Originally published as H. Rehbein, H. Mueller-Ebhardt, K. Somiya, C. Li, R. Schnabel, K. Danzmann and Y. Chen, *Phys. Rev. D* **76**, 062002 (2007).

5.1 Introduction

First-generation laser interferometric gravitational-wave (GW) detectors (LIGO [1], VIRGO [2], GEO [3] and TAMA [4]) are reaching design sensitivities. These interferometers are usually Michelson interferometers with Fabry-Perot cavities in the arms, with power recycling (PR) at the laser input port (with the exception of GEO, which uses *dual-recycling* [5]), and operating close to the dark-port condition.

In order to have a flexible sensitivity to specific astrophysical sources, and for other technical reasons such as lowering power at the beam splitter (BS), second-generation interferometers, such as Advanced LIGO [6], plan to use the so-called signal recycling (SR) configuration, in which an additional mirror is placed at the dark port of a Fabry-Perot Michelson interferometer, modifying the optical resonant structure of the interferometer. The adjustment of the location and reflectivity of the signal recycling mirror varies the optical resonance frequency and bandwidth, respectively. Near the optical resonance, sensitivity to GWs is improved. When the signal recycling cavity, the cavity formed by the input test-mass mirrors and the signal recycling mirror is neither resonant nor anti-resonant with respect to the carrier frequency, the optical configuration is called *detuned* signal recycling. In these detuned configurations, the optical resonance of the interferometer is away from the carrier frequency, creating a peak sensitivity to GWs away from DC.

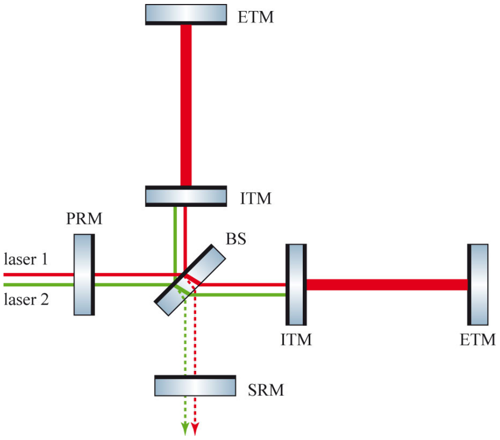

Figure 5.1: Schematic plot of a power and signal recycled Michelson interferometer with arm cavities and double readout. The added local readout sensing the ITM is realized by a secondary laser which does not resonate in the arm cavities.

As demonstrated theoretically by Buonanno and Chen [7, 8, 9] and experimentally by Somiya et al. [10] and Miyakawa et al. [11], detuned signal recycling also makes the power inside the interferometer depend on the motion of the mirrors, creating an *optical spring*, and can shift the eigenfrequency of the test masses from the pendulum frequency (~ 1Hz) up to the detection band. The optical spring helps to improve the interferometer's response to GWs around the optomechanical resonant frequency, even allowing the interferometer to surpass the free-mass Standard Quantum

Limit (SQL). However, the quantum-noise-limited sensitivity of optical-spring interferometers at frequencies below the optomechanical resonant frequency is dramatically lower than the one of non-optical-spring interferometers. Such a limitation in sensitivity is caused by the optical spring, which rigidly connects the front and the end mirror of the arm cavities at frequencies below the optomechanical resonance. The general principle underlying this effect has already been explained in the works of Braginsky, Gorodetsky and Khalili, namely in their proposal of the *optical bar* detection scheme [12]. In order to understand this more conveniently, we need to use the local inertial frame of the BS, in which the effect of GWs can be described completely as a tidal force field, which induces forces only on the end test-mass mirrors (ETMs), but not on the input test-mass mirrors (ITMs). We make the approximation that the ITMs and the BS are colocated. In this frame, the propagation of the light is unaffected by GWs. Remember that the optical spring connects the ITM and the ETM. At frequencies substantially below the optomechanical resonance, the optical spring behaves like a rigid optical bar, connecting the ITM and the ETM of each arm rigidly. It is then easy to understand that the carrier light, which senses the change in arm-cavity length, or the difference in ITM and ETM motion, cannot be used to measure GW efficiently at these frequencies. On the other hand, since the ITM and the ETM are rigidly connected, they both move, in the local inertial frame of the BS, by 1/2 the amount the ETM would have moved if there were no optical spring present (assuming ITM and ETM to have equal masses). To illustrate this situation, assume that a low-frequency GW with amplitude h is incident from right above our detector (with arm-length L), then in the local inertial frame of the BS, the motion of the ETM of a non-optical-spring interferometer would be Lh, the motion of ITM and ETM of an optical-spring interferometer below resonance will be both $\sim Lh/2$. For this reason, if one also measures the local motion of the ITM using an additional *local readout* scheme, one can recover low-frequency sensitivity dramatically. Note that as viewed by the local meter, the ITM has an effective mass that is equal to the total mass of the ITM and the ETM. If one applies a local readout scheme to the ETM, the same sensitivity recovery is possible, since the ETM also moves with respect to a free colocated mirror by $-Lh/2$. Braginsky, Gorodetsky and Khalili proposed an optical bar detection scheme, in which only the local motion of the ITM is measured [12]. In this sense, what we are proposing can be considered as directly incorporating the optical-bar scheme into currently planned second-generation interferometers.

Local readout schemes have also been proposed for interferometers without optical spring, with a different motivation. In those interferometers, the motion of mirrors with respect to their local inertial frames are caused by radiation-pressure noise (if we only consider signal and quantum noise sources); results of local readout schemes can thus be used to cancel radiation-pressure noise and improve low-frequency sensitivity [13, 14]. Furthermore, such schemes are able to cancel parts of the classical noise. Our treatment here can also be viewed as a generalization of these schemes because by setting detuning in our treatment to zero will recover their results.

From an astrophysical point of view, the addition of the local readout scheme, which broadens the detection band, will allow the interferometer to search for multiple sources simultaneously, as well as to examine a wider frequency range of the same source. As an example, we will explore how the increase in detection bandwidth can allow us to detect more efficiently the population of compact binary objects with a broad range of masses (and hence signal frequency band).

In order to construct the local meter, we consider a scheme where a second carrier is injected into the bright port, which does not enter the arm cavities, but instead senses the location of the ITMs, as shown in Fig. 5.1. An alternative strategy would be attaching auxiliary interferometers at the ETMs. These two strategies are quite equivalent in the ideal situation, but differ from each other in terms of difficulty in implementation in terms of quantum noise and in terms of technical noise sources such as laser noise as we will discuss in some more details.

This paper is organized as follows. In Sec. 5.2, we study the dynamics, sensing, and control of our double readout interferometer. In Sec. 5.2.1, we write down and solve the joint Heisenberg equations of motion of test masses, beam splitter, and optical fields; in Sec. 5.2.2, we evaluate the optimal combined GW sensitivity of the two readout channels; in Sec. 5.2.3, we prove that the use of control schemes do not affect this sensitivity. In Sec. 5.4 we show the benefit, which the local readout scheme will provide for the detection of intermediate-mass black holes, using a realistic Advanced LIGO noise budget. In Sec. 5.4 we consider practical issues for a possible implementation in Advanced LIGO. In Sec. 5.5 we summarize our main conclusions.

5.2 Dynamics, Sensing, and Control

5.2.1 Equations of Motion

Let us consider a configuration where the ITMs' motion of a signal and power recycled Michelson interferometer with arm cavities is locally sensed by a small interferometer which has the ITMs as its end mirrors (cf.Fig. 5.1). This is realized by injecting a second carrier into the bright port, which does not resonate in the arms (preferably anti-resonant). Because the frequency (and the polarization) of the second carrier is (are) different from that of the first, we effectively obtain two interferometers in one scheme where parameters such as detuning and mirror reflectivities for each interferometer can be chosen independently; input vacuum fluctuations associated with the two lasers are also independent.

Throughout this paper, we will assume the GW with amplitude h as incident from right above the interferometer, with a polarization that maximizes the response of our L-shaped Michelson interferometers. In the following we will list the Heisenberg equation of motions in frequency domain [15, 7, 8, 9, 16] for the differential mode of motion (i.e., opposite in the two arms) of the input mirrors $\hat{x}_{\mathrm{ITM}}$ and the end mirrors $\hat{x}_{\mathrm{ETM}}$, respectively, as well as for the BS motion normal to its reflective surface $\hat{x}_{\rm BS}$ and for the two measurement outputs $\hat{y}^{(i)}$

$$\begin{aligned}
\hat{x}_{\rm ITM} &= -R_{xx}(\Omega)\ \Big[\hat{F}^{(1)}(\Omega) + R^{(1)}_{FF}(\Omega)\ (\hat{x}_{\rm ETM} - \hat{x}_{\rm ITM}) - \hat{F}^{(2)}(\Omega) - R^{(2)}_{FF}(\Omega)\ (\hat{x}_{\rm ITM} + \sqrt{2}\ \hat{x}_{\rm BS})\Big] \\
&\quad + \hat{\xi}_{\rm ITM}\,, \qquad (5.1) \\
\hat{x}_{\rm ETM} &= R_{xx}(\Omega)\ \Big[\hat{F}^{(1)}(\Omega) + R^{(1)}_{FF}(\Omega)\ (\hat{x}_{\rm ETM} - \hat{x}_{\rm ITM})\Big] + L\ h + \hat{\xi}_{\rm ETM}\,, \qquad (5.2) \\
\hat{x}_{\rm BS} &= R^{\rm BS}_{xx}(\Omega)\ \Big[\hat{F}^{(2)}(\Omega) + R^{(2)}_{FF}(\Omega)\ (\hat{x}_{\rm ITM} + \sqrt{2}\ \hat{x}_{\rm BS}) + \hat{F}^{(1)}_{\rm BP}(\Omega) + \hat{F}^{(2)}_{\rm BP}(\Omega)\Big] + \hat{\xi}_{\rm BS}\,, \qquad (5.3) \\
\hat{y}^{(1)} &= \hat{Y}^{(1)}_1(\Omega)\ \sin\zeta^{(1)} + \hat{Y}^{(1)}_2(\Omega)\ \cos\zeta^{(1)} \\
&\quad + \Big[R^{(1)}_{Y_1F}(\Omega)\ \sin\zeta^{(1)} + R^{(1)}_{Y_2F}(\Omega)\ \cos\zeta^{(1)}\Big]\,(\hat{x}_{\rm ETM} - \hat{x}_{\rm ITM})\,, \qquad (5.4) \\
\hat{y}^{(2)} &= \hat{Y}^{(2)}_1(\Omega)\ \sin\zeta^{(2)} + \hat{Y}^{(2)}_2(\Omega)\ \cos\zeta^{(2)} \\
&\quad + \Big[R^{(2)}_{Y_1F}(\Omega)\ \sin\zeta^{(2)} + R^{(2)}_{Y_2F}(\Omega)\ \cos\zeta^{(2)}\Big]\,(\hat{x}_{\rm ITM} + \sqrt{2}\ \hat{x}_{\rm BS})\,. \qquad (5.5)
\end{aligned}$$

Note that $\hat{x}_{\rm ITM}$ and $\hat{x}_{\rm ETM}$ account for the differential motion between two mirrors while $\hat{x}_{\rm BS}$ describes the motion of a single mirror with an angle of 45 degrees. This explains the factor of $\sqrt{2}$ in front of the BS motion. The outgoing fields at the dark port belonging to the two different carriers are each sensed by homodyne detection such that the measurement outputs are a certain combination of amplitude and phase quadratures (described by the phases $\zeta^{(1),(2)}$). Note that we have labeled all quantities with superscripts (1) and (2) for the large-scale interferometer and the local meter (the small interferometer, formed by the BS and the ITMs), respectively. The operators $\hat{F}^{(i)}$ and $\hat{F}^{(i)}_{\rm BP}$ describe the radiation pressure forces which would act on fixed mirrors caused by the incoming vacuum fields at the dark port and the laser light fluctuations from the bright port, respectively. The operators $\hat{Y}^{(i)}_j$ account for the shot noise in case of fixed mirrors. Each optical component is subject to classical noise generated by the corresponding operator $\hat{\xi}$ and has its own mechanical susceptibility R_{xx}. The susceptibilities $R^{(i)}_{FF}$ describe the optical springs [7] and $R^{(i)}_{Y_iF}$ the transformation of the mirror motion into the two outputs. In the following we will present all these quantities more detailed while all appearing parameters are summarized in tab. 5.1.

The free radiation pressure force and the free shot noise in each of the two interferometers are given by [9]

$$\begin{aligned}
\hat{F}^{(i)} &= \sqrt{\frac{\epsilon^{(i)}\theta^{(i)}m\hbar}{2}}\,\frac{(\mathrm{i}\Omega - \epsilon^{(i)})\ \hat{a}^{(i)}_1 + \lambda^{(i)}\ \hat{a}^{(i)}_2}{(\Omega - \lambda^{(i)} + \mathrm{i}\epsilon^{(i)})(\Omega + \lambda^{(i)} + \mathrm{i}\epsilon^{(i)})}\,, \\
\hat{Y}^{(i)}_1 &= \frac{((\lambda^{(i)})^2 - (\epsilon^{(i)})^2 - \Omega^2)\ \hat{a}^{(i)}_1 + 2\lambda^{(i)}\epsilon^{(i)}\ \hat{a}^{(i)}_2}{(\Omega - \lambda^{(i)} + \mathrm{i}\epsilon^{(i)})(\Omega + \lambda^{(i)} + \mathrm{i}\epsilon^{(i)})}\,, \\
\hat{Y}^{(i)}_2 &= \frac{-2\lambda^{(i)}\epsilon^{(i)}\ \hat{a}^{(i)}_1 + ((\lambda^{(i)})^2 - (\epsilon^{(i)})^2 - \Omega^2)\ \hat{a}^{(i)}_2}{(\Omega - \lambda^{(i)} + \mathrm{i}\epsilon^{(i)})(\Omega + \lambda^{(i)} + \mathrm{i}\epsilon^{(i)})}\,,
\end{aligned}$$

where $\theta^{(i)} = \frac{8P^{(i)}\omega^{(i)}_0}{mL^{(i)}c}$ has units of frequency cube. Note that $P^{(i)}$ refers to the circulating power in each arm, respectively. Here $\hat{a}_1^{(i)}$ and $\hat{a}_2^{(i)}$ are the amplitude and phase quadrature operators of the incoming vacuum fields at the dark port [15], associated with the first and second carrier field, respectively. The susceptibilities are given by [9]

$$\begin{aligned}
R_{xx}^{\mathrm{BS}} &= -\frac{\sqrt{2}}{m_{\mathrm{BS}}\Omega^2}\,,\\
R_{xx} &= -\frac{2}{m\Omega^2}\,,\\
R_{FF}^{(i)} &= \frac{\theta^{(i)}m}{4}\frac{\lambda^{(i)}}{(\Omega-\lambda^{(i)}+\mathrm{i}\epsilon^{(i)})(\Omega+\lambda^{(i)}+\mathrm{i}\epsilon^{(i)})}\,,\\
R_{Y_1F}^{(i)} &= \sqrt{\frac{\epsilon^{(i)}\theta^{(i)}m}{2\hbar}}\frac{\lambda^{(i)}}{(\Omega-\lambda^{(i)}+\mathrm{i}\epsilon^{(i)})(\Omega+\lambda^{(i)}+\mathrm{i}\epsilon^{(i)})}\,,\\
R_{Y_2F}^{(i)} &= -\sqrt{\frac{\epsilon^{(i)}\theta^{(i)}m}{2\hbar}}\frac{\epsilon^{(i)}-\mathrm{i}\Omega}{(\Omega-\lambda^{(i)}+\mathrm{i}\epsilon^{(i)})(\Omega+\lambda^{(i)}+\mathrm{i}\epsilon^{(i)})}\,,
\end{aligned}$$

where the (free) optical resonant frequency of the large-scale interferometer at $\Omega=-\lambda^{(1)}-\mathrm{i}\epsilon^{(1)}$ is determined by

$$\begin{aligned}
\lambda^{(1)} &= \gamma_o\frac{2\rho_{\mathrm{SR}}\sin(2\phi)}{1+\rho_{\mathrm{SR}}^2+2\rho_{\mathrm{SR}}\cos(2\phi)}\,,\\
\epsilon^{(1)} &= \gamma_o\frac{1-\rho_{\mathrm{SR}}^2}{1+\rho_{\mathrm{SR}}^2+2\rho_{\mathrm{SR}}\cos(2\phi)}\,.
\end{aligned}$$

As already mentioned, the second carrier does not resonate in the arm cavities and therefore the local meter is just equivalent to a interferometer configuration without cavities in the arms. Thus, in Eq. (5.3) we only take into account the forces on the BS due to field fluctuations around the second carrier, in the same way as in Ref. [17]: the first two terms in the bracket on the right-hand side of Eq. (5.3) are due to dark-port fluctuations around the second carrier, while the third and fourth term, given by

$$\begin{aligned}
\hat{F}_{\mathrm{BP}}^{(1)} &= \gamma_0\frac{L^{(1)}\sqrt{\theta^{(1)}m\hbar(1-\rho_{\mathrm{PR}}^2)\gamma_0}}{\sqrt{2}c(-\gamma_0(1-\rho_{\mathrm{PR}})+\mathrm{i}(1+\rho_{\mathrm{PR}})\Omega)}\,b_1^{(1)}\,,\\
\hat{F}_{\mathrm{BP}}^{(2)} &= \sqrt{\frac{\theta^{(2)}mL^{(2)}\hbar(1+\rho_{\mathrm{PR}})}{2c(1-\rho_{\mathrm{PR}})}}\,b_1^{(2)}\,,
\end{aligned}$$

are forces due to bright-port fluctuations, where $b_1^{(i)}$ are the amplitude quadrature of fluctuations around the first and second carrier, at the input port. Forces due to fluctuations around the first carrier are usually negligible, because the intensity of the first carrier at the beam splitter is lower than that of the second carrier; in addition, fluctuations associated with the first carrier also do not build up as much as those associated with the second carrier, both in common and in differential mode.

In Eq. (5.4), we make the approximation that the first carrier only senses the cavity length,

Table 5.1: Technical data and parameter values for large-scale interferometer and local meter used throughout the calculations[2].

Symbol	physical meaning	value
m	single mirror mass	40 kg
$m_{\rm BS}$	beam splitter mass	40 kg
$c/\omega_0^{(1)}$	laser wavelength of 1st carrier	1064 nm
$P^{(1)}$	circulating power of 1st carrier	$0.1, \ldots, 0.8$ MW
$L^{(1)}$	large-scale interferometer arm length	4 km
$\rho_{\rm PR}$	power recycling mirror reflectivity	$\sqrt{0.94}$
ϕ	detuning phase for 1st carrier	$0, \ldots, \pi$
$\rho_{\rm SR}$	signal recycling mirror reflectivity	$\sqrt{0.93}$
γ_o	cavity half bandwidth for 1st carrier	$2\pi \times 15$ Hz
$\zeta^{(1)}$	detection angle for 1st carrier	$0, \ldots, \pi$
$c/\omega_0^{(2)}$	laser wavelength of 2nd carrier	1064 nm
$P^{(2)}$	circulating power of 2nd carrier	$0, \ldots, 16$ kW
$L^{(2)}$	local meter arm length	15 m
$\lambda^{(2)}$	detuning for 2nd carrier	0 Hz
$\epsilon^{(2)}$	cavity half bandwidth for 2nd carrier	$2\pi \times 4$ kHz
$\zeta^{(2)}$	detection angle for 2nd carrier	0

$\hat{x}_{\rm ETM} - \hat{x}_{\rm ITM}$, ignoring the slight difference between its sensitivities to ITM and ETM, as well as motion of the BS. In Eq. (5.5), the second carrier only senses the ITM and BS motions, since it does not enter the arm cavities.

The operators $\hat{\xi}_{\rm ITM}$, $\hat{\xi}_{\rm ITM}$ and $\hat{\xi}_{\rm BS}$ model the classical noise at ITM, ETM and BS, respectively. We assume that they are uncorrelated but all have the same spectrum, namely, one fourth of the classical noise spectrum generally expected for the differential mode of motion. By using the following only non-vanishing correlation functions

$$\begin{aligned}
\langle \hat{a}_k^{(i)}(\Omega)\ (\hat{a}_l^{(j)})^\dagger(\Omega')\rangle_{\rm sym} &= \pi\ \delta(\Omega-\Omega')\ \delta_{ij}\ \delta_{kl}\,,\\
\langle \hat{b}_k^{(i)}(\Omega)\ (\hat{b}_l^{(i)})^\dagger(\Omega')\rangle_{\rm sym} &= \pi\ \delta(\Omega-\Omega')\ \delta_{kl}\ S_1^{(i)}(\Omega)\,,\\
\langle \hat{\xi}_{\rm ITM}(\Omega)\ (\hat{\xi}_{\rm ITM})^\dagger(\Omega')\rangle_{\rm sym} &= 2\pi\ \delta(\Omega-\Omega')\ S_{\rm cl}(\Omega)\,,\\
\langle \hat{\xi}_{\rm ETM}(\Omega)\ (\hat{\xi}_{\rm ETM})^\dagger(\Omega')\rangle_{\rm sym} &= 2\pi\ \delta(\Omega-\Omega')\ S_{\rm cl}(\Omega)\,,\\
\langle \hat{\xi}_{\rm BS}(\Omega)\ (\hat{\xi}_{\rm BS})^\dagger(\Omega')\rangle_{\rm sym} &= \pi\ \delta(\Omega-\Omega')\ S_{\rm cl}(\Omega)\,,
\end{aligned} \tag{5.6}$$

we obtain the single-sided noise spectral densities. Here $S_1^{(i)}(\Omega)$ is the spectrum of technical input laser noise while $S_{\rm cl}(\Omega)$ characterizes the spectrum of all the other classical noise sources. In further calculations we will assume amplitude laser noise to be white and ten times in power above shot noise level. For other classical noise sources, we use the current noise budget of Advanced LIGO, as given in *Bench* [18]; contributions such as suspension thermal noise, seismic noise, thermal fluctuations in the coating and gravity gradient noise are presented in Fig. 5.4.

Note that we can obtain two input-output relations from the equation of motions in Eq. (5.1-5.5) and write them in the following compact form

$$\hat{y}^{(1)} = \vec{n}_1^T\ \vec{\nu} + s_1\ h\,, \quad \hat{y}^{(2)} = \vec{n}_2^T\ \vec{\nu} + s_2\ h\,, \tag{5.7}$$

where $\vec{\nu}^T = (\hat{a}_1^{(1)}, \hat{a}_2^{(1)}, \hat{a}_1^{(2)}, \hat{a}_2^{(2)}, \hat{b}_1^{(1)}, \hat{b}_1^{(2)}, \hat{\xi}_{\rm ITM}, \hat{\xi}_{\rm ETM}, \hat{\xi}_{\rm BS})$ and T denotes transposed. Here the two vectors $\vec{n}_{1,2}$ are the linear transfer functions from the noise channels $\vec{\nu}$ into the two output channels, while the two functions $s_{1,2}$ are the linear transfer functions from the signal, i.e., the GW strain h, into the output channels.

5.2.2 Combined Sensitivity

Now we seek for a linear combination of the two output channels, $\hat{y}^{(1)}$ and $\hat{y}^{(2)}$,

$$\hat{y} = K_1(\Omega)\ \hat{y}^{(1)} + K_2(\Omega)\ \hat{y}^{(2)}\,, \tag{5.8}$$

which has optimal sensitivity to gravitational waves. In this optimization, we only consider the signal referred noise spectral density of $\hat{y}$,

$$S_h(\Omega) = \frac{\begin{pmatrix} K_1 & K_2 \end{pmatrix} \mathbf{N} \begin{pmatrix} K_1^* \\ K_2^* \end{pmatrix}}{\begin{pmatrix} K_1 & K_2 \end{pmatrix} \mathbf{S} \begin{pmatrix} K_1^* \\ K_2^* \end{pmatrix}}\,, \tag{5.9}$$

with

$$\mathbf{N} \equiv \begin{bmatrix} \vec{n}_1^T \\ \vec{n}_2^T \end{bmatrix} \begin{bmatrix} \mathbb{1}_4 & & & & \\ & S_{\rm l}^{(1)} & & & \\ & & S_{\rm l}^{(2)} & & \\ & & & 2S_{\rm cl}\mathbb{1}_2 & \\ & & & & S_{\rm cl} \end{bmatrix} \begin{bmatrix} \vec{n}_1^* & \vec{n}_2^* \end{bmatrix}, \tag{5.10}$$

and

$$\mathbf{S} \equiv \begin{pmatrix} s_1 s_1^* & s_1 s_2^* \\ s_2 s_1^* & s_2 s_2^* \end{pmatrix}, \tag{5.11}$$

where $\mathbb{1}_k$ stands for a k-dimensional identity matrix. One way of obtaining the minimum noise is to impose the constraint that the value of the denominator always remains unity, and minimize the numerator under this constraint. Note that an overall rescaling of the vector (K_1, K_2) does not

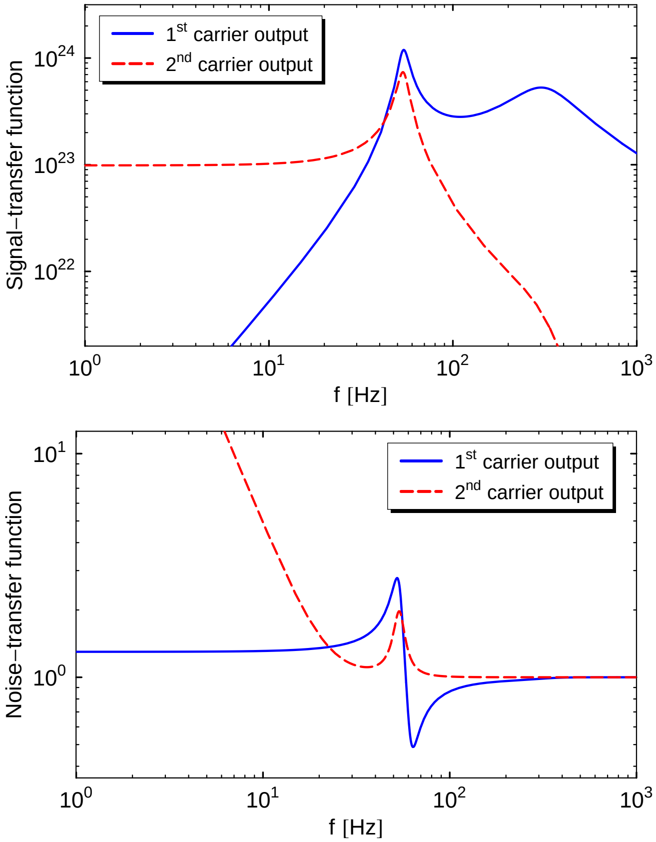

Figure 5.2: Example for the signal (top panel) and noise (bottom panel) transfer functions in a signal recycled Michelson interferometer with two carriers and double readout, for a configuration with the parameters as given in tab. 5.1 but $\zeta^{(1)} = 0$, $\phi = \pi/2 - 0.014\pi$ and $P^{(1)} = 800\,\mathrm{kW}$).

affect S_h. The resulting minimum noise is one over the bigger eigenvalue of the 2-by-2 matrix

$$\mathbf{M} \equiv \mathbf{N}^{-1}\mathbf{S}\,, \tag{5.12}$$

with the corresponding eigenvector providing the optimal filters (K_1, K_2).

We now illustrate the local readout scheme using the following configuration: the parameters are given in tab. 5.1 as well as phase quadrature readout $\zeta^{(1)} = 0$, signal recycling cavity detuning phase $\phi = \pi/2 - 0.014\pi$ and power $P^{(1)} = 800\,\mathrm{kW}$ of the first carrier are used. In Fig. 5.2 we plot the individual signal and noise-transfer functions of the first and second carriers, for the configuration with $P^{(2)} = 4\,\mathrm{kW}$. As we can see from these plots, the first carrier mainly senses frequencies above the optical-spring resonance with signal transfer function suppressed at lower frequencies by the optical spring; the second carrier offers complementary sensitivity for frequencies below the optical-spring resonance, when the ITM is dragged together with the ETM by the optical spring. As a consequence, as we see in the top panel of Fig. 5.3, at frequencies above the optical-spring resonance, the optimal combination depends mostly on the first readout, while at frequencies below

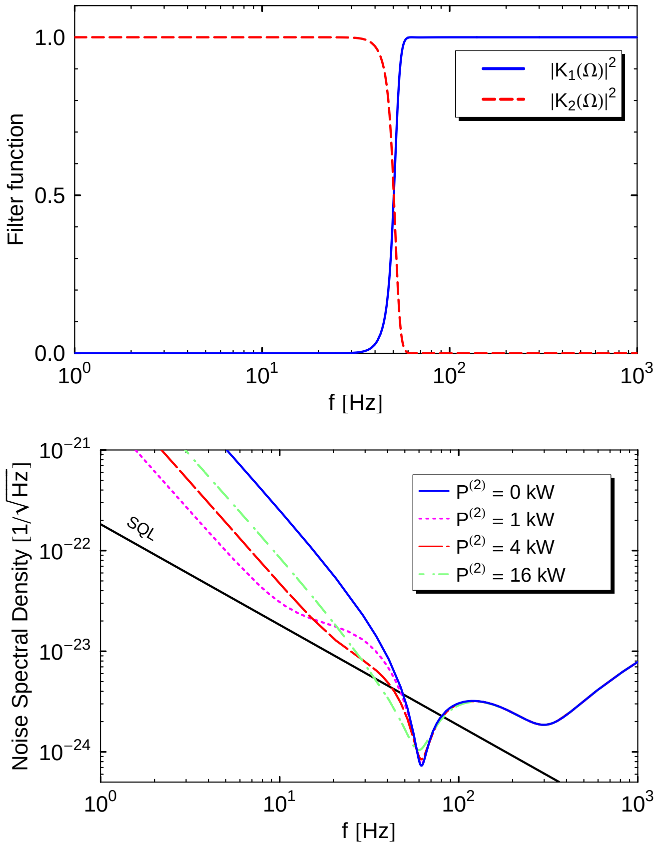

Figure 5.3: Top panel: filter functions K_1 and K_2, for the same configuration as in Fig. 5.2. Here each filter function is rescaled such that it gives the percentage of how much GW strain it feeds into the combined output. Bottom panel: quantum noise curves for our proposed scheme with different powers of 2nd carrier. Again phase quadrature readout $\zeta^{(1)} = 0$, signal recycling cavity detuning phase $\phi = \pi/2 - 0.014\pi$ and power $P^{(1)} = 800\,\text{kW}$ of 1st carrier are used.

the optical-spring resonance, the optimal combination depends mostly on the second readout.

Noise curves with optimal filters are plotted for different powers of the second carrier (0 kW, 1 kW, 4 kW and 16 kW) in the bottom panel of Fig. 5.3 where only quantum noise is taken into account. This plot illustrates that the local readout scheme can directly improve the sensitivity only below the optomechanical resonance frequency. It turns out that 4 kW in each arm of the local meter already gives a remarkable increase in sensitivity. In the following studies we fix $P^{(2)} = 4$ kW.

One could imagine that the combination of a signal recycled Michelson interferometer with a local readout may indirectly help improving the sensitivity at high frequencies or increasing the detection bandwidth once an overall optimization to a broadband source is performed. The underlying effect is that the sensitivity of the large-scale interferometer can be shifted to higher frequencies by choosing its detection angle to be closer to the phase quadrature while the local meter helps to maintain sensitivity at low frequencies. This will be studied more carefully in Sec. 5.3.

5.2.3 Control

As it has been shown in Refs. [7, 8, 9] the optical spring introduces an instability, which must be stabilized using a feedback control system. In single-readout systems, it is easy to show that such a control system does not give rise to any fundamental change in our GW sensitivity [7, 8, 9], intuitively because signal and noise are fed back with the same proportion onto the test masses. Our double readout system is more complex, but the same intuition still applies. If we denote $\vec{x} \equiv (\hat{x}_{\rm ITM}, \hat{x}_{\rm ETM}, \hat{x}_{\rm BS})^T$ and $\vec{y} \equiv (\hat{y}^{(1)}, \hat{y}^{(2)})^T$, the Eqs. (5.1)–(5.5) can be written schematically as:

$$\vec{x} = \mathbf{A}(\Omega)\vec{x} + \mathbf{B}(\Omega)\vec{\nu} + \vec{C}(\Omega)h + \mathbf{D}(\Omega)\vec{y}\,, \tag{5.13}$$

$$\vec{y} = \mathbf{F}(\Omega)\vec{x} + \mathbf{G}(\Omega)\vec{\nu}\,. \tag{5.14}$$

Here matrix $\mathbf{A}$ describes mirror dyanmics, matrix $\mathbf{B}$ describes how the noise sources in $\vec{\nu}$ are applied as forces onto the mirrors, vector $\vec{C}$ describes how GW signal h directly influences the mirrors, $\mathbf{F}$ describes how the output channels $\vec{y}$ sense the various motions $\vec{x}$, $\mathbf{G}$ describes sensing noise in $\vec{y}$, and finally $\mathbf{D}$ describes the feedback. Solving Eqs. (5.13) and (5.14) jointly, we obtain

$$\vec{y} = [\mathbb{1}_2 - \mathbf{HD}]^{-1}\left[[\mathbf{HB} + \mathbf{G}]\vec{\nu} + \mathbf{H}\vec{C}h\right]\,, \tag{5.15}$$

where we have defined $\mathbf{H} \equiv \mathbf{F}(\mathbb{1}_2 - \mathbf{A})^{-1}$. In Eq. (5.15) the only dependence of $\vec{y}$ on the control system is through $\mathbf{D}$, which only appears in the first factor on the right-hand side. The optimal sensitivity, which is obtained by maximizing signal referred noise spectrum of $(K_1\ K_2)\ \vec{y}$, is then clearly invariant with respect to changes in $\mathbf{D}$.

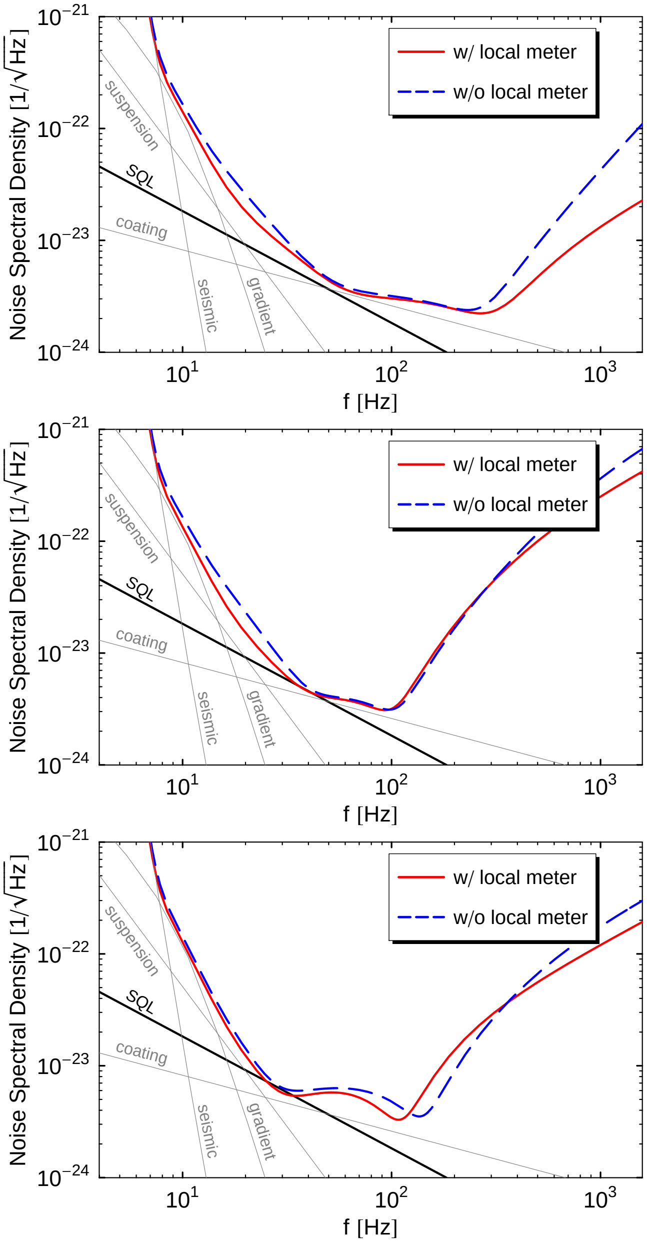

Figure 5.4: Noise curves for the scheme with local readout (power of 2nd carrier fixed to $P^{(2)} = 4\,\mathrm{kW}$) and without local readout both optimized for binary systems with total mass $M = 2.8\ M_\odot$ (upper left), $M = 40\ M_\odot$ (upper right) and $M = 120\ M_\odot$ (lower). Special parameters used for optimizations are given in tab. 5.2 and all others in tab. 5.1. Here classical noise (grey lines) is included. Single contributions of the classical noise are labeled according to their appearance: suspension thermal noise results from the fluctuations in the suspension system; seismic noise is due to motion of the ground; thermal fluctuations in the coating dominates the one in the substrate; gravity gradient noise accounts for time-changing Newtonian gravitational forces.

5.3 Improvements in Advanced LIGO Sensitivity

5.3.1 Matched-Filtering Signal-to-Noise Ratio

To quantify the astrophysical merit of various configurations, we will calculate the improvement in the matched-filtering signal to-noise ratio (SNR) or the detectable distance for a given threshold SNR, respectively, for inspiral waves from compact binary systems. For a known waveform (in the frequency domain) $h(f)$, the optimal SNR achievable by correlating the data with a known template is

$$\rho = 2\sqrt{\int_0^\infty \mathrm{d}f \; \frac{|h(f)|^2}{S_h(f)}}, \tag{5.16}$$

where $S_h(f)$ is the single-sided noise spectral density. For compact binary objects, the lowest post-Newtonian approximation gives (see, e.g., [19])

$$|h(f)| = \frac{G^{5/6}\mu^{1/2}M^{1/3}}{\sqrt{30}\pi^{2/3}c^{3/2}D} \; f^{-7/6} \; \Theta(f_{\max} - f), \tag{5.17}$$

with

$$M = (M_1 + M_2), \quad \text{and} \quad \mu = \frac{M_1 M_2}{M_1 + M_2}, \tag{5.18}$$

where μ, M, M_1 and M_2 are the reduced, total and single masses of the binary and D is the distance from the source to the detector. Here the amplitude is the one where rms average over all directions is already taken into account. There is an upper cutoff frequency, $f_{\max}$, in Eq. (5.17) beyond which the systems undergoes a transition from adiabatic inspiral into non-adiabatic merger, and Eq. (5.17) is no longer a valid approximation. This frequency is usually taken to be the GW frequency at the last stable circular orbit given, for a test mass in a Schwarzschild space time with mass M

$$f_{\max} \approx 4400 \text{ Hz} \left(\frac{M_\odot}{M}\right). \tag{5.19}$$

A lower cutoff frequency $f_{\min}$ should also be applied to the integration in Eq. (5.16), below which it is no longer possible to treat the system as stationary. We take $f_{\min} \approx 7$ Hz. Considering binaries of averaged orientation the observable distance for a given SNR ρ_0 reaches

$$D = \sqrt{\frac{2}{15}} \frac{G^{5/6}\mu^{1/2}M^{1/3}}{\pi^{2/3}c^{3/2}\rho_0} \sqrt{\int_{f_{\min}}^{f_{\max}} \mathrm{d}f \; \frac{f^{-7/3}}{S_h(f)}}\,. \tag{5.20}$$

In this paper, we assume event rate to be proportional to the cube of detectable distance, i.e.,

$$\mathcal{R} \propto D^3\,. \tag{5.21}$$

Table 5.2: Parameters used when optimizing our proposed double readout scheme and the usual Advanced LIGO like configuration each for different binary systems[4].

$M/M_\odot$	parameters w/ local meter			parameters w/o local meter			improvement
	$P^{(1)}$ in kW	ϕ in rad	$\zeta^{(1)}$ in rad	$P^{(1)}$ in kW	ϕ in rad	$\zeta^{(1)}$ in rad	in event rate
2.8	800	0.48π	0.7π	800	0.48π	0.49π	29 %
20	450	0.47π	0.58π	500	0.48π	0.48π	28 %
30	250	0.46π	0.46π	200	0.46π	0.49π	30 %
40	150	0.45π	0.43π	150	0.45π	0.46π	33 %
80	100	0.45π	0.38π	100	0.45π	0.46π	44 %
120	100	0.46π	0.32π	100	0.47π	0.41π	42 %
160	110	0.47π	0.25π	100	0.47π	0.30π	45 %
200	110	0.48π	0.25π	100	0.48π	0.27π	48 %

5.3.2 Improvement in the Event Rate

The tools reviewed in the previous subsection enable us to optimize a specific interferometer configuration for given binary inspirals by maximizing its SNR with respect to certain interferometer parameters. Note that we now take also classical noise into account as it is indicated by the grey lines in Fig. 5.4. In this paper we assume that Advanced LIGO refers to a signal recycled interferometer without local readout and optimized for neutron star-neutron star (NS-NS) binary systems, i.e., binary system with $M = (1.4 + 1.4)\ M_\odot$. We then vary the optical power $P^{(1)}$, detuning $\phi^{(1)}$ and detection angle $\zeta^{(1)}$ in such a way that the SNR of the signal recycled interferometer without local readout is maximized for the total mass of a given binary system in tab. 5.2. When we optimize our scheme, we maximize the SNR varying the same set of parameters of the large-scale interferometer (cf. tab. 5.2) but with imposing a fixed power for the second carrier ($P^{(2)} = 4\,\mathrm{kW}$), requiring the second carrier to be resonant in the signal recycling cavity ($\lambda^{(2)} = 0$), and fixing a detection quadrature phase of $\zeta^{(2)} = 0$ (i.e., detecting the phase quadrature). Such a prescription is justified because a local meter with such a short arm length, low power and finesse (as we have chosen) is mostly dominated simply by shot noise.

If we compare the two schemes with and without an added local meter at the binary mass they are optimized for we find moderate improvement in event rates (cf. last column in tab. 5.2). The improvement increases for higher binary masses since our scheme helps to enhance sensitivity mainly at low frequencies. Such a moderate improvement has been limited mainly due to low-frequency classical noise.

The advantage of the local readout scheme can be appreciated better when we realize that there are different populations of likely sources (e.g., binary total mass M can reside in a range, $\mathcal{M}$), whose signals extend to different frequency bands. We need to investigate how good a configuration optimized for a particular system with total mass M would perform for other possible masses in $\mathcal{M}$. In this paper, we consider $\mathcal{M} = [M_\odot,\ 630\,M_\odot]$ with maximum mass determined by the condition $f_{\max} = f_{\min}$. In Fig. 5.5, we show the improvements in event rates (with respect to Advanced LIGO baseline, optimized for NS-NS binaries) obtainable by Advanced LIGO configurations (solid lines) and double readout configurations (dashed lines) for binaries with $M \in \mathcal{M}$, when the configurations are optimized specifically for $M = 2.8\,M_\odot$ (black), $40\,M_\odot$ (dark gray) and $120\,M_\odot$ (light gray). In Fig. 5.4, we show the corresponding noise spectral densities of these configurations together with classical noise. Figures 5.5 and 5.4 provides us with at least two possible applications of the double readout scheme.

Detector with broader frequency band. The sensitivity of the double readout configuration optimized for $2.8\,M_\odot$ systems (solid curve on the upper left panel of Fig. 5.4) is broader in band and globally better than the baseline design of Advanced LIGO (dashed curve in the same figure) particularly at higher frequencies; this demonstrates that when an overall optimization is performed, the local readout can indirectly improve sensitivity at higher frequencies. Although Fig. 5.5 (solid curve) does not show a significant increase in binary event rates, this configuration is potentially interesting for detecting other sources above 300 Hz, for example pulsars and Low-Mass X-ray Binaries.

Detector for intermediate-mass black-hole binaries. The double readout configuration optimized for $40\,M_\odot$ systems (dark gray curve in Fig. 5.5) has the same sensitivity to low-mass binary systems as Advanced LIGO baseline (up to $M = 10\,M_\odot$), while improving event rates for $60\,M_\odot$ to $300\,M_\odot$ by factors of 2 to 4.5. This allows us to build a detector sensitive to the more speculative (yet in some sense astrophysically more interesting) intermediate-mass black-hole binaries, without sacrificing sensitivity at low-mass systems which are more certain to exist. As we see from dashed curves in Fig. 5.5, such broad improvement simultaneously for systems with different total masses is not achievable by single-readout Advanced LIGO-like configurations. It is also interesting to note that this configuration only requires a circulating power of 150 kW in the arms.

The improvement in event rate increases significantly for higher binary masses (cf. gray curve in Fig. 5.5 optimized for $M = 120\,M_\odot$) since the local meter helps to enhance sensitivity mainly at low frequencies. But if we optimize for such high masses the sensitivity for lower masses cannot keep up with Advanced LIGO.

It turns out that our scheme even improves sensitivity in the low-frequency regime when sensitivity is dominated by classical noise, as can be seen in Fig. 5.5, since for high binary masses the dashed curves meet at a factor of $(4/3)^{3/2}$ below the solid curves. We explain this factor in the appendix.

5.4 Implementation Issues

In this section we discuss the possibility of implementing this technique explicitly in the Advanced LIGO detector. In fact, the so-called central Michelson degree of freedom in the detector, already to be measured to keep the signal extraction port of the interferometer in dark fringe, is exactly what

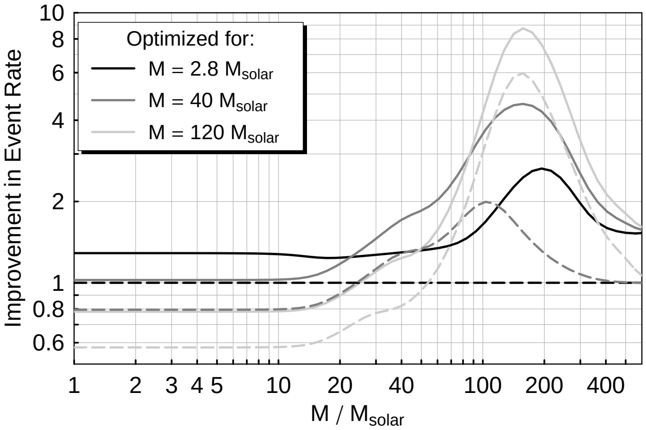

Figure 5.5: Improvement in the event rate compared to Advanced LIGO versus total binary mass with fixed optimization parameters for each curve. Signal-recycled interferometer with (solid lines) and without (dashed lines) local readout are optimized for three different binary masses. Power of 2nd carrier is fixed to $P^{(2)} = 4$ kW.

our local readout scheme proposes to measure. However, sensitivity of the current Michelson control signal must be improved dramatically in order to be turned into our regime. We note that more precise measurement of this Michelson degree of freedom also helps to decrease control-loop noise, which is shot noise imposed on the control signal coupling to the main signal due to unavoidable imbalances [20].

Optical power. In the baseline design, a pair of radio frequency (RF) sidebands created around the main carrier frequency will be injected to probe the motion as it is already done in current detectors. However, the power level of current RF sidebands is not high enough for our local readout. In the baseline design, the input power is 125 W, which is amplified to ~ 1.0 kW at each ITM, due to power recycling. Only about 1% of the power at the input port is pumped into the RF sidebands that resonate in the power recycling cavity but not in the arms. Taking into account the fact that the RF sidebands do not enter the arm cavities and thus suffer from less optical losses, the power of the Michelson-control sidebands at the ITM is currently planned to be $\sim 34\,\mathrm{W}$. Thus, one needs to raise the current power by ~ 120 times in order to achieve $P^{(2)} = 4\,\mathrm{kW}$. Another more realistic way of realization is to use a phase-locked secondary laser with its frequency shifted by an odd number of half free-spectral ranges from the primary laser to satisfy the off-resonant condition in the arms. Furthermore, this subcarrier should almost be in dark fringe at the signal extraction port and should be resonant in both recycling cavities. To achieve a circulating power of $P^{(2)} = 4\,\mathrm{kW}$ for the subcarrier we even need a little more input power than for the primary laser. But we can hope to use the higher-power laser for the sub-carrier while the parametric instability [21, 22] in the arm cavity may limit the power of the primary laser. Indeed, a circulating power of $P^{(2)} = 4\,\mathrm{kW}$ is only a few times more than the carrier power of the current GEO detector, which has a similar topology compared to the local meter.

Detection. Each signal at the dark port should be extracted with some reference field, which will be another set of RF sidebands in the RF readout scheme, or DC offset light in the DC readout scheme. The former one leaks through the dark port via macroscopic asymmetry in the central Michelson interferometer, and the latter one leaks through the dark port via microscopic asymmetry between two arm cavities. Either way, the reference fields for the carrier and the sub-carrier should be isolated before the photo detection, otherwise the reference field which is not used for the signal extraction will just impose extra shot noise. One way to solve the problem is to make use of orthogonal polarizations. Before the photo detection, the carrier and the sub-carrier accompanied with the reference fields can be separated by a polarized beam splitter, which is all-reflective to one polarization and transmissive to the other. In addition, it is easy to combine the two beams before injection into the interferometer without losing the power. An alternative way to the orthogonal polarizations is to use a cavity that can separate the beams at different frequencies, where one resonates in the cavity while the other does not. The cavity, a so-called output-mode-cleaner, is already planned to be used at the detection port in Advanced LIGO. In the same way an input mode cleaner cavity can be used to combine two beams before the injection into the interferometer.

Alternative configuration. One may also place the local meters around the ETMs. In this case, a single laser beam, which can be different in frequency from the carrier light, should be split and brought to each end of the arms so that laser noise can be cancelled out after taking a subtraction of the two ETMs' motion measurements. A cavity can be implemented as well as it is proposed for a radiation-pressure-noise reduction method in [13, 14]. In this way the secondary laser for the local readout does not need such high power and there is no concern of a heat problem at the BS and the ITMs. However, in this case much more additional optical components are required to realize this configuration.

5.5 Conclusion

Motivated by the optical-bar schemes [12] and quantum-locking schemes [13, 14], we have proposed injecting a second laser beam into detuned signal recycled Michelson interferometers, sensing the differential motion of the input mirrors, and improving low-frequency sensitivities of these interferometers, currently at low frequencies being limited by the rigidity of the optical spring. We derived the optimal combined sensitivity of this double readout scheme, and demonstrated that this optimal sensitivity is invariant with respect to the application of a feedback control scheme.

Taking into account the current classical noise budget of Advanced LIGO as well constraints on optical power, we performed an optimization of our double readout schemes toward the detection of compact binary inspirals. This scheme is shown either to be able to broaden the detection band and (indirectly) significantly improving high-frequency sensitivities, or to allow the detection of intermediate-mass black-hole binaries with a broad frequency range without sacrificing sensitivity to neutron-star binaries and stellar-mass black-hole binaries.

We also discussed briefly how the sensing of the Michelson degree of freedom in the currently plan of Advanced LIGO can be made dramatically more sensitive and turned into our local readout scheme.

Finally, we would like to point out that this scheme should be further investigated as a candidate design for third-generation detectors, possible in conjunction with the injection of squeezed vacuum states [23, 24] into the interferometer's dark port [25, 26].

5.6 Appendix: Double-Readout Scheme Dominated by Classical Noise

Suppose at low frequencies, sensing noise is negligible, and noise is dominated by the classical force noise acting on the mirrors. Then, the first carrier offers the following

$$\hat{y}^{(1)} \propto \hat{\xi}_{\rm ETM} - \hat{\xi}_{\rm ITM} + Lh\,, \tag{5.22}$$

where $\xi_{\rm ETM}$ and $\xi_{\rm ITM}$ are classical noise on the ITM and the ETM, respectively. The output of the second carrier is proportional to

$$\hat{y}^{(2)} \propto \hat{\xi}_{\rm ETM} + \hat{\xi}_{\rm ITM} + 2\sqrt{2}\hat{\xi}_{\rm BS} + Lh\,, \tag{5.23}$$

where $\xi_{\rm BS}$ is the classical noise acting on the BS. Suppose again that $\xi_{\rm ITM}$, $\xi_{\rm ETM}$, and $\xi_{\rm BS}$ have independent noise at the same level for ITM and ETM but half as high for the BS (cf. Eqs. (5.6)). We obtain that the optimal filter uses three fourths of the output of the large-scale interferometer and one fourth of the small interferometer in the units as above. This is in contrast to the optimal filter functions when only quantum noise is taken into account as in the left panel of Fig. 5.3. Then the combined output is given by

$$\hat{y} \propto \xi_{\rm ETM} - \frac{1}{2}\xi_{\rm ITM} + \frac{1}{\sqrt{2}}\xi_{\rm BS} + Lh\,. \tag{5.24}$$

Then the large-scale interferometer's noise spectral density versus the optimal noise spectral density reads $2/\frac{3}{2}$ which gives the factor in Fig. 5.5. In this way the double readout is able to cancel some fraction of the classical noise.

5.7 Bibliography

[1] D. Shoemaker and The LIGO Scientific Collaboration, *Nucl. Inst. and Meth. A* **517**, 154 (2004).

[2] L. D. Fiore and VIRGO collaboration, *Class. Quant. Grav.* **19**, 1421 (2002).

[3] B. Willke et al., *Class. Quant. Grav.* **19**, 1377 (2002).

[4] M. Ando and TAMA collaboration, *Phys. Rev. Lett.* **86**, 3950 (2001).

[5] G. Heinzel, A. Freise, H. Grote, K. Strain, and K. Danzmann, *Class. Quant. Grav.* **19**, 1547 (2002).

[6] www.ligo.caltech.edu/advLIGO.

[7] A. Buonanno and Y. Chen, *Phys. Rev. D* **64**, 042006 (2001).

[8] A. Buonanno and Y. Chen, *Phys. Rev. D* **65**, 042001 (2002).

[9] A. Buonanno and Y. Chen, *Phys. Rev. D* **67**, 062002 (2003).

[10] K. Somiya, P. Beyersdorf, K. Arai, S. Sato, S. Kawamura, O. Miyakawa, F. Kawazoe, S. Sakata, A. Sekido, and N. Mio, *Appl. Opt.* **44**, 3179 (2005).

[11] O. Miyakawa, et al., *Phys. Rev. D* **74**, 022001 (2006).

[12] V. B. Braginsky, M. L. Gorodetsky, and F. Y. Khalili, *Phys. Lett. A* **232**, 340 (1997).

[13] S. Kawamura, O. Miyakawa, and K. Somiya, "Reduction of radiation pressure noise using an auxiliary interferometer in a laser interferometric gravitational wave antenna", unpublished manuscript (2001).

[14] J. M. Courty, A. Heidmann, and M. Pinard, *Phys. Rev. Lett.* **90**, 083601 (2003).

[15] H. J. Kimble, Y. Levin, A. B. Matsko, K. S. Thorne, and S. P. Vyatchanin, *Phys. Rev. D* **65**, 022002 (2001).

[16] T. Corbitt, Y. Chen, and N. Mavalvala, *Phys. Rev. A* **72**, 013818 (2005).

[17] J. Harms, R. Schnabel, and K. Danzmann, *Phys. Rev. D* **70**, 102001 (2004).

[18] http://www.ligo.mit.edu/bench/bench.html.

[19] T. Damour, B. R. Iyer, and B. S. Sathyaprakash, *Phys. Rev. D* **62**, 084036 (2000).

[20] K. Somiya, O. Miyakawa, P. Fritschel, and R. Adhikali, LIGO-T060272-00-I (2006).

[21] V. B. Braginsky, S. E. Strigin, and S. P. Vyatchanin, *Phys. Lett. A* **287**, 331 (2001).

[22] V. B. Braginsky, S. E. Strigin, and S. P. Vyatchanin, *Phys. Lett. A* **305**, 111 (2002).

[23] H. Vahlbruch, S. Chelkowski, B. Hage, A. Franzen, K. Danzmann, and R. Schnabel, *Phys. Rev. Lett.* **97**, 011101 (2006).

[24] K. McKenzie, N. Grosse, W. P. Bowen, S. E. Whitcomb, M. B. Gray, D. E. McClelland, and P. K. Lam, *Phys. Rev. Lett.* **93**, 161105 (2004).

[25] J. Harms, Y. Chen, S. Chelkowski, A. Franzen, H. Vahlbruch, K. Danzmann, and R. Schnabel, *Phys. Rev. D* **68**, 042001 (2003).

[26] A. Buonanno and Y. Chen, *Phys. Rev. D* **69**, 102004 (2004).

Chapter 6

Optimal Quantum Filtering in Advanced LIGO Interferometers

With the continuous improvements of measurement sensitivities in gravitational-wave interferometers, investigations of quantum mechanical behaviors of macroscopic test masses become feasible. Quantum mechanical experiments to double optical spring device is studied, yet these tools will apply to Advanced LIGO interferometer , which has arm lengths of a few kilometers and test masses weights of a few kilograms. To observe these macroscopic effects, we must extract signals from various environment noises, such as seismic noise, suspension thermal noise and mirror thermal noise. We have found that the Wiener filter is a useful tool to achieve this goal. In this chapter, we apply and extend the classical Wiener filter to this type of experiments and demonstrate not only for practical use of noise reduction, but also theoretical meaning of calculating the result of state collapse. Furthermore, we also build a natural connection between classical Wiener filter and quantum filter via the path integral approach.

Paper in preparation

6.1 Introduction

The continuous quantum measurement of macroscopic objects was first investigated in the context of gravitational wave detection [1]. In laser interferometer gravitational wave detectors, incoming gravitational waves induce very weak tidal forces on mirror-endowed test masses. These are approximately free masses since they are hung from seismic isolation stacks as pendulums with eigenfrequency much below the detection band. The interferometer measures the change in the test-mass mirror's relative positions. The position observable, however, does not have commuting Heisenberg operators at different times. This gives a standard quantum limit (SQL) for such interferometers

[1],

$$S_h^{\mathrm{SQL}} = \frac{8\hbar}{m\Omega^2 L^2}, \tag{6.1}$$

for the dimensionless gravitational-wave signal $h(t) = \Delta L/L$. Here m is the mass of each identical test mass, L is the cavity length, ΔL is the displacement of the test mass under tidal forces, Ω is the frequency of the gravitational-wave and $\hbar$ is the Planck's constant. Because gravitational-wave sources are usually distant objects, in order to detect the signal, the design sensitivities of laser interferometric gravitational-wave (GW) detectors (LIGO/VIRGO/TAMA/GEO) must reach or surpass the SQL. Examples of methods that can beat SQL include (i) injecting squeezed vacuum into an interferometer's dark port [2], (ii) implementing frequency-dependent homodyne detection [3], and (iii) speed-meter designs [4], (iv) modifying the test-mass dynamics with an optical spring [22, 23, 24]. Meanwhile it is also necessary to reduce the classical noises such as the thermal noise.

As the design sensitivities approach the SQL, it becomes feasible that we use interferometers to do macroscopic quantum mechanical experiments. By macroscopic we mean that the instruments have arm lengths of a few kilometers and test mass weights of a few tens of kilograms, or somewhat smaller in the case of the MIT experiment. For example, if the noise is below the SQL, nearly pure quantum states can be prepared via measurement induced state collapse. After that we can do many interesting quantum mechanical experiments such as quantum teleportation, quantum swapping and so on. We can also investigate quantum mechanical entanglement between the optical field and the test masses, as well as entanglement between test masses [6].

Because the motions of the test masses are way smaller than $\lambda/\mathcal{F}$, where λ is the wavelength and $\mathcal{F}$ is the finesse of the cavity, the system can be well approximated by a linear system with Gaussian white noise; classical theories of optimal filtering and stochastic control for linear systems are applicable to the current problem. The key results from Wiener filtering and optimal stochastic control will be very helpful when we analyze the data from these experiments. In this chapter we apply and extend the theory of Wiener filtering to some typical macroscopic quantum mechanical experiments.

6.2 Optimal Wiener Filtering and Its Relation to Ordinary Linear Regression

6.2.1 Wiener Filter

In this subsection we present the Wiener filter which as the optimal least-mean-square estimate of a linear system. After that we will show the analogy between Wiener filter and linear regression in finite dimension. The results in this subsection will be used in Sec. 6.4 when we discuss the state preparation problem in Advanced LIGO interferometers (AdvLIGO [5]).

Suppose that we have a stable linear quantum mechanical system with a complete set of linear observables $\{X(t), -\infty < t < \infty\}$. We further assume that $X(t)$ does not depend on initial conditions, but instead depends only on the states of the incoming fields, with dependence decays exponentially to the distant past. In order to gain some information of this system we measure the states of a probe, which are denoted by $\{Y(t), -\infty < t < \infty\}$. We further assume that our linear quantum system satisfies causality and the quantum nondemolition (QND) condition, which means

$$[Y(t'), X(t)] = 0, \forall t' < t \quad [Y(t), Y(t')] = 0, \forall t, t'. \tag{6.2}$$

Our goal is to use $\{Y(t'), -\infty < t' < t\}$ to predict the value of $X(t)$.

It turns out that the linear optimal estimate can be obtained by doing the following decomposition,

$$X(t) = \int_{-\infty}^{t} dt' K(t-t') Y(t') + R(t), \tag{6.3}$$

where the first term on the right-hand side is our linear optimal estimate of $X(t)$ given the measurement history of $\{Y(t'), -\infty < t' < t\}$. The second term, $R(t)$, is the residual noise that is uncorrelated to $Y(t')$, i.e.,

$$\langle R(t) Y(t') \rangle = 0, \forall t' < t. \tag{6.4}$$

This is very similar to the ordinary linear regression where we decompose $X(t)$ into a vector in the linear space spanned by $\{Y(t') : -\infty < t' < t\}$ and a noise term which is orthogonal to $Y(t')$. The orthogonality here is according to the inner product defined by taking covariance,

$$\langle A, B \rangle \equiv E[AB] - E[A]E[B]. \tag{6.5}$$

We will use this correspondence between Wiener filter and ordinary linear regression later in this section.

Once we have the decomposition, the optimal estimate of $X(t)$ is just the conditional mean

$$\begin{aligned} \hat{X}(t) &\equiv E[X(t) | Y(t') = y(t'), \forall t' < t] \\ &= \int_{-\infty}^{t} dt' K(t-t') y(t') + E[R(t) | Y(t') = y(t'), \forall t' < t] \\ &= \int_{-\infty}^{t} dt' K(t-t') y(t'). \end{aligned} \tag{6.6}$$

The second equality holds because $R(t)$ is independent of $\{Y(t') : -\infty < t' < t\}$ and $E[R(t)] = 0$. It is also easy to show that the conditional variance of the estimate $\hat{X}$ is,

$$\mathrm{Var}[X(t)|Y(t') = y(t'), \forall t' < t] = E[R^2(t)] = E\left[\left(X(t) - \int_{-\infty}^{t} dt' K(t-t')Y(t')\right)^2\right]. \tag{6.7}$$

The kernel $K(t)$ that minimizes the conditional variance is called the Wiener filter, which filters the measurement in $Y(t')$ and yields the best estimate of $X(t)$. To determine $K(t)$, we need to solve the so-called Wiener-Hopf equation

$$C_{XY}(t - t'') - \int_{-\infty}^{t} dt' K(t-t')C_{YY}(t' - t'') = 0, \quad \forall t'' < t, \tag{6.8}$$

where C_{XY} is the covariance between X and Y and C_{YY} is the variance of Y. This equation is straightforward to solve through the Wiener-Hopf method if the power spectra $S_{XY}(\Omega)$ and $S_{YY}(\Omega)$ of the stationary process $\{X(t), Y(t)\}$ are rational polynomials. We present the solution here; further references can be found in [7, 8, 9].

First we can rewrite Eq. (6.8) as

$$C_{XY}(x) - \int_{0}^{\infty} K(y)C_{YY}(x - y)dy = 0, \forall x > 0. \tag{6.9}$$

We can extend the definition of the filter function by letting $K(y) = 0, \forall y < 0$. This definition makes K to be a causal function and allows us to rewrite Eq. (6.8) as

$$C_{XY}(x) - \int_{-\infty}^{\infty} K(y)C_{YY}(x - y)dy = 0, \forall x > 0, K \text{ causal}. \tag{6.10}$$

After applying a Fourier transform to Eq. (6.10), we obtain a function in Ω,

$$L(\Omega) = S_{XY}(\Omega) - \tilde{K}(\Omega)S_{YY}(\Omega) \tag{6.11}$$

that must be analytic in the lower-half complex plane–so that Eq. (6.10) holds for $x > 0$. Here $\tilde{K}$ is the Fourier transform of $K(y)$, which must be analytic in the upper-half complex plane. Note that our convention for Fourier transform is

$$F(\Omega) = \int_{-\infty}^{\infty} f(t)e^{i\Omega t}dt, \quad f(t) = \int_{-\infty}^{\infty} F(\Omega)e^{-i\Omega t}\frac{d\Omega}{2\pi}. \tag{6.12}$$

In order to obtain $\tilde{K}$, we first factor $S_{YY}(\Omega) = \phi^{+}_{YY}(\Omega)\phi^{-}_{YY}(\Omega)$, in such a way that $\phi^{+}_{YY}(\Omega)$ only has poles and zeros in the lower-half complex plane (i.e., $\phi^{+}_{YY}(\Omega)$ and $1/\phi^{+}_{YY}(\Omega)$ both analytic in the upper-half complex plane), and that $\phi^{-}_{YY}(\Omega)$ only has poles and zeros in the upper-half complex plane (i.e., $\phi^-_{YY}(\Omega)$ and $1/\phi^-_{YY}(\Omega)$ both analytic in the lower-half complex plane). The condition that $L(\Omega)$ is analytic in the lower-half complex plane is equivalent to the condition that $L(\Omega)/\phi^-_{YY}(\Omega)$ is analytic in the lower-half complex plane, i.e.,

$$\frac{L(\Omega)}{\phi^-_{YY}(\Omega)} = \frac{S_{XY}(\Omega)}{\phi^-_{YY}(\Omega)} - \tilde{K}(\Omega)\phi^+_{YY}(\Omega) \tag{6.13}$$

must be analytic in the lower-half plane. We then need to break S_{XY}/ϕ^-_{YY} into a sum of two pieces, each analytic in one of the half planes, and have

$$\left[\frac{S_{XY}(\Omega)}{\phi^-_{YY}(\Omega)}\right]_- + \left[\frac{S_{XY}(\Omega)}{\phi^-_{YY}(\Omega)}\right]_+ - \tilde{K}(\Omega)\phi^+_{YY}(\Omega), \tag{6.14}$$

where $[\ldots]_+$ means being analytic in the upper-half plane, and $[\ldots]_-$ means being analytic in the lower-half plane. We must then make the last two items cancel with each other and require

$$\tilde{K}(\Omega) = \frac{1}{\phi^+_{YY}(\Omega)}\left[\frac{S_{XY}(\Omega)}{\phi^-_{YY}(\Omega)}\right]_+ . \tag{6.15}$$

This gives the causal Wiener filter

$$K(t-t') = \int_{-\infty}^{\infty}\frac{d\Omega}{2\pi}\frac{1}{\phi^+_{YY}(\Omega)}\left[\frac{S_{XY}(\Omega)}{\phi^-_{YY}(\Omega)}\right]_+ e^{-i\Omega(t-t')}, \tag{6.16}$$

which is clearly a causal function because each term involved here is analytic in the upper-half plane. We can plug the causal filter K in Eq. (6.16) into Eq. (6.7) and obtain the conditional variance

$$\mathrm{Var}[X(t)|Y(t') = y(t'), \forall -\infty < t' < t] = \int_{-\infty}^{\infty}\frac{d\Omega}{2\pi}\left[S_{XX}(\Omega) - \left[\frac{S_{XY}(\Omega)}{\phi^-_{YY}(\Omega)}\right]_+ \left[\frac{S_{XY}(\Omega)}{\phi^-_{YY}(\Omega)}\right]^*_+\right]. \tag{6.17}$$

We note that the above Wiener filtering is causal because it only uses the information of $\{Y(t'), -\infty < t' \le t\}$. If we were allowed to use the whole information $\{Y(t'), -\infty < t < \infty\}$, we would construct a similar but non-causal Wiener filter $K(t)$, which would be given by

$$K(t) = \int_{-\infty}^{\infty}\frac{d\Omega}{2\pi}\frac{S_{XY}(\Omega)}{S_{YY}(\Omega)}e^{-i\Omega t}. \tag{6.18}$$

The conditional variance based on the non-causal Wiener filtering is

$$\mathrm{Var}[X(t)|Y(t') = y(t'), -\infty < t' < \infty] = \int_{-\infty}^{\infty}\frac{d\Omega}{2\pi}\left[S_{XX}(\Omega) - \frac{S_{XY}(\Omega)S^*_{XY}(\Omega)}{S_{YY}(\Omega)}\right]. \tag{6.19}$$

However, because $[X(t), Y(t')] \neq 0$ for $t' > t$, quantum non-causal filters are subtle to define. Variances defined in this way could violate the Heisenberg Uncertainty Principle.

These results will be used in the following subsection.

6.2.2 Wiener Filtering Viewed as Linear Regression

In this subsection we will build the correspondence between the Wiener filter and ordinary linear regression. There are two reasons to do so. On one hand, the Wiener filter is constructed in the frequency domain so a time-domain method is desired for completeness. On the other hand, as we will see shortly, macroscopic quantum mechanical experiments in LIGO interferometers will require the technique of multivariate Wiener filtering. In the proposed MIT experiments [10, 11], the double optical spring scheme has been shown to provide a stable optomechanical trap [11]. At the output port of this device it is easy to separate the carrier field and its sidebands from the subcarrier field and its sidebands. This can be accomplished by using laser lights with different polarizations. In order to obtain information about the end mirror's position and momentum we must detect both the carrier and subcarrier lights. In this case we will have two readouts $Y_{1,2}(t)$ and consequently we need to do two-channel Wiener filtering. If we continue our approach in frequency domain we need to do the following factorization

$$\begin{pmatrix} S_{Y_1Y_1}(\Omega) & S_{Y_1Y_2}(\Omega) \\ S_{Y_2Y_1}(\Omega) & S_{Y_2Y_2}(\Omega) \end{pmatrix} = \Phi_+(\Omega)\Phi_-(\Omega), \tag{6.20}$$

where $\Phi_+(\Omega)(\Phi_-(\Omega))$ and its matrix inverse $\Phi_+^{-1}(\Omega)(\Phi_-^{-1}(\Omega))$ are analytic in the upper-half (lower-half) complex plane. This goal can be achieved by the so-called symmetric factors extraction method [14] which is quite complicated. In this subsection, after building the correspondence between Wiener filtering and ordinary finite-dimensional linear regression, we can obtain a simple numerical algorithm for doing multivariate Wiener filtering in the time domain.

Ordinary linear regression applies to problems where there is a linear dependence between the response X and n predictors $Y_1, \ldots, Y_n$. This dependence is subject to an error ϵ such that

$$X = \beta_1 Y_1 + \ldots + \beta_n Y_n + \epsilon, \tag{6.21}$$

where β_i are the corresponding coefficients. Without loss of generality we can assume X and $\vec{Y} \equiv (Y_1, Y_2, \ldots, Y_n)^T$ are zero mean random variables with known covariances. Then it is quite straightforward to show that if the error ϵ is statistically uncorrelated with $\vec{\beta} \equiv (\beta_1, \beta_2, \ldots, \beta_n)^T$, $\vec{\beta}$ must satisfy

$$\vec{\beta} = \left[\mathrm{Var}(\vec{Y})\right]^{-1} \mathrm{Cov}(\vec{Y}, X), \tag{6.22}$$

so that X and its estimate $\hat{X} \equiv \vec{\beta}^T \cdot \vec{Y}$ has the minimal difference in the mean square sense. We note the similarity between Eq. (6.3) and Eq. (6.21) where both equations try to project X into linear spaces spanned by the measurement data and the errors are perpendicular to the linear spaces. This similarity is most obvious when we derive the non-causal Wiener filter from the ordinary least square. Let us discretize the measurement time t to integers. After measuring $Y(t), t = -\infty, \ldots, -1, 0, 1, \ldots, \infty$, we can give a linear estimate of X by $\hat{X} = \vec{\beta}^T \cdot Y$ where $\vec{\beta}$ is calculated according to Eq. (6.22). Hence $\vec{\beta}$ satisfies the equation

$$\left[\mathrm{Var}(\vec{Y})\right]^{-1} \vec{\beta} = \mathrm{Cov}(\vec{Y}, X). \tag{6.23}$$

If we consider $\mathrm{Var}(\vec{Y}), \mathrm{Cov}(\vec{Y}, X)$ and $\vec{\beta}$ to be functions that are defined on integers, we can rewrite Eq. (6.23) in a component form

$$\sum_{i=-\infty}^{\infty} C_{YY}(i)\beta(j) = C_{XY}(i+j), \quad j = -\infty, \ldots, -1, 0, 1, \ldots, \infty \tag{6.24}$$

where $C_{YY}(i)$ and $C_{YX}(i)$ are autocorrelation and cross correlation functions of the random processes $\{Y(t), X(t)\}$. In the continuous limit, Eq. (6.24) reduces to

$$\int_{-\infty}^{\infty} \beta(y) C_{YY}(x-y) dy = C_{XY}(x), \tag{6.25}$$

which is the same equation that the non-causal Wiener filter satisfies [7, 8]. Therefore if we measure $\{Y(t), t = -\infty, \ldots, -1, 0, 1, \ldots, \infty\}$ and make an ordinary linear regression, the resulting coefficients $\vec{\beta}$ will approach the non-causal Wiener filter $K(t)$ in the continuous limit.

To further explore this correspondence, we give a numerical example where the ordinary linear regression of the history $\{Y(t), t = -\infty, \ldots, -1, 0\}$ yields the causal Wiener filter. In Fig. 6.1 we show the comparison between the causal Wiener filtering and the ordinary linear regression, for the stochastic processes $\{X(t), Y(t)\}$ with power spectra

$$\begin{aligned} S_{XX}(\Omega) &= \frac{1}{\Omega^2 + 7^2}, \\ S_{XY}(\Omega) &= \frac{1}{(\Omega^2 + 4.5^2)(\Omega^2 + 3 \times 4.5^2)}, \\ S_{YY}(\Omega) &= \frac{1}{\Omega^2 + 2^2}. \end{aligned} \tag{6.26}$$

The solid line is the optimal Wiener filter and the dots are the ordinary linear regression coefficients. We find a nice agreement between two methods.

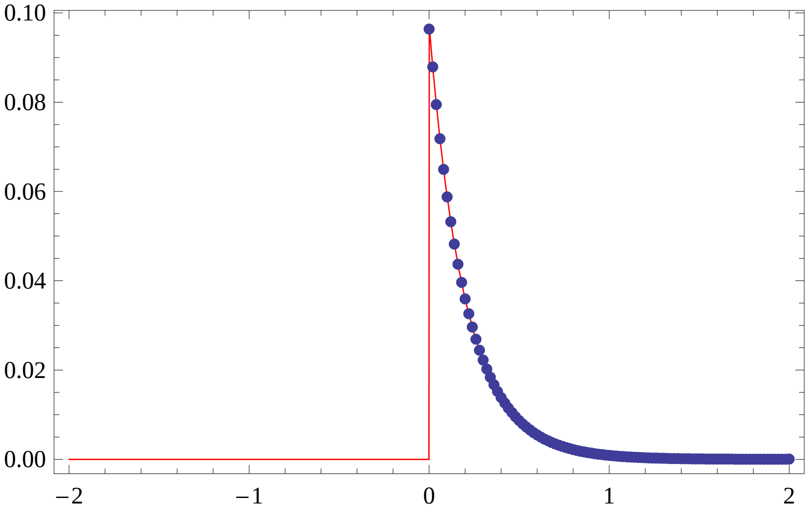

Figure 6.1: Comparison between the optimal Wiener filter and the ordinary linear regression for stochastic processes $\{X(t), Y(t)\}$ with power spectra equation (6.26). The solid line is the optimal Wiener filter and the dots are the ordinary linear regression coefficients.

6.3 Quantum Filtering via the Path Integral Approach

In this section, we show how to obtain the result of causal Wiener filtering via the path integral approach. $X(t)$ are Heisenberg operator of system observables and $Y(t)$ are measurement data. In macroscopic quantum mechanical experiments, usually the object is the mirror and the the probe is the optical field. We denote the object's density matrix by $\rho_o(t)$ and consider its evolution under a linear continuous measurement. Our goal is to describe the estimation of the object's quantum state when the measurement results are given. Different from the usual treatment of this problems (such as [18, 19, 20]), we consider the case that not only backaction but also measurement noises are non-Markovian. This section is largely based on discussions with Yasushi Mino.

In the Heisenberg picture, we assume the Hamiltonian of the entire system (i.e., the object and the probe) is described by

$$\hat{H} = \hat{H}_o + \hat{H}_p + \hat{H}_e + \hat{H}_{\text{measure}} + \hat{H}_{\text{int}}, \tag{6.27}$$

where $\hat{H}_o$, $\hat{H}_p$ and $\hat{H}_e$ consist of operators for the object, the probe and the environment respectively. They describe the free-evolution of these operators and we do not need to consider their specific forms in this subsection. $\hat{H}_{\text{measurement}}$ and $\hat{H}_{\text{int}}$ describe the quantum measurement process of the object by the probe and the interaction of the object with the environment respectively. We next calculate the evolution of the object's density matrix under continuous measurements and the interaction with the environment. For this purpose, we adopt the interaction picture and assume we have the free-evolution operators of the object, the probe and the environment, which we denote by $\hat{X}^{(0)}, \hat{a}_i^{(0)}(t)$ and $\hat{b}_j^{(0)}(t)$ respectively.

We denote the evolution operator by $\hat{U}(t, t_0)$ which satisfies

$$i\hbar \frac{d}{dt}\hat{U} = (\hat{H}_{\text{measurement}} + H_{\text{int}})\hat{U}, \quad \hat{U}(t_0, t_0) = \hat{I}, \tag{6.28}$$

where $\hat{I}$ is the identity operator. The evolution of the entire system (the object, the probe and the environment) is described by

$$\rho(t) = \hat{U}(t, t_0)\rho(t_0)\hat{U}(t, t_0)^\dagger, \tag{6.29}$$

where $\rho(t)$ is the density matrix of the entire system. For simplicity we assume that the initial density matrix is described by $\rho(t_0) = \rho_o(t_0) \otimes \rho_p(t_0) \otimes \rho_e(t_0)$, where $\rho_o(t_0), \rho_p(t_0)$ and $\rho_e(t_0)$ are the initial density matrices for the object, the probe and the environment respectively. By taking appropriate state reductions over the probe and the environment, one can derive the evolution of the object's density matrix.

The environment is an uncontrolled system which introduces a noise to the object's quantum state. We do not know the initial state or the final state of the environment. However, we may have a statistical property of the environment such as its temperature; specifically, we know the spectrum of $\hat{b}_j^{(0)}$. The typical way to deal with the environment is to take the thermal state as the initial density matrix for the environment and to take the trace over the final state of the environment. By taking the trace we consider all the possible final states of the environment with statistical weight. On the other hand, we control the probe's initial state in order to maximize the detection efficiency. We also have a measurement record of the probe with which we can infer to which state the object has been collapsed. By taking the state reduction of the probe to the specific state followed by the measurement record, we can describe the conditioned evolution of the object's density matrix.

6.3.1 Evaluating Conditional Expectations via the Generating Functional

Our full system is made up of the object, the probe and the environment. Because we are looking at Gaussian states, the first and second moments contain the full information about the system's evolution. In this subsection, we present some formal expressions for the conditional expectations and covariances of the object variable X given that we have continuously measured the probe variable Y.

First let us consider a single measurement of the probe. Let $\mathcal{H} = \mathcal{H}_o \otimes \mathcal{H}_p \otimes \mathcal{H}_e$ be the full Hilbert space of the system which consists of the object, the probe and the environment. $\rho(t)$ is the full density matrix for the system. Suppose we measure the probe variable Y at time $t = t_1$ and obtain the result y_1. Then the reduced conditional density matrix for the object can be written as

$$\rho_o(t_1) = \mathrm{Tr}_e[\langle y_1|\rho(t_1)|y_1\rangle] = \mathrm{Tr}_{e,p}[\delta(Y - y_1)\rho(t_1)], \tag{6.30}$$

where we have used the relation

$$\langle y_1|\rho(t_1)|y_1\rangle = \mathrm{Tr}_p[|y_1\rangle\langle y_1|\rho(t_1)] = \mathrm{Tr}_p[\delta(Y - y_1)\rho(t_1)]. \tag{6.31}$$

In order to calculate the conditional expectation of some observable X of the object, we need to evaluate the following expression

$$E[X|Y = y_1] = \mathrm{Tr}_o[X\rho_o(t_1)] = \mathrm{Tr}_{e,p,o}[X\delta(Y - y_1)\rho(t_1)] = \mathrm{Tr}_{e,p,o}[X(t_1)\delta(Y(t_1) - y_1)\rho], \tag{6.32}$$

where ρ is the initial density matrix for the object, the probe and the environment.

To continue our discussion, we consider continuous quantum non-demolition (QND) measurements. Assume we make a series of measurements of the past history of the probe and obtain $\{y(t'), -\infty < t' < t\}$. Generalizing the result for a single measurement, we obtain the conditional expectation for the observable X as

$$E[X(t)|Y(t') = y(t'); t' \leq t] = \mathrm{Tr}_{e,p,o}\left\{X(t)\prod_{-\infty<t'\leq t}\delta(Y(t') - y(t'))\rho\right\}. \tag{6.33}$$

Using the identity that

$$\delta(x) = \int \frac{dk}{2\pi}e^{ikx}, \tag{6.34}$$

we have

$$\begin{aligned} & E[X(t)|Y(t') = y(t'); t' \leq t] \\ = \quad & \mathrm{Tr}_{e,p,o}\left\{X(t)\prod_{-\infty<t'\leq t}\int\frac{dk(t')}{2\pi}\exp[ik(t')(Y(t') - y(t'))]\rho\right\} \\ = \quad & \mathrm{Tr}_{e,p,o}\left\{X(t)\int\mathcal{D}k(t')\exp\left[i\int_{-\infty}^{t}dtk(t')(Y(t') - y(t'))\right]\rho\right\}, \end{aligned} \tag{6.35}$$

where $\mathcal{D}k(t')$ is the functional integral which is used frequently in the path integral approach [21]. In order to regularize the integral measure we require that the functional integral satisfy the normalization condition

$$\mathrm{Tr}_{e,p,o}\left\{I_o\int\mathcal{D}k(t')\exp\left[i\int_{-\infty}^{t}dt'k(t')(Y(t') - y(t'))\right]\rho\right\} = 1, \tag{6.36}$$

where I_o is the identity operator in the Hilbert space of the object.

In practice when the system becomes stable via some mechanism such as damping or feedback control, the conditional expectation will still depend on the measurement results. But the conditional variance will not depend on the initial conditions or the measurement results. Therefore in the following we will focus on evaluating the conditional variance.

The calculation of the path integral will be largely simplified after introducing the following generating functional [21]

$$J(\beta) \equiv \log \left\{ \mathrm{Tr}_{e,p,o} \left[e^{\beta X(t)} \int \mathcal{D}k(t') e^{i \int_{-\infty}^{t} dt' k(t')(Y(t') - y(t'))} \right] \right\}. \tag{6.37}$$

It is easy to show that

$$\begin{aligned} \left.\frac{dJ}{d\beta}\right|_{\beta=0} &= E[X(t)|Y(t') = y(t'); -\infty < t' \le t], \\ \left.\frac{d^2J}{d\beta^2}\right|_{\beta=0} &= E[X(t)^2|Y(t') = y(t'); -\infty < t' \le t] - E[X(t)|Y(t') = y(t'); -\infty < t' \le t]^2 \\ &= \mathrm{Var}[X(t)|Y(t') = y(t'); -\infty < t' \le t]. \end{aligned} \tag{6.38}$$

These expressions will be used in the following subsection.

6.3.2 Application to High-Finesse Fabry-Perot Michelson Interferometer

In this section we apply the above formalism to a high sensitivity position measurement device, such as Advanced LIGO. As we mentioned before the conditional mean of the observable will depend on the specific measurement history but the conditional variance will not. Without loss of generality, we can assume the measurement results of the probe are always zero, i.e.,

$$y(t') = 0, -\infty < t' \le t. \tag{6.39}$$

It is fairly straightforward to generalize the results in this subsection to non-zero measurement results but the notations will be more complicated.

We first consider the effect of the environment. Because we do not have direct access to the environment, the usual way of dealing with the environment is by taking an ensemble average. Specifically, when we write out the quantum Langevin equation to obtain the frequency domain expressions for the object and the probe, we describe the environment by its damping effect as well as a noise term $W(\omega)$ with the power spectrum [19]

$$\frac{\langle W(\omega)W^\dagger(\omega') + W^\dagger(\omega')W(\omega)\rangle}{2} = \frac{\gamma_m}{2\omega_m} 2\pi\omega\delta(\omega - \omega'), \tag{6.40}$$

and

$$[W(\omega), W(\omega')] = -\frac{\gamma_m}{\omega_m} 2\pi\omega\delta(\omega - \omega'), \tag{6.41}$$

where γ_m and ω_m are the damping rate and resonant frequency of the mirror. In the following calculation, we will use these relations to describe the environment.

We also need to specify the expressions for the object (the mirror) and the probe (the laser field). We introduce the frequency domain decomposition of $X(t), Y(t)$ according to

$$\begin{aligned} X(t) &= \int_0^\infty d\omega[X(\omega)e^{i\omega t} + X^\dagger(\omega)e^{-i\omega t}], \\ Y(t) &= \int_0^\infty d\omega[Y(\omega)e^{i\omega t} + Y^\dagger(\omega)e^{-i\omega t}], \end{aligned} \tag{6.42}$$

where the frequency domain expressions $X(\omega), Y(\omega)$ have been worked out for several interferometers [17, 22, 23, 24]. When the whole system is stable the probe only depends on the input radiation field while the mirror depends on both the input radiation field and the environment noise. In calculating the input-output relation we use the so-called two-photon formalism [25, 26] where

$$\begin{aligned} X(\omega) &= K_{o,1}a_1 + K_{o,2}a_2, \\ Y(\omega) &= K_{p,1}a_1 + K_{p,2}a_2, \end{aligned} \tag{6.43}$$

where the correlated two-photon modes field amplitudes are defined by [25, 26]

$$a_1 = \frac{a_+ + a_-^\dagger}{\sqrt{2}}, \quad a_2 = \frac{a_+ - a_-^\dagger}{\sqrt{2}i}, \tag{6.44}$$

and

$$a_+ \equiv a_{\omega_0+\omega}, \quad a_- \equiv a_{\omega_0-\omega}, \tag{6.45}$$

are the usual annihilation operators of the input radiation fields.

Below we find it more convenient to do the calculation in $a_\pm$ not $a_{1,2}$ so we rewrite Eq. (6.43) as

$$\begin{aligned} X(\omega) &= K_{o,+}a_+ + K_{o,-}a_-^\dagger, \\ Y(\omega) &= K_{p,+}a_+ + K_{p,-}a_-^\dagger. \end{aligned} \tag{6.46}$$

The explicit forms of the susceptibility functions $(K_{o,\pm}, K_{p,\pm})$ depend on the specific optical topology of the system and some of them have been worked out in Refs. [17, 22, 23, 24].

Because we assume the system to be stable and the input optical field to be in its vacuum state, following Ref. [17], the (single-sided) spectral densities can be calculated as

$$\begin{aligned} S_{XY}(\omega) &= \frac{\langle 0|XY^\dagger + Y^\dagger X|0\rangle}{2\pi} = K_{o,+}K^*_{p,+} + K_{o,-}K^*_{p,-}, \\ S_{XY}(\omega) &= \frac{\langle 0|XX^\dagger + X^\dagger X|0\rangle}{2\pi} = |K_{o,+}|^2 + |K_{o,-}|^2 \\ S_{YY}(\omega) &= \frac{\langle 0|YY^\dagger + Y^\dagger Y|0\rangle}{2\pi} = |K_{p,+}|^2 + |K_{p,-}|^2. \end{aligned} \tag{6.47}$$

Because the system is assumed to be stable and stationary, we only need to evaluate the conditional variance at $t = 0$. Hence the generating functional can be rewritten as

$$J(\beta) = \langle e^{\beta X(0)} \prod \int dk(t) e^{i\int_{-\infty}^{0} dt k(t) Y(t)} \rangle. \tag{6.48}$$

If we define a new function $\tilde{k}(t)$ such that

$$\tilde{k}(t) = \begin{cases} k(t), & t \le 0 \\ 0, & t > 0, \end{cases} \tag{6.49}$$

then Eq. (6.48) can be rewritten as

$$\begin{aligned} J(\beta) &= \langle e^{\beta X(0)} \prod \int \mathcal{D}k(t) e^{i\int_{-\infty}^{\infty} dt \tilde{k}(t) Y(t)} \rangle \\ &= \langle e^{\beta X(0)} \prod \int \mathcal{D}\tilde{k}(t) e^{i\int_{-\infty}^{\infty} dt \tilde{k}(t) Y(t)} \rangle. \end{aligned} \tag{6.50}$$

In the frequency domain, we have

$$J(\beta) = \langle e^{\beta \int d\omega (X(\omega) + X^\dagger(\omega))} \prod_{\forall \tilde{k}(\omega),\text{analytical in lower half plane}} \int \mathcal{D}\tilde{k}(\omega) \mathcal{D}\tilde{k}^*(\omega) e^{i\int_0^\infty d\omega [\tilde{k}(\omega) Y^\dagger + \tilde{k}^*(\omega) Y]} \rangle. \tag{6.51}$$

Note that we have introduced a constraint to the possible functions $\tilde{k}(\omega)$ in the functional integration. Below when we do Gaussian integration, we require that the integration transform preserves this constraint. Specifically if we want to transform the integration variables as follows

$$\tilde{k}(\omega) \to a(\omega)\tilde{k}(\omega) + b(\omega), \tag{6.52}$$

we require that $a(\omega), 1/a(\omega), b(\omega)$ all be analytical in the lower half plane. In order to simplify $J(\beta)$ we need to use the causality condition. From

$$0 = [X(0), Y(t)] = \int d\omega (K_{o,+}K^*_{p,+} - K_{o,-}K^*_{p,-}) e^{-i\omega t}, \quad t \le 0, \tag{6.53}$$

we know $K_{o,+}K^*_{p,+} - K_{o,-}K^*_{p,-}$ is analytical in the lower half plane. Therefore,

$$\int_{-\infty}^{\infty} d\omega \tilde{k}(\omega) K_{o,+}K^*_{p,+} - K_{o,-}K^*_{p,-} = 0, \quad \forall\, \tilde{k}(\omega) \text{ is analytical in the lower half plane.} \tag{6.54}$$

Combing Eq. (6.46) and Eq. (6.54) and using the property that $X(t), Y(t)$ are Hermitian operators we have

$$\int_0^{\infty} d\omega \tilde{k}(\omega)(K_{o,+}K^*_{p,+} - K_{o,-}K^*_{p,-}) + \int_0^{\infty} d\omega \tilde{k}^*(\omega)(K^*_{o,-}K_{p,-} - K^*_{o,+}K_{p,+}) = 0, \tag{6.55}$$

where we require $\tilde{k}(\omega)$ to be the Fourier transform of a real function $k(t)$ and hence analytical in the lower half plane. This useful identity allows us to simplify Eq. (6.51) as follows (we use R^- to denote the set of functions that are analytic in the lower half plane).

$$\begin{aligned} & J(\beta) \\ = \; & e^{\frac{\beta^2}{2}\int_0^\infty d\omega S_{XX}} \times \\ \prod_{\forall \tilde{k} \in R^-} & \int \mathcal{D}\tilde{k}(\omega)\mathcal{D}\tilde{k}^*(\omega) \exp\left\{\int_0^\infty d\omega \left[-\frac{1}{2}|\tilde{k}|^2 S_{YY} + \beta\tilde{k}K_{o,+}K^*_{p,+} + \beta\tilde{k}^*K^*_{o,-}K_{p,-}\right]\right\} \\ = \; & e^{\frac{\beta^2}{2}\int_0^\infty d\omega S_{XX}} \times \\ \prod_{\forall \tilde{k} \in R^-} & \int \mathcal{D}\tilde{k}(\omega)\mathcal{D}\tilde{k}^*(\omega) \exp\left\{\int_0^\infty d\omega \left[-\frac{1}{2}|\tilde{k}|^2 S_{YY} + \frac{1}{2}i\beta\tilde{k}S_{XY} + \frac{1}{2}i\beta\tilde{k}^*S^*_{XY}\right]\right\}, \end{aligned} \tag{6.56}$$

where the first equality comes from applying the Baker-Campbell-Hausdorff formula to Eq. (6.51) and the second equality comes from Eq. (6.47) and Eq. (6.55).

Similar to the procedure in Sec. 6.2 we can decompose $S_{YY} = A_+A_-$, where $A_+\,(A_-)$ and $1/A_+\,(1/A_-)$ are analytical in the upper(lower) half plane. After that we can apply an integration transformation

$$\tilde{k} \to \hat{k} = \tilde{k}A_-, \quad \tilde{k}^* \to \hat{k}^* = \tilde{k}^*A_+, \tag{6.57}$$

and obtain

$$J(\beta) = e^{\frac{\beta^2}{2}\int d\omega S_{XX}} \int \mathcal{D}\hat{k}\mathcal{D}\hat{k}^* \exp\left\{\int d\omega \left[-\frac{1}{2}|\hat{k}|^2 + \frac{1}{2}i\beta\hat{k}\frac{S_{XY}}{A_-} + \frac{1}{2}i\beta\hat{k}^*\frac{S^*_{XY}}{A_+}\right]\right\}. \tag{6.58}$$

If we decompose S_{XY}/A_- as

$$\frac{S_{XY}}{A_-} = B_+ + B_-, \tag{6.59}$$

where B_+ (B_-) are analytical in the upper (lower) half plane, we have

$$\int d\omega \hat{k} B_- = 0, \tag{6.60}$$

and therefore

$$\begin{aligned} J(\beta) &= e^{\frac{\beta^2}{2}} \int \mathcal{D}\hat{k}\mathcal{D}\hat{k}^* \exp\left\{\int d\omega \left[-\frac{1}{2}|\hat{k}|^2 + \frac{1}{2}i\beta\hat{k}B_+ + \frac{1}{2}i\beta\hat{k}^* B_-\right]\right\} \\ &= \exp\left\{\frac{\beta^2}{2}\int d\omega\left[S_{XX} - \left(\frac{S_{XY}}{A_-}\right)_+ \left(\frac{S_{XY}}{A_-}\right)_+^*\right]\right\}. \end{aligned} \tag{6.61}$$

Taking logarithm and doing two derivatives with respect to β, we recover the standard results in Sec. 6.2, Eq. (6.16). We also note that if we have nonzero measurements ($y(t) \neq 0$) by taking the first derivative we will recover Eq. (6.5), which is the optimal linear estimate [15].

6.4 Application to the MIT Squeezer Experiment

6.4.1 Multivariate Wiener Filtering for a Double Optical Spring Interferometer

In this subsection, we apply the multivariate Wiener filter to the double optical spring experiment at MIT [10, 11]. It is well known that a single optical spring connected to a free mass always makes an unstable system [23]. By contrast, the double optical spring configuration can provide a stable optomechanical trap [11]. At the output of the device it is easy to separate the carrier field and its sidebands from the subcarrier field and its sidebands. This can be achieved by using optical fields with orthogonal polarizations. Here we theoretically investigate whether it is possible to put the gram-scale mirror oscillator close to its ground state by considering the conditioning produced by continuous homodyne detections of both the carrier and the subcarrier's output fields.

Let us consider a single detuned cavity with a movable end mirror where two fields, the carrier and the subcarrier with orthogonal polarizations, are injected into the cavity. The output fields are measured by homodyne detections. As shown in Ref. [23, 24], a detuned cavity makes the power inside the interferometer depend on the motion of the mirror. This creates the so-called optical spring, which is always unstable. To make the system stable, we realize that it is possible to create damping which goes along with having an anti-restoring force. By adjusting the detuning of the carrier and subcarrier, i.e., adding an optical spring and an anti-restoring force, one can generate an effective optical spring with anti-damping (or anti-spring with damping) which is stable. We will use the formalism in [22, 23, 24] to describe the equations of motion.

The suspended mirror is a harmonic oscillator with eigenfrequency ω_m and velocity damping rate

$\gamma_m = \omega_m/Q$. The fluctuations associated to this dissipation are described by ξ which has a white noise spectrum

$$\langle \xi(\Omega)\xi^\dagger(\Omega')\rangle = 2\pi\delta(\Omega-\Omega')m\gamma_m 2k_BT. \tag{6.62}$$

Then the frequency domain equations of motion for the positions of the mirror $x(\Omega)$ and the phase quadratures $y_{1,2}(\Omega)$ are given by

$$\begin{aligned}
&x(\Omega) = R_{xx}(\Omega)\times \\
&\left((F_1(\Omega)+F_2(\Omega)) - [(K_{\rm re,1}(\Omega)+K_{\rm re,2}(\Omega)) + i\Omega(K_{\rm im,1}(\Omega)+K_{\rm im,2}(\Omega))]x(\Omega)+\xi(\Omega)\right), \\
&y_1(\Omega) = Y_1(\Omega) + R_{Y_1F_1}(\Omega)x(\Omega), \\
&y_2(\Omega) = Y_2(\Omega) + R_{Y_2F_2}(\Omega)x(\Omega),
\end{aligned} \tag{6.63}$$

where $K_{\rm re,j}$ and $\Omega K_{\rm im,j}$ are the real and imaginary parts of the ponderomotive rigidities generated by carrier and subcarrier and are given by

$$\begin{aligned}
K_{\rm re,j}(\Omega) &= \frac{m\theta_j\delta_j(\gamma_j^2+\delta_j^2-\Omega^2)}{4[\Omega^4+2(\gamma_j^2-\delta_j^2)+(\gamma_j^2+\delta_j^2)^2]} \approx \frac{m\theta_j\delta_j}{4(\gamma_j^2+\delta_j^2)}, \\
K_{\rm im,j}(\Omega) &= \frac{m\theta_j\delta_j\gamma_j}{2[\Omega^4+2(\gamma_j^2-\delta_j^2)+(\gamma_j^2+\delta_j^2)^2]} \approx \frac{m\theta_j\delta_j\gamma_j}{2(\gamma_j^2+\delta_j^2)^2},
\end{aligned} \tag{6.64}$$

where δ_j are the detunings of carrier and subcarrier, $\gamma_j = \tau_j c/(4L)$ are the cavity bandwidths and $\theta_j = 8P_j\omega_j/(mLc)$ are the coupling constants of the mirror and lights. Here the approximation in Eq. (6.64) holds in the large bandwidth limit $\gamma_j \gg \Omega$. Note that the input laser power I_j is related to the intracavity power P_j by

$$P_j = \frac{2I_j\tau_j}{2-\tau_j-2\sqrt{1-\tau_j}\cos[2\delta_jL/c]}. \tag{6.65}$$

The quantities describing the "free" radiation pressure $F_j(\Omega)$ and the "free" shot noise $Y_j(\Omega)$ for carrier and subcarrier are given by [24]

$$\begin{aligned}
F_j(\Omega) &= \sqrt{\frac{m\hbar\theta_j\gamma_j}{2}}\frac{(i\Omega-\gamma_j)a_1^{(j)}(\Omega)+\delta_j a_2^{(j)}(\Omega)}{(\Omega-\delta_j+i\gamma_j)(\Omega+\delta_j+i\gamma_j)}, \\
Y_j(\Omega) &= \frac{-2\delta_j\gamma_j a_1^{(j)}(\Omega)+(\delta_j^2-\gamma_j^2-\Omega^2)a_2^{(j)}(\Omega)}{(\Omega-\delta_j+i\gamma_j)(\Omega+\delta_j+i\gamma_j)},
\end{aligned} \tag{6.66}$$

and the susceptibilities of the system are [24]

$$\begin{aligned} R_{xx} &= -\frac{1}{m(\Omega-(a-ib))(\Omega-(-a-ib))}, \\ R_{Y_jF_j} &= -\sqrt{\frac{m\theta_j\gamma_j}{2\hbar}}\frac{\gamma_j-i\Omega}{(\Omega-\delta_j+i\gamma_j)(\Omega+\delta_j+i\gamma_j)}, \end{aligned} \tag{6.67}$$

where the mechanical resonant frequency is $\Omega_m = a+ib$ with $a=\sqrt{\omega_m^2-\gamma_m^2/4}$ and $b=\gamma_m/2$. The numerical values of the parameters are shown in table 6.1.

Table 6.1: Parameters in double optical springs

Symbol	Physical Meaning	Numerical Value
m	end mirror mass	1 g
ω_m	pendulum eigenfrequency	$2\pi\times 172$ Hz
I_1	carrier laser input power	4.76 W
c/ω_1	laser wavelength	1064 nm
γ_1	carrier half-cavity bandwidth	$2\pi\times 10,600$ Hz
δ_1	detuning of the carrier	$3\gamma_1$
I_2	subcarrier laser input power	0.24W
c/ω_2	subcarrier laser wavelength	1064 nm
γ_2	subcarrier half-cavity bandwidth	$2\pi\times 10,600$Hz
δ_2	detuning of subcarrier	$-0.5\gamma_2$
T	temperature	300K
Q	suspension quality factor	10^4

The unconditional uncertainty is usually limited by thermal noise which cannot be suppressed by the optical spring [11]

$$V_{xx}V_{pp}-V_{xp}^2 \geq \left(\frac{\gamma_m k_B T}{\gamma_{\rm os}\omega_{\rm os}}\right)^2 \gg \frac{\hbar^2}{4}, \tag{6.68}$$

where V_{xx}, V_{pp} and V_{xp} are the variances and covariances of x and p. However, the conditional variances can be removed to a large extent. For a mirror with a high quality factor, it is possible to approach the quantum mechanical ground state as we show below. In Fig.6.2, we show that the measurement uncertainty (V_{xx}, V_{xp}, and V_{pp} are calculated using the discrete linear regression method) decreases as we increase the quality factor of the mirror. Alternatively we can also decrease the temperature to achieve the quantum mechanical ground state of the mirror. Here $V_{xx}V_{pp}-V_{xp}^2 > \hbar^2/4$ even for $T=0$ because of the remaining entanglement between test mass and cavity mode.

6.5 Conclusion

In this chapter, we have extended classical optimal filtering methods to macroscopic quantum mechanical experiments in laser interferometers. We showed that multivariate Wiener filtering can be

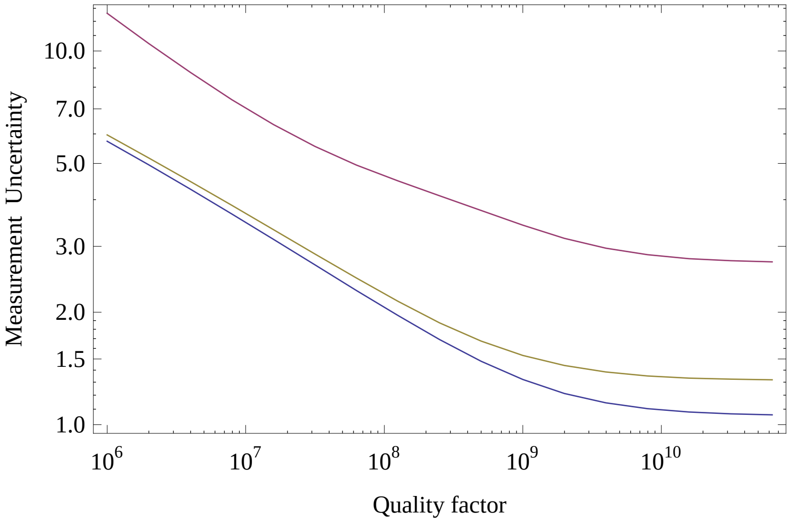

Figure 6.2: Uncertainty versus quality factor. Following [13], we measure test-mass uncertainty by $\sqrt[4]{4(V_{xx}V_{pp} - V_{xp}^2)/\hbar^2}$. The bottom line is the conditional uncertainty from multivariate Wiener filtering. The top line is the measurement uncertainty for carrier light and the middle line for subcarrier light. The temperature is $T = 300$K.

.

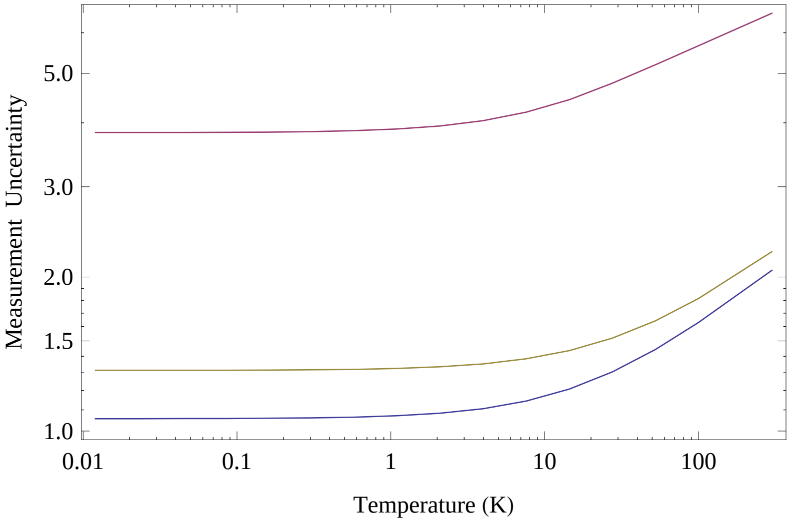

Figure 6.3: Uncertainty versus temperature. Following [13], we measure test-mass uncertainty by $\sqrt[4]{4(V_{xx}V_{pp} - V_{xp}^2)/\hbar^2}$. The bottom line is the conditional uncertainty from multivariate Wiener filtering. The top line is the measurement uncertainty for carrier light and the middle line for subcarrier light. The quality factor is $Q = 10^8$.

.

used to suppress the thermal noise so that the suspended mirror can achieve its quantum mechanical ground state when increasing the quality factor and/or reducing the temperature. With the preparation of quantum ground states, one can do several interesting experiments such as quantum swapping and quantum teleportation. In another related study, we found that the stochastic optimal control method can help quantum swapping experiments of two interferometers.

In summary, we found that it is feasible to design some quantum mechanical experiments that use the advanced LIGO interferometer, and we showed that in such experiments the theory of filter and control is crucial to eliminating the impact of environment thermal noises.

6.6 Bibliography

[1] C. M. Caves et al., Rev. Mod. Phys. **52**, 341 (1980); V. B. Braginsky and F.Y. Khalili, *Quantum Measurement* (Cambridge University Press, Cambridge, England, 1999); V. B. Braginsky, Sov. Phys. JETP **26**, 831 (1968).

[2] W. G. Unruh, *Quantum Optics, Experimental Gravitation, and Measurement Theory* (Plenum, New York, 1982), p. 647; C. M. Caves, Phys. Rev. Lett. **54**, 2465 (1985); M. T. Jaekel and S. Reynaud, Europhys. Lett. **13**, 301 (1990).

[3] S. P. Vyatchanin and A. B. Matsko, JETP **77**, 218 (1993); S. P. Vyatchanin and E. A. Zubova, Phys. Lett. A **203**, 269 (1995); S. P. Vyatchanin and A. B. Matsko, JETP **82**, 1007 (1996); **83**, 690 (1996); S. P. Vyatchanin, Phys. Lett. A **239**, 201 (1998).

[4] P. Purdue, Phys. Rev. D **66**, 022001 (2002); P. Purdue and Y. Chen, Phys. Rev. D **66**, 122004 (2002).

[5] P. Fritschel, arXiv:gr-qc/0308090.

[6] H. Mueller-Ebhardt, et. al., Phys. Rev. Lett. **100**, 013601 (2008)

[7] A. Papoulis, *Probability, Random Variables, and Stochastic Processes*, 3rd Edition, McGraw-Hill International Edition, 1991.

[8] A. Papoulis, *Signal Analysis*, McGraw-Hill International Edition, 1984.

[9] H.V. Poor, *An Introduction to Signal Detection and Estimation*, 2nd Edition, Springer 1994.

[10] T. Corbitt et al., Phys. Rev. A **73**, 023801 (2006).

[11] T. Corbitt et al., Phys. Rev. Lett. **98**, 150802 (2006).

[12] F.L. Lewis, *Optimal Estimation*, John Wiley & Sons, Inc. 1986.

[13] H. Rehbein, H. Müller-Ebhardt. and Y. Chen, paper in preparation.

[14] M. Davis, IEEE Trans. Autom. Control **8**, 296 (1963).

[15] Y. Chen, private communication.

[16] C. W. Gardiner and M. J. Collett, Phys. Rev. A **31**, 3761 (1985)

[17] H. J. Kimble, Y. Levin, A. B. Matsko, K.S. Thorne and S.P. Vyatchanin, Phys. Rev. D **65**, 022002 (2001).

[18] D. Vitali et.al, quant-ph/0111067.

[19] V. Giovannetti and D. Vitali, Phys. Rev. A **63**, 023812 (2001).

[20] A. Hopkins et.al, Phys. Rev. B **68**, 235328 (2003).

[21] M.E. Peskin and D.V.Schroeder,*An Introduction to Quantum Field Theory*, Westview Press 1995.

[22] A. Bounanno and Y. Chen, Phys. Rev. D **64**, 042006 (2001).

[23] A. Bounanno and Y. Chen, Phys. Rev. D **65**, 042001 (2002).

[24] A. Bounanno and Y. Chen, Phys. Rev. D **67**, 062002 (2003).

[25] C.M.Caves and B.L.Schumaker,Phys. Rev. A **31**, 3068 (1985).

[26] B.L.Schumaker and C.M.Caves,Phys. Rev. A **31**, 3093 (1985).

Chapter 7

Analytical Solutions for Expanding Fireballs

Many models of Gamma Ray Bursts (GRBs) as well as of Soft Gamma Ray repeaters (SGRs) involve a fireball: an optically thick concentration of radiation energy with a high ratio of energy density to rest mass. We study the asymptotic behavior of an ultra-relativistic fireball consisting of electron-positron pairs and photons. We show that in the ultra-relativistic limit, after photons decouple from the pairs, the photon distribution function remains a blackbody spectrum in some appropriate Lorentz frame, allowing us to define an effective Lorentz factor and temperature for the photon gas. We also study the freezing out of electron-positron pairs and their asymptotic Lorentz factor γ_∞. The dependence of these quantities on initial conditions can be described by simple scaling laws. We apply our results to SGR 1806-20, and find that the energy carried by electron-positron pairs is higher than calculated by former estimates, but is still an order of magnitude short of the minimum energy required to produce the observed afterglow. A viable solution of the energy budget is that the fireball is loaded by baryons or electromagnetic flux.

Originally published as C. Li and R. Sari, *Astrophys. J.* **677** 425 (2008).

7.1 Introduction

The release of a large amount of energy into a compact region can lead to an opaque electron-positron-photon fireball. The formation and evolution of fireballs are of interest in astrophysics, especially for the understanding of GRBs at cosmological distances [2, 3, 4, 5, 9] and SGRs [6, 7, 8]. The evolution of an electron-positron-photon fireball consists of several phases [1, 4]. Initially, the electrons, positrons and photons are in thermal equilibrium due to high temperature and large optical depth. As the fireball expands, its temperature decreases, and the equilibrium number density of electrons and positrons decreases. The optical depth for pair annihilation drops below unity, and their density deviates from thermal equilibrium below a temperature of about 20 keV. Around the same time, the optical depth for photon scattering drops below unity so that photons decouple from pairs and begin freestreaming. Further expansion causes the density of electron-positron pairs to decrease, but their total number is now conserved. The Lorentz factor of electrons increases until the optical depth for scattering off photons becomes small. Then the pairs decouple from the photons and therefore no longer accelerate. If we consider the fireball as a steady state wind, there will be a constant number of pairs per unit time $\dot{N}_\infty$ arriving at infinity with Lorentz factor γ_∞.

In this paper we analytically study these fireball processes. We assume a steady-state wind and focus on deriving exact solutions for $\dot{N}_\infty$ and γ_∞. These quantities have only been estimated to an order of magnitude previously [1, 11]. We prove in §7.2 that after photons decouple from the pairs, the photons remain thermal in a Lorentz frame that is accelerating as $\gamma_{ph} \propto r$. We define the Lorentz factor of this frame, γ_{ph}, as the Lorentz factor of the photons. When the fireball is optically thick, the pairs Lorentz factor γ_e is almost equal to that of the photons γ_{ph} since the photons are dragging the pairs. As the fireball expands and becomes sufficiently optically thin, γ_{ph} and γ_e start to deviate from each other, with $\gamma_e < \gamma_{ph}$. Finally γ_e approaches its coasting value γ_∞.

In §7.3 we calculate the number of pairs per unit time that survive or freeze out once the annihilation timescale becomes longer than the dynamical time. We arrive at an exact expression under the assumption that the pairs Lorentz factor during freeze out is very similar to that of the photons and that the temperature at freeze out, $k_B T_\pm$, is significantly below the electron rest mass. In §7.4 we derive an expression for the coasting Lorentz factor. We generalized our results in §7.5 for the case that the fireball is loaded with some amount of baryons and their associated electrons, or with magnetic fields. We discuss the applications to SGRs in §7.6.

7.2 Freely Streaming Photons

The sudden release of a large amount of energy in a compact region produces an expanding fireball. Relativistic dynamics in spherical geometry ensures that the matter expands such that its Lorentz factor is proportional to the radius [4, 9]. Before the photons reach the photosphere, they are in thermal equilibrium, and the distribution function is of blackbody form. If, at some radius the photons begin to stream freely without scattering, then, as we will show below, photons remain thermalized as long as we observe them in a Lorentz frame that continues to accelerate linearly with distance, $\gamma_{ph} \propto r$. As a side note, we mention that since this relation is true for no scattering, γ_{ph} continues to increase all the way to the observer. For example, in the giant flare of SGR 1806-20 the observed 200 keV photons, when they reach the observer, have a thermal distribution with a temperature of 4×10^{-12} eV if viewed in a frame that has a Lorentz factor $\gamma_{ph} = 5 \times 10^{16}$.

In Fig. 7.1, photons emitted from point 1 on the photosphere arrive at point 2. θ_{10} and θ_{20}

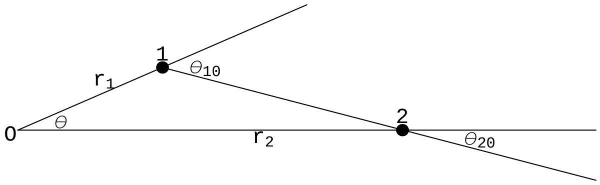

Figure 7.1: A photon emitted at point 1 is received at point 2. Point O is the origin of the fireball, point 1 lies on the photosphere; point 2 is an arbitrary point outside the photosphere. All the angles are exaggerated since $\theta, \theta_{10}, \theta_{20} \ll 1$.

are angles measured in the observer frame. Correspondingly, θ_1 and θ_2 denote the same angles measured in the comoving frames of the photon gas at point 1 and 2. When the fireball reaches photosphere, $\gamma_{ph} \gg 1$, which means that the transverse optical depth is of the order $\gamma_{ph}^2 \gg 1$, thus point 2 can only receive tiny amount of photons which are emitted from high-latitude regions on the photosphere. Therefore it is reasonable to assume

$$\theta \ll 1, \quad \theta_{10} \ll 1, \quad \theta_{20} \ll 1. \tag{7.1}$$

We note that although θ_{10}, θ_{20} are very small, their counterparts θ_1, θ_2 in the comoving frames can be large. From Liouville's theorem, the phase space distribution function is conserved along each collisionless trajectory. Thus we get the relation for the photon distribution function:

$$f(\nu_2, \theta_2) = f(\nu_{20}, \theta_{20}) = f(\nu_{10}, \theta_{10}) = f(\nu_1, \theta_1). \tag{7.2}$$

Here the second equality is from Liouville's theorem and the first and third equalities are from the Lorentz invariance of the phase space distribution function. Since we assume the photon distribution at point 1 is that of a blackbody in its comoving frame, we obtain

$$f(\nu_2, \theta_2) = f(\nu_1, \theta_1) = \frac{1}{e^{h\nu_1/k_B T_1} - 1}. \tag{7.3}$$

In order to express the photon distribution function at point 2 in terms of photon frequency ν_2 and angle θ_2, we need to do Lorentz transformations at points 1 and 2 and use the relation $\nu_{10} = \nu_{20}$ for collisionless photons. We obtain:

$$\frac{\nu_1}{T_1} = \frac{\nu_2 \gamma_{ph,2}}{T_1 \gamma_{ph,1}} (1 + \beta_2 \cos\theta_2) \gamma_{ph,1}^2 (1 - \beta_1 \cos\theta_{10}) \cong \frac{\nu_2 \gamma_{ph,2}}{T_1 \gamma_{ph,1}}, \tag{7.4}$$

where $\gamma_{ph,1}, \gamma_{ph,2}$ denote corresponding photon Lorentz factors at points 1 and 2. In the above argument, we use Eq. 7.1, $r_1/\gamma_{ph,1} = r_2/\gamma_{ph,2}$ and a geometrical relation $r_1\theta_{10} = r_2\theta_{20}$. Therefore the photon distribution function at point 2 is

$$f(\nu_2,\theta_2) = \frac{1}{e^{h\nu_1/k_BT_1}-1} = \frac{1}{e^{h\nu_2/(k_BT_1\gamma_{ph,1}/\gamma_{ph,2})}-1}. \tag{7.5}$$

Therefore, by defining the photon Lorentz factor γ_{ph} to be proportional to r, the photon distribution function remains a blackbody spectrum in this comoving frame, with the corresponding temperature inversely proportional to r. As such, the distribution function is isotropic, $f(\nu_2,\theta_2) = f(\nu_2)$. In other words, if we observe the freely-streaming photons in a carefully chosen Lorentz frame, we will always observe an isotropic blackbody spectrum. In deriving this conclusion, we have only used the following properties of freestreaming photons: $\gamma_{ph} \propto r, \theta_{10} \ll 1$. The result is therefore quite general.

Clearly, the free streaming of photons is a valid assumption only when the optical depth for scattering is well below unity. It is therefore important to explain why those conclusions continue to hold even when the optical depth is around unity. The collision effect vanishes as long as the electron-positron pairs are thermal. It is the photons that keep the electrons thermal as the fireball expands. However, at the photosphere, where the photons escape and the optical depth for scattering of a photon off an electron is of order unity, the density of photons far exceeds that of pairs. An order of magnitude estimate gives the photon-to-pair number ratio to be

$$e^{(m_ec^2)/k_BT} \sim e^{(511)/20} \sim 10^{11}, \tag{7.6}$$

where we have substitute the temperature $T \sim 20$ keV at the photosphere, which will be explained below in §7.3. Therefore, the last few collisions that a photon experiences are with electrons that have already been scattered by many photons. Due to the rest mass of the pairs, the criterion for the electrons to stay thermal is that the photon-to-pair number ratio exceeds $m_ec^2/k_BT \sim 20$, which is easily satisfied.

The observed flux per energy interval as seen by a stationary observer is

$$\frac{dF}{d\nu} = \frac{4\pi h\nu^3}{c^2}\int_{-1}^{1}\frac{\mu d\mu}{\exp\left[\gamma h\nu(1-\beta\mu)/k_BT\right]-1}. \tag{7.7}$$

Here, γ and T are the Lorentz factor and temperature of the photon gas at the observer. Similar expressions for this spectrum were obtained by Goodman [2] and Grimsrud & Wasserman [1]. In the limit of large γ, this can be reduced to

$$\frac{dF}{d\nu} = \frac{4\pi\nu^2k_BT}{c^2\gamma}\ln\left(\frac{2\gamma k_BT}{h\nu}\right), \tag{7.8}$$

at low energies and

$$\frac{dF}{d\nu} = \frac{4\pi\nu^2 k_B T}{c^2\gamma} \exp\left(\frac{-h\nu}{2\gamma k_B T}\right), \tag{7.9}$$

at high energies. Compared to a blackbody, the peak of the flux is broader, and the slope at low energies is slightly shallower. Note that the product γT appearing in the exponent and in the logarithm is independent of distance, while the ratio T/γ appearing in the prefactors is decreasing as distance square as expected.

7.3 Freeze Out of Pairs

In this section we assume that the fireball has a constant luminosity (steady wind) and consider the freeze out of electron-positron pairs. This assumption is valid if the variability timescale is longer that the light crossing time at the source. Initially the fireball is hot. The electron-positron pairs and photons are in thermal equilibrium with each other. Therefore, for a given temperature, the density of pairs is completely determined. Near the photosphere, photons decouple from the pairs. But due to the large ratio between the numbers of photons and pairs (Eq. 7.6), pairs are still accelerated efficiently by photons. On the other hand, because the local expansion rate is larger than the pair annihilation rate, the pair annihilation process gradually stops and the number of pairs emitted per unit time freezes to some limiting value $\dot{N}_\infty$. Therefore, in this section we assume $\gamma_e = \gamma_{ph} \propto r$ when calculating $\dot{N}_\infty$. We define the effective initial radius of the fireball by $r_i \equiv r/\gamma_{ph}$. This definition allows r_i to be somewhat different from the actual radius where the energy is released (e.g., the radius of a neutron star).

The equation describing the evolution of the number of pairs is [1]

$$\frac{d\dot{N}}{dr} = -\frac{r_i^2\langle\sigma_{ann}v\rangle}{4\pi r^4 c^2}(\dot{N}^2 - \dot{N}_{e,eq}^2), \qquad \dot{N}_{e,eq} = \frac{8\pi c r^3}{h^3 r_i}(2\pi m_e k_B T)^{3/2} e^{-m_e c^2/k_B T}, \tag{7.10}$$

where $\dot{N} \equiv 4\pi r^2 n_e \gamma_e c$ is the number of pairs emitted per unit time and $\langle\sigma_{ann}v\rangle$ is the pair annihilation cooling rate, which is almost constant for $k_B T \ll m_e c^2$ (Ref. [10]). Throughout the paper, we assume $k_B T \ll m_e c^2$ and adopt the cgs unit. When the temperature is high enough, electron-positron pairs are in thermal equilibrium with photons. With the expansion and cooling of the fireball, the equilibrium is broken at some temperature $T_\pm$, and the number of pairs freezes afterwards.

We start with a rough estimate of the condition when the equilibrium breaks

$$\frac{d\dot{N}}{dr} \sim \frac{\dot{N}}{r} \sim \frac{r_i^2\langle\sigma_{ann}v\rangle}{4\pi r^4 c^2}\dot{N}^2 \sim \frac{r_i^2\langle\sigma_{ann}v\rangle}{4\pi r^4 c^2}\dot{N}_{e,eq}^2. \tag{7.11}$$

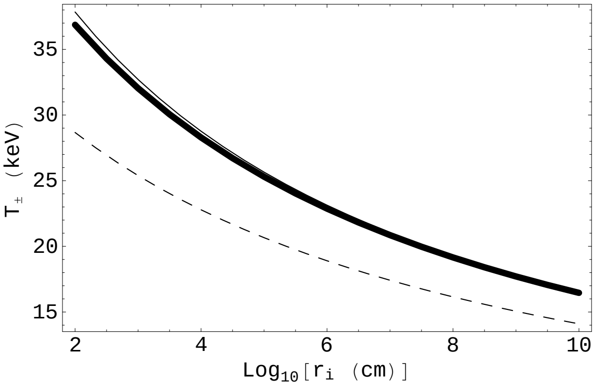

Figure 7.2: The comparison between the numerically exact solution of Eq. (7.13) and our analytical approximation Eq. (7.14). The horizontal axis is the logarithm of initial distance r_i in unit of centimeters. Dashed line: our first approximation T_1 in Eq. (7.14), solid line: our second approximation T_2 in Eq. (7.14), thick solid line: numerical solution of Eq. (7.13)

As an order of magnitude estimation, the total number of pairs at the equilibrium-breaking point is

$$\dot{N}_\pm \sim \frac{4\pi c^2}{r_i^2} \frac{r_\pm^3}{\langle \sigma_{ann} v \rangle}. \tag{7.12}$$

The corresponding temperature $T_\pm$ is determined by ($\dot{N}_\pm \sim \dot{N}_{e,eq}$)

$$\frac{c}{r_i \langle \sigma_{ann} v \rangle (2\pi m_e k_B T_\pm)^{3/2}} = \frac{2}{h^3} e^{-m_e c^2 / k_B T_\pm}. \tag{7.13}$$

Eq. 7.13 serves as our definition of $T_\pm$, the temperature at which pair annihilation is no longer effective. The right hand side has an exponential dependence which is highly sensitive to $T_\pm$, while the left hand side depends only weakly on $T_\pm$. Therefore, we can solve this equation iteratively. We start with $T_0 = m_e c^2 / k_B$. Assume that at step n we have obtained an approximate solution $T_\pm \approx T_n$; then at step $n+1$ we can substitute T_n to the left hand side of Eq. 7.13 and solve for T_{n+1}. This iterative method converges very fast. We have tried some typical values of initial conditions and found that, after two iterations, T_2 is already very close to the numerical values of $T_\pm$. Elegant analytical expressions for T_1 and T_2 can be written in terms of the dimensionless quantity $x \equiv (2\pi)^{1/2} \alpha^2 (r_i / \lambda_e)$ where $\alpha = 1/137$ is the fine structure constant and λ_e is the Compton wavelength of the electron.

$$\begin{aligned} T_1 &= \frac{m_e c^2 / k_B}{\ln x}, \\ T_\pm \approx T_2 &= \frac{m_e c^2 / k_B}{\ln x - (3/2) \ln \ln x}. \end{aligned} \tag{7.14}$$

Fig. 7.2 shows T_1 and T_2 as functions of r_i as well as the exact solution to Eq. 7.13. For $r_i > 10^4$

cm the analytical expression T_2 is accurate to within 2 percent.

It is easy to relate $T_\pm$ to the temperature at the photosphere. There are two differences here. First, the average velocity times the cross section in Thomson scattering is larger than that in pair annihilation since $\langle\sigma_{ann}v\rangle = 3\sigma_T c/8$. Furthermore there are twice as many pairs that are involved in Thomson scattering. These two reasons lead to a lower temperature than $T_\pm$, which is also given by Eq. 7.14 but with $x = (16/3)(2\pi)^{1/2}\alpha^2(r_i/\lambda_e)$; typical values are around 20 keV, which we used in §7.2.

Based on these estimates, we introduce the following dimensionless quantities

$$\dot{N} = \frac{4\pi r_i c^2}{\langle\sigma_{ann}v\rangle}\left(\frac{T_i}{T_\pm}\right)^3 \mathcal{N}, \qquad r = \frac{T_i r_i}{T_\pm}\mathcal{R}, \tag{7.15}$$

and Eq. 7.10 is converted into a dimensionless form:

$$\frac{d\mathcal{N}}{d\mathcal{R}} = -\frac{\mathcal{N}^2}{\mathcal{R}^4} + \frac{1}{\mathcal{R}} e^{-\frac{2m_e c^2(\mathcal{R}-1)}{k_B T_\pm}}. \tag{7.16}$$

We are ultimately interested in

$$\mathcal{N}_\infty(T_\pm) \equiv \lim_{\mathcal{R}\to\infty} \mathcal{N}(\mathcal{T}_\pm, \mathcal{R}), \tag{7.17}$$

since this provides the flux of pairs arriving at infinity. The solution of Eq. 7.16 depends weakly on $T_\pm$ if $k_B T_\pm \ll m_e c^2$. In the appendix, we have derived an approximate analytical expression

$$\mathcal{N}_\infty(T_\pm) = \frac{3}{1 + (\ln 8 - 3\gamma_{Eu})T_\pm - 3T_\pm \ln T_\pm}, \tag{7.18}$$

where $\gamma_{Eu} = 0.577216\ldots$ is the Euler constant. Numerical integration of Eq. 7.16 results in $\mathcal{N}_\infty(T_\pm = 23 \text{ keV}) = 1.95$, while the approximate Eq. 7.18 gives $\mathcal{N}_\infty(T_\pm = 23 \text{ keV}) = 2.09$. Here $T_\pm = 23$ keV corresponds to $r_i = 10^6$ cm. From Eq. 7.15, we then obtain the number of pairs per unit time arriving at infinity,

$$\dot{N}_\infty \approx 1.95 \frac{4\pi r_i c^2}{\langle\sigma_{ann}v\rangle}\left(\frac{T_i}{T_\pm}\right)^3. \tag{7.19}$$

For more general $T_\pm$, we use Eq. 7.18 to obtain

$$\dot{N}_\infty \approx \frac{3}{1 + (\ln 8 - 3\gamma_{Eu})T_\pm - 3T_\pm \ln T_\pm} \frac{4\pi r_i c^2}{\langle\sigma_{ann}v\rangle}\left(\frac{T_i}{T_\pm}\right)^3. \tag{7.20}$$

In Fig 7.5, we plot the fractional error of the analytical expression to the numerical solution. From this comparision, we see that the analytical expression Eq. 7.20 is an accurate expression for the number of pairs arriving at infinity per unit time.

7.4 Coasting of Pairs

Even after the photons decouple from the pairs, the pairs are still accelerated by the free-streaming photons due to the large ratio between the numbers of photons and pairs. The consequence is that the Lorentz factor for pairs continues to grow. At large radii, the acceleration gradually stops, and the pairs enter their coasting phase. In this section we calculate the coasting Lorentz factor γ_∞. The equation governing the evolution of the electron Lorentz factor is [1]

$$\frac{d\gamma_e}{dr} = \frac{\sigma_{tot} F_0}{m_e c^3}, \tag{7.21}$$

where $\sigma_{tot} = \sigma_a + \sigma_s$ is the total cross section for both absorption and scattering, and F_0 is the energy flux of photons in the rest frame of pairs. Since we have already proven that the photon distribution function is a blackbody in the local rest frame of free-streaming photons, we can do a simple Lorentz transformation to get the energy flux in the rest frame of electrons. This is different from the method of [1], who calculate a multipole expansion of the photon distribution function and only retain up to quadrupole terms. The relative Lorentz factor of the photon rest frame with respect to the pairs rest frame is

$$\gamma \cong \frac{1}{2}(\frac{\gamma_{ph}}{\gamma_e} + \frac{\gamma_e}{\gamma_{ph}}). \tag{7.22}$$

So we get the energy flux F_0 and Eq. 7.21 is converted into

$$\frac{d\gamma_e}{dr} = \frac{aT_{ph}^4}{3}\left[\left(\frac{\gamma_{ph}}{\gamma_e}\right)^2 - \left(\frac{\gamma_e}{\gamma_{ph}}\right)^2\right]\frac{\sigma_{tot}}{m_e c^2}, \tag{7.23}$$

where $T_{ph} = T_i r_i/r$ and $\gamma_{ph} = r/r_i$ are the photon temperature and Lorentz factor, and the radiation constant $a = 8\pi^5 k_B^4/15h^3c^3$. Using the transformation

$$\Gamma = \gamma_e \left(\frac{3m_e c^2}{r_i a T_i^4 \sigma_{tot}}\right)^{1/4}, \quad R = r\left(\frac{3m_e c^2}{r_i a T_i^4 \sigma_{tot}}\right)^{1/4}, \tag{7.24}$$

the equation governing the acceleration of electrons can be written in dimensionless form as

$$\frac{d\Gamma}{dR} = \frac{1}{R^4}\left[\left(\frac{R}{\Gamma}\right)^2 - \left(\frac{\Gamma}{R}\right)^2\right]. \tag{7.25}$$

Numerical integration of this dimensionless equation shows that the asymptotical limit is $\Gamma(R \to \infty) \approx 1.46$. Thus the coasting Lorentz factor is

$$\gamma_\infty \approx 1.46\left(\frac{8\pi^5 r_i T_i^4 k_B^4 \sigma_{tot}}{45 m_e h^3 c^5}\right)^{1/4}. \tag{7.26}$$

The kinetic energy flux arriving at infinity is given by $L_{\pm,\infty} = 2\gamma_\infty m_e c^2 \dot{N}_\infty$, or since the photons luminosity is given by $L = (16\pi/3)cr_i^2 aT_i^4$,

$$\begin{aligned} L_{\pm,\infty} &= 11.6\left(\frac{k_B^4 m_e^3 c^7}{h^3 a^4}\right)^{1/4} \frac{\sigma_{tot}^{1/4}}{\langle\sigma_{ann} v\rangle} \frac{L}{T_\pm^3 r_i^{3/4}} = 0.19\frac{m_e^{3/4} h^{9/4} c^{15/4} L}{\sigma_T^{3/4}(k_B T_\pm)^3 r_i^{3/4}}, \\ \gamma_\infty &= \gamma_{\infty,pure} \equiv 0.237\left(\frac{k_B^4}{m_e h^3 c^9 a^4}\right)^{1/4} \frac{\sigma_{tot}^{1/4} L}{T_i^3 r_i^{7/4}} = 0.549\left(\frac{\sigma_T L}{m_e c^3 r_i}\right)^{1/4}, \end{aligned} \tag{7.27}$$

where in the last equalities we have substitute $\sigma_{tot} \sim \sigma_T$ and $\langle\sigma_{ann} v\rangle \sim 3\sigma_T c/8$. We introduce the subscript "pure" here to stress that this result is for a pure radiation fireball.

7.5 Baryonic Loading

The generalization of our current results to a loaded fireball is straightforward. For simplicity, let us consider a fireball loaded with some protons and their associated electrons. As discussed in [11], the electrons that accompany the protons contribute to the opacity while the protons contribute to the inertia. Therefore, we can replace m_e in Eq. 7.27 by the average mass per electron

$$\bar{m}_e = \frac{2N_\pm m_e + N_p m_p}{2N_\pm + N_p}, \tag{7.28}$$

and obtain accurate results for a baryonic loaded fireball. Let us denote the mass loading rate to be $\dot{M}_p$ and define $\eta = L/\dot{M}_p c^2$ to characterize a loaded fireball. There are three critical values of this ratio:

$$\eta_1 = \frac{L}{2\dot{N}_\infty m_e c^2} = \frac{3}{16\mathcal{N}_\infty(T_\pm)}\left(\frac{L\sigma_T T_\pm^3}{4\pi r_i m_e c^3 T_i^3}\right), \tag{7.29}$$

corresponds to a loaded fireball with equal mass for protons and pairs,

$$\eta_2 = \frac{L}{2\dot{N}_\infty m_p c^2} = \frac{3}{16\mathcal{N}_\infty(T_\pm)}\left(\frac{L\sigma_T T_\pm^3}{4\pi r_i m_p c^3 T_i^3}\right), \tag{7.30}$$

marks equal number densities of pairs and protons and

$$\eta_3 = \left(\frac{m_e}{m_p}\right)^{1/4} \gamma_{\infty,pure} = 1.03\left(\frac{L\sigma_T}{4\pi m_p c^3 r_i}\right)^{1/4}, \tag{7.31}$$

is defined by the condition that the photons have effectively transferred all their energy to the protons (Eq. 7.27). Here we have improved the results of [11] by adding accurate factors before the expressions in the parentheses. The scaling relations in Eq. 7.27 have already been obtained by [11],

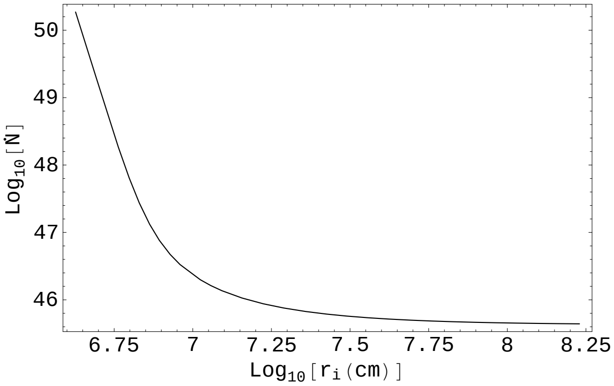

Figure 7.3: The number of pairs per unit time in SGRs, the values of parameters are $r_i = 10^6$ cm, $L = 10^{47}$ erg/s. We have taken the logarithm (to base 10) of the horizontal and vertical axes.

so we can modify their Eqs. (17,18) to include our numerical accurate factors here and obtain

$$\gamma_{\infty,load} = \begin{cases} \gamma_{\infty,pure}, & \eta_1 \ll \eta, \\ (\eta/\eta_1)^{1/4}\gamma_{\infty,pure}, & \eta_2 \ll \eta \ll \eta_1, \\ \eta_3, & \eta_3 \ll \eta \ll \eta_2, \\ \eta, & \eta \ll \eta_3. \end{cases} \tag{7.32}$$

The energy that remains in the ejecta is

$$L_{\infty,load} = \begin{cases} L_{\infty,pure}, & \eta_1 \ll \eta, \\ (\eta/\eta_1)^{-3/4}L_{\infty,pure}, & \eta_2 \ll \eta \ll \eta_1, \\ \eta_3/\eta L, & \eta_3 \ll \eta \ll \eta_2, \\ L, & \eta \ll \eta_3, \end{cases} \tag{7.33}$$

where $L_{\infty,pure} = 2m_e c^2 \dot{N}_{\infty,pure}\gamma_{\infty,pure}$ and L is the photons luminosity. Here we note that we can use $\bar{m}_e$ defined in Eq. 7.28 to obtain accurate results near the transition point $\eta \sim \eta_1$. When $\eta \ll \eta_2$, the number of electrons that are associated with baryons exceeds the number of pairs, our calculation of the surviving number of pairs is no longer valid since the excess amount of electrons will more easily annihilate positrons. The number of surviving positrons will be smaller than our estimate for $\dot{N}_\infty$ (Eq. 7.19). However, this has no energetic consequence since in this case the energy is carried by the baryons instead of the pairs.

7.6 Application to SGRs

We have numerically solved Eq. 7.16 and 7.21 for typical values of parameters for SGRs. In Fig. 7.3, we plot the number of pairs per unit time in SGRs. Clearly the electron-positron pairs freeze out.

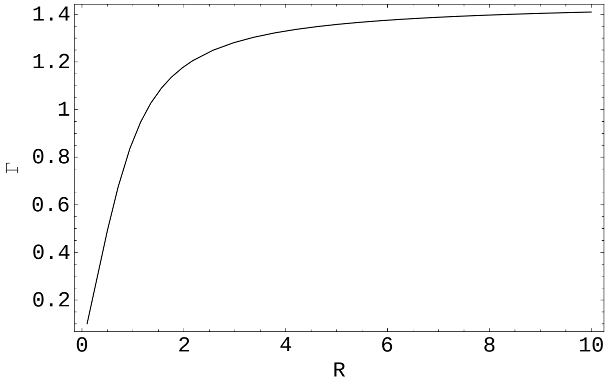

Figure 7.4: The normalized electron Lorentz factor Γ defined in Eq. (7.24). Here we plot the numerical solution to the dimensionless equation Eq. (7.25).

In Fig. 7.4 we plot the evolution of the electron Lorentz factor. This figure shows that the Lorentz factor of electron-positron pairs increases and reaches its asymptotic value.

Let us compare these numerical results with their former estimates [1, 11]. Consider the situation of a typical SGR where an energy E is deposited in the vicinity of a neutron star within the duration time t. In this case, the number of electrons emitted per unit time is

$$\dot{N}_\infty = 4\pi r^2 n_e \gamma_e c \approx 1.95 \frac{4\pi r_i c^2}{\langle\sigma_{ann} v\rangle}\left(\frac{T_i}{T_\pm}\right)^3 \approx 1.8 \times 10^{45} L_{47}^{3/4} r_{i,6}^{-1/2}, \tag{7.34}$$

where the luminosity $L = 16\pi r_i^2 ac T_i^4/3$ is measured in units of 10^{47} erg/s and r_i in units of 10^6 cm. For comparison, Eq. (61) of Grimsrud & Wasserman [1] gives the emission rate of the pairs as $\dot{N}_\infty \approx 4\pi r_i c^2 T_i^3/\langle\sigma_{ann} v\rangle T_\pm^3$, which is about half of our estimate.[1]

Based on the photon luminosity $L = (16\pi/3) c r_i^2 a T_i^4$, we obtain the initial temperature to be

$$T_i = 195 keV L_{47}^{1/4} r_i^{-1/2}. \tag{7.35}$$

This estimate agrees very well with the observation [12]. In addition, the giant flare from SGR 1806-20 has an optically thin thermal spectrum [12]. From this evidence it is reasonable to conjecture that we have directly observed the photons from the fireball. This is different from the usual GRBs, where we observe the non-thermal photons from the shocks between the fireball and the environment.

From Eq. 7.26, we find that the coasting Lorentz factor is (assuming $\sigma_{tot} \approx \sigma_T$, the Thomson cross section)

$$\gamma_\infty \approx 7.0 \times 10^2 L_{47}^{1/4} r_{i,6}^{-1/4}. \tag{7.36}$$

---

[1] Note the small differences between the definitions of $T_\pm$ of our Eq. 7.13 and Eq. (54) of Grimsrud & Wasserman [1]. We have also defined our initial radius r_i such that the initial Lorentz factor $\gamma_i = 1$. We have taken these small differences into account when comparing with their results.

In Eq.(71) of Grimsrud & Wasserman [1], $\gamma_\infty \approx 5.3 \times 10^2 L_{47}^{1/4} r_{i,6}^{-1/4}$, which is smaller than our value. This is because they only expanded the flux of photons to quadrupole terms (Eqs.(36) and (66) of Grimsrud & Wasserman [1]).

Finally, after combining Eqs. 7.34 and 7.36, the total kinetic energy of electron positron pairs is

$$E_\infty = 2 m_e c^2 \dot{N}_\pm t \gamma_\infty \approx 2.1 \times 10^{41} \mathrm{erg} E_{46} r_{i,6}^{-3/4}. \tag{7.37}$$

This result is slightly larger than previous estimates [1, 11]. It is shown in Nakar et al. [11] that the amount of kinetic energy in the pair outflow is too small to produce the observed radio flux. Our numerical results that arrive at a slightly higher pair energy can not solve the energy budget problem either. It is still two orders of magnitude short of producing the observed radio afterglow. Thus a pure electron-positron-photon fireball can not explain SGR 1806-20. A viable explanation is that the fireball is loaded with baryons or an electromagnetic field. As we have shown above, the ejecta of a heavy baryonic loaded fireball can carry enough energy and explain the observations. Electromagnetic loading is also quite natural since the magnetar model of SGR assume the central engine to be a neutron star with strong magnetic field [7]. The radio afterglow produced by this loaded fireball is further discussed in Taylor & Granot [14] and Wang et al. [16].

7.7 Appendix: The Analytical Solution of Equation (7.16)

Here we consider the limiting solution of Eq. 7.16. To simplify our expressions, we measure temperature by the electron mass, i.e., we convert the temperature by $T \rightarrow k_B T / m_e c^2$. Therefore the three constants k_B, m_e, c will not appear in this section.

As $T_\pm$ decreases, the dimensionless radius where equilibrium is effectively broken gets closer and closer to unity. Therefore we can divide the solution of Eq. 7.16 into two intervals, $\mathcal{R} \in [\mathcal{R}_0, 1]$ and $\mathcal{R} \in [1, \infty)$, here $\mathcal{R}_0$ is some fiducial radius where we set the initial condition to be $\mathcal{N}(T_\pm, \mathcal{R}_0) = \mathcal{R}^{3/2} e^{-(\mathcal{R}_0 - 1)/T_\pm}$. When $\mathcal{R} \in [\mathcal{R}_0, 1]$, we can approximate Eq. 7.16 by

$$\frac{d\mathcal{N}}{d\mathcal{R}} = -\mathcal{N}^2 + e^{-\frac{2(\mathcal{R}-1)}{T_\pm}}. \tag{7.38}$$

The solution to this equation has an analytical form

$$\mathcal{N}(T_\pm, \mathcal{R}) = \frac{e^{-(\mathcal{R}-1)/T_\pm} [2 K_1(T_\pm e^{-(\mathcal{R}-1)/T_\pm}) - C_0 I_1(T_\pm e^{-(\mathcal{R}-1)/T_\pm})]}{2 K_0(T_\pm e^{-(\mathcal{R}-1)/T_\pm}) + C_0 I_0(T_\pm e^{-(\mathcal{R}-1)/T_\pm})}, \tag{7.39}$$

here I_0, I_1, K_0, K_1 are the modified Bessel functions of the first and second kinds and C_0 is the integration constant to be determined by the initial condition. When $x \ll 1$, we can use the

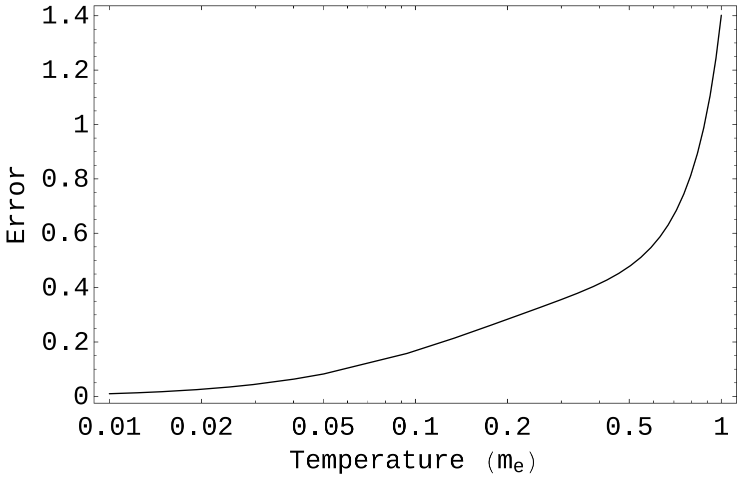

Figure 7.5: The relative error of our analytical solution compared to the numerical solution. As the equilibrium temperature $T_{\pm}$ decreases, our analytical formula Eq. 7.44 becomes closer to the numerical exact solution.

following asymptotic forms of those modified Bessel functions [15]

$$K_{1,0}(x) \gg I_{1,0}(x), \quad K_1(x) = \frac{1}{x} + O(x^2), \quad K_0(x) = -\gamma_{Eu} + \ln 2 - \ln x + O(x^2), \tag{7.40}$$

where $\gamma_{Eu} = 0.577216\ldots$ is the Euler constant. Plugging these relations into Eq. (A2), we obtain the analytical solution at $R = 1$ according to

$$\mathcal{N}(T_{\pm}, 1) = \frac{1}{T_{\pm}(-\gamma_{Eu} + \ln 2 - \ln T_{\pm})}. \tag{7.41}$$

Given this as the initial condition, we can solve Eq. 7.16 in the interval $\mathcal{R} \in [1, \infty)$. This time we approximate Eq. 7.16 as

$$\frac{d\mathcal{N}}{d\mathcal{R}} = -\frac{\mathcal{N}^2}{\mathcal{R}^4}, \tag{7.42}$$

which has the analytical solution

$$\lim_{T_{\pm}\to 0} \mathcal{N}(T_{\pm}, \mathcal{R}) = \frac{-1}{\frac{1}{3\mathcal{R}^3} + C_1}, \tag{7.43}$$

where C_1 is another integration constant determined by the initial condition Eq. 7.41. Substituting the initial condition Eq. 7.41, we obtain the analytical expression for the number of freeze-out pairs according to

$$\mathcal{N}_{ana} = \frac{3}{1 + (\ln 8 - 3\gamma_{Eu})T_{\pm} - 3T_{\pm} \ln T_{\pm}}. \tag{7.44}$$

In Fig. 7.5 we plot the relative error

$$\Delta \equiv \frac{\mathcal{N}_{ana} - \mathcal{N}_{num}}{\mathcal{N}_{num}}, \tag{7.45}$$

where $\mathcal{N}_{ana}$ is the number of freeze-out pairs obtained via direct numerical integration and $\mathcal{N}_{ana}$ is the number of freeze-out pairs obtained by the analytical method here. From Fig. 7.5 we see that as $T_{\pm}$ decreases, our analytical formula becomes closer to the numerical solution. For example, when $T_{\pm} \leq 0.1 m_e$, our analytical formula Eq. 7.44 only introduces an error which is smaller than 17 percent.

7.8 Bibliography

[1] O. M. Grimsrud & I. Wasserman, 1998, MNRAS, 300, 1158.

[2] J. Goodman, 1986, ApJ, 308, L47.

[3] B. Paczynski, 1986, ApJ, 308, L43.

[4] A. Shemi & T. Piran, 1990, ApJ, 365, L55.

[5] P. Mészáros, P. Laguna & M. J. Rees, 1993, ApJ, 415, 181.

[6] C. Kouveliotou, et al. 1998 Nature 393 235.

[7] C. Thompson & R. Duncan, 1995 MNRAS 275 255.

[8] C. Thompson & R. Duncan, 1996 ApJ 473 322.

[9] T. Piran, A. Shemi & R. Narayan, 1993, MNRAS, 263, 861.

[10] R. Svensson, 1982, ApJ, 258, 321.

[11] E. Nakar, T. Piran & R. Sari, 2005, ApJ, 635, 516.

[12] K. Hurley, et.al., 2005 Nature, 434, 1098.

[13] G. B. Taylor & J. Granot, 2006, Mod. Phys. Lett. A 21, 2171.

[14] X. Wang et. al., 2005, ApJ, 623, L29.

[15] Arfken G. B., 2005, *Mathematical Methods for Physicists*, Elsevier Academic Press, Burlington Massachusetts.

Chapter 8

Direct Reconstruction of the Dark Energy Scalar-Field Potential

While the accelerated expansion of the Universe is by now well established, an underlying scalar field potential possibly responsible for this acceleration remains unconstrained. We present an attempt to reconstruct this potential using recent SN data, under the assumption that the acceleration is driven by a single scalar field. Current approaches to such reconstructions are based on simple parametric descriptions of either the luminosity distance or the dark energy equation of state (EOS). We find that these various approximations lead to a range of derived evolutionary histories of the dark energy equation of state (although there is considerable overlap between the different potential shapes allowed by the data). Instead of these indirect reconstruction schemes, we discuss a technique to determine the potential directly from the data by expressing it in terms of a binned scalar field. We apply this technique to a recent SN dataset, and compare the results with model-dependent approaches. In a similar fashion to direct estimates of the dark energy equation of state, we advocate direct reconstruction of the scalar field potential as a way to minimize prior assumptions on the shape, and thus minimize the introduction of bias in the derived potential.

Originally published as C. Li, D. E. Holz and A. Cooray, *Phys.Rev.D* **75**, 103503 (2007).

8.1 Introduction

Distance estimates to Type Ia supernovae (SNe) are currently a preferred probe of the expansion history of the Universe [1], and have led to the discovery that the expansion is accelerating [2]. It is now believed that a mysterious dark energy component, with an energy density ~70% of the total energy density of the universe, is responsible for the accelerated expansion [3]. While the presence of acceleration is now well established by various cosmological probes, the underlying physics remains a complete mystery. As the precise nature of the dark energy has profound implications, understanding its properties is one of the biggest challenges today.

With the advent of large surveys for Type Ia supernovae, such as the Supernova Legacy Survey (SNLS)[1] and Essence[2], among others, it is hoped that we will study details of the expansion, and thereby elucidate the physics responsible for the acceleration. Under the assumption that the dark energy is due to a single scalar field rolling down a potential, several studies have considered how future data might be used to reconstruct the potential, either based on various analytical descriptions of the luminosity distance [4], or through specific assumptions about the potential, such as a polynomial function in the scalar field [5]. It is already well established that certain parametric descriptions of the distance lead to biased estimates for the dark energy equation-of-state (EOS) and the potential [7]. While improved parametric forms of fitting functions have been suggested [8, 10], it is unclear how to select an optimal approach for reconstructing the dark energy scalar field potential from SN distances (for a review of various possibilities, see Ref. [11]).

In this paper we discuss issues related to potential and dark energy EOS reconstruction by making use of a recent set of SN data from the SNLS survey [12]. The sample includes 73 high redshift SNe complemented with a sample of 44 nearby supernovae [12]. We compare and contrast a variety of methods to reconstruct the potential and the dark energy EOS. We write the luminosity distance either as a simple polynomial expansion in redshift, or as a Padé approximation [13] (which avoids some of the known problems in the polynomial expansion when taking derivatives [14, 7, 8]). In addition to approximating the luminosity distance, we also explore two approximations to the EOS: $w(z) = w_0 + w_a(1 - a)$ [15, 16] and $w(z) = w_0 - \alpha \ln(1 + z)$ [8].

Based on our model reconstruction of the potential, we find that while there is significant overlap of the allowed $V(\phi)$ region favored by each of the four reconstruction methods, the models give rise to different histories for the EOS, especially within the two parameter plane, w–w' (the EOS parameter, w, and its time derivative, $w' \equiv dw/d\ln a$, as functions of redshift [17]). We argue that existing parametric fitting functions for either distance or the EOS lead to biased reconstructions of the potential. In the literature, however, there exist model-independent approaches to the reconstruction of the dark energy density [18] and the EOS [19], which bin the parameters directly as a function of redshift, with the number and width of the bins determined by the statistical quality of data. These estimates can also be arranged to be uncorrelated [19], allowing unique insights into the evolution without being subject to prior assumed redshift dependencies. Here we suggest a similar model-independent approach to the reconstruction of the scalar potential from SN data. Instead of utilizing a polynomial expansion for the potential [5], which assumes a limited range of models (once the expansion is truncated at a certain order), we propose a binning scheme for the potential that

---

[1] http://www.cfht.hawaii.edu/SNLS/

[2] http://www.ctio.noao.edu/wsne/

can be applied to data with a minimal, and easily controlled and understood, number of assumptions for the potential shape.

The paper is organized as follows: In the next section we review techniques for reconstructing the scalar-field potential from SN distances. We also reconstruct the EOS as a function of the redshift, and use this to study the w–w' plane (which has been advocated as a way to characterize the underlying potential responsible for the dark energy component by separating the regime into "freezing" and "thawing" potentials [17]; see, also [20] for a Monte-Carlo exploration). In section 8.3 we explore the impact of different parameterizations on the derived evolutionary histories. While we observe these differences with ~ 115 SN data points, future large SN datasets may lead to apparently inconsistent results. In section 8.4, following the approach to model-free estimates of the dark energy EOS [19], we present a model-independent estimate of the scalar field potential. We conclude with a summary of our main results in section 8.5.

8.2 Potential via Parametric Forms

For this study we make use of SN data from SNLS [12]. Due to complications related to independent data sets (e.g., differing calibration, color correction, extinction correction), we do not attempt to increase the sample size by combining other SN datasets. The measurements from Ref. [12] present the quantity $\mu_B = m_B - M$ for 117 SNe, with 73 of these at redshifts greater than 0.2[3]. This distance modulus is related to the luminosity distance through $\mu_B = 5\log_{10} d_L$, while the luminosity distance is related to the comoving radial distance via $d_L = c(1+z)r(z)/H_0$, where $r(z) = \int_0^z dz'/H(z')$ with $H(z)$ the expansion rate of the Universe. When model fitting the data, we fix $M = 19.3 \pm 0.03$ to the value determined by SNLS. We take the central value; further uncertainty will be incorporated into $\sigma_{\rm int}$, as discussed below.

In our reconstruction of the potential, we describe $r(z)$ through two parametric forms widely used in the literature. First, we expand $r(z)$ as a simple power law [4] such that

$$r(z) = z + a_2 z^2 + a_3 z^3 + a_4 z^4 \,. \tag{8.1}$$

Note that the coefficient of the first order term is exactly one. Since this polynomial expansion has known problems when estimating the derivatives of $r(z)$ (e.g., Figure 3 of Ref. [8], and also Ref. [9]), we also consider a Padé form for $r(z)$ with Ref. [13]:

$$r(z) = 2\frac{z + c_1(1-\sqrt{1+z})}{c_2(1+z) + c_3\sqrt{1+z} + 2 - c_1 - c_2 - c_3} \,, \tag{8.2}$$

---

[3] The distance estimates for two high-redshift SNe lie more than 3σ away from the best-fit relation in the Hubble diagram. As in Ref. [12], we exclude these two data points and only make use of 115 data points to model fit the data.

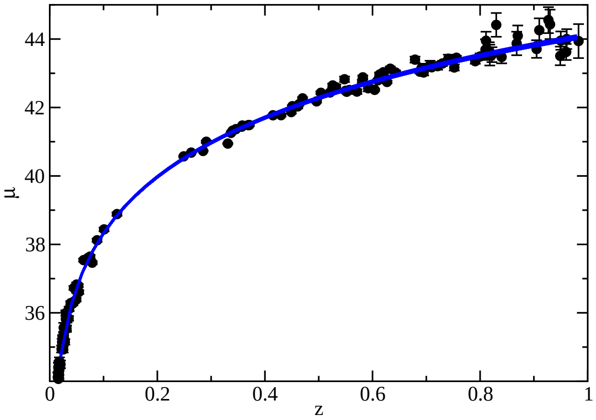

Figure 8.1: Hubble diagram for 115 Type Ia SNe used in the present analysis. The error bars are on μ_B only. We also include an additional constant error, $\sigma_{\rm int} = 0.13$, to account for the SN intrinsic dispersion. For reference we also plot 300 curves drawn uniformly from the 2σ consistent likelihood fits to the data using the Taylor expansion with $r(z) = z + a_2 z^2 + a_3 z^3 + a_4 z^4$.

such that as $z \to 0$, $r(z) \to z$. In this form, using $r(z \to \infty)$, one can additionally constrain the parameters with:

$$\begin{aligned} 3\Omega_M &\leq \frac{4c_2 + 2c_3 - c_1}{2 - c_1} \\ 1 \leq \tfrac{1}{c_2} &\leq \frac{1}{2}\int_1^\infty \frac{dx}{\sqrt{1 - \Omega_M + \Omega_M x^3}} \,. \end{aligned} \tag{8.3}$$

In addition to the two fitting forms for $r(z)$, we also determine $r(z)$ through model parameterizations for $w(z)$, including $w(z) = w_0 + (1-a)w_a$ [15, 16] and $w(z) = w_0 + \alpha \ln(1+z)$ [8]. Since from w it is possible to determine the distance, these approximations allow us to once again reconstruct the dark energy potential.

In each of two parametric descriptions of $r(z)$ we have three free parameters. We parameterize $w(z)$ with two parameters, and include Ω_m as a third free parameter (under the assumption of a flat universe; weakening this assumption significantly degrades our ability to measure anything about the potential with existing data). When showing results related to potentials or EOS as a function of redshift, we take a prior on Ω_m such that the probability is Gaussian with a mean of 0.25 and a standard deviation given by $\sigma = 0.05$ [3]. In each case, to obtain the join likelihood distribution of the parameters given the data, we perform a likelihood analysis:

$$\chi^2(p_i) = \sum_{i=1}^{N} \frac{[\mu - \mu_B(z_i)]^2}{\sigma^2_{\mu_B} + \sigma^2_{\rm int}} \,, \tag{8.4}$$

where, following Ref. [12], in addition to statistical uncertainty in μ_B we include an additional Gaussian uncertainty, $\sigma_{\rm int} = 0.13$, representing the intrinsic dispersion of SN absolute magnitudes, M. We ignore complications related to covariances in the Hubble diagram, either due to effects related to calibration [21] or fundamental limitations such as gravitational lensing correlation of SN flux [22] or peculiar velocities [23]. The posterior probability distribution is taken to be $P(p_i|\mu) \propto e^{-\frac{1}{2}\chi^2(p_i)}$, and we marginalize the likelihood over the uncertainty in Ω_m, assuming a Gaussian prior distribution.

Once the joint probability distribution for parameters is determined, we sample the 1σ and 2σ range allowed by these parameters to draw a fixed (> 600) number of independent $r(z)$ curves consistent with the data. For each of these distance curves, $r_i(z)$, we obtain the scalar-field potential, in dimensionless units such that $\tilde{V}(\tilde{\phi}) = V(\phi)/\rho_{\rm crit} = V/(3H_0^2/8\pi G)$, through Ref. [4]

$$\tilde{V}(\tilde{\phi}) \quad = \quad \left[\frac{1}{(d\tilde{r}/dz)^2} + \frac{1+z}{3}\frac{d^2\tilde{r}/dz^2}{(d\tilde{r}/dz)^3}\right] - \frac{1}{2}\Omega_M(1+z)^3\,, \tag{8.5}$$

where $\tilde{r} = H_0 r$. For each of the $r_i(z)$ estimates, we also randomly draw Ω_m from a Gaussian prior distribution as described above. The mapping between z and ϕ, the scalar field value, is obtained through

$$\begin{aligned}\frac{d\tilde{\phi}}{dz} \quad &= \quad -\frac{d\tilde{r}/dz}{(1+z)} \\ &\times \quad \left[-\frac{1}{4\pi}\frac{(1+z)d^2\tilde{r}/dz^2}{(d\tilde{r}/dz)^3} - \frac{3}{8\pi}\Omega_M(1+z)^3\right]^{1/2}\,,\end{aligned} \tag{8.6}$$

where $\tilde{\phi} = \phi/m_{\rm Pl}$. Furthermore, for models where we parameterize $r(z)$, we can also extract the dark energy EOS as

$$w(z) = \frac{1+z}{3}\frac{3\Omega_m(1+z)^2 + 2(d^2r_i/dz^2)/(dr_i/dz)^3}{\Omega_m(1+z)^3 - (dr_i/dz)^{-2}} - 1\,. \tag{8.7}$$

When selecting models associated with scalar fields, we require that $d\tilde{\phi}/dz > 0$, such that $w \geq -1$. Even in the case of $w(z)$ parameterizations where model fits allow $w < -1$, we ignore $w(z)$ below this value as single scalar-field models do not naturally give rise to such EOS.

8.3 Biases in Model-Dependent Estimates

In Fig. 8.1 we show the Hubble diagram for the 115 data points from Ref. [12] used in this analysis. For reference, we also plot $\sim$ 300 distance curves which are 2σ consistent curves drawn from the

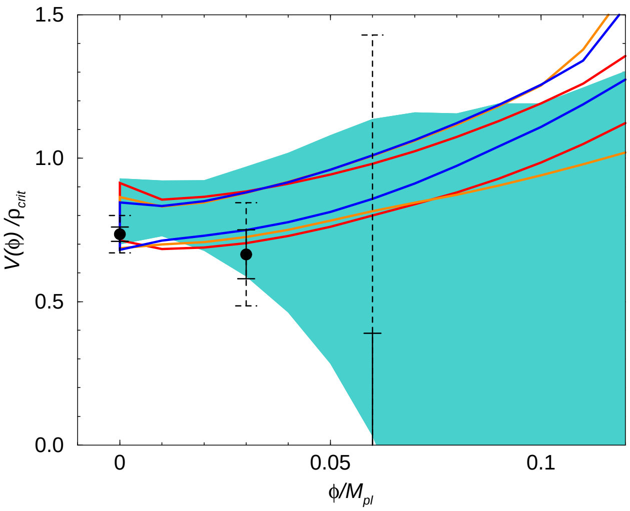

Figure 8.2: The normalized quintessence potential $\tilde{V}(\phi)$ versus $\phi/m_{\rm Pl}$. The shaded region is allowed at the 2σ confidence level when using the Taylor expansion for $r(z)$. The red lines mark the same when using a Padé approximation to the distance. The orange and blue lines are for the cases where $w(z)$ is parameterized by $w(z) = w_0 + \alpha \ln(1+z)$ and $w(z) = w_0 + w_a(1-a)$, respectively. Here $\phi = 0$ corresponds to $z = 0$, while $\phi > 0.1$ generally corresponds to $z > 1$ (depending on $d\phi/dz$). The points with error bars show the 1σ (solid) and 2σ (dashed) model-independent estimates of the potential described in section 8.4 (see equation (8.8)). While there is considerable overlap in the allowed region, there are also significant differences in terms of the redshift evolution of the EOS.

likelihood distribution for parameters under the Taylor expansion for $r(z)$. The best fit model with this parameterizations has a chi-square value of 113.1 with 112 degrees of freedom. Note that in Ref. [12], $\sigma_{\rm int}$ is tuned so that $\chi^2 = 1$ for the best fit model under standard-ΛCDM cosmological fits to the data. We use their best-fit value, $\sigma_{\rm int} = 0.13$, and do not take this intrinsic uncertainty as an additional free parameter in our modelling. The exact value of the intrinsic dispersion does not impact our comparison of different approaches to the reconstruction of the quintessence potential. It is to be emphasized that all of our parameterizations of either distance or the EOS yield comparable χ^2 values for the best-fit model. This suggests that all four of the reconstruction methods outlined above are indistinguishable within the redshift range considered.

As discussed in the previous section, for each of the four parameterizations we determine a best-fit $r(z)$ to the SN data. We then use Monte-Carlo method to generate models within 2σ of this best-fit, generating over 600 instances of $w(z)$ and $V(\phi)$, all of which are consistent with the underlying SN dataset at the 2σ level. In Fig. 8.2 we show the potentials reconstructed from each of the four methods, with the bands encapsulating 95% of the distribution of the individual models. Due to the behavior of the Taylor expansion at high z, and the fact that we do not restrict the coefficients of the polynomial expansion to follow a flat universe, this parametrization gives rise to a large range of acceptable potentials which satisfy the data. The Padé parametrization of $r(z)$, as well as the $w(z)$ models, significantly improve the constraints on allowed potential shapes. This is because the

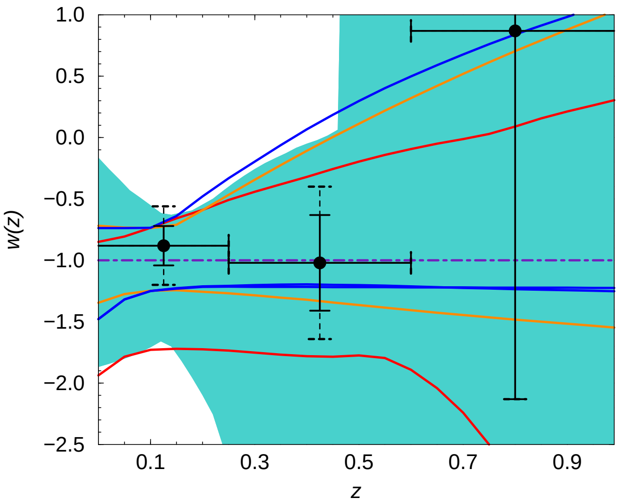

Figure 8.3: The dark energy EOS, $w(z)$, as a function of redshift. The curves show the 2σ allowed values and correspond to the potentials shown in Fig. 8.2. Note that if we impose $\partial\phi/dz > 0$, then $w > -1$, as single scalar-field models do not lead to $w < -1$. However, as shown, most of the parameterizations allow the region below $w < -1$. When constructing the potentials shown in Fig. 2, we apply the condition that $\partial\phi/dz > 0$. Note that the $w(z)$ parameterizations, with two free parameters, are the most restrictive parametrization in the regime $z < 0.3$. Over the redshift range probed, the different parameterizations generally agree with each other. The plotted error bars show the 1σ and 2σ errors of $w_i(z)$ when the EOS is subdivided into three bins in redshift, with $w_i(z)$ directly measured from data and no restrictions on its values. A Gaussian prior has been taken on Ω_m with a 1σ uncertainty of 0.05 with $w(z)$ parameterizations.

parameters in the Padé approximation are additionally constrained to satisfy criteria related to the behavior of $r(z)$ as $z \to \infty$, as well as by the assumption of a flat universe [13]. When fitting the $w(z)$ parameterizations to the data, we were able to impose a prior on Ω_m based on existing cosmological information (this was not possible when using $r(z)$ fitting functions). While we find some overlap in the 2σ allowed region in the ϕ–$V(\phi)$ plane between the four approaches, there are also noticeable inconsistencies. Analysis of an identical dataset with different approximations to V or w lead to differing resulting best-fit potentials.

The differences related to potential shapes between the four methods are best captured in terms of evolutionary histories for the dark-energy EOS. In Fig. 8.3 we summarize the best-fit $w(z)$ results for each of the four reconstruction techniques. Note that some of our parameterizations allow $w(z) < -1$, but due to our assumption that the dark energy arises from a scalar-field potential where $w(z)$ is always expected to be greater than -1, we restrict the allowed parameter space to be the region where $w(z) > -1$. Similarly to Fig. 8.2, we find considerable overlap between different reconstruction schemes in the $w(z)$ versus redshift plane, with most models indicating that as the redshift is decreased, $w(z)$ tends to values between -0.8 and -1.0 at $z = 0$. In terms of our direct $w(z)$ parameterizations, with $w(z) = w_0 + (1-a)w_a$ we find $w_0 = -1.12 \pm 0.14$ and $w_a = 0.38 \pm 0.49$ at the 68% confidence level. In the case of $w(z) = w_0 + \alpha \ln(1+z)$ we find $w_0 = -1.08 \pm 0.11$ and

$\alpha = 0.35 \pm 0.75$. As shown in prior studies [14], $w(z)$ parameterizations allow for a minimum $w(z)$ region at a certain pivot redshift. For the dataset used here, this pivot redshift is at $z \sim 0.12$, and at the 2σ confidence level we find that the pivot point satisfies $-1.23 < w_p \equiv w(z = 0.12) < -0.74$, using $w(z) = w_0 + (1 - a)w_a$. It is important to note that all the parameterizations are consistent with a cosmological constant.

In Figs. 8.2 and 8.3 we show the 2σ bands of best-fit models to the data, under different parameterizations of the distance or dark energy EOS. In addition to this outer envelope, we are also interested in the distribution of the individual $w(z)$ models within the 2σ bands. We thus study the behavior of the models in the w–w' plane, which has been suggested as a natural venue in which to distinguish models [17]. We Monte-Carlo 600 scalar potentials, $V(\phi)$, and evolution histories, $w(z)$, within the 2σ regime of the best-fit parameters for each of the four fitting functions. In Fig. 8.4 we plot w and w' at $z = 0.1$ and $z = 0.5$ for each Monte-Carlo model, with the scatter of points being 2σ consistent with our underlying SN data set.

Based on the evolutionary behavior of simple scalar-field models in the w–w' plane, it has been suggested that one can separate potentials into "thawing" and "freezing" regions, based on their shapes [17]. These regions are delineated in Fig. 8.4, for comparison with our individual Monte-Carlo models. It is apparent that the different parametrization approaches yield separate, though often overlapping, regions within the w–w' plane. In addition, the models are not necessarily well contained within the thawing or freezing regions, with a freezing model in one parametrization ending up as a thawing model in another, or with models ending up in between thawing or freezing, or well outside of either regime. Using generic numerical models for the potential shape, this behavior has also recently been highlighted in Ref. [20]. By applying additional constraints on allowable potentials (especially at high z), Ref. [17] find much tighter confinement in the w–w' plane.

Any statement regarding the shape of the scalar potential, as determined from data, is thus crucially dependent upon the underlying parameterizations. For example, for the Taylor expansion approach w' is largely negative at $z = 0.5$, while it is positive at $z = 0.1$. Under the Padé approximation, w' is negative at both $z = 0.1$ and $z = 0.5$, with w tightly clustered ($-0.9 \lesssim w \lesssim -0.8$) at $z = 0.1$ and relatively unconstrained at $z = 0.5$. Although the reconstructed potentials show significant overlap (see Fig. 8.2), the distributions in the w–w' plane are less consistent among different parameterizations. Thus, while there is motivation from theoretical arguments for using the w–w' plane for potential recognition, there is no obvious, parametrization independent way to convert distance data to constraints in this plane.

The differences seen in Fig. 8.4 are attributable to the different parametric forms used to approximate the distance or the dark energy EOS. To paraphrase our results: you get out what you put in. Furthermore, the fitting forms to both the distance and the EOS are motivated by their ability to fit data, and possess no clear physical motivation. Fig. 8.4 thus emphasizes the need for

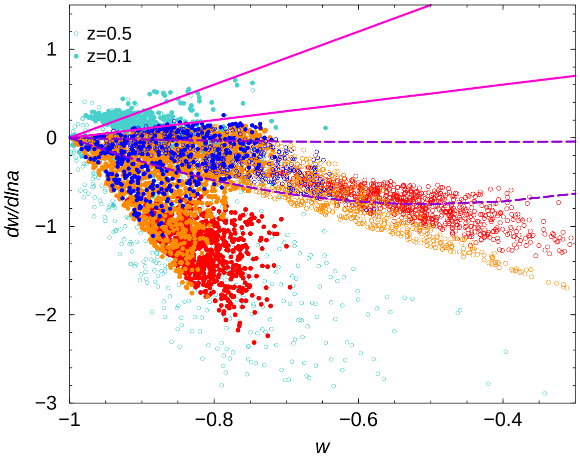

Figure 8.4: w versus $dw/d\ln a$. The data points show the EOS and its time derivative for 600 model potentials uniformly drawn at the 2σ confidence level at redshift of 0.1 (filled symbols) and 0.5 (open symbols). The cyan, red, orange, and blue data points show potentials selected under the Taylor expansion, Padé approximation, $w(z) = w_0 + \alpha \ln(1 + z)$ and $w(z) = w_0 + w_a(1 - a)$ model fits to the data, respectively. For comparison, we also plot the thawing (dashed) and freezing (solid) potential regions, following Ref. [17]. There are considerable differences in w and $dw/d\ln a$ values, and the evolution captured by two redshifts, between the four approaches. These values do not satisfy the expectations under simple model criteria for the dark energy potentials, though all of these potentials, and the $w(z)$ curves, are consistent with the data at the 2σ confidence level.

an approach which makes minimal assumptions about the underlying potential, thereby maximizing the measurement of a completely unknown scalar field. The less we assume about the potential, the more powerful the ensuing measurement of its shape. Such an approach is presented in the following section.

8.4 Model-Free Estimates

Thus far we have discussed results based on assumed parameterizations for either distance or dark energy EOS. These parameterizations lead to conclusions that are subject to the assumed parameterizations. It is desirable to make model independent estimates of dark energy. In the case of the EOS $w(z)$, one could approach this by binning $w(z)$ in redshift [19]. Applying this to our SNLS dataset, we evaluate $w(z)$ over three bins in redshift, $0 < z_1 < 0.25$, $0.25 < z_2 < 0.6$, and $0.6 < z_3 < 1.0$, assuming $w(z_i)$ constant in each bin.

The resulting best-fit to the SN data is shown by the data points with 1σ and 2σ error bars in Fig. 8.3. We find $w(z_1) = -0.88 \pm 0.28$ and $w(z_2) = -1.02^{+0.94}_{-1.26}$ with no useful constraint for $w(z)$ in the z_3 bin. Although these bins are correlated at the 10% level, it is possible to decorrelate the binned $w_i(z)$ estimates following the approach of Ref. [19]. While only three bins are attempted here, as SN sample sizes increase, one can consider larger numbers of bins, each narrower in redshift. The estimates shown in Fig. 8.3 are consistent with estimates based on both fitting functions to the

EOS, $w(z) = w_0 + w_a(1-a)$ and $w(z) = w_0 + \alpha \ln(1+z)$. As discussed in Ref. [19], the binned estimates capture the dark energy EOS with minimal prior assumptions on the parameterization. This is expected to maximize the information one can extract from the data, while minimizing the introduction of biases.

As discussed and noted elsewhere [7, 8], the scalar-field potential reconstruction is also subject to prior assumptions on the fitting form. To avoid biases and to make statements that are not subject to assumed parametrization, it is useful to directly construct the potential from data. Recent approaches in the literature consider fitting distance data to a potential expanded as a polynomial in the scalar field with $V(\phi) = \sum_{i=0}^{\infty} V_i \phi^i$ [5, 6, 20]. Since we are forced to truncate the expansion at low order (for example, at cubic order with existing data [5]), the potential is no longer arbitrary, but rather has a very limited range of possible shapes.

Instead of assuming a specific family of shapes for $V(\phi)$, we propose a "model-free" extraction of the potential directly from the data. We make two assumptions about the scalar field potential: (1) that it is a piecewise continuous function, and (2) that its structure is "uniform" in the ϕ range explored by the data. For $(N-1)\Delta\phi < \phi < N\Delta\phi$, we describe the potential as a function of the field with constant gradients, $dV/d\phi$, over binned intervals, $\Delta\phi$:

$$V(\phi) = V_0 + \sum_{i=1}^{N-1} (dV/d\phi)_i \Delta\phi + (\phi - (N-1)\Delta\phi)(dV/d\phi)_N \, . \tag{8.8}$$

Assumption (1) above ensures continuity of $V(\phi)$, which is necessary since one evolves the potential through the dynamic equation for the field as $\ddot{\phi} + 3H\dot{\phi} + dV/d\phi = 0$, and discontinuities would lead to infinite derivatives. This requirement is unnecessary when considering parameter-free estimates of the dark energy EOS, which is allowed discontinuous jumps in redshift. Both the constant-value and the constant-slope approaches to parameterizing the dark energy EOS lead to similar conclusions [19]. Assumption (2) states that our bins in ϕ are fixed width: $\Delta\phi$ is a constant, independent of ϕ. This assumption could be relaxed (e.g., finer bins near $\phi = 0$), but this would lead to additional parameters, in addition to introducing model-dependent assumptions into the analysis. The expansion of $V(\phi)$ in Eq. 8.8 appears to make the least offensive assumptions possible, and thereby offers the basis with which to maximally constrain the full range of possible underlying potentials.

We apply the above potential description to SNLS data following the same approach as Ref. [5], with three free parameters: V_0, $(dV/d\phi)_1$ for $0 < \phi < 0.03$, and $(dV/d\phi)_2$ for $\phi > 0.03$. The sizes of the bins are chosen by the range of ϕ we are able to constrain, which is in turn related to both the redshift range of the SN dataset and the shape of the potential. Note that we take $\phi = 0$ to coincide with $z = 0$. Instead of $(dV/d\phi)_2$, we convert the gradient to a data point at $\phi = 0.06$, although we find only an upper limit, as this gradient is not strongly constrained by existing data. In Fig. 8.2

we show the estimated potential and error bars at the 1σ and 2σ level. The potential values allowed by the data are generally consistent with other indirect reconstructions based on fitting forms for the distance or the EOS. While fitting forms lead to largely positive $V(\phi)$ at $\phi > 0.05$, our binned approach finds only an upper limit in this range.

While we have described the potential with only three parameters, this can be straightforwardly generalized to additional bins as the statistics and quality of the SN samples improve. In addition, we make a minimal number of assumptions regarding the potential, and thus are not biased for or against any particular shapes for the scalar field potential. The proposed approach is similar to the case where the EOS is binned and directly measured from the data without specifying a model for the evolution. As SN data samples increase in size, we believe such a model independent approach will become a powerful tool in extracting information about underlying scalar field potentials.

8.5 Summary

We have presented a reconstruction of a single scalar-field potential using recent SN data from the SNLS survey [12]. We have shown that reconstructions based on various approximations to the distance and the EOS lead to differing evolution histories of the dark energy EOS, particularly when the models are examined in the w–w' plane. In this plane the same data can lead to large movements in best-fit models, depending on the specific approximations to distance or EOS which are being utilized. Thus the underlying model assumptions lead to biases, compromising our ability to distinguish evolutionary behaviors of the dark energy. At present the models are only weakly constrained by the data, and thus this model dependence, although apparent, is not a critical failure. As the data improves, however, a model-independent approach will be essential to determining an otherwise completely unknown scalar-field potential.

As an alternative to existing indirect reconstruction schemes, we have thus proposed a technique which establishes the potential directly from the data with only minimal assumptions about the underlying shape of the potential. We take the potential to be a binned scalar field, piecewise linear and continuous, but otherwise completely arbitrary. Given the simplicity of these assumptions, this potential is unlikely to introduce biases in the determination of a completely unconstrained, underlying potential. We have demonstrated this approach with current SN data, comparing the results to parameterized analysis. The ensuing constraints, although weaker, are expected to be robust and unbiased. It has been found that direct binning approaches to the dark energy EOS hold great promise for establishing model-independent measurements [19]. We propose a similar approach to reconstructing the underlying dark energy scalar field potential, allowing us to make assumption-free statements about the nature of the completely unknown and mysterious field potentially responsible for the accelerating expansion of the Universe.

8.6 Bibliography

[1] A. G. Riess et al., B. J. Barris et al., arXiv:astro-ph/0310843; R. A. Knop et al., arXiv:astro-ph/0309368; J. L. Tonry et al., Astrophys. J. **594**, 1 (2003).

[2] S. Perlmutter et al., Astrophys. J. **517**, 565 (1999); A. Riess et al., Astron. J. **116**, 1009 (1998).

[3] D. N. Spergel et al. [WMAP Collaboration], Astrophys. J. Suppl. **148**, 175 (2003);

[4] D. Huterer and M. S. Turner, *Phys. Rev. D***60** 081301 (1999).

[5] M. Sahlen, A. R. Liddle and D. Parkinson, Phys. Rev. D **72**, 083511 (2005) [arXiv:astro-ph/0506696].

[6] M. Sahlen, A. R. Liddle and D. Parkinson, Phys. Rev. D **75**, 023502 (2007) [arXiv:astro-ph/0610812].

[7] J. Weller and A. Albrecht, Phys. Rev. D **65**, 103512 (2002) [arXiv:astro-ph/0106079].

[8] B. F. Gerke and G. Efstathiou, "Probing quintessence: Reconstruction and parameter estimation from supernovae", Mon. Not. Roy. Astron. Soc. **335**, 33 (2002) [arXiv:astro-ph/0201336].

[9] J. Jonsson, A. Goobar, R. Amanullah, and L. Bergstrom, JCAP **09**, 007 (2004)

[10] Z. K. Guo, N. Ohta and Y. Z. Zhang, Phys. Rev. D **72**, 023504 (2005) [arXiv:astro-ph/0505253].

[11] V. Sahni and A. Starobinsky, Int.J.Mod.Phys. D **15** (2006) 2105-2132 [arXiv:astro-ph/0610026].

[12] P. Astier et al., Astron. Astrophys. **447** 31 (2006), astro-ph/0510447.

[13] T. D. Saini, S. Raychaudhury, V. Sahni and A. A. Starobinsky, Phys. Rev. Lett. **85**, 1162 (2000) [arXiv:astro-ph/9910231].

[14] D. Huterer and M. S. Turner, Phys. Rev. D **71**, 123527 (2001).

[15] M. Chevallier, D. Polarski Int. J. Mod. Phys. D **10**, 213 (2001) [arXiv:gr-qc/0009008]

[16] E. V. Linder, *Phys. Rev. Lett.* **90** 091301 (2003)

[17] R. R. Caldwell and E. V. Linder, Phys. Rev. Lett. **95**, 141301 (2005) [arXiv:astro-ph/0505494].

[18] Y. Wang and M. Tegmark, Phys. Rev. D **71**, 103513 (2005) [arXiv:astro-ph/0501351].

[19] D. Huterer and A. Cooray, Phys. Rev. D **71**, 023506 (2005) [arXiv:astro-ph/0404062].

[20] D. Huterer and H. V. Peiris, Phys. Rev. D **75**, 083503 (2007) [arXiv:astro-ph/0610427].

[21] A. G. Kim and R. Miquel, Astropart. Phys. **24**, 451 (2006) [arXiv:astro-ph/0508252].

[22] A. Cooray, D. Huterer and D. Holz, Phys. Rev. Lett. **96**, 021301 (2006) [arXiv:astro-ph/0509581].

[23] L. Hui and P. B. Greene, Phys. Rev. D **73**, 123526 (2006) [arXiv:astro-ph/0512159]; A. Cooray and R. R. Caldwell, Phys. Rev. D **73**, 103002 (2006) [arXiv:astro-ph/0601377].

Chapter 9

Weak Lensing of the Cosmic Microwave Background by Foreground Gravitational Waves

Weak lensing distortion of the background cosmic microwave background (CMB) temperature and polarization patterns by the foreground density fluctuations is well studied in the literature. We discuss the gravitational lensing modification to CMB anisotropies and polarization by a stochastic background of primordial gravitational waves between us and the last scattering surface. While density fluctuations perturb CMB photons via gradient-type deflections only, foreground gravitational waves distort CMB anisotropies via both gradient- and curl-type displacements. The latter is a rotation of background images, while the former is related to the lensing convergence. For a primordial background of inflationary gravitational waves, with an amplitude corresponding to a tensor-to-scalar ratio below the current upper limit of ∼0.3, the resulting modifications to the angular power spectra of CMB temperature anisotropy and polarization are below the cosmic variance limit. At tens of arcminute angular scales and below, these corrections, however, are above the level at which systematics must be controlled in all-sky anisotropy and polarization maps with no instrumental noise and other secondary and foreground signals.

Originally published as C. Li and A. Cooray, *Phys. Rev. D* **74**, 023521 (2006).

9.1 Introduction

The weak lensing of cosmic microwave background (CMB) anisotropies and polarization by intervening mass fluctuations, or scalar perturbations, is now well studied in the literature [1, 2], with a significant effort spent on improving the accuracy of analytical and numerical calculations (see, recent review in [3]). The non-Gaussian pattern of CMB anisotropies and polarization created by non-linear mapping associated with lensing angular deflections aids the extraction of certain statistical properties of the foreground mass distribution [4]. Weak lensing deflections by intervening mass also *leak* CMB polarization power in the E-mode to the B-mode [5]. This lensing B-mode signal presents a significant confusion when searching for primordial gravitational wave signatures in the CMB polarization [6]. The lensing reconstruction techniques discussed in the literature, however, allow the possibility to "clean" CMB polarization maps and to search for a background of inflationary gravitational waves with an energy scale as low as 10^{15} GeV [7].

Similar to gravitational lensing by density perturbations, if there is a background of gravitational waves in the foreground, then one would expect metric perturbations associated with these waves to distort and gravitationally lens background images [8]. While the lensing deflections by the density field can be written as the gradient of the projected gravitational potential, lensing displacements due to gravitational waves can be decomposed to both a gradient and a curl-like component [9, 10, 11]. In these two components, gradient-type displacements are related to the lensing convergence, while curl-type displacements are related to the image rotation, though both types of displacements lead to image shear. While linear density perturbations do not produce rotations, second-order corrections to weak lensing by scalar perturbations, such as due to the coupling of two lenses along the line of sight, can produce rotational modes [12].

While the study of CMB lensing by foreground density fluctuations is now well developed [3], the discussion of CMB lensing by foreground gravitational waves is limited. In the context of large-scale structure weak lensing surveys with galaxy shapes [13], the rotational power spectrum of background galaxy images when lensed by primordial gravitational waves in the foreground is discussed in Ref. [10]. In the context of lensing reconstruction with CMB temperature and polarization maps, the curl component of the displacement field can be used to monitor systematics [11], though lensing by gravitational waves will leave a non-zero contribution to the curl component.

Here, we extend the calculation in Ref. [10] and study both the curl and the gradient modes of the deflection field from primordial gravitational waves that intervene CMB photons propagating from the last scattering surface. Our calculations are both useful and important given the increasing interest on, and plans for, high-sensitivity CMB anisotropy and polarization measurements, including a potential space-based mission after Planck, called CMBpol in the future. Such an experiment is expected to study polarization B-modes in exquisite detail and it is important to understand potentially interesting secondary signals beyond those that are routinely mentioned in the literature. Based on the calculations presented here, we find that gravitational lensing of CMB by a background of primordial gravitational waves from inflation, with an amplitude below the current tensor-to-scalar ratio upper limit of 0.3, will produce an undetectable modification to anisotropy and polarization power spectra. Moreover, since the corrections are below the cosmic variance level, it is unlikely that one needs to account for these secondary corrections when making precise cosmological

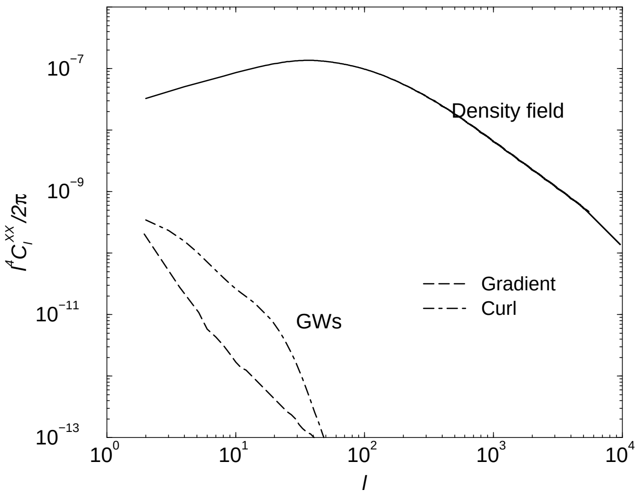

Figure 9.1: Lensing-deflection power spectra. Here, we show the gradient component from density perturbations (top curve), the curl (dot-dashed line) and gradient (dashed line) components from foreground inflationary gravitational waves. We have taken a background of gravitational waves with an amplitude for the power spectrum corresponding to roughly a tensor-to-scalar ratio of 0.3 or a Hubble parameter during inflation of 2×10^{14} GeV.

measurements.

This paper is organized as follows. In Section 9.2, we discuss lensing by foreground gravitational waves by discussing both the gradient and curl components of the displacement field. Section 9.3 presents expressions for the weak lensing correction to the CMB anisotropy and polarization power spectra. We conclude with a discussion of our results in Section 9.4.

9.2 The Spectrum of Expansion and Rotation

To establish the lensing correction to CMB anisotropy and polarization maps by foreground gravitational waves, we first need to calculate the photon displacement on the spherical sky by gravitational waves in the foreground. We make use of synchronous coordinates and take the metric of a Friedman-Robertson-Walker cosmological model as

$$g_{\mu\nu} = a^2 \begin{pmatrix} -1 & 0 \\ 0 & \mathbf{I} + \mathbf{H} \end{pmatrix} , \tag{9.1}$$

where the scale factor is $a(\eta)$, and the conformal time is denoted by η with the value today of η_0. Here, $\mathbf{H}$ is the transverse ($\nabla \cdot \mathbf{H} = 0$), symmetric ($\mathbf{H} = \mathbf{H}^{\mathrm{T}}$), and traceless ($\mathrm{Tr}\ \mathbf{H} = 0$) tensor metric perturbation associated with gravitational waves, while $\mathbf{I}$ is the identity matrix. The photon propagation is governed by the geodesic equation

$$\frac{d^2 x^\mu}{d\lambda^2} + \Gamma^\mu_{\alpha\beta} \frac{dx^\alpha}{d\lambda} \frac{dx^\beta}{d\lambda} = 0. \tag{9.2}$$

By changing variables to the conformal time η from the affine parameter λ, the geodesic equation in the presence of foreground gravitational waves is [10]

$$\ddot{\mathbf{r}} = \frac{1}{2}\left(\dot{\mathbf{r}} \cdot \dot{\mathbf{H}} \cdot \dot{\mathbf{r}}\right)\dot{\mathbf{r}} - (\mathbf{I} + \mathbf{H})^{-1} \cdot \left[\dot{\mathbf{r}} \cdot \frac{d}{d\eta}\mathbf{H} - \frac{1}{2}\nabla_H \left(\dot{\mathbf{r}} \cdot \mathbf{H} \cdot \dot{\mathbf{r}}\right)\right] , \tag{9.3}$$

where, to simplify the notation, we have not written out the explicit dependence of η in each of these terms. In here, the overdot represents the derivative with respect to the conformal time. The full derivative $d/d\eta$ can be separated to $\partial/\partial\eta + \dot{\mathbf{r}} \cdot \nabla$. Here, and throughout, ∇_H denotes the gradient that applies only to the metric perturbation $\mathbf{H}$; when not subscripted with H, the gradient should be interpreted as the one that applies to all terms, including the line-of-sight directional vector $\mathbf{n}$.

As gravitational fluctuation is very weak today, hereafter we neglect $\mathbf{H}(\eta_0)$, and choose the initial conditions of the trajectory to be

$$\mathbf{r}(\eta_0) = 0 \ , \quad \dot{\mathbf{r}}(\eta_0) = -\hat{\mathbf{n}} \, . \tag{9.4}$$

We find that the general displacement on the celestial sphere induced by primordial gravitational waves is

$$\mathbf{r}(\eta) = \hat{\mathbf{n}}(\eta_0 - \eta) - \int_{\eta}^{\eta_0} d\eta' \times \left(\mathbf{H} \cdot \hat{\mathbf{n}} + \frac{1}{2}(\eta' - \eta)[(\hat{\mathbf{n}} \cdot \dot{\mathbf{H}} \cdot \hat{\mathbf{n}})\hat{\mathbf{n}} - \nabla_H(\hat{\mathbf{n}} \cdot \mathbf{H} \cdot \hat{\mathbf{n}})]\right)_{(\eta', \mathbf{x}')} , \tag{9.5}$$

where $\mathbf{x}' = (\eta_0 - \eta')\hat{\mathbf{n}}$. Similar to Ref. [10], we have evaluated the trajectory on the unperturbed path following the so-called Born approximation. One could potentially evaluate corrections to this approximation in terms of a perturbative correction to the path length, but these would be at the second order in metric perturbations and will be ignored.

The total displacement can be separated to a part along the line of sight and a part perpendicular to it. The radial displacement leads to a time-delay effect, similar to the lensing timedelay associated with foreground potentials [14]. This timedelay couples to the radial gradient of the CMB, due to finite extent of the last scattering surface, while the angular displacement couples to the angular gradient. As discussed in Ref. [15], the overall correction to CMB anisotropy spectra from the timedelay effect is subdominant since the spatial gradient of the CMB is, at least, two orders of magnitude smaller compared to the angular gradient. There are also geometrical cancelations that make the time-delay effect smaller relative to angular deflections. Thus, we ignore the radial displacement and only consider the transverse component related to gravitational lensing angular deflections.

Using the transverse displacement, the angular deflection projected on the spherical sky is $\vec{\Delta} = [\mathbf{r}(\eta) - (\hat{\mathbf{n}} \cdot \mathbf{r})\hat{\mathbf{n}}]/(\eta_0 - \eta)$. These two-dimensional displacements can be related to usual quantities in gravitational lensing with the convergence and the rotation defined as [9]

$$\kappa \equiv -\frac{\Delta^{a}{}_{:a}}{2}, \quad \text{and} \quad \omega \equiv \frac{(\Delta_a \epsilon^{ab})_{:b}}{2}\,, \tag{9.6}$$

respectively.

Similarly, we note that the general displacement on the celestial sphere can be decomposed to two components,

$$\Delta_a = -\sum_{lm}(h^{\oplus}_{lm} Y_{lm:a} + h^{\otimes}_{lm} Y_{lm:b}\epsilon^{b}{}_{a}), \tag{9.7}$$

where

$$\begin{aligned} h^{\oplus}_{lm} &= \frac{1}{l(l+1)}\int d\hat{\mathbf{n}} Y^{*}_{lm}\Delta_a{}^{:a} = -\frac{2}{l(l+1)}\int d\hat{\mathbf{n}} Y^{*}_{lm}\kappa, \\ h^{\otimes}_{lm} &= \frac{1}{l(l+1)}\int d\hat{\mathbf{n}} Y^{*}_{lm}\Delta_a{}^{:b}\epsilon^{a}{}_{b} = \frac{2}{l(l+1)}\int d\hat{\mathbf{n}} Y^{*}_{lm}\omega, \end{aligned} \tag{9.8}$$

where $\oplus$ and $\otimes$ denote the gradient- and curl-type deflections, respectively. For simplicity, we have dropped the dependence on the directional vector parameterized by $\hat{\mathbf{n}}$. The lensing by foreground density perturbations to the firstorder only leads to a gradient-like displacement, while both components are generated when lensed by gravitational waves. We now calculate both the convergence and the rotational spectrum of the displacement field due to foreground stochastic gravitational waves.

9.2.1 Gradient Spectrum

Gradient deflections are associated with the expansion and, as defined above, can be described in terms of the convergence: $\kappa(\hat{\mathbf{n}}) \equiv -\Delta^{a}{}_{:a}/2$. In general the transverse divergence of a vector $\vec{A}$ can be rewritten as

$$\frac{1}{\sin\theta}\frac{\partial}{\partial\theta}(\sin\theta A_\theta) + \frac{1}{\sin\theta}\frac{\partial A_\phi}{\partial\phi} = r\left(\nabla\cdot\vec{A} - (\hat{\mathbf{n}}\cdot\nabla)(\hat{\mathbf{n}}\cdot\vec{A}) - \frac{2\hat{\mathbf{n}}\cdot\vec{A}}{r}\right), \tag{9.9}$$

where $r = \eta_0 - \eta'$. When substituting the form of $\mathbf{r}(\eta)$ from equation (9.5), the gradient terms here lead to terms that are due to $\nabla\cdot\hat{\mathbf{n}}$ and $\nabla\cdot\mathbf{H}$. We first consider the former and making use of the fact that $\partial_i \hat{n}_j = (\delta_{ij} - \hat{n}_i\hat{n}_j)/(\eta_0 - \eta')$, we separate contributions to convergence to two components and write $\kappa(\hat{\mathbf{n}}) = \kappa_1 + \kappa_2$ as

$$\begin{aligned}
\kappa_1 &= -\frac{1}{2}\int_{\eta_s}^{\eta_0} d\eta'\left(\frac{\eta_0-\eta'}{\eta_0-\eta_s}\right)(\hat{\mathbf{n}}\cdot\nabla_H)(\hat{\mathbf{n}}\cdot\mathbf{H}\cdot\hat{\mathbf{n}}) \\
&\quad -\frac{3}{2(\eta_0-\eta_s)}\int_{\eta_s}^{\eta_0} d\eta'(\hat{\mathbf{n}}\cdot\mathbf{H}\cdot\hat{\mathbf{n}}), \\
\kappa_2 &= -\frac{1}{4}\int_{\eta_s}^{\eta_0} d\eta'\left(\frac{\eta_0-\eta'}{\eta_0-\eta_s}\right)(\eta'-\eta_s)\nabla_H^2(\hat{\mathbf{n}}\cdot\mathbf{H}\cdot\hat{\mathbf{n}}) \\
&\quad +\frac{1}{4}\int_{\eta_s}^{\eta_0} d\eta'\left(\frac{\eta_0-\eta'}{\eta_0-\eta_s}\right)(\eta'-\eta_s)(\hat{\mathbf{n}}\cdot\nabla_H)^2(\hat{\mathbf{n}}\cdot\mathbf{H}\cdot\hat{\mathbf{n}}) \\
&\quad +\frac{1}{\eta_0-\eta_s}\int_{\eta_s}^{\eta_0} d\eta'(\eta'-\eta_s)(\hat{\mathbf{n}}\cdot\nabla_H)(\hat{\mathbf{n}}\cdot\mathbf{H}\cdot\hat{\mathbf{n}})\,,
\end{aligned} \tag{9.10}$$

where we have explicitly simplified the calculation by including terms associated with $\nabla\cdot\hat{\mathbf{n}}$.

Note that we have also replaced $\eta \to \eta_s$ corresponding to the conformal time at the last scattering surface of CMB. To simplify, we decompose the metric perturbation into the Fourier component,

$$\mathbf{H}(\mathbf{x},\eta) = \frac{1}{(2\pi)^{3/2}}\int d^3\mathbf{k}e^{i\mathbf{k}\cdot\mathbf{x}}T(k,\eta)\sum_{j=1}^{2}H_j(\mathbf{k})\mathbf{e}_j(\mathbf{k})\,, \tag{9.11}$$

where we have introduced the gravitational wave transfer function that describes the time evolution of the metric perturbation with $\mathbf{H}_j(\mathbf{k},\eta) = T(k,\eta)H_j(\mathbf{k})\mathbf{e}_j(\mathbf{k})$.

The terms in equation (9.10) can be simplified as

$$\begin{aligned}
\kappa_1 &= -\frac{1}{2}\int_{\eta_s}^{\eta_0} d\eta'\frac{1}{(2\pi)^{3/2}}\int d^3\mathbf{k}e^{i\mathbf{k}\cdot\mathbf{x}'}T(k,\eta') \\
&\quad \left(\frac{\eta_0-\eta'}{\eta_0-\eta_s}\right)\times\sum_j H_j(\mathbf{k})[\hat{\mathbf{n}}\cdot\mathbf{e}_j(\mathbf{k})\cdot\hat{\mathbf{n}}](i\mathbf{k}\cdot\hat{\mathbf{n}}) \\
&\quad -\frac{3}{2(\eta_0-\eta_s)}\int_{\eta_s}^{\eta_0} d\eta'\frac{1}{(2\pi)^{3/2}}\int d^3\mathbf{k}e^{i\mathbf{k}\cdot\mathbf{x}'} \\
&\quad \times T(k,\eta')\sum_j H_j(\mathbf{k})[\hat{\mathbf{n}}\cdot\mathbf{e}_j(\mathbf{k})\cdot\hat{\mathbf{n}}], \\
\kappa_2 &= \int_{\eta_s}^{\eta_0} d\eta'\frac{\eta'-\eta_s}{4}\frac{1}{(2\pi)^{3/2}}\int d^3\mathbf{k}e^{i\mathbf{k}\cdot\mathbf{x}'}T(k,\eta') \\
&\quad \left(\frac{\eta_0-\eta'}{\eta_0-\eta_s}\right)\times\sum_j \mathbf{H}_j(\mathbf{k})[\mathbf{k}^2-(\hat{\mathbf{n}}\cdot\mathbf{k})^2][\hat{\mathbf{n}}\cdot\mathbf{e}_j(\mathbf{k})\cdot\hat{\mathbf{n}}] \\
&\quad +\frac{1}{\eta_0-\eta_s}\int_{\eta_s}^{\eta_0} d\eta'(\eta'-\eta_s)\frac{1}{(2\pi)^{3/2}}\int d^3\mathbf{k}e^{i\mathbf{k}\cdot\mathbf{x}'} \\
&\quad \times T(k,\eta')\sum_j H_j(\mathbf{k})[\hat{\mathbf{n}}\cdot\mathbf{e}_j(\mathbf{k})\cdot\hat{\mathbf{n}}](i\mathbf{k}\cdot\hat{\mathbf{n}}).
\end{aligned} \tag{9.12}$$

Here, $\mathbf{x}' = (\eta_0-\eta')\hat{\mathbf{n}}$ and $\mathbf{e}_j$ represents the symmetric, traceless polarization tensor that obeys Tr $[\mathbf{e}_j(\mathbf{k})\cdot\mathbf{e}_k(\mathbf{k})] = 2\delta_{jk}$ and $\mathbf{k}\cdot\mathbf{e}_j(\mathbf{k}) = 0$ with j in equation (9.12) summing over the two linear polarization states.

Since gravitational waves trace the wave equation with

$$\ddot{\mathbf{H}} - \nabla^2\mathbf{H} + 2\frac{\dot{a}}{a}\mathbf{H} = 16\pi G a^2 \mathbf{P}\,, \tag{9.13}$$

where $\mathbf{P}$ is the tensor part of the anisotropic stress, say from neutrinos (see, Ref. [16] for details); The term in the right-hand side acts as a damping term for the evolution of gravitational waves and is important for modes that enter the horizon before matter-radiation equality, with a smaller correction for modes enter horizon after matter-radiation equality. Since these corrections are not more than 30%, while the amplitude of the gravitational wave background is uncertain to more than orders of magnitude, we ignore such subtleties here assuming no anisotropic stress; for a cosmological model dominated by matter, in Fourier space, one can write the evolution of $\mathbf{H}$ in terms of the transfer function as $T(k,\eta) = 3j_1(k\eta)/(k\eta)$.

We define the power spectrum of metric perturbations as

$$\langle H_i(\mathbf{k}) H_j^*(\mathbf{k})\rangle = (2\pi)^3 P_T(k)\delta_{ij}\delta^{(3)}(\mathbf{k}-\mathbf{k}')\,, \tag{9.14}$$

where we assume isotropy and equal density of gravitational waves in the two polarization states i and j. Following Ref. [10], we normalize the power spectrum to the Hubble parameter during inflation and take

$$P_T(k) = \frac{8\pi}{(2\pi)^3}\left(\frac{H_I}{M_{\rm Planck}}\right)^2 k^{-3}\,. \tag{9.15}$$

Using this three-dimensional power spectrum for metric perturbations, the angular power spectrum of gradient-type deflections is

$$\begin{aligned} C_l^{h^\oplus} &= \frac{1}{2l+1}\sum_{m=-l}^{m=l}\langle|h^\oplus_{lm}|^2\rangle \qquad (9.16)\\ &= \frac{4}{(2l+1)l^2(l+1)^2}\sum_{m=-l}^{m=l}\langle|\int d\hat{\mathbf{n}} Y^*_{lm}(\hat{\mathbf{n}})\kappa(\hat{\mathbf{n}})|^2\rangle \\ &= \frac{\pi}{l^2(l+1)^2}\frac{(l+2)!}{(l-2)!}\int d^3\mathbf{k} P_T(k)|T_1+T_2+T_m^\oplus|^2, \end{aligned}$$

where the terms are again

$$\begin{aligned}
T_1 &= -k\int_{\eta_s}^{\eta_0} d\eta'\left(\frac{\eta_0-\eta'}{\eta_0-\eta_s}\right)T(k,\eta') \\
&\quad\times\left[\partial_x(x^{-2}j_l(x))|_{x=k(\eta_0-\eta')}\right] \\
&\quad-\frac{3}{\eta_0-\eta_s}\int_{\eta_s}^{\eta_0} d\eta' T(k,\eta')(x^{-2}j_l(x))|_{x=k(\eta_0-\eta')}, \\
T_2 &= \frac{k^2}{2}\int_{\eta_s}^{\eta_0} d\eta'\left(\frac{\eta_0-\eta'}{\eta_0-\eta_s}\right)(\eta'-\eta_s)T(k,\eta') \\
&\quad\times\left[(1+\partial_x^2)(x^{-2}j_l(x))|_{x=k(\eta_0-\eta')}\right] \\
&\quad+\frac{2k}{\eta_0-\eta_s}\int_{\eta_s}^{\eta_0} d\eta'(\eta'-\eta_s)T(k,\eta') \\
&\quad\times\left[\partial_x(x^{-2}j_l(x))|_{x=k(\eta_0-\eta')}\right]. \qquad (9.17)
\end{aligned}$$

Note that the convergence power spectrum due to gravitational wave deflections is $C_l^{\kappa\kappa} = l^2(l+1)^2 C_l^{h\oplus}/4$.

In Eq. (9.16) we have also introduced an additional correction to the gradient-type deflection spectrum with the term $T_m^{\oplus}$. As discussed in [10], this is associated with the gradient-type deflection pattern or convergence related to shearing of the last scattering surface by gravitational waves present at that surface. To calculate this correction, we first evaluate the displacement vector at the last scattering surface

$$\mathbf{r}_m = -\frac{\mathbf{H}}{2}\cdot\hat{\mathbf{n}}(\eta_0-\eta_s)\,, \qquad (9.18)$$

and then project this displacement vector to obtain the transverse displacement vector of

$$\Delta_m = \frac{\mathbf{r}_m - (\mathbf{r}_m\cdot\hat{\mathbf{n}})\hat{\mathbf{n}}}{\eta_0-\eta_s}\,. \qquad (9.19)$$

This vector can be decomposed to the gradient- and curl-types deflections. Making use of the fact that the convergence is $\kappa(\hat{\mathbf{n}}) \equiv -\Delta^a_{m:a}/2$ and taking the Fourier transforms, we write the required term in the Eq. (9.16) as

$$\begin{aligned}
T_m^{\oplus} &= -\frac{k}{2}(\eta_0-\eta_s)T(k,\eta_s)\left[\partial_x(x^{-2}j_l(x))|_{x=k(\eta_0-\eta_s)}\right] \\
&\quad - T(k,\eta_s)(x^{-2}j_l(x))|_{x=k(\eta_0-\eta_s)}\,. \qquad (9.20)
\end{aligned}$$

This completes the calculation of gradient-type deflection power spectrum by taking into account the lensing by intervening gravitational waves between the last scattering surface and the observer and the metric-shear correction related to gravitational waves present at the last scattering surface from which photons propagate.

9.2.2 Curl Spectrum

Rotation is defined to be $\omega(\hat{\mathbf{n}}) \equiv \frac{1}{2}(\Delta_a \epsilon^{ab})_{:b}$, which leads to

$$\omega(\hat{\mathbf{n}}) \equiv -\frac{1}{2}\hat{\mathbf{n}} \cdot (\nabla \times \mathbf{r}(\hat{\mathbf{n}}, \eta_s)) \,. \tag{9.21}$$

Equation (9.5) gives

$$\omega \;=\; \frac{1}{2}\int_{\eta_s}^{\eta_0} d\eta' \left[\hat{\mathbf{n}} \cdot (\nabla \times \mathbf{H}) \cdot \hat{\mathbf{n}}\right] \,, \tag{9.22}$$

since $\nabla \times \hat{\mathbf{n}} = 0$. Here we define the curl of the second rank tensor $\mathbf{H}$ by $(\nabla \times \mathbf{H})_{il} = \epsilon_{ijk}\partial_j H_{kl}$.

The curl-type deflection spectrum from this term is [10],

$$\begin{aligned} C_l^{h^\otimes} &= \frac{1}{2l+1}\sum_{m=-l}^{m=l}\langle |h_{lm}^\otimes|^2\rangle \\ &= \frac{4}{(2l+1)l^2(l+1)^2}\sum_{m=-l}^{m=l}\langle |\int d\hat{\mathbf{n}} Y_{lm}^*(\hat{\mathbf{n}})\omega(\hat{\mathbf{n}})|^2\rangle \\ &= \frac{\pi}{l^2(l+1)^2}\frac{(l+2)!}{(l-2)!}\int d^3\mathbf{k} P_T(k)|T_3 + T_m^\otimes|^2, \end{aligned} \tag{9.23}$$

where

$$T_3 \;=\; 2k\int_{\eta_s}^{\eta_0} d\eta' T(k,\eta')(x^{-2}j_l(x))|_{x=k(\eta_0-\eta')} \,. \tag{9.24}$$

Again, one can write the power spectrum of rotation as $C_l^{\omega\omega} = l^2(l+1)^2 C_l^{h^\otimes}/4$.

Here also we include the correction to the rotational spectrum due to metric perturbations at the last scattering surface. Similar to convergence, by following the same procedure as before but taking $1/2([\Delta_m]_a\epsilon^{ab})_{:b}$ of Equation (9.19), we get

$$T_m^\otimes = k(\eta_0 - \eta_s)T(k,\eta_s)(x^{-2}j_l(x))|_{x=k(\eta_0-\eta_s)}. \tag{9.25}$$

For comparison, we note that density fluctuations along the line of sight lead to gradient-type deflections only. The resulting contributions are described in terms of the angular power spectrum of projected potential $C_l^{\phi\phi}$ that is well studied in the literature [2]. We do not repeat those derivations here, but will provide a comparison of lensing under gravitational waves and lensing by mass in the discussion later.

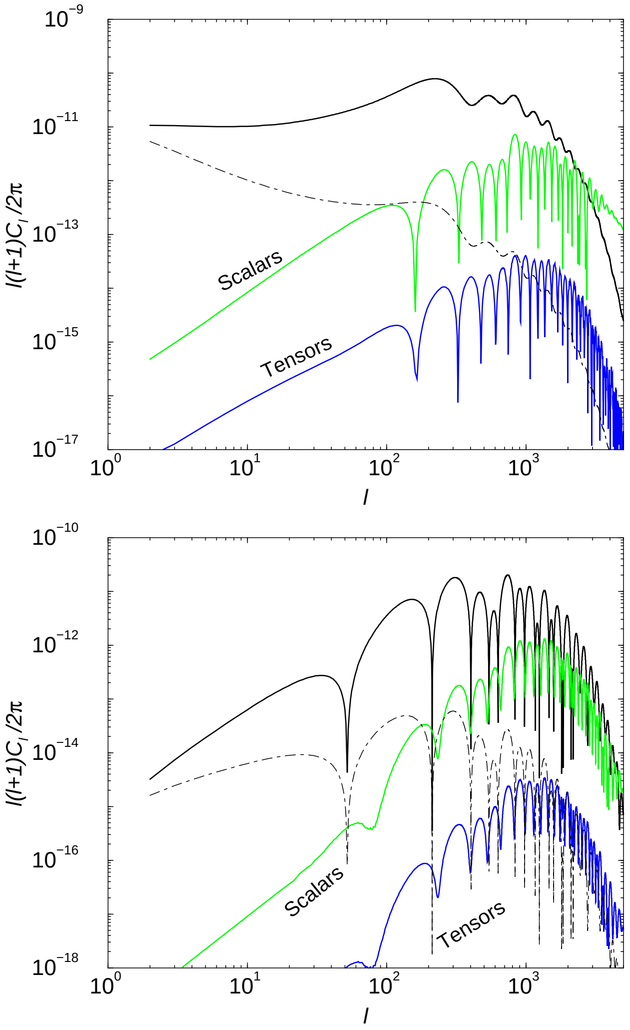

Figure 9.2: The lensing modification to CMB power spectra for density perturbations and for gravitational waves. *Top:* Temperature fluctuations. The top curve is the primordial power spectrum. The middle curve is the secondary anisotropy contribution, $|\tilde{C}_l - C_l|$, to the temperature power spectrum from lensing by density perturbations, and the lower curve is for lensing by gravitational waves, assuming the maximum IGW background consistent with current data with the deflection power spectra shown in Figure 9.1. *Bottom:* Temperature-E polarization cross correlation, with curves following the left panel. In both panels, thin long-dashed line is C_l/l at each multipole with C_l related to the intrinsic anisotropy spectrum; while the cosmic variance is $C_l/\sqrt{l}$, C_l/l denotes the level at which one must control the systematics, if the effects resulting systematics apply to a wide range of multipoles. The lensing by density fluctuations cannot be ignored as the corrections are well above the cosmic variance limit and will be detectable in upcoming anisotropy data. The lensing by foreground gravitational waves, however, are below the cosmic variance limit, suggesting that they will remain undetectable, but above the systematic level when $l > 10^3$.

9.3 Lensing of CMB by Gravitational Waves

In this section, we will discuss the analytical calculation related to how foreground gravitational waves modify the background CMB temperature anisotropy and polarization patterns. Here, we will concentrate on the angular power spectra of CMB observables. The lensing of CMB by foreground density fluctuations is formulated in Ref. [2] and we follow the same procedure here. Since deflection field power spectra peak at large angular scales, we present an analytical formulation as appropriate for the spherical sky. The calculation we consider here, however, is perturbative, and one expects important corrections beyond the first order in the deflection angle. For foreground gravitational waves, such issues can be ignored as the overall modification to the anisotropy and polarization spectra is small.

9.3.1 Temperature Anisotropies

Following Ref. [2], the lensed temperature field $\tilde{\theta}$ can be expressed as

$$\tilde{\theta}(\hat{\mathbf{n}}) = \theta(\hat{\mathbf{n}} + \boldsymbol{\Delta}) = \theta(\hat{\mathbf{n}}) + \nabla^a\theta \cdot \Delta_a + \frac{1}{2}\nabla^b\nabla^a\theta \cdot \Delta_a\Delta_b \, , \tag{9.26}$$

where $\theta(\hat{\mathbf{n}})$ is the unlensed temperature fluctuation in the direction $\hat{\mathbf{n}}$. The temperature field can be expanded to multipole moments such that $\theta(\hat{\mathbf{n}}) = \sum_{lm} \theta_{lm} Y_{lm}(\hat{\mathbf{n}})$. Taking the spherical harmonic moment of equation (9.26) and using equation (9.7), we find

$$\begin{aligned}
\tilde{\theta}_{lm} &= \theta_{lm} + \int d\hat{\mathbf{n}} Y^*_{lm} \left[\nabla^a\theta \cdot \Delta_a + \frac{1}{2}\nabla^b\nabla^a\theta \cdot \Delta_a\Delta_b\right] \\
&= \theta_{lm} - \sum_{l_1m_1l_2m_2} \Big(I^{\oplus}_{lml_1m_1l_2m_2} \theta_{l_1m_1} h^{\oplus}_{l_2m_2} \\
&+ I^{\otimes}_{lml_1m_1l_2m_2} \theta_{l_1m_1} h^{\otimes}_{l_2m_2} \Big) \\
&+ \frac{1}{2} \sum_{l_1m_1l_2m_2l_3m_3} \Big(J^{\oplus}_{lml_1m_1l_2m_2l_3m_3} \theta_{l_1m_1} h^{\oplus}_{l_2m_2} h^{\oplus *}_{l_3m_3} \\
&+ J^{\otimes}_{lml_1m_1l_2m_2l_3m_3} \theta_{l_1m_1} h^{\otimes}_{l_2m_2} h^{\otimes *}_{l_3m_3} \Big),
\end{aligned} \tag{9.27}$$

where the integrals are

$$\begin{aligned}
I^{\oplus}_{lml_1m_1l_2m_2} &= \int d\hat{\mathbf{n}} Y^*_{lm} Y^{:a}_{l_1m_1} Y_{l_2m_2:a}, & I^{\otimes}_{lml_1m_1l_2m_2} &= \int d\hat{\mathbf{n}} Y^*_{lm} Y^{:a}_{l_1m_1} Y_{l_2m_2:b} \epsilon^b{}_a, \\
J^{\oplus}_{lml_1m_1l_2m_2l_3m_3} &= \int d\hat{\mathbf{n}} Y^*_{lm} Y^{:ab}_{l_1m_1} Y_{l_2m_2:a} Y^*_{l_3m_3:b}, & J^{\otimes}_{lml_1m_1l_2m_2l_3m_3} &= \int d\hat{\mathbf{n}} Y^*_{lm} Y^{:ab}_{l_1m_1} Y_{l_2m_2:c} Y^*_{l_3m_3:d} \epsilon^c{}_a \epsilon^d{}_b \, .
\end{aligned} \tag{9.28}$$

The lensed temperature anisotropy power spectrum spectrum is

$$C_l^{\tilde{\theta}} = C_l^{\theta} + \sum_{l_1 l_2} C_{l_1}^{\theta} \left(C_{l_2}^{h^{\oplus}} S_1^{\oplus} + C_{l_2}^{h^{\otimes}} S_1^{\otimes} \right) \quad + C_l^{\theta} \sum_{l_1} \left(C_{l_1}^{h^{\oplus}} S_2^{\oplus} + C_{l_1}^{h^{\otimes}} S_2^{\otimes} \right), \tag{9.29}$$

where

$$\begin{aligned} S_1^{\oplus} &= \sum_{m_1 m_2} |I^{\oplus}_{lml_1m_1l_2m_2}|^2, \\ S_1^{\otimes} &= \sum_{m_1 m_2} |I^{\otimes}_{lml_1m_1l_2m_2}|^2, \\ S_2^{\oplus} &= \frac{1}{2} \sum_{m_1} J^{\oplus}_{lmlml_1m_1l_1m_1} + \text{c.c.}, \\ S_2^{\otimes} &= \frac{1}{2} \sum_{m_1} J^{\otimes}_{lmlml_1m_1l_1m_1} + \text{c.c.}\,, \end{aligned} \tag{9.30}$$

and c.c. is the complex conjugate. The terms $S_1^{\oplus}$ and $S_2^{\oplus}$ are similar to those involving lensing by foreground density perturbations [2]. First, the integral $I^{\oplus}_{lml_1m_1l_2m_2}$ can be simplified through integration by parts and noting $\nabla^2 Y_{lm} = -l(l+1) Y_{lm}$ and the general integral of three spin-spherical harmonics over the sky:

$$\begin{aligned} &\int d\hat{\mathbf{n}} ({}_{s_1}Y^*_{l_1m_1})({}_{s_2}Y_{l_2m_2})({}_{s_3}Y_{l_3m_3}) = \\ &(-1)^{m_1+s_1} \sqrt{\frac{(2l_1+1)(2l_2+1)(2l_3+1)}{4\pi}} \\ &\times \begin{pmatrix} l_1 & l_2 & l_3 \\ s_1 & -s_2 & -s_3 \end{pmatrix} \begin{pmatrix} l_1 & l_2 & l_3 \\ -m_1 & m_2 & m_3 \end{pmatrix}, \end{aligned} \tag{9.31}$$

when $s_1 = s_2 + s_3$. We note that under parity inversion, ${}_sY_{lm} \to (-1)^l {}_{-s}Y_{lm}$, which is a useful property when we discuss lensing modifications to the CMB polarization field.

With $s_i = 0$ and noting that ${}_0Y_{lm} = Y_{lm}$,

$$\begin{aligned} I^{\oplus}_{lml_1m_1l_2m_2} &= \frac{1}{2}[l_1(l_1+1) + l_2(l_2+1) - l(l+1)](-1)^m \\ &\times \sqrt{\frac{(2l+1)(2l_1+1)(2l_2+1)}{4\pi}} \\ &\times \begin{pmatrix} l & l_1 & l_2 \\ 0 & 0 & 0 \end{pmatrix} \begin{pmatrix} l & l_1 & l_2 \\ -m & m_1 & m_2 \end{pmatrix}. \end{aligned} \tag{9.32}$$

Using the orthonormality relation of Wigner-3j symbols

$$\sum_{m_1 m_2} \begin{pmatrix} l_1 & l_2 & l_3 \\ m_1 & m_2 & m_3 \end{pmatrix} \begin{pmatrix} l_1 & l_2 & l_3 \\ m_1 & m_2 & m_3 \end{pmatrix} = \frac{1}{2l_3+1}\,, \tag{9.33}$$

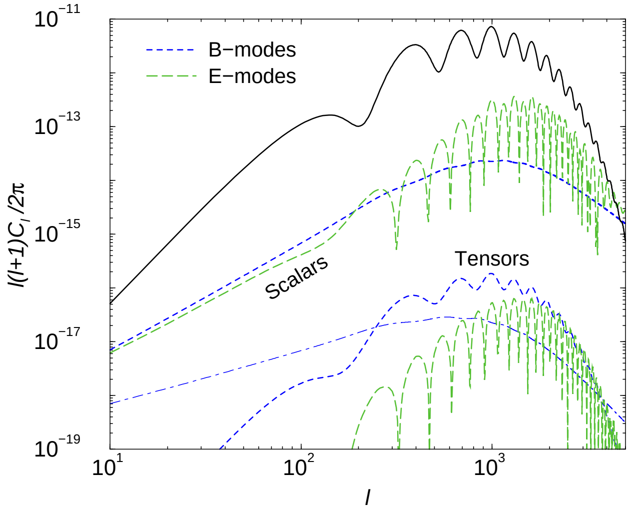

Figure 9.3: The lensing modification to CMB polarization spectra for density perturbations and for gravitational waves. From top to bottom, these curves are for primordial power spectrum in the E-mode (solid line), lensing correction to E-mode from density fluctuations (long -dashed line), lensing correction to B-mode from density fluctuations (short-dashed line labeled “Scalars”), lensing correction to B-mode from gravitational waves (short-dashed line labeled “Tensors”), and the lensing correction to E-mode from gravitational waves (long-dashed line). For reference, the thin dot-dashed line is the systematic level of the B-mode lensing power spectrum, C_l/l, from the density field. While the corrections from lensing by foreground gravitational waves is below the cosmic variance limit of the lensing B-mode power spectrum and, again, undetectable in anisotropy maps, they may become a source of systematic in all-sky maps with no instrumental noise and other secondary signals and foregrounds.

we can write

$$S_1^{\oplus} = \frac{1}{2l+1}(F_{ll_1l_2}^{\oplus})^2, \tag{9.34}$$

with

$$\begin{aligned} F_{ll_1l_2}^{\oplus} &= \frac{1}{2}\left[l_1(l_1+1) + l_2(l_2+1) - l(l+1)\right] \\ \times \quad &\sqrt{\frac{(2l+1)(2l_1+1)(2l_2+1)}{4\pi}} \begin{pmatrix} l & l_1 & l_2 \\ 0 & 0 & 0 \end{pmatrix} . \end{aligned} \tag{9.35}$$

Though tedious, the calculation related to $S_1^{\otimes}$ can be simplified using the gradient relation for spherical harmonics by raising and lowering of the spin [17]:

$$\nabla Y_{lm} = \sqrt{\frac{l(l+1)}{2}}[{}_1Y_{lm}\mathbf{m}_+ - {}_{-1}Y_{lm}\mathbf{m}_-], \tag{9.36}$$

where

$$\mathbf{m}_{\pm} = \frac{1}{\sqrt{2}}(e_{\hat{\theta}} \mp ie_{\hat{\phi}}) . \tag{9.37}$$

Combining these derivatives with the general integral in equation (9.31) leads to

$$\begin{aligned} I_{lml_1m_1l_2m_2}^{\otimes} &= -\frac{i}{2}\sqrt{l_1(l_1+1)l_2(l_2+1)}(-1)^m \\ \times \quad &\sqrt{\frac{(2l+1)(2l_1+1)(2l_2+1)}{4\pi}} \\ \times \quad &\begin{pmatrix} l & l_1 & l_2 \\ -m & m_1 & m_2 \end{pmatrix} \begin{pmatrix} l & l_1 & l_2 \\ 0 & -1 & 1 \end{pmatrix} \left[1-(-1)^{l+l_2+l_2}\right] . \end{aligned} \tag{9.38}$$

Again using the orthonormality relation in equation (9.33),

$$S_1^{\otimes} = \frac{1}{2l+1}\left(F_{ll_1l_2}^{\otimes}\right)^2, \tag{9.39}$$

with

$$\begin{aligned} F_{ll_1l_2}^{\otimes} &= \frac{1}{2}\sqrt{l_1(l_1+1)l_2(l_2+1)} \begin{pmatrix} l & l_1 & l_2 \\ 0 & -1 & 1 \end{pmatrix} \\ &\sqrt{\frac{(2l+1)(2l_1+1)(2l_2+1)}{4\pi}} \left[1-(-1)^{l+l_1+l_2}\right] . \end{aligned} \tag{9.40}$$

To calculate $S_2^{\otimes}$ and $S_2^{\oplus}$, we first note that

$$\sum_{m_1} Y_{l_1 m_1 : a} Y^*_{l_1 m_1 : b} = \frac{l_1(l_1+1)(2l_1+1)}{8\pi} g_{ab}, \tag{9.41}$$

where g_{ab} is the usual metric of unit sphere,

$$g_{ab} = \begin{pmatrix} 1 & 0 \\ 0 & \sin^2\theta \end{pmatrix} . \tag{9.42}$$

These allow us to show that

$$\begin{aligned} S_2^{\oplus} &\equiv \frac{1}{2}\sum_{m_1} J^{\oplus}_{lmlml_1m_1l_1m_1} + \text{c.c.} \\ &= -l(l+1)l_1(l_1+1)\frac{2l_1+1}{8\pi} . \end{aligned} \tag{9.43}$$

Also $S_2^{\otimes} = S_2^{\oplus}$. Finally, combining all expressions, we can write

$$\begin{aligned} C_l^{\tilde{\theta}} &= C_l^{\theta} - l(l+1)RC_l^{\theta} \\ &+ \sum_{l_1 l_2} \frac{C_{l_1}^{\theta}}{2l+1}\left[C_{l_2}^{h^{\oplus}}(F^{\oplus}_{ll_1l_2})^2 + C_{l_2}^{h^{\otimes}}(F^{\otimes}_{ll_1l_2})^2\right] , \end{aligned} \tag{9.44}$$

where $F^{\oplus}_{ll_1l_2}$ and $F^{\otimes}_{ll_1l_2}$ are given in equations (9.35) and (40), respectively, and

$$R = \sum_{l_1} l_1(l_1+1)\frac{2l_1+1}{8\pi}\left[C_{l_1}^{h^{\oplus}} + C_{l_1}^{h^{\otimes}}\right] . \tag{9.45}$$

This expression is similar to that of equation (62) of Ref. [2] when $C_{l_1}^{h^{\otimes}} = 0$ and $C_{l_1}^{h^{\oplus}}$ is identified as the power spectrum of projected lensing potentials due to intervening density perturbations between us and the CMB.

9.3.2 Polarization

The lensing effect on CMB polarization can be described similar to temperature anisotropies by making use of the remapping ${}_{\pm}\tilde{X}(\hat{\mathbf{n}}) = {}_{\pm}X(\hat{\mathbf{n}}) + \nabla_i\phi(\hat{\mathbf{n}})\nabla^i{}_{\pm}X(\hat{\mathbf{n}}) + \ldots +$, where ${}_{\pm}X = Q \pm iU$, where we have simplified the notation by replacing the spin-dependent gradients with a covariant derivative that acts on the spin components of the symmetric tensors that are traceless. Here, we have also ignored the rotation needed to align the polarization basis vectors between the lensed and unlensed fields, but this rotation is unimportant when considering displacements along the lines of constant azimuthal angles [18]. We refer the reader to Refs. [18, 19] for details of our shorthand notation and why it can be used for the lensing of the polarization pattern on the spherical sky.

While our notation here is simple and follows that of Ref. [2], the final result is the same as what one gets by using the standard notation of differential geometry. This is due to the fact that the overlapping integrals involving spin harmonics that we will perform remain consistent with our simplified notation.

As is well known, the CMB polarization components form a spin-2 field and are expanded in terms of the spin-weighted spherical harmonics such that ${}_{\pm}X(\hat{\mathbf{n}}) = \sum_{lm} {}_{\pm}X_{lm\,\pm2}Y_{lm}(\hat{\mathbf{n}})$. Instead of Stokes parameters, the more popular, E and B modes are are given by

$$
{}_{\pm}X_{lm} = E_{lm} \pm iB_{lm} \tag{9.46}
$$

. We will discuss lensing modifications to angular power spectra of E and B modes as well as the cross correlation between E and θ, while cross-correlation between E and B, and between B and θ are ignored as these are zero through parity arguments. Furthermore, the modifications to polarization by lensing do not violate parity conservation.

Taking the spherical harmonic moment of the polarization field under lensing, we write

$$
\begin{aligned}
{}_{\pm}\tilde{X}_{lm} &= {}_{\pm}X_{lm} \\
&- \sum_{l_1m_1l_2m_2} \Big[{}_{\pm}X_{l_1m_1} \Big({}_{\pm2}I^{\oplus}_{lml_1m_1l_2m_2} h^{\oplus}_{l_2m_2} \\
&+ {}_{\pm2}I^{\otimes}_{lml_1m_1l_2m_2} h^{\otimes}_{l_2m_2} \Big) \Big] \\
&+ \frac{1}{2} \sum_{l_1m_1l_2m_2l_3m_3} \Big[{}_{\pm}X_{l_1m_1} \Big({}_{\pm2}J^{\oplus}_{lml_1m_1l_2m_2l_3m_3} h^{\oplus}_{l_2m_2} h^{\oplus *}_{l_3m_3} \\
&+ {}_{\pm2}J^{\otimes}_{lml_1m_1l_2m_2l_3m_3} h^{\otimes}_{l_2m_2} h^{\otimes *}_{l_3m_3} \Big) \Big],
\end{aligned} \tag{9.47}
$$

where

$$
\begin{aligned}
{}_{\pm2}I^{\oplus}_{lml_1m_1l_2m_2} &= \int d\hat{\mathbf{n}} ({}_{\pm2}Y^{*}_{lm})({}_{\pm2}Y^{:a}_{l_1m_1}) Y_{l_2m_2:a}, \\
{}_{\pm2}J^{\oplus}_{lml_1m_1l_2m_2l_3m_3} &= \int d\hat{\mathbf{n}} ({}_{\pm2}Y^{*}_{lm})({}_{\pm2}Y^{:ab}_{l_1m_1}) Y_{l_2m_2:a} Y^{*}_{l_3m_3:b}, \\
{}_{\pm2}I^{\otimes}_{lml_1m_1l_2m_2} &= \int d\hat{\mathbf{n}} ({}_{\pm2}Y^{*}_{lm})({}_{\pm2}Y^{:a}_{l_1m_1}) Y_{l_2m_2:b} \epsilon^{b}{}_{a}, \\
{}_{\pm2}J^{\otimes}_{lml_1m_1l_2m_2l_3m_3} &= \int d\hat{\mathbf{n}} ({}_{\pm2}Y^{*}_{lm})({}_{\pm2}Y^{:ab}_{l_1m_1}) Y_{l_2m_2:c} Y^{*}_{l_3m_3:d} \epsilon^{c}{}_{a} \epsilon^{d}{}_{b}\,.
\end{aligned}
$$

After straightforward but tedious algebra, the lensed power spectra of $\tilde{E}$-modes, $\tilde{B}$-modes, and the cross correlation between $\tilde{E}$-modes and $\tilde{\theta}$ are

$$\begin{aligned}
C_l^{\tilde{E}} &= C_l^E + \frac{1}{2}\sum_{l_1 l_2}\left[C_{l_1}^{h^\oplus}\,{}_2S_1^\oplus + C_{l_1}^{h^\otimes}\,{}_2S_1^\otimes\right]\left[(C_{l_2}^E + C_{l_2}^B) + (-1)^L(C_{l_2}^E - C_{l_2}^B)\right] \\
&+ C_l^E\sum_{l_1}(C_{l_1}^{h^\oplus}\,{}_2S_2^\oplus + C_{l_1}^{h^\otimes}\,{}_2S_2^\otimes), \\
C_l^{\tilde{B}} &= C_l^B + \frac{1}{2}\sum_{l_1 l_2}\left[C_{l_1}^{h^\oplus}\,{}_2S_1^\oplus + C_{l_1}^{h^\otimes}\,{}_2S_1^\otimes\right]\left[(C_{l_2}^E + C_{l_2}^B) + (-1)^L(C_{l_2}^B - C_{l_2}^E)\right] \\
&+ C_l^B\sum_{l_1}(C_{l_1}^{h^\oplus}\,{}_2S_2^\oplus + C_{l_1}^{h^\otimes}\,{}_2S_2^\otimes), \\
C_l^{\tilde{\theta}\tilde{E}} &= C_l^{\theta E} + \frac{1}{2}\sum_{l_1 l_2}(1+(-1)^L)(C_{l_1}^{h^\oplus}\,{}_{02}S_1^\oplus + C_{l_1}^{h^\otimes}\,{}_{02}S_1^\otimes)C_{l_2}^{\theta E} \\
&+ \frac{1}{4}C_l^{\theta E}\sum_{l_1}\left(C_{l_1}^{h^\oplus}({}_2S_2^\oplus + S_2^\oplus) + C_{l_1}^{h^\otimes}({}_2S_2^\otimes + S_2^\otimes)\right)\,, \qquad (9.48)
\end{aligned}$$

where $L = l + l_1 + l_2$ and

$$\begin{aligned}
{}_2S_1^\oplus &= \sum_{m_1 m_2}|{}_{\pm 2}I_{lml_1m_1l_2m_2}^\oplus|^2, \qquad (9.49) \\
{}_2S_1^\otimes &= \sum_{m_1 m_2}|{}_{\pm 2}I_{lml_1m_1l_2m_2}^\otimes|^2, \\
{}_2S_2^\oplus &= \frac{1}{2}\sum_{m_1}{}_{\pm 2}J_{lmlml_1m_1l_1m_1}^\oplus + \text{c.c.}, \\
{}_2S_2^\otimes &= \frac{1}{2}\sum_{m_1}{}_{\pm 2}J_{lmlml_1m_1l_1m_1}^\otimes + \text{c.c.}, \\
{}_{02}S_1^\oplus &= \sum_{m_1 m_2}(I_{lml_1m_1l_2m_2}^\oplus\ {}_{+2}I_{lml_1m_1l_2m_2}^\oplus), \\
{}_{02}S_1^\otimes &= \sum_{m_1 m_2}(I_{lml_1m_1l_2m_2}^\otimes\ {}_{+2}I_{lml_1m_1l_2m_2}^\otimes).
\end{aligned}$$

To simplify terms in Eq. (9.49), we again make use of the integral relations outlined earlier when describing lensing of temperature anisotropies. In the case of polarization, these relations need to be generalized for integrals over spin-weighted spherical harmonics. First, the integral related to the gradient spectra is straightforward. Making use of the fact that $\nabla^2\,{}_{\pm 2}Y_{lm} = [-l(l+1)+4]\,{}_{\pm 2}Y_{lm}$ and using equation (9.31), we find

$$\begin{aligned}
{}_2S_1^\oplus &= \frac{1}{2l+1}|{}_2F_{ll_1l_2}^\oplus|^2, \\
{}_2F_{ll_1l_2}^\oplus &= \frac{1}{2}[l_1(l_1+1) + l_2(l_2+1) - l(l+1)] \\
&\times\sqrt{\frac{(2l+1)(2l_1+1)(2l_2+1)}{4\pi}}\begin{pmatrix} l & l_1 & l_2 \\ 2 & 0 & -2 \end{pmatrix}\,. \qquad (9.50)
\end{aligned}$$

This is exactly the relation that one encounters when lensing the polarization field by foreground density fluctuations [2].

The integral related to the curl-type displacement is tedious, but can be simplified using relations involving raising and lowering of the spin and gradient of the spin-weighted spherical harmonic. To calculate

$$
{}_2I^{\otimes}_{lml_1m_1l_2m_2} \quad = \quad \int d\hat{\mathbf{n}}({}_{\pm 2}Y^*_{lm})_{\pm 2}Y_{l_1m_1:a}Y_{l_2m_2:b}\epsilon^{ba} \,, \tag{9.51}
$$

we note

$$
\begin{aligned}
\mathbf{m}_- \cdot \nabla_s Y_{lm} \quad &= \quad \sqrt{\frac{(l-s)(l+s+1)}{2}}\,{}_{s+1}Y_{lm}, \\
\mathbf{m}_+ \cdot \nabla_s Y_{lm} \quad &= \quad -\sqrt{\frac{(l+s)(l-s+1)}{2}}\,{}_{s-1}Y_{lm} \ ,
\end{aligned} \tag{9.52}
$$

and the relation

$$
(\mathbf{m}_+)_i(\mathbf{m}_-)_j + (\mathbf{m}_-)_i(\mathbf{m}_+)_j = g_{ij}, \tag{9.53}
$$

to write $\nabla\ {}_sY_{lm} = (\mathbf{m}_+\mathbf{m}_- + \mathbf{m}_-\mathbf{m}_+)\cdot\nabla_s Y_{lm}$ as

$$
{}_sY_{lm} = \sqrt{\frac{(l-s)(l+s+1)}{2}}\ {}_{s+1}Y_{lm}\mathbf{m}_+ - \sqrt{\frac{(l+s)(l-s+1)}{2}}\,{}_{s-1}Y_{lm}\mathbf{m}_-.
$$

This leads to

$$
\begin{aligned}
{}_2I^{\otimes}_{lml_1m_1l_2m_2} &= \int d\hat{\mathbf{n}}({}_{+2}Y^*_{lm})_{+2}Y_{l_1m_1:a}Y_{l_2m_2:b}\epsilon^{ba} \\
= \quad & i(-1)^m\sqrt{\frac{l_2(l_2+1)}{2}}\sqrt{\frac{(2l+1)(2l_1+1)(2l_2+1)}{4\pi}} \\
& \begin{pmatrix} l & l_1 & l_2 \\ -m & m_1 & m_2 \end{pmatrix} \Bigg(\sqrt{\frac{(l_1+2)(l_1-1)}{2}} \begin{pmatrix} l & l_1 & l_2 \\ 2 & -1 & -1 \end{pmatrix} \\
& \quad -\sqrt{\frac{(l_1-2)(l_1+3)}{2}} \begin{pmatrix} l & l_1 & l_2 \\ 2 & -3 & 1 \end{pmatrix}\Bigg) \,,
\end{aligned} \tag{9.54}
$$

such that

$$
\begin{aligned}
{}_2S^{\otimes}_1 \quad &= \quad \sum_{m_1m_2} |{}_2I^{\otimes}_{lml_1m_1l_2m_2}|^2 = \frac{1}{2l+1}|{}_2F^{\otimes}_{ll_1l_2}|^2, \qquad (9.55) \\
{}_2F^{\otimes}_{ll_1l_2} \quad &= \quad \sqrt{\frac{l_2(l_2+1)(2l+1)(2l_1+1)(2l_2+1)}{8\pi}} \\
& \left(\sqrt{\frac{(l_1+2)(l_1-1)}{2}} \begin{pmatrix} l & l_1 & l_2 \\ 2 & -1 & -1 \end{pmatrix} - \sqrt{\frac{(l_1-2)(l_1+3)}{2}} \begin{pmatrix} l & l_1 & l_2 \\ 2 & -3 & 1 \end{pmatrix}\right) \,.
\end{aligned}
$$

Furthermore, with $s = \pm 2$, equation (9.43) can be generalized to

$$
{}_2S_2^{\oplus} = -\frac{1}{2}[l(l+1)-4]l_1(l_1+1)\frac{2l_1+1}{4\pi}\,, \tag{9.56}
$$

and as in the case of lensed temperature anisotropies,

$$
{}_{+2}S_2^{\otimes} = {}_{+2}S_2^{\oplus}. \tag{9.57}
$$

For the cross-correlation between E-modes and the temperature, we find

$$
\begin{aligned}
{}_{02}S_1^{\oplus} &= \frac{1}{2l+1}(F^{\oplus}_{ll_1l_2})({}_{+2}F^{\oplus}_{ll_1l_2}),\\
{}_{02}S_1^{\otimes} &= \frac{1}{2l+1}(F^{\otimes}_{ll_1l_2})({}_{+2}F^{\otimes}_{ll_1l_2})\,.
\end{aligned} \tag{9.58}
$$

Putting the terms together, we can write the lensed power spectra in polarization as

$$
\begin{aligned}
C_l^{\tilde{E}} &= C_l^E - (l^2+l-4)RC_l^E\\
&+\frac{1}{2(2l+1)}\sum_{l_1l_2}\left[C_{l_1}^{h^{\oplus}}({}_2F^{\oplus}_{ll_1l_2})^2 + C_{l_1}^{h^{\otimes}}({}_2F^{\otimes}_{ll_1l_2})^2\right]\left[(C_{l_2}^E + C_{l_2}^B) + (-1)^L(C_{l_2}^E - C_{l_2}^B)\right],\\
C_l^{\tilde{B}} &= C_l^B - (l^2+l-4)RC_l^B\\
&+\frac{1}{2(2l+1)}\sum_{l_1l_2}\left[C_{l_1}^{h^{\oplus}}({}_2F^{\oplus}_{ll_1l_2})^2 + C_{l_1}^{h^{\otimes}}({}_2F^{\otimes}_{ll_1l_2})^2\right]\left[(C_{l_2}^E + C_{l_2}^B) - (-1)^L(C_{l_2}^E - C_{l_2}^B)\right],\\
C_l^{\tilde{\theta}\tilde{E}} &= C_l^{\theta E} - (l^2+l-2)RC_l^{\theta E}\\
&+\frac{1}{2l+1}\sum_{l_1l_2}\left[C_{l_1}^{h^{\oplus}}(F^{\oplus}_{ll_1l_2})({}_{+2}F^{\oplus}_{ll_1l_2}) + C_{l_1}^{h^{\otimes}}(F^{\otimes}_{ll_1l_2})({}_{+2}F^{\otimes}_{ll_1l_2})\right]C_{l_2}^{\theta E}\,,
\end{aligned} \tag{9.59}
$$

with R from equation (9.45).

The case of CMB lensing by foreground density fluctuations is simply the replacement of $C_{l_1}^{h^{\oplus}}$ with the power spectrum of projected potentials and with $C_{l_1}^{h^{\otimes}} = 0$. The lensing contribution to the B-mode from the foreground density field [5] act as the main contaminant in detecting the primary gravitational wave signal in B-modes of polarization. To see the extent to which lensing by gravitational waves themselves may become important in B-mode polarization studies, we will assume C_l^B to be zero and present a comparison between $C_l^{\tilde{B}}$ from density fluctuations and $C_l^{\tilde{B}}$ from gravitational waves. As we find, the secondary lensing from gravitational waves is smaller than the cosmic variance level of lensing B-modes from density perturbations and will remain undetectable in anisotropy maps. While below the cosmic variance limit, $C_l/\sqrt{l}$, for anisotropy measurements, systematics must generally be controlled to a level far below this; if systematics apply to a wide range of multipoles, then one must control their effects to C_l/l. For lensing by foreground gravitational waves at the maximum amplitude, we find that the corrections are above this level when $l > 10^3$

suggesting that one only needs to be concerned of these signals in all sky maps with no instrumental noise and other secondary signals.

9.4 Results and Discussion

In Figure 9.1, we show a comparison of $C_l^{h\otimes}$, $C_l^{h\oplus}$ and the angular power spectrum of deflection angle from projected density perturbations along the line of sight to η_s at a redshift of 1100 corresponding to the CMB last scattering surface. In calculating the power spectra of lensing from foreground gravitational waves, we have assumed an amplitude for the tensor modes with a value for H_I in equation (9.15) of 2×10^{14} GeV. This corresponds to a tensor-to-scalar ratio of 0.3, which is roughly the upper limit allowed by current CMB and large-scale structure observations [20].

The curl spectrum of deflections from gravitational waves has been previously discussed in the literature in the context of weak lensing surveys with galaxy shapes [10]. The gradient-type displacement spectrum from gravitational waves discussed here is also important and cannot be ignored when calculating modifications to CMB temperature and polarization anisotropies. Note that $C_l^{h\otimes}$ and $C_l^{h\oplus}$ peak at large angular scales corresponding to $\ell = 2$ to $\ell = 10$. To compare lensing by gravitational waves and lensing by mass, we calculate the rms deflection angle through $\theta^2_{\rm rms} = [\sum l(l+1)(2l+1)/4\pi(C_l^{h\otimes} + C_l^{h\oplus})]$. For gravitational waves related spectra shown in Figure 1, $\theta_{\rm rms}$ is 3.62×10^{-5} radians or roughly 7 arcsecs, which is a factor of 20 smaller than the rms deflection angle for CMB photons under density fluctuations, where $\theta_{\rm rms} \sim 7 \times 10^{-4}$. The coherence scale, where the rms drops to half of its peak value, is about ~ 60 degrees for lensing by gravitational waves, while for density perturbations the coherence scale is about a degree. With such a large coherence scale and a small rms deflection angle, foreground gravitational waves deflect large patches of the CMB sky by the same angle of about 6 arcsecs, resulting in an overall small modification to the CMB anisotropy and polarization spectra, when compared to the case with density fluctuations alone.

The differences between lensing by density perturbations and lensing by gravitational waves is clear in Figure 9.2, where we show modifications to the temperature power spectrum and the cross power spectrum between temperature and E-modes of polarization. The secondary lensing correction from the foreground gravitational waves is smaller than the cosmic variance level of intrinsic CMB anisotropies. Even with perfect CMB observations devoid of instrumental noise, it is unlikely that the lensing modification by primordial gravitational waves in the foreground of CMB will be detectable. As shown in Figure 9.2, however, the corrections are above the systematic level of C_l/l for primordial anisotropy measurements when $l > 10^3$. Thus, in the extreme case where one is dealing with perfect all-sky maps cleaned of foregrounds and other secondary signals, one could be concerned that these effects act as a source of systematic error for primordial anisotropy measurements. As is clear from

Figure 9.2, while lensing by gravitational waves is not significant, lensing of the CMB by foreground density perturbations will be detectable as the modifications are well above the cosmic variance limit.

In Figure 9.3, we summarize our results related to lensing of polarization anisotropies in terms of the power spectra or E- and B-modes. Again, the lensing effect by foreground gravitational waves is below the cosmic variance level of the dominant signal in the E- and B-mode maps, but above the systematic level. In the case of B-modes, lensing by density perturbations will remain the main contaminant in searching for gravitational wave signatures from the primary B-mode power spectrum. Lensing signals by foreground gravitational waves are unlikely to affect reconstruction techniques that attempt to remove the lensed B-modes when searching for a low amplitude gravitational wave background [4].

While we have only considered angular displacements on the sky, gravitational waves also contribute to a variation along the line of sight that can be described as a time-delay effect. Just as angular displacement couples to the angular gradient of the CMB, the radial displacement couples to the radial gradient of the CMB. These effects, however, are smaller due to lack of radial structure in the perturbations that form the primordial anisotropy spectrum in the CMB, such as the acoustic peaks. There are also geometric cancellations associated with the projection of line-of-sight time-delay modulations to an anisotropy pattern on the CMB sky [15]. Thus, it is unlikely that our conclusions related to lensing by foreground gravitational waves are affected by including the time-delay effect.

In general, our results are consistent with those of Ref. [10] who studied the possibility of measuring the gravitational wave background amplitude using weak lensing surveys of galaxy shapes and using the curl mode of the shear. Even with an optimistic survey with a large surface density of galaxies to measure shapes, the gravitational wave signal in the shear remains undetectable below the noise.

To summarize our calculation, while weak lensing distortion of the cosmic microwave background (CMB) temperature and polarization patterns by foreground density fluctuations is well studied in the literature, we noted the lack of a detailed description related to lensing modifications by foreground gravitational waves or tensor perturbations. Here, we have presented an analytical formulation on how CMB anisotropies and polarization patterns are distorted by a stochastic background of primordial gravitational waves between us and the last scattering surface. Our analytical formulation is useful when studying general lensing of any background source by foreground gravitational waves.

While density fluctuations perturb CMB photons via gradient-type displacements only, gravitational waves distort CMB anisotropies via both the gradient- and the curl-type displacements. The latter can be described as a rotation of background images in the presence of foreground gravitational waves while the former is related to the lensing convergence. For a primordial background of gravitational waves from inflation with an amplitude corresponding to a tensor-to-scalar ratio below the current upper limit of ~ 0.3, the resulting modifications to the angular power spectra of CMB temperature anisotropy and polarization are below the cosmic variance limit, but above the systematic level. Thus, it is unlikely that planned high sensitivity CMB observations warrant an accounting of the secondary contributions discussed here as they are not expected to affect precise parameter measurements; if observations are all-sky measurements with no instrumental noise, then these effects may be present in the form of systematic corrections to the primary anisotropy and polarization measurements.

9.5 Bibliography

[1] See, e.g., U. Seljak and M. Zaldarriaga, Phys. Rev. Lett. **82**, 2636 (1999) [arXiv:astro-ph/9810092]; Phys. Rev. D **60**, 043504 (1999) [arXiv:astro-ph/9811123]; M. Zaldarriaga and U. Seljak, Phys. Rev. D **59**, 123507 (1999) [arXiv:astro-ph/9810257]; W. Hu, Phys. Rev. D **64**, 083005 (2001) [arXiv:astro-ph/0105117].

[2] W. Hu, Phys. Rev. D **62**, 043007 (2000) [arXiv:astro-ph/0001303].

[3] A. Lewis and A. Challinor, Phys.Rept. **429** (2006) 1-65 [arXiv:astro-ph/0601594].

[4] W. Hu and T. Okamoto, Astrophys. J. **574**, 566 (2002) [arXiv:astro-ph/0111606]; M. Kesden, A. Cooray, and M. Kamionkowski, Phys. Rev. D **67**, 123507 (2003) [arXiv:astro-ph/0302536]; C. M. Hirata and U. Seljak, Phys. Rev. D **68**, 083002 (2003) [arXiv:astro-ph/0306354].

[5] M. Zaldarriaga and U. Seljak, Phys. Rev. D **58**, 023003 (1998) [arXiv:astro-ph/9803150].

[6] M. Kamionkowski, A. Kosowsky, and A. Stebbins, Phys. Rev. Lett. **78**, 2058 (1997) [arXiv:astro-ph/9609132]; U. Seljak and M. Zaldarriaga, Phys. Rev. Lett. **78**, 2054 (1997) [arXiv:astro-ph/9609169].

[7] M. Kesden, A. Cooray, and M. Kamionkowski, Phys. Rev. Lett. **89**, 011304 (2002) [arXiv:astro-ph/0202434]; L. Knox and Y.-S. Song, Phys. Rev. Lett. **89**, 011303 [arXiv:astro-ph/0202286]; U. Seljak and C. Hirata, Phys. Rev. D **69**, 043005 (2004) [arXiv:astro-ph/0310163].

[8] N. Kaiser and A. H. Jaffe, Astrophys. J. **484**, 545 (1997) [arXiv:astro-ph/9609043].

[9] A. Stebbins, preprint, arXiv:astro-ph/9609149.

[10] S. Dodelson, E. Rozo and A. Stebbins, Phys. Rev. Lett. **91**, 021301 (2003) [arXiv:astro-ph/0301177].

[11] A. Cooray, M. Kamionkowski and R. R. Caldwell, Phys. Rev. D **71**, 123527 (2005) [arXiv:astro-ph/0503002].

[12] A. Cooray and W. Hu, Astrophys. J. **574**, 19 (2002) [arXiv:astro-ph/0202411]; C. Shapiro and A. Cooray, arXiv:astro-ph/0601226. C. M. Hirata and U. Seljak, Phys. Rev. D **68**, 083002 (2003) [arXiv:astro-ph/0306354].

[13] J. Miralda-Escude, Astrophys. J. **380**, 1 (1991); R. D. Blandford, A. B. Saust, T. G. Brainerd and J. Villumsen, Mon. Not. Roy. Astron. Soc. **251**, 600 (1991); N. Kaiser, Astrophys. J. **388**, 272 (1992); For recent reviews, see, M. Bartelmann and P. Schneider, Phys. Rept. **340**, 291 (2001); P. Schneider Gravitational Lensing: Strong, Weak & Micro, Lecture Notes of the 33rd Saas-Fee Advanced Course, (Berlin: Springer-Verlag)

[14] I. I. Shapiro, Phys. Rev. Lett, **13** 789 (1964)

[15] W. Hu and A. Cooray, Phys. Rev. D **63**, 023504 (2001) [arXiv:astro-ph/0008001].

[16] J. R. Pritchard and M. Kamionkowski, Annals Phys. **318**, 2 (2005) [arXiv:astro-ph/0412581].

[17] J. N. Goldberg, et al. J. Math. Phys., 7, **863** (1967).

[18] A. Challinor and G. Chon, Phys. Rev. D **66**, 127301 (2002) [arXiv:astro-ph/0301064].

[19] T. Okamoto and W. Hu, Phys. Rev. D **67**, 083002 (2003) [arXiv:astro-ph/0301031];

[20] D. N. Spergel,et.al, ApJS, **170**, 377 (2007) [arXiv:astro-ph/0603449].

Chapter 10

Non-Gaussian Covariance of CMB B-modes of Polarization and Parameter Degradation

The B-mode polarization lensing signal is a useful probe of the neutrino mass and to a lesser extent the dark energy equation of state as the signal depends on the integrated mass power spectrum between us and the last scattering surface. This lensing B-mode signal, however, is non-Gaussian and the resulting non-Gaussian covariance to the power spectrum cannot be ignored as correlations between B-mode bins are at a level of 0.1. For temperature and E-mode polarization power spectra, the non-Gasussian covariance is not significant, where we find correlations at the 10^{-5} level even for adjacent bins. The resulting degradation on neutrino mass and dark energy equation of state is about a factor of 2 to 3 when compared to the case where statistics are simply considered to be Gaussian. We also discuss parameter uncertainties achievable in upcoming experiments and show that at a given angular resolution for polarization observations, increasing the sensitivity beyond a certain noise value does not lead to an improved measurement of the neutrino mass and dark energy equation of state with B-mode power spectrum. For Planck, the resulting constraints on the sum of the neutrino masses is $\sigma_{\Sigma m_\nu} \sim 0.2$ eV and on the dark energy equation of state parameter we find, $\sigma_w \sim 0.5$.

Originally published as C. Li, T. L. Smith and A. Cooray, *Phys. Rev. D* **75**, 083501 (2007).

10.1 Introduction

The applications of cosmic microwave background (CMB) anisotropy measurements are well known [1]; its ability to constrain most, or certain combinations of, parameters that define the currently favorable cold dark matter cosmologies with a cosmological constant is well demonstrated with anisotropy data from Wilkinson Microwave Anisotropy Probe [2]. Furthermore the advent of high sensitivity CMB polarization experiments with increasing sensitivity [3] suggests that we will soon detect the small amplitude B-mode polarization signal. While at degree scales one expects a unique B-mode polarization signal due to primordial gravitational waves [4], at arcminute angular scales the dominant signal will be related to cosmic shear conversion of E-modes to B-modes by the large-scale structure during the photon propagation from the last scattering surface to the observer today [5].

This weak lensing of cosmic microwave background (CMB) polarization by intervening mass fluctuations is now well studied in the literature [6, 7], with a significant effort spent on improving the accuracy of analytical and numerical calculations (see, recent review in Ref. [8]). As discussed in recent literature [9], the lensing B-mode signal carries important cosmological information on the neutrino mass and possibly the dark energy, such as its equation of state [9], as the lensing signal depends on the integrated mass power spectrum between us and the last scattering surface, weighted by the lensing kernel. The dark energy dependence involves the angular diameter distance projections while the effects related to a non-zero neutrino mass come from suppression of small scale power below the free-streaming scale.

Since the CMB lensing effect is inherently a non-linear process, the lensing corrections to CMB temperature and polarization are expected to be highly non-Gaussian. This non-Gaussianity at the four-point and higher levels are exploited when reconstructing the integrated mass field via a lensing analysis of CMB temperature and polarization [10]. The four-point correlations are of special interest since they also quantify the sample variance and covariance of two-point correlation or power spectrum measurements [11]. A discussion of lensing covariance of the temperature anisotropy power spectrum is available in Ref. [12]. In the case of CMB polarization, the existence of a large sample variance for B-modes of polarization is already known [13], though the effect on cosmological parameter measurements is yet to be quantified. Various estimates on parameter measurements in the literature ignore the effect of non-Gaussianities and could have overestimated the use of CMB B-modes to tightly constrain parameters such as a neutrino mass or the dark energy equation of state. To properly understand the extent to which future polarization measurements can constrain these parameters, a proper understanding of non-Gaussian covariance is needed.

Here, we discuss the temperature and polarization covariances due to gravitational lensing. Initial calculations on this topic are available in Refs. [13, 14], while detailed calculations on the CMB lensing trispectra are in Ref. [15]. Here, we focus mainly on the covariance and calculate them under the exact all-sky formulation; for flat-sky expressions of the trispectrum, we refer the reader to Ref. [10]. We extend those calculations and also discuss the impact on cosmological parameter estimates. This paper is organized as follows: In §10.2, we introduce the basic ingredients for the present calculation and present covariances of temperature and polarization spectra. We discuss our results in §10.3 and conclude with a summary in §10.4.

10.2 Calculational Method

The lensing of the CMB is a remapping of temperature and polarization anisotropies by gravitational angular deflections during the propagation. Since lensing leads to a redistribution of photons, the resulting effect appears only at second order [8]. In weak gravitational lensing, the deflection angle on the sky is given by the angular gradient of the lensing potential, $\delta(\hat{\mathbf{n}}) = \nabla\phi(\hat{\mathbf{n}})$, which is itself a projection of the gravitational potential Φ:

$$\phi(\mathbf{m}) = -2\int_0^{r_0} dr \frac{d_A(r_0 - r)}{d_A(r) d_A(r_0)} \Phi(r, \hat{\mathbf{m}}r)\,, \tag{10.1}$$

where $r(z)$ is the comoving distance along the line of sight, r_0 is the comoving distance to the surface of last scattering, and $d_A(r)$ is the angular diameter distance. Taking the multipole moments, the power spectrum of lensing potentials is now given through

$$\langle \phi^*_{lm} \phi_{lm} \rangle = \delta_{ll'} \delta_{mm'} C_l^{\phi}\,, \tag{10.2}$$

as

$$C_l^{\phi} = \frac{2}{\pi} \int k^2\, dk P(k) I_l^{\rm len}(k) I_l^{\rm len}(k)\,, \tag{10.3}$$

where

$$\begin{aligned} I_l^{\rm len}(k) &= \int_0^{r_0} dr W^{\rm len}(k,r) j_l(kr)\,, \\ W^{\rm len}(k,r) &= -3\Omega_m \left(\frac{H_0}{k}\right)^2 F(r) \frac{d_A(r_0 - r)}{d_A(r) d_A(r_0)}\,, \end{aligned} \tag{10.4}$$

where $F(r) = G(r)/a(r)$ and $G(r)$ is the growth factor, which describes the growth of large-scale density perturbations. In our calculations we will generate $C_l^{\phi\phi}$ based on a non-linear description of the matter power spectrum $P(k)$. In the next three subsections we briefly outline the power spectrum covariances under gravitational lensing for temperature and polarization E- and B-modes. In the numerical calculations described later, we take a fiducial flat-ΛCDM cosmological model with $\Omega_b = 0.0418$, $\Omega_m = 0.24$, $h = 0.73$, $\tau = 0.092$, $n_s = 0.958$, $A(k_0 = 0.05\ \mathrm{Mpc}^{-1}) = 2.3 \times 10^{-9}$, $m_\nu = 0.05$ eV, and $w = -1$. This model is consistent with recent measurements from WMAP [2].

10.2.1 Temperature Anisotropy Covariance

The trispectrum for the unlensed temperature can be written in terms of the multipole moments of the temperature θ_{lm} as [15]

$$\begin{aligned} \langle \theta_{l_1m_1}\theta_{l_2m_2}\theta_{l_3m_3}\theta_{l_4m_4}\rangle &= C^{\theta}_{l_1}C^{\theta}_{l_4}(-1)^{m_1+m_4}\delta^{m_1-m_3}_{l_1l_3}\delta^{m_2-m_4}_{l_2l_4} + C^{\theta}_{l_1}C^{\theta}_{l_3}(-1)^{m_1+m_3}\delta^{m_1-m_2}_{l_1l_2}\delta^{m_3-m_4}_{l_3l_4} \\ &+ C^{\theta}_{l_1}C^{\theta}_{l_2}(-1)^{m_1+m_2}\delta^{m_1-m_4}_{l_1l_4}\delta^{m_2-m_3}_{l_2l_3}\,. \end{aligned} \tag{10.5}$$

It is straightforward to derive the following expression for the multipole moment of lensed θ field as a perturbative equation related to the deflection angle [7]:

$$\tilde{\theta}_{lm} = \theta_{lm} + \sum_{l_1m_1l_2m_2} \phi_{l_1m_1}\theta_{l_2m_2}I^{mm_1m_2}_{ll_1l_2} + \frac{1}{2}\sum_{l_1m_1l_2m_2l_3m_3} \phi_{l_1m_1}\theta_{l_2m_2}\phi^*_{l_3m_3}J^{mm_1m_2m_3}_{ll_1l_2l_3}\,, \tag{10.6}$$

where the mode-coupling integrals between the temperature field and the deflection field, $I^{mm_1m_2}_{ll_1l_2}$ and $J^{mm_1m_2m_3}_{ll_1l_2l_3}$, are defined in [15, 16].

As for the covariance of the temperature anisotropy powerspectrum, we write

$$\mathrm{Cov}_{\theta\theta} \equiv \frac{1}{2l_1+1}\frac{1}{2l_2+1}\sum_{m_1m_2}\langle \tilde{\theta}_{l_1m_1}\tilde{\theta}^*_{l_1m_1}\tilde{\theta}_{l_2m_2}\tilde{\theta}^*_{l_2m_2}\rangle - \tilde{C}^{\theta}_{l_1}\tilde{C}^{\theta}_{l_2} = \mathcal{O} + \mathcal{P} + (\mathcal{Q}+\mathcal{R})\delta_{l_1l_2}, \tag{10.7}$$

where the individual terms are

$$\begin{aligned} \mathcal{O} &= \frac{2}{(2l_1+1)(2l_2+1)}\sum_L C^{\phi}_L\left[(F_{l_1Ll_2}C^{\theta}_{l_2})^2 + (F_{l_2Ll_1}C^{\theta}_{l_1})^2\right], \\ \mathcal{P} &= \frac{4}{(2l_1+1)(2l_2+1)}\sum_L C^{\phi}_L C^{\theta}_{l_1}C^{\theta}_{l_2}F_{l_1Ll_2}F_{l_2Ll_1}, \\ \mathcal{Q} &= \frac{4}{(2l_1+1)^2}\sum_{L,l'} C^{\phi}_L C^{\theta}_{l'}C^{\theta}_{l_1}(F_{l_1Ll'})^2, \\ \mathcal{R} &= -\frac{(l_1(l_1+1))}{2\pi(2l_1+1)}\sum_L C^{\phi}_L(C^{\theta}_{l_1})^2L(L+1)(2L+1)\,, \end{aligned} \tag{10.8}$$

and the last two terms, which are related to the Gaussian variance, can be written in terms of the lensed temperature anisotropy power spectrum as

$$\mathcal{Q}+\mathcal{R} = \frac{2}{2l_1+1}(\tilde{C}^{\theta}_{l_1})^2\,, \tag{10.9}$$

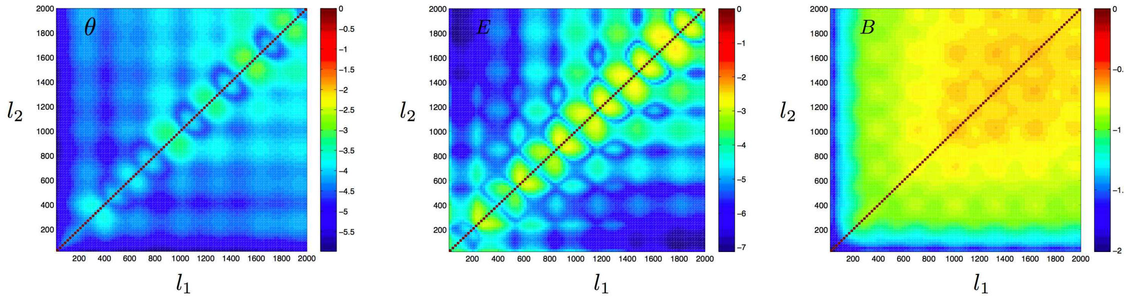

Figure 10.1: The correlation matrix [Eq. (10.24)] for temerature (left), E-mode (middle), and B-mode (right) power spectra between different l values. The color axis is on a log scale and each scale is different for each panel. As is clear from this figure, the off-diagonal correlation is weak for both θ and E-mode power spectra, but is more than 0.1 for most entries for the B-mode power spectrum. This clearly shows that the non-Gaussianities are most pronounced for the B-mode signal and will impact the information extraction from the angular power spectrum of B-modes than under the Gaussian variance alone. The B-mode covariance shown in the left panel agrees with Figure 5 of Ref. [14].

where

$$\begin{aligned}
\tilde{C}_l^\theta &= [1-(l^2+l)R]C_l^\theta + \sum_{l_1 l_2} C_{l_1}^\phi \frac{(F_{l l_1 l_2})^2}{2l+1} C_{l_2}^\theta, \qquad (10.10)\\
R &= \frac{1}{8\pi}\sum_{l_1} l_1(l_1+1)(2l_1+1)C_{l_1}^\phi,\\
F_{l l_1 l_2} &= \frac{1}{2}[l_1(l_1+1)+l_2(l_2+1)-l(l+1)]\sqrt{\frac{(2l+1)(2l_1+1)(2l_2+1)}{4\pi}}\begin{pmatrix} l & l_1 & l_2 \\ 0 & 0 & 0 \end{pmatrix}.
\end{aligned}$$

We note that Eqs. (10.10) are readily derivable when considering the lensing effect on the temperature anistropy spectrum as in Ref. [7].

10.2.2 E-Mode Polarization Covariance

Similar to the case with temperature, the trispectrum for an unlensed E-field can be written in terms of the multipole moments of the E-mode E_{lm}:

$$\begin{aligned}
\langle E_{l_1m_1}E_{l_2m_2}E_{l_3m_3}E_{l_4m_4}\rangle &= C_{l_1}^E C_{l_4}^E (-1)^{m_1+m_4}\delta_{l_1l_3}^{m_1-m_3}\delta_{l_2l_4}^{m_2-m_4}\\
&+ C_{l_1}^E C_{l_3}^E (-1)^{m_1+m_3}\delta_{l_1l_2}^{m_1-m_2}\delta_{l_3l_4}^{m_3-m_4}\\
&+ C_{l_1}^E C_{l_2}^E (-1)^{m_1+m_2}\delta_{l_1l_4}^{m_1-m_4}\delta_{l_2l_3}^{m_2-m_3}\,. \qquad (10.11)
\end{aligned}$$

To complete the calculation, besides the trispectrum of the unlensed E-field in Eq. (10.11), we also require the expression for the trispectrum of the lensing potentials. Under the Gaussian hypothesis for the primordial E-modes and ignoring non-Gaussian corrections to the ϕ field, the lensing trispectra is given by

$$\begin{aligned}
\langle \phi_{l_1m_1}\phi_{l_2m_2}\phi_{l_3m_3}\phi_{l_4m_4}\rangle &= C^{\phi}_{l_1}C^{\phi}_{l_4}(-1)^{m_1+m_4}\delta^{m_1-m_3}_{l_1l_3}\delta^{m_2-m_4}_{l_2l_4} \\
&+ C^{\phi}_{l_1}C^{\phi}_{l_3}(-1)^{m_1+m_3}\delta^{m_1-m_2}_{l_1l_2}\delta^{m_3-m_4}_{l_3l_4} \\
&+ C^{\phi}_{l_1}C^{\phi}_{l_2}(-1)^{m_1+m_2}\delta^{m_1-m_4}_{l_1l_4}\delta^{m_2-m_3}_{l_2l_3}. \qquad (10.12)
\end{aligned}$$

For simplicity, we assume that there is no primordial B field such as due to a gravitational wave background and find the following expression for the lensed E-field:

$$\begin{aligned}
\tilde{E}_{lm} = E_{lm} + \frac{1}{2}\sum_{l_1m_1l_2m_2}\phi_{l_1m_1}E_{l_2m_2}\,{}_{+2}I^{mm_1m_2}_{ll_1l_2}(1+(-1)^{l+l_1+l_2}) \\
+\frac{1}{4}\sum_{l_1m_1l_2m_2l_3m_3}\phi_{l_1m_1}E_{l_2m_2}\phi^*_{l_3m_3}\,{}_{+2}J^{mm_1m_2m_3}_{ll_1l_2l_3}(1+(-1)^{l+l_1+l_2+l_3})\,, \qquad (10.13)
\end{aligned}$$

where the expressions for the mode coupling integrals ${}_{+2}I^{mm_1m_2}_{ll_1l_2}$ and ${}_{+2}J^{mm_1m_2m_3}_{ll_1l_2l_3}$ are described in Refs. [15, 16].

As for the covariance of E-mode power spectrum, we write

$$\mathrm{Cov}_{\mathrm{EE}} \equiv \frac{1}{2l_1+1}\frac{1}{2l_2+1}\sum_{m_1m_2}\langle \tilde{E}_{l_1m_1}\tilde{E}^*_{l_1m_1}\tilde{E}_{l_2m_2}\tilde{E}^*_{l_2m_2}\rangle - \tilde{C}^E_{l_1}\tilde{C}^E_{l_2} = \mathcal{H}+\mathcal{I}+(\mathcal{J}+\mathcal{K})\delta_{l_1l_2}, \qquad (10.14)$$

where

$$\begin{aligned}
\mathcal{H} &= \frac{1}{(2l_1+1)(2l_2+1)}\sum_L C^{\phi}_L\left[({}_2F_{l_1Ll_2}C^E_{l_2})^2+({}_2F_{l_2Ll_1}C^E_{l_1})^2\right](1+(-1)^{l_1+l_2+L}), \\
\mathcal{I} &= \frac{2}{(2l_1+1)(2l_2+1)}\sum_L C^{\phi}_L C^E_{l_1}C^E_{l_2}(1+(-1)^{l_1+L+l_2})\,{}_2F_{l_1Ll_2}\,{}_2F_{l_2Ll_1}, \\
\mathcal{J} &= \frac{2}{(2l_1+1)^2}\sum_{L,l'} C^{\phi}_L C^E_{l'}C^E_{l_1}(1+(-1)^{l_1+L+l'})({}_2F_{l_1Ll'})^2, \\
\mathcal{K} &= -\frac{(l_1(l_1+1)-4)}{2\pi(2l_1+1)}\sum_L C^{\phi}_L(C^E_{l_1})^2L(L+1)(2L+1)\,. \qquad (10.15)
\end{aligned}$$

The last two terms can be written in terms of the lensed power spectrum of E-mode anisotropies as

$$\mathcal{J}+\mathcal{K} = \frac{2}{2l_1+1}(\tilde{C}^E_{l_1})^2\,, \qquad (10.16)$$

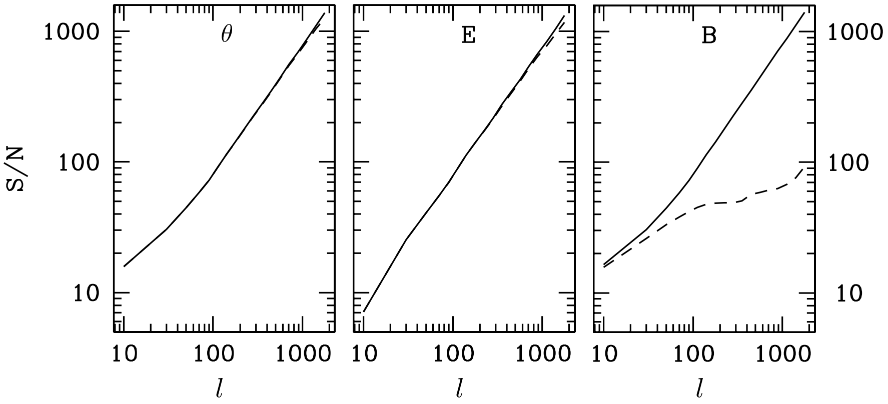

Figure 10.2: Here we show the cumulative signal-to-noise ratio for a detection of the power spectrum (Eq. (10.30)) for temperature (left), E-mode (middle), and B-mode (right) polarization power spectra. The solid line is the case with a Gaussian covariance whereas the dashed line is with a non-Gaussian covariance. We can see that for the case of the temperature and E-mode polarization there is little difference between the Gaussian and non-Gaussian covariance, but for the B-mode polarization there is a difference of a factor of ~ 10 at large l values.

where

$$\begin{aligned}
\tilde{C}_l^E &= [1-(l^2+l-4)R]C_l^E + \frac{1}{2}\sum_{l_1 l_2} C_{l_1}^{\phi}\frac{({}_2F_{ll_1l_2})^2}{2l+1}C_{l_2}^E(1+(-1)^{l+l_1+l_2}), \qquad (10.17)\\
R &= \frac{1}{8\pi}\sum_{l_1} l_1(l_1+1)(2l_1+1)C_{l_1}^{\phi},\\
{}_2F_{ll_1l_2} &= \frac{1}{2}[l_1(l_1+1)+l_2(l_2+1)-l(l+1)]\sqrt{\frac{(2l+1)(2l_1+1)(2l_2+1)}{4\pi}}\begin{pmatrix} l & l_1 & l_2\\ 2 & 0 & -2\end{pmatrix}.
\end{aligned}$$

Note that $\tilde{C}_l^E$ is the power spectrum of the lensed E-modes.

10.2.3 B-Mode Polarization Covariance

The calculation related to B-mode power spectrum polarization is similar to the case of the E-modes except that we assume that the B-mode polarization is generated solely the lensing of the E-mode polarization. Based on previous work (Ref. [7]), we write the multipole moments of the lensed B-modes as

$$\begin{aligned}
i\tilde{B}_{lm} &= \frac{1}{2}\sum_{l_1m_1l_2m_2}\phi_{l_1m_1}E_{l_2m_2}\,{}_{+2}I_{ll_1l_2}^{mm_1m_2}(1-(-1)^{l+l_1+l_2})\\
&+ \frac{1}{4}\sum_{l_1m_1l_2m_2l_3m_3}\phi_{l_1m_1}E_{l_2m_2}\phi^*_{l_3m_3}\,{}_{+2}J_{ll_1l_2l_3}^{mm_1m_2m_3}(1-(-1)^{l+l_1+l_2+l_3}). \qquad (10.18)
\end{aligned}$$

Here, we will only calculate the B-mode trispectrum with terms involving C_l^{ϕ} since we will make the assumption that corrections to B-modes from the bispectrum and higher-order non-Gaussianities of

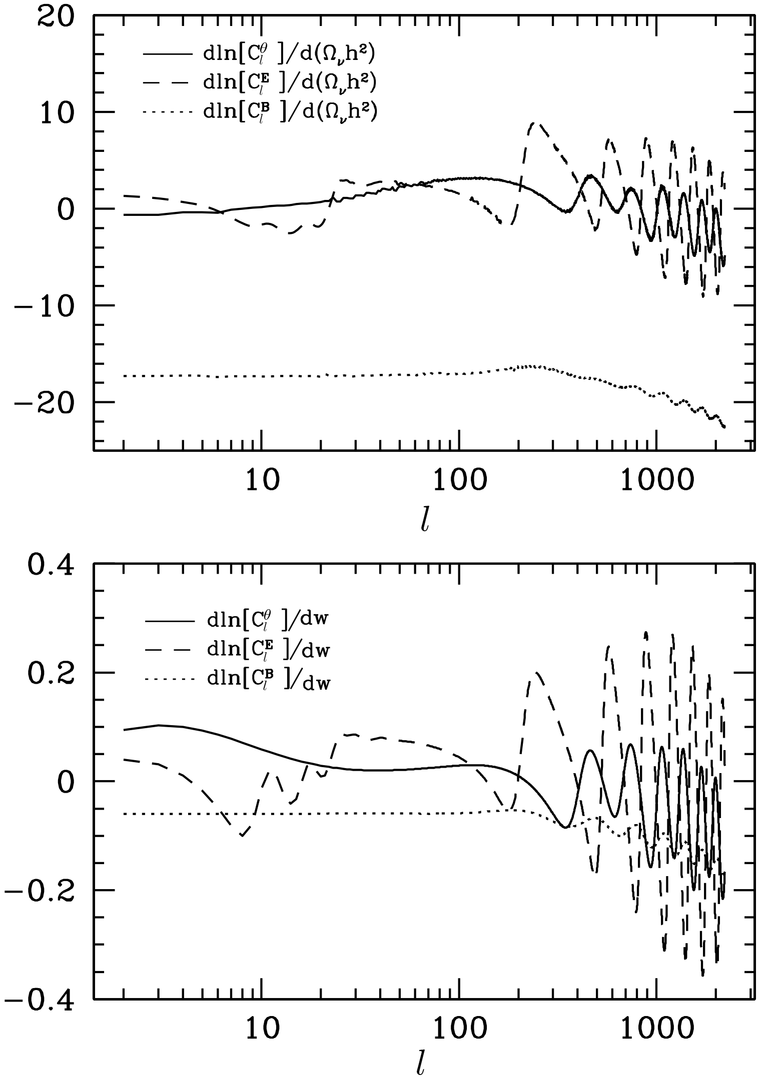

Figure 10.3: The derivatives of the temperature (θ), E-mode, and B-mode power spectra with respect to the sum of the neutrino masses ($\propto \Omega_\nu h^2$, top panel) and the dark energy equation of state, w (bottom panel). It is clear that in the case of the sum of the neutrino masses the addition of the B-mode polarization greatly increases sensitivity. In both cases we find that large l information also increases sensitivity. We note that the derivative of the temperature power spectrum with respect to neutrino mass agrees with that shown in Fig. 3 of Ref. [18].

the lensing ϕ field are subdominant. Thus, using the first term of the expansion, we write

$$\begin{aligned}
&\langle \tilde{B}_{l_1m_1}\tilde{B}_{l_2m_2}\tilde{B}_{l_3m_3}\tilde{B}_{l_4m_4}\rangle = \frac{1}{16}\sum_{L_1M_1l'_1m'_1}\sum_{L_2M_2l'_2m'_2}\sum_{L_3M_3l'_3m'_3}\sum_{L_4M_4l'_4m'_4}\\
&\langle \phi_{L_1M_1}\phi_{L_2M_2}\phi_{L_3M_3}\phi_{L_4M_4}\rangle\langle E_{l'_1m'_1}E_{l'_2m'_2}E_{l'_3m'_3}E_{l'_4m'_4}\rangle\\
&\times {}_{+2}I_{l_1m_1L_1M_1l'_1m'_1}\,{}_{+2}I_{l_2m_2L_2M_2l'_2m'_2}\,{}_{+2}I_{l_3m_3L_3M_3l'_3m'_3}\,{}_{+2}I_{l_4m_4L_4M_4l'_4m'_4}\\
&\times(1-(-1)^{l_1+L_1+l'_1})(1-(-1)^{l_2+L_2+l'_2})(1-(-1)^{l_3+L_3+l'_3})(1-(-1)^{l_4+L_4+l'_4}),
\end{aligned}$$

where

$$_{+2}I_{lml_1m_1l_2m_2} \quad = \quad {}_2F_{ll_1l_2}(-1)^m\begin{pmatrix} l & l_1 & l_2\\ -m & m_1 & m_2\end{pmatrix}. \tag{10.19}$$

The covariance of the B-mode angular power spectrum can be now defined as

$$\mathrm{Cov_{BB}} \equiv \frac{1}{2l_1+1}\frac{1}{2l_2+1}\sum_{m_1m_2}\langle \tilde{B}_{l_1m_1}\tilde{B}^*_{l_1m_1}\tilde{B}_{l_2m_2}\tilde{B}^*_{l_2m_2}\rangle - \tilde{C}^B_{l_1}\tilde{C}^B_{l_2}\,. \tag{10.20}$$

After some straightforward but tedious algebra, we obtain

$$\mathrm{Cov_{BB}} = \mathcal{A}+\mathcal{B}+\mathcal{C}+\delta_{l_1l_2}\mathcal{D}, \tag{10.21}$$

where the terms are given by

$$\begin{aligned}
&\mathcal{A} = \frac{2}{4(2l_1+1)(2l_2+1)}\sum_{L=1}^{N_\phi}\\
&\left[\frac{(C^\phi_L)^2}{2L+1}\left(\sum_{l'=|l_1-L|}^{l_1+L}C^E_{l'}(1-(-1)^{l_1+L+l'})({}_2F_{l_1Ll'})^2\right)\left(\sum_{l'=|l_2-L|}^{l_2+L}C^E_{l'}(1-(-1)^{l_2+L+l'})({}_2F_{l_2Ll'})^2\right)\right],
\end{aligned}$$

$$\begin{aligned}
&\mathcal{B} = \frac{2}{4(2l_1+1)(2l_2+1)}\sum_{l'=1}^{N_E}\\
&\left[\frac{(C^E_{l'})^2}{2l'+1}\left(\sum_{L=|l_1-l'|}^{l_1+l'}C^\phi_L(1-(-1)^{l_1+L+l'})({}_2F_{l_1Ll'})^2\right)\left(\sum_{L=|l_2-l'|}^{l_2+l'}C^\phi_L(1-(-1)^{l_2+L+l'})({}_2F_{l_2Ll'})^2\right)\right],
\end{aligned}$$

$$\begin{aligned}
\mathcal{C} &= \frac{2}{16(2l_1+1)(2l_2+1)} \sum_{L_1=1}^{N_\phi} \sum_{l'_1=|l_1-L_1|}^{l_1+L_1} \sum_{l'_2=|l_2-L_1|}^{l_2+L_1} \sum_{L_2=|l_1-l'_2|}^{l_1+l'_2} \\
&\quad C^{\phi}_{L_1} C^{\phi}_{L_2} C^{E}_{l'_1} C^{E}_{l'_2} \left[{}_2F_{l_1 L_1 l'_1} {}_2F_{l_1 L_2 l'_2} {}_2F_{l_2 L_1 l'_2} {}_2F_{l_2 L_2 l'_1} \right] \begin{Bmatrix} L_1 & l'_1 & l_1 \\ L_2 & l'_2 & l_2 \end{Bmatrix} (-1)^{l_1+L_1+l'_1+l_2+L_2+l'_2} \\
&\quad (1-(-1)^{l_1+L_1+l'_1})(1-(-1)^{l_1+L_2+l'_2})(1-(-1)^{l_2+L_1+l'_2})(1-(-1)^{l_2+L_2+l'_1}), \\
\mathcal{D} &= \frac{2}{4(2l_1+1)^3} \left(\sum_{Ll'} C^{\phi}_{L} C^{E}_{l'} [1-(-1)^{l_1+L+l'}] ({}_2F_{l_1 L l'})^2 \right)^2 = \frac{2}{2l_1+1} (\tilde{C}^B_{l_1})^2, \qquad (10.22)
\end{aligned}$$

where

$$\tilde{C}^B_l = \frac{1}{2} \sum_{l_1 l_2} C^{\phi}_{l_1} \frac{({}_2F_{l l_1 l_2})^2}{2l+1} C^{E}_{l_2} (1-(-1)^{l+l_1+l_2}). \qquad (10.23)$$

Unlike the calculation for the covariances of the lensed temperature and polarization E-mode, the numerical calculation related to covariance of the B-modes is complicated due to the term $\mathcal{C}$, which involves a Wigner-6j symbol. These symbols can be generated using the recursion relation outlines in appendix of Ref. [15], though we found that such recursions are subject to numerical instabilities when one of the l values is largely different from the others and the l values are large. In these cases, we found that values accurate to better than a ten percent of the exact result can be obtained through semiclassical formulae [17]. In any case, we found that $\mathcal{C}$ is no more than 1% of $\mathcal{A}$, $\mathcal{B}$, and these terms are in turn no more than 10% of $\mathcal{D}$. The same situation happens to those expressions in flat-sky approach [20].

10.3 Results and Discussion

We begin our discussion on the parameter uncertainties in the presence of non-Gaussian covariance by first establishing that one cannot ignore them for the B-mode power sptectrum. In Figure 10.1 we show the correlation matrix, which is defined as

$$r_{ij} \equiv \frac{\mathrm{Cov}_{XY}(i,j)}{\sqrt{\mathrm{Cov}_{XY}(i,i)\mathrm{Cov}_{XY}(j,j)}}. \qquad (10.24)$$

This correlation normalizes the diagonal to unity and displays the off-diagonal terms as a value between 0 and 1. This facilitates an easy comparison on the importance of non-Gaussianities between temperature, E-, and B-modes of polarization. As shown in Figure 10.1, the off-diagonal entries of temperature and E-modes are roughly at the level of 10^{-5} suggesting that non-Gaussian covariance is not a concern for these observations out to multipoles of 2000 [12], while for B-modes the correlations are at the level above 0.1 and are significant.

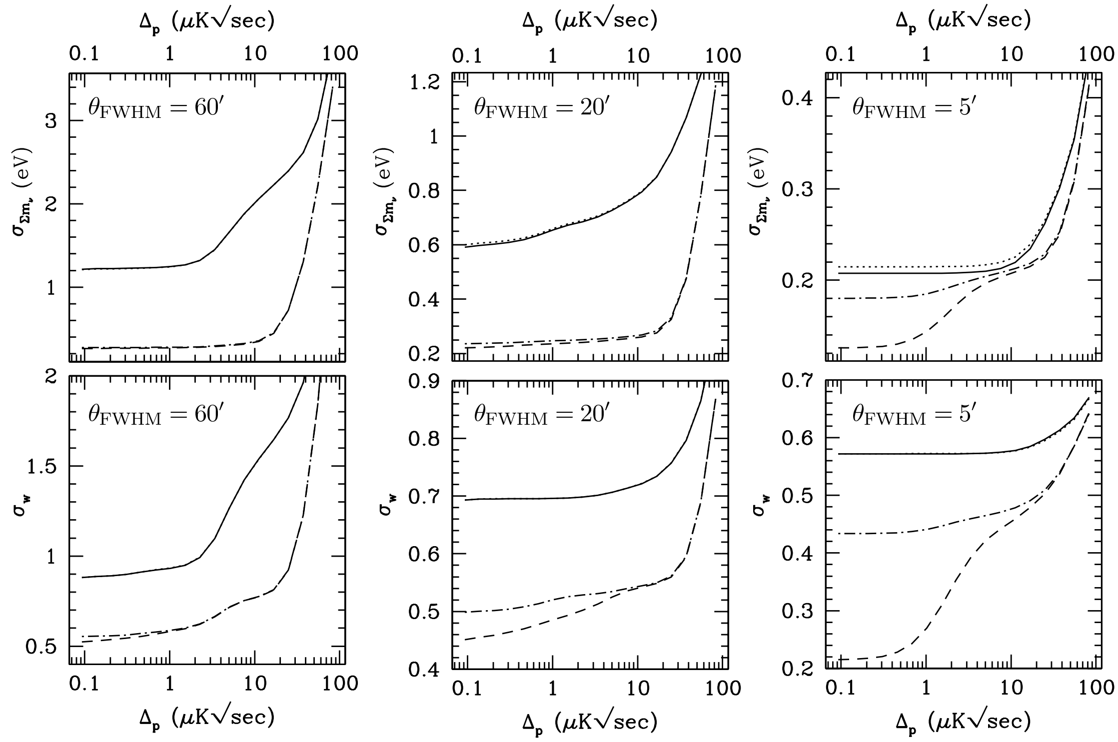

Figure 10.4: The expected error on the sum of the neutrino masses (top three panels) and the dark energy equation of state, w (bottom three panels) as a function of experimental noise for three different values of the beam width, $\theta_{\rm FWHM}$. The solid line considers Gaussian covariance with just temperature information, the dotted line considers non-Gaussian covariance with just temperature information, the dashed line considers Gaussian covariance with both temperature and polarization (E- and B-mode), and the dot-dashed line considers non-Gaussian covariance with both temperature and polarization. It is clear that as the beam width is decreased the estimated error on the sum of the neutrino masses and w is increasingly overly optimistic when just the Gaussian covariance is used in the Fisher matrix calculation. We choose 5 bins uniformly spacing between $l = 5$ and $l = 100$, while we choose 13 bins logarithmic uniformly spacing between $l = 100$ and $l = 2000$. This choice of bins are sparser compared to [20]. From the expressions of covariance matrix [Eqs.(10.7, 10.14, 10.22)], we know the Gaussian parts are diagonal and therefore the larger the bin is, the more important the non-Gaussian effect is. So the non-Gaussian effects in our bandpower statistics are more obvious than those in [20].

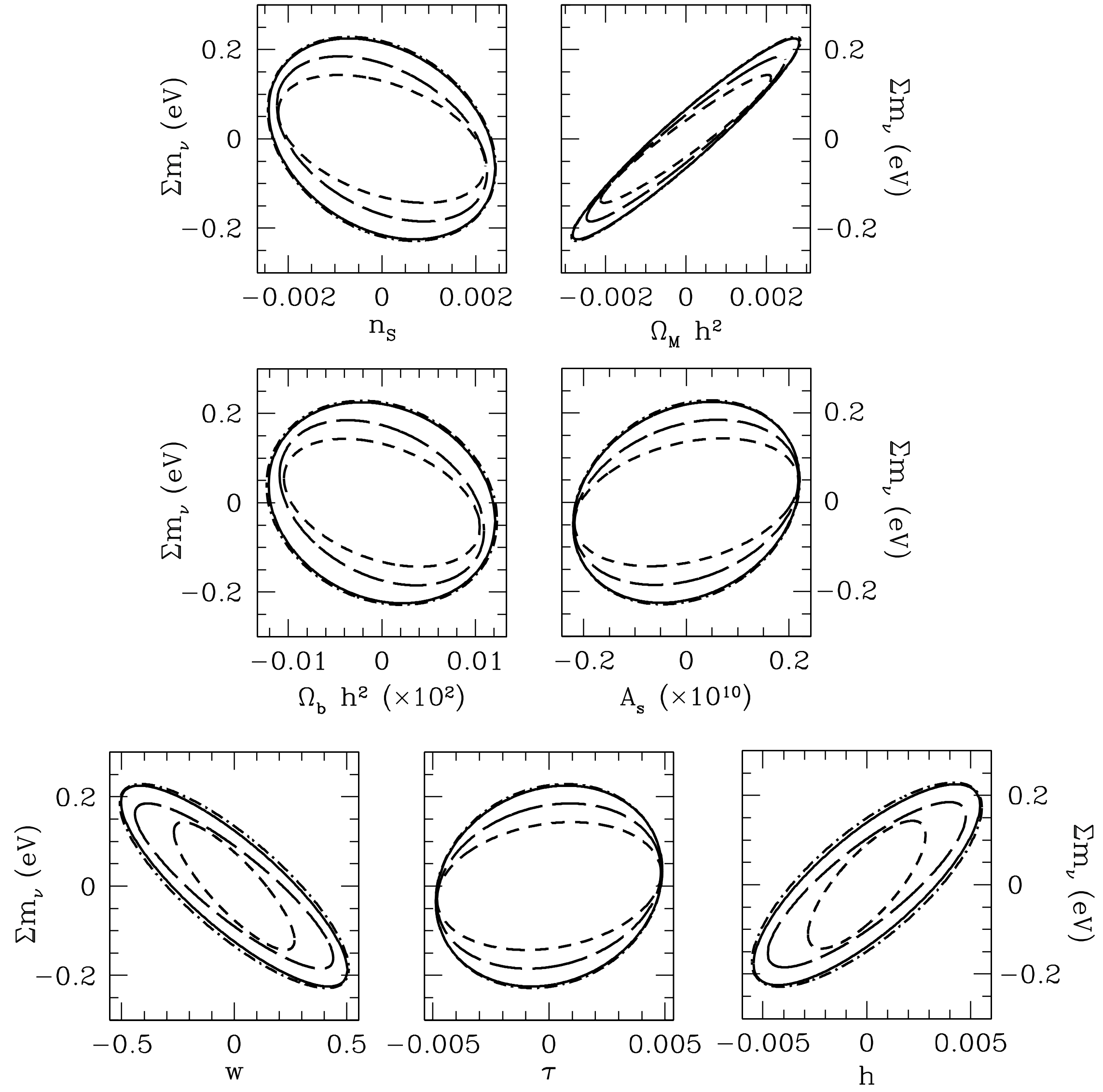

Figure 10.5: The error ellipses from our Fisher matrix calculation. We have varied eight parameters, and show the error ellipses for each parameter with Σm_ν. The dot-dashed ellipse is the expected error from Planck with just a Gaussian covariance, the solid ellipse is same but with a non-Gaussian covariance. The short-dashed ellipse is for an experiment with the same beam width as Planck ($\theta \sim 5'$) but with decreased noise ($1\ \mu\mathrm{K}\sqrt{\mathrm{sec}}$ as opposed to $25\ \mu\mathrm{K}\sqrt{\mathrm{sec}}$) with a Gaussian covariance and the long-dashed ellipse is the same but with a non-Gaussian covariance.

Below when we calculate the signal-to-noise ratio and Fisher matrices, we use the band powers as observables with logrithmic bins in the multipole space. Our band power estimator for two quantities of X- and Y-fields involving temperature and polarization maps is

$$\hat{\Delta}^2_{XY,i} = \frac{1}{\alpha_i}\sum_{l=l_{i1}}^{l_{i2}}\sum_{m=-l}^{l}\frac{l}{4\pi}X_{lm}Y^*_{lm}, \tag{10.25}$$

where $\alpha_i = l_{i2} - l_{i1}$ is an overall normalization factor given by the bin width. The angular power spectra are

$$\Delta^2_i = \langle\hat{\Delta}^2_i\rangle = \frac{1}{4\pi\alpha_i}\sum_l (2l+1)lC_l^{B,E,\theta}\,, \tag{10.26}$$

while the full covariance matrix is

$$\langle(\hat{\Delta}^2_i - \Delta^2_i)(\hat{\Delta}^2_j - \Delta^2_j)\rangle = S^G_{ii}\delta_{ij} + S^N_{ij}\,, \tag{10.27}$$

with the Gaussian part

$$\begin{aligned} S^G_{ii} &= \frac{2}{(4\pi)^2\alpha_i^2}\sum_{l_1=l_{i1}}^{l_1=l_{i2}}(2l_1+1)l_1^2(C_{l_1}^{B,E,\theta} + N_{l_1})^2, \\ N_l &= \left(\frac{\Delta_p}{T_{\rm CMB}}\right)^2 e^{l(l+1)\theta^2_{\rm FWHM}/8\ln 2}, \end{aligned} \tag{10.28}$$

and the non-Gaussian part is

$$S^N_{ij} = \frac{1}{(4\pi)^2\alpha_i\alpha_j}\sum_{l_1 l_2}(2l_1+1)(2l_2+1)l_1 l_2({\rm Cov}^N_{B,E,\theta})\,. \tag{10.29}$$

To further quantify the importance of non-Gaussianities for B-modes, in Figure 10.2, we plot the cumulative signal-to-noise ratio for the detection of the power spectra as a function of the band powers. These are calculated as

$$({\rm SN})_{XY} = \sum_{\Delta_i\Delta_j} C^{XY}_{\Delta_i}{\rm Cov}^{-1}_{XY}(\Delta_i,\Delta_j)C^{XY}_{\Delta_j}\,, \tag{10.30}$$

by ignoring the instrumental noise contribution to the covariance. As shown, there is no difference in the signal-to-noise ratio for the temperature and E-mode power spectra measurement due to non-Gaussian covariances, while there is a sharp reduction in the cumulative signal-to-noise ratio for a detection of the B-modes. This reduction is significant and can be explained through the effective reduction in the number of independent modes at each multipole from which clustering measurements can be made. In the case of Gaussian statistics, at each multipole l, there are $2l+1$

modes to make the power spectrum measurements. In the case of non-Gaussian statistics with a covariance, this number is reduced further by the correlations between different modes. If N is the number of independent modes available under Gaussian statistics, a simple calculation shows that the effective number of modes are reduced by $[1+(N-1)r^2]$ when the modes are correlated by an equally distributed correlation coefficient r among all modes. With $N = 2l+1$ and substituting a typical correlation coefficient r of 0.15, we find that the cumulative signal-to-noise ratio should be reduced by a factor of 7 to 8 when compared to the case where only Gaussian statistics are assumed. This is consistent with the signal-to-noise ratio estimates shown in Figure 10.2 based on an exact calculation using the full covariance matrix that suggests a slightly larger reduction due to the fact that some of the modes are more strongly correlated than the assumed average value.

To calculate the overall impact on cosmological parameter measurements using temperature and polarization spectra, we make use of the Fisher information matrix given for tow parameters μ and ν as

$$F_{\mu\nu} = \sum_{X=B,E,\theta} \sum_{ij} \frac{\partial(\Delta_i^X)^2}{\partial p_\mu} (\mathrm{Cov}_{XX}^{-1}) \frac{\partial(\Delta_j^X)^2}{\partial p_\nu}, \tag{10.31}$$

where the summation is over all bins. While this is the full Fisher information matrix, we will divide our results to with and without non-Gaussian covariance as well as to information on parameters present within temperature, and E- and B-modes of polarization.

Since B-modes have been generally described as a probe of neutrino mass and the dark energy equation of state, in Figure 10.3, we show $\partial C_l/\partial m_\nu$ and $\partial C_l/\partial w$ to show the extent to which information on these two quantities are present in the spectra. It is clear that B-modes are a strong probe of neutrino mass given that the sensitivity of temperature and E-modes are smaller compared to the fractional difference in the B-modes. Furthermore, B-modes also have some senitivity to the dark energy equation of state, but fractionally, this sensitivity is smaller compared to the information related to the neutrino mass.

In Figure 10.4, we summarize parameter constraints on these two parameters as a function of the instrumental noise for different values of resolution with and without non-Gaussian covariance. While for low resolution experiments the difference between Gaussian and non-Gaussian extraction is marginal, non-Gaussianities become more important for high resolution experiments where one probes B-modes down to large multipoles. In this case, the parameters extraction is degraded by up to a factor of more than 2.5 for both the neutrino mass and the dark energy equation of state. We have not attempted to calculate the parameter errors for experiments with resolution better than 5 arcminutes. This is due to the fact that such experiments will probe multipoles higher than 2000 and we are concerned that we do not have a full description of the non-Gaussian covariance at such small scales due to uncertainties in the description of the matter power spectrum at non-linear scales.

As described in Ref. [8], the CMB lensing calculation must account for non-linearities and their importance only become significant for small angular scale anisotropy experiments. Furthermore, we also do not think any of the upcoming B-mode polarization experiments with high sensitivity, which will be either spacebased or balloonborne, will have large apertures to probe multipoles above 2000.

The value of 2000 where we stop our calculations is also consistent with Planck. Since Planck HFI experiment will have a total focal plane polarization noise of about 25 μK $\sqrt{\text{sec}}$, based on Figure 10.4, we find that it will constrain the neutrino mass to be below 0.22 eV and the dark energy equation of state will be determined to an accuracy of 0.5. Note that the combination of Planck noise and resolution is such that one does not find a large difference between Gaussian and non-Gaussian statistics, but on the other hand, experiments that improve the polarization noise well beyond Planck must account for non-Gaussian noise properly. In future, there are plans for a Inflation Probe or a CMBpol mission that will make high sensitive observations in search for a gravitational wave background. If such an experiment reach an effective noise level of 1 μK $\sqrt{\text{sec}}$ and has the same resolution as Planck, the combined polarization observations can constrain the neutrino mass to be about 0.18, while the dark energy equation of state will be known to an accuracy of 0.44. This is well above the suggested constraint from Gaussian noise level. This suggests that while highly sensitive B-mode measurements are desirable for studies involving the gravitational wave background, they are unlikely to be helpful for increasingly better constraints on the cosmological parameters.

The non-Gaussianities in the B-modes, while providing information on gravitational lensing, limit accurate parameter estimates from the power spectrum alone. This is contrary to some of the suggestions in the literarture that have indicated high precision of measurements on parameters such as the neutrino mass and the dark energy equation of state with CMB B-mode power spectrum by ignoring issues related to non-Gaussian correlations. Furthermore, while atmospheric oscillations suggest a mass-squared difference of $\Delta m_\nu^2 \sim 10^{-3}$ for two of the neutrino species, it is unlikely that one will be able to distinguish between mass hierarchies with CMB polarization observations alone if one of the two masses related to the atmospheric oscillation result is close to zero ([19]). This is discouraging, but understanding the information present in CMB polarization beyond powerspectra, such as direct measurements of non-Gaussianities themselves, could potentially allow an improvement.

From Figure 10.4 we see that as we decrease Δ_p the measurement errors on the parameters asymptote to a constant value. We can understand this in the following way. As we see from Eq. (10.28), the noise blows up exponentially at large l and therefore sets an effective cutoff l_0. Only the band powers which are smaller than l_0 contribute to parameter estimates. Therefore, if we decrease Δ_p, we increase the number of band powers we can observe and hence obtain better sensitivity with negligible instrumental noise for $l \lesssim l_0$. Therefore, the curves in Figure 10.4 become flatter as we decrease Δ_p. The same situation applies to Figure 10.5. Figure 10.4 also shows that as we decrease the beam width, $\theta_{\rm FWHM}$, we see the Gaussian covariance becomes more significant. This is a result of the fact that the Gaussian covariance grows in significance with increasing l.

In Figure 10.5, to highlight the impact on cosmological parameters beyond the neutrino mass and dark energy equation of state, we also show constraints from the Fisher matrix calculation. We show error ellipses calculated with and without the non-Gaussian lensing covariance for two different experiments: Planck, with $\theta_{\rm FWHM} = 5'$ and $\Delta_p = 25\ \mu{\rm K}\sqrt{\rm sec}$ and "super-Planck" with $\theta_{\rm FWHM} = 5'$ and $\Delta_p = 1\ \mu{\rm K}\sqrt{\rm sec}$. This comparison shows that while parameters such as m_ν and w are affected, parameters such as τ, $\Omega_m h^2$ are not affected by non-Gaussian information. This is due to the fact that the cosmological information on these parameters come from temperature and E-modes rather than B-modes. This highlights the fact that the issues discussed here are primarily a concern for the B-mode measurements and extraction of parameters, especially the parameters that have been recognized to be mostly constrained by the B-mode measurements, and not for temperature and E-modes.

10.4 Summary

The B-mode polarization lensing signal is a useful probe of certain cosmological parameters such as the neutrino mass and the dark energy equation of state as the signal depends on the integrated mass power spectrum between us and the last scattering surface. This lensing B-mode signal, however, is non-Gaussian and the resulting non-Gaussian covariance to the power spectrum cannot be ignored when compared to the case of temperature and polarization E-mode anisotropy covariances. The resulting degradation on neutrino mass and dark energy equation of state is about a factor of 2 when compared to the case where statistics are simply considered to be Gaussian. We discuss parameter uncertainties achievable in upcoming experiments.

10.5 Bibliography

[1] L. Knox, Phys. Rev. D, **52** 4307 (1995); G. Jungman, M. Kamionkowski, A. Kosowsky and D.N. Spergel,Phys. Rev. D, **54** 1332 (1995); J.R. Bond, G. Efstathiou and M. Tegmark, Mon. Not. R. Astron. Soc., **291** L33 (1997); M. Zaldarriaga, D.N. Spergel and U. Seljak, Astrophys. J., **488** 1 (1997); D.J. Eisenstein, W. Hu and M. Tegmark, Astrophys. J., **518** 2 (1999)

[2] D. N. Spergel *et al.*, ApJS, **170**, 377 (2007) [arXiv:astro-ph/0603449].

[3] B. G. Keating, A. G. Polnarev, N. J. Miller and D. Baskaran, Int.J.Mod.Phys. **A21** (2006) 2459-2479 [arXiv:astro-ph/0607208].

[4] M. Kamionkowski, A. Kosowsky, and A. Stebbins, Phys. Rev. Lett. **78**, 2058 (1997) [arXiv:astro-ph/9609132]; U. Seljak and M. Zaldarriaga, Phys. Rev. Lett. **78**, 2054 (1997) [arXiv:astro-ph/9609169].

[5] M. Zaldarriaga and U. Seljak, Phys. Rev. D **58**, 023003 (1998) [arXiv:astro-ph/9803150].

[6] See, e.g., U. Seljak and M. Zaldarriaga, Phys. Rev. Lett. **82**, 2636 (1999) [arXiv:astro-ph/9810092]; Phys. Rev. D **60**, 043504 (1999) [arXiv:astro-ph/9811123]; M. Zaldarriaga and U. Seljak, Phys. Rev. D **59**, 123507 (1999) [arXiv:astro-ph/9810257]; W. Hu, Phys. Rev. D **64**, 083005 (2001) [arXiv:astro-ph/0105117].

[7] W. Hu, Phys. Rev. D **62**, 043007 (2000) [arXiv:astro-ph/0001303].

[8] A. Lewis and A. Challinor, Phys.Rept. **429** (2006) 1-65 [arXiv:astro-ph/0601594].

[9] M. Kaplinghat, L. Knox and Y. S. Song, Phys. Rev. Lett. **91**, 241301 (2003) [arXiv:astro-ph/0303344]; K. Ichikawa, M. Fukugita and M. Kawasaki, Phys. Rev. D **71**, 043001 (2005) [arXiv:astro-ph/0409768]; J. Lesgourgues, L. Perotto, S. Pastor and M. Piat, Phys. Rev. D **73**, 045021 (2006) [arXiv:astro-ph/0511735].

[10] W. Hu and T. Okamoto, Astrophys. J. **574**, 566 (2002) [arXiv:astro-ph/0111606]; M. Kesden, A. Cooray, and M. Kamionkowski, Phys. Rev. D **67**, 123507 (2003) [arXiv:astro-ph/0302536]; C. M. Hirata and U. Seljak, Phys. Rev. D **68**, 083002 (2003) [arXiv:astro-ph/0306354].

[11] R. Scoccimarro, M. Zaldarriaga and L. Hui, Astrophys. J., **527**, 1 (1999); D. J. Eisenstein and M. Zaldarriaga, Astrophys. J., **546**, 2 (2001). A. Cooray and W. Hu, Astrophys. J., **554**, 56 (2001).

[12] A. Cooray, Phys. Rev. D **65**, 063512 (2002) [arXiv:astro-ph/0110415].

[13] K. M. Smith, W. Hu and M. Kaplinghat, Phys. Rev. D **70**, 043002 (2004) [arXiv:astro-ph/0402442].

[14] S. Smith, A. Challinor and G. Rocha, Phys. Rev. D **73**, 023517 (2006) [arXiv:astro-ph/0511703].

[15] W. Hu, Phys. Rev. D **64**, 083005 (2001) [arXiv:astro-ph/0105117].

[16] C. Li and A. Cooray, Phys. Rev. D **74**, 023521 (2006) [arXiv:astro-ph/0604179].

[17] K. Schulten and R. G. Gordon, J. of Math. Phys., **16**, 1971 (1975).

[18] D. Eisenstein, W. Hu and M. Tegmark, Astrophys. J. **518**, 2 (1999)

[19] J. Lesgourgues and S. Pastor, Phys. Rept. **429**, 307 (2006) [arXiv:astro-ph/0603494].

[20] K. M. Smith, W. Hu and M. Kaplinghat, Phys. Rev. D **74** 123002 (2006) [arXiv:astro-ph/0607315].